



2018 STIC Incentive Project (BFRP-RC Standardization) – Final Report (December 2021)

Federal Project No: STIC-004-A; FPID 443377-1

This is the seventh and final report for the Basalt Fiber-Reinforced Polymer (BFRP) Bar Standardization for Reinforced Concrete (RC) with the FHWA allocation memorandum dated March 1, 2018. Part 1 of this report details progress from June 2021 to December 2021. Part 2 of this report summarizes the goals and achievements from the entire project period March 2018 to December 2021.

Part 1 – Progress for final interim period: June 2021 to December 2021.

- i. **Demonstration Project #1 (Link-Slab)** – The final report under Research Contract ***BDV34 986-02*** for has been completed and is included in ***Appendix B***. This report found that BFRP reinforcing performed adequately in restraining shrinkage cracking of the link-slab during approximately one-year after construction.

Part 2 – Final Report Summary: March 2021 to December 2021.

Description of the work:

This project intended to develop standard (guide) design specification, and standard material and construction specifications for basalt fiber-reinforced polymer (BFRP) bars for the internal reinforcement of structural concrete. Tasks involved:

- i. **Goal 1:** Establishing initial design and durability parameters using current state-of-the-art BFRP test data with ***ACI 440.1R*** as a design model framework, supplemented with ***AASHTO's LRFD Bridge Design Guide Specification for GFRP Reinforced Concrete - 2nd Edition (BDGS-2)*** published December 2018.
Achievement 1: It was determined to initially implement BFRP design and durability parameters using the same criteria as that for glass FRP reinforcing. FDOT Research Project ***BDV30 986-01 Final Report*** provided recommendations for design and future refinement (*see Appendix A*).
- ii. **Goal 2:** Develop any necessary FDOT design modifications to ***BDGS-2*** criteria for inclusion of BFRP reinforcing in the ***Structures Design Manual***.
Achievement 2: ***BDV30 986-01 Final Report*** – Chapter 6 design recommendations were incorporated into the ***2020 Structures Manual*** published January 2020, by including

BFRP in *Volume 4 – Fiber Reinforced Polymer Guidelines, Chapter 2*. No increase in BFRP design parameters above those currently established for GFRP were proposed, until additional testing is performed to refine the environmental reduction factors under different limit states. One limitation for BFRP reinforcing was added to avoid using this material in continuously submerged applications until additional research was completed. This requirement is included in *Structures Manual – Volume 4, Section 2.1*. The limitation was included due to inconclusive long-term performance in submerged saltwater applications due to the presence of iron oxides in the basalt fibers. Additional investigation on long-term durability reduction factors is ongoing under the separately funded FDOT research project [BE694 - Improving Testing Protocol and Material Specifications for BFRP Bars](#) to investigate these issues.

- iii. **Goal 3:** Develop FDOT material specification for acceptance similar to the 2017 *ASTM D7957: Standard Specification for Solid Round Glass Fiber Reinforced Polymer Bars for Concrete Reinforcement*.

Achievement 3: Incorporated BFRP reinforcing into *FDOT Standard Specification Section 932-3* in the July 2020 Workbook. The requirements are identical to GFRP reinforcing except the inclusion of an additional qualification test in *Table 932-8* to include Horizontal Shear Strength testing under ASTM D4475, with a minimum strength limit of 5.5 ksi.

Additional chemical constituent requirements to define basalt fibers, was included in FDOT *Materials Manual – Section 12.1, Table 1*, until ASTM material specifications for basalt fibers can be established.

All these requirements were based on [BDV30 986-01 Final Report](#) – Chapter 6 recommendations.

- iv. **Goal 4:** Develop any modifications to the FDOT Construction Specifications based on the current GFRP reinforcing requirements in *BDGS-2* and *FDOT Specification Section 415*.

Achievement 4: No changes to *Section 416* were necessary since the same requirements applicable to GFRP reinforcing were applicable to BFRP reinforcing, and FRP rebar is identified generically in this section without reference to a specific fiber material type.

- v. **Goal 5:** Develop BFRP Reinforcing Database for collection of current and future test results.

Achievement 5: It was determined not to pursue a permanent databased due to lack of sustained funding and resources. Results for BFRP testing are publicly available under this project research in Final Report [BDV30 986-01](#), Chapter 3; previous research in 2014 under [BDK-977-05 “Degradation Assessment of Internal Continuous Fiber Reinforcement in Concrete Environment”](#), Chapter 5; and a separate ongoing research project [BE694 “Testing Protocol and Material Specification for BFRP Rebars” Chapter 4](#).

- vi. **Goal 6:** Deliver a designer focus live workshop in central Florida (and national event if funding permits). Post the delivered training material on [FDOT FRP Innovation](#) website for broader access and future updating.

Achievement 6: The following training was delivered during the project and now accessible from [FDOT FRP Innovation](#) website:

(a) FRP-RC Designer Training held under 3 sessions at the FDOT Transportation Symposium (FTS-2019) on June 4th, 2019 (see [FDOT Transportation Symposium FRP-RC Design - Part 1, Part 2, & Part 3](#));

(b) Peer Exchange BFRP-RC Designer Training was provided to Hawaii DOT Bridge Office on July 22, 2019 (see BFRP-RC Design - [Part 1, Part 2, Part 3, & Part 4](#)) in conjunction with [BEI-2019](#);

(c) [BEI-2019](#) FRP Composites II (Session B-9) on BFRP-RC for coastal and marine structures was provide as the Bridge Engineering Institute conference July 23-25.

Additionally, several papers on BFRP-RC were presented and published in the

[Conference Proceedings](#):

- pp 514-523, “Basalt FRP-RC Standardization for Florida DOT Structures”.
- pp 527-531, “Effect of the Fiber Content on the Tensile Strength Properties of Basalt Fiber Reinforced Polymer Rebars”.
- pp 551-562, “Bond-to-Concrete Characteristic of Basalt Fiber Reinforced Polymer Rebars”.

- vii. **Goal 7:** Demonstration #1 (BFRP-RC Link-Slab) – Develop small demonstration application for use of BFRP reinforcing, and monitor shrinkage and temperature effects overtime.

Achievement 7: Plans where developed and construction completed for FRP-RC link-slab on pedestrian bridge in Port Charlotte, FL (along US 41) where BFRP longitudinal reinforcing was used in place of GFRP reinforcing. Construction of BFRP-RC link slab on Morning Star Waterway bridge was completed in April 2020, with embedded strain gages and data loggers installed March 6-7. Temperature and strain data in the longitudinal BFRP bars was recorded hourly over two periods first from 3/7/2020 to 8/2/2020, then from 11/14/2020 to 2/28/2021. The final report for Research Contract [BDV34 986-02](#). (See [Appendix B](#)), contains construction information and monitoring data results. Concrete strains in the link-slab varied daily by approximately 500 microstrains, but surface cracking on the link-slab was very minimal. District 1 Bridge Maintenance will continue to visually monitor this link-slab every 2-years as part of the routine bridge inspection program.

- viii. **Goal 8:** Demonstration #2 (BFRP Closed Stirrup Fabrication) - An additional demonstration project was added in early 2021 to show the feasibility of fabricating BFRP bent bars with good mechanical performance. Currently for standard GFRP stirrups under [Index 415-010](#), two overlapping U-shaped bars are utilized for building up closed shapes. A closed stirrup with 5 ~ 90-degree corner bends, similar to steel stirrups ([Index 415-001](#), Type 4) was to be fabricated and tested to determine if the minimum mechanical performance for bent bars could be achieved with this more complex shape. The bent shape was based on those typically used for seawall-bulkhead caps, but could possibly be scaled up for pile bent caps.

Achievement 8: Laboratory testing of stirrups was able to verify that the BFRP stirrups exceeded current GFRP/BFRP specification requirements for use on FDOT projects. The straight portion of the bent #4 bar exceeded the minimum requirements for

straight bars (21.6 kips). The bent portion of the stirrup was not tested since the specimen size was too small. See *Appendix C* for Final Test Report.

Project Breakdown and Schedule

The project was broken into three phases, although there was significant overlap between Phases 2 & 3 due to delays in Demonstration #1 due to COVID-19, and addition of Demonstration #2 later in the project as funding became available. **Table 1** shows a summary of the project Phases. There were two research contracts with Florida Universities (Florida State University and North Florida University) and separate testing service performed by the University of Miami's, Structures & Material Laboratory for Demonstration #2.

Phase 1 - was the most extensive and involved the development of BFRP reinforcing standards through evaluation the various tasks of: Existing information collection and curation; Testing of 3 different manufacturers BFRP rebar and two sizes (#3 & #5); Test data and analysis; and Recommendations for Design, Construction and Materials specifications.

Phase 2 - involved two demonstrations for BFRP applications: Monitoring of a link-slab construction project; and fabrication of closed stirrup bent bars with physical testing. The initial conceived test result database for BFRP rebar, was not pursued.

Phase 3 - involved Technology Transfer through presentation of material at several events, and posting this material on the [FDOT Structures FRP-Innovation webpage](#) as detailed in Achievement 6.

PROJECT PHASE	1	2	3
PROJECT WORK TASKS	Develop Standards: <i>(BDV30 986-01)</i> <ul style="list-style-type: none"> Design Specification Materials Qualification and Verification Test Procedures Construction Specification 	<ul style="list-style-type: none"> Demo #1: Full-scale Link-Slab and Monitoring; <i>(BDV34 986-02)*</i> Demo #2: Seawall-bulkhead cap closed BFRP stirrup fabrication and Bar Testing 	<ul style="list-style-type: none"> Technology Transfer <i>(FTS-2019 & BEI-2019)</i> Final Report
PROJECT DELIVERABLES	<ul style="list-style-type: none"> LRFD Guide Design Specification Testing Specification FDOT Construction Specification updates Research Report BDV30 986-01 including Test Results for BFRP straight bars. (Appendix A) 	<ul style="list-style-type: none"> Electronic Database of physical and mechanical properties Research Report BDV34 986-02 (Appendix B) Test Report for Bent Bars (Appendix C) 	Technology Transfer Presentations and posting on FDOT FRP-Innovation webpage for information dissemination and training.
PROJECT TIMELINE	Month 1-11	Month 7- 15 <u>45*</u>	Month 15-17 & 24 <u>45*</u>

Table 1- Project Summary (added 11/30/20), * completion delayed due to COVID-19.

Budget

1. BDV30 986-01 – Performance Evaluation, Material and Specification Development for Basalt Fiber Reinforced Polymer (BFRP) Reinforcing Bars Embedded in Concrete (\$80,446.35).
2. BDV34 986-02 - Instrumentation and Monitoring for BFRP-RC link-slab (\$38,992.15). Cost of BFRP Bars from Basalt World Corp., two invoices (\$644.48 + \$342.20).
3. BFRP Rebar Closed Stirrup Laboratory Testing at University of Miami’s Structures Research Laboratory, two invoices (\$1104 + \$1308 = \$2,412).
4. Additional FDOT staff hours for project oversight and training not included in total.

Project Line Item	FHWA STIC Funds	FDOT Funds (20% match)	Total Budget
Phase 1 <i>BDV30 986-01 – Performance Evaluation</i>	\$80,446.35	\$0.00	\$80,466.35
Phase 2 <i>BDV34 986-02 Demo #1 Monitoring</i> <i>Demo #1 BFRP Rebar Materials</i> <i>Demo #2 Bent Bar Testing</i>	\$14,591.75 \$986.68 \$1,308.00	\$24,400.40 \$1,104.00	\$38,992.15 \$986.68 \$2412.00
Phase 3 <i>Technology Transfer & Final Report</i>		Cost not tracked (include in overhead)	
Total Project	\$97,332.78	\$25,504.40	\$122,837.18

Table 2- Project Phase Funding Distribution as paid 12/31/2021.

Project Schedule

Work Phase	Month																									
	1	2	3	4	5	6	7	8	9	10	11	12	13	14	15	16	18	22	32	33	34	35	36	42	45*	
1a. Develop Design, Materials and Construction Specifications	█																									
1b. BFRP straight bar testing						█	█	█	█																	
2a. Demo #1: Full-scale slab instrumentation and monitoring										█	█	█	█	█				█	█	█	█	█	█			
2b. Demo #2: bulkhead cap closed stirrup fabrication and testing																						█	█	█		
3. Technology Transfer Workshop and Final Report															█	█										█

Table 3- Project Timeline: Month 1 = April 2018; Month 45 = December 2021.

* Completion delayed, due to COVID-19.

Appendices included:

Appendix A - **BDV30-986-01** Final Report – “Performance Evaluation, Material and Specification Development for Basalt Fiber Reinforced Polymer (BFRP) Reinforcing Bars Embedded in Concrete” (170 pages)

Appendix B - **BDV34-986-02** Final Report – “Instrumentation and Monitoring of FRP bars in Bridge Deck Link-Slab” (93 pages)

Appendix C – ***Test Report Number: R-5.10_12-08-20_FDOT*** - “Evaluation of Non-Metallic Fiber Reinforced Polymer (FRP) Bars For Concrete Reinforcement” (BFRP Closed Stirrups) (10 pages)

Appendix A

BDV30-986-01 Final Report – “Performance Evaluation, Material and Specification Development for Basalt Fiber Reinforced Polymer (BFRP) Reinforcing Bars Embedded in Concrete”

(170 pages)

Final Report

**Performance Evaluation, Material and Specification Development for
Basalt Fiber Reinforced Polymer (BFRP) Reinforcing Bars
Embedded in Concrete**

Contract Number BDV30 TWO 986-01
FSU Project ID: 042088

Submitted to:

Florida Department of Transportation
Research Center
605 Suwannee Street
Tallahassee, Florida 32399-0450

Steven Nolan, Ph.D.
Project Manager
FDOT State Materials Office



Prepared by:

Raphael Kampmann, Ph.D.
Principal Investigator
Michelle Rambo-Roddenberry, Ph.D., P.E.
Co-Principal Investigator
Srichand Telikapalli, M.E.
Graduate Research Assistant



**FAMU-FSU
Engineering**

FAMU-FSU College of Engineering
Department of Civil and Environmental Engineering
2525 Pottsdamer Street
Tallahassee, FL 32310

06/30/2019

Disclaimer

The opinions, findings, and conclusions expressed in this report are those of the author(s) and not necessarily those of the Florida Department of Transportation or the U.S. Department of Transportation.

Acknowledgements

The authors would like to thank the Florida Department of Transportation (FDOT) for financial support for this study and for a progressive approach toward an implementation of FRP rebars in concrete construction. Special thanks go to Steven Nolan and Chase Knight for technical and engineering support. Likewise, engineering advice and technical know-how was provide by Francisco De Caso from the University of Miami, who effectively acted as a co-PI. His FRP rebar knowledge and advices were indispensable for this report. In addition, many people have contributed to the successful completion of this research project, and this study would have not been possible without their assistance and help. Andre Schmidt and Tim Schneider worked tirelessly on numerous test setups, experiments, and other research tasks to obtain important data and to conducted the relevant analysis procedures. Susanna Becker and Jessica Frahling supported many tasks and were always available and helpful when called upon. Steven Squillacote provided exceptional hands-on support for all preparation tasks and for any laboratory efforts. In addition, the authors would like to thank the High Performance Material Institute (HPMI) for providing test equipment; specifically Marquese Pollard provided a lot of help for all tensile and shear tests that were conducted for this research.

Executive Summary

Florida is a coastal state with bridge infrastructure exposed to aggressive environments through direct and indirect contact with saline solutions. Due to this exposure, conventional black steel reinforcement that is traditionally used for bridges is corroding prematurely, resulting in early structural deterioration which in-turn may cause huge financial and personal losses. In a successful effort to overcome such corrosion and deteriorating effects, reinforcing bars (rebars) made from fiber reinforced polymers (FRP) were developed. FRP rebars are composite materials, in which fibers, resin, and sizing (interface material between fibers and resin) are the main constituent materials. Different fiber types are used to produce such rebars, and the most common type in the US is glass fiber. In the former Soviet Bloc, continuous fibers made from basalt rock were favored and since the collapse of the Union of Soviet Socialist Republics (USSR), previously proprietary/military technologies have been made public and continuous basalt fibers (CBF) have entered the world market as a viable alternative to glass fibers. CBF are now used to produce basalt fiber reinforced polymers (BFRP) in rebar applications and these rebars are now imported or produced in the North America. Various types of BFRP rebars with dissimilar sizes, physical and strength properties, are currently produced to be used for civil engineering construction. In this project, representative and commonly available BFRP rebars were tested to evaluate various physical properties (cross-sectional properties, fiber content, and moisture absorption properties) and different strength characteristics (horizontal and transverse shear, tensile strength, elastic modulus, and bond-to-concrete properties) according to ASTM standards, in an effort to develop basalt specific acceptance criteria for FDOT Specifications Section 932, which governs the use of non-metallic auxiliary materials for civil engineering construction.

BFRP rebars from three different manufacturers, two different production lots, and two most commonly used rebar sizes (# 3 and # 5) were included in this study. The obtained results were

used to evaluate the performance of each rebar type in a relativistic comparison to existing benchmark values for glass FRP (GFRP) rebars. The fiber content test proved that all tested samples had consistent and nearly identical results with acceptable performance. Moisture absorption property of the rebars varied significantly based on the manufacturers, type of raw materials used, and the production techniques. Transverse shear strength of the tested BFRP rebars proved to be 116% stronger than GFRP bars. Tensile strength measurements and horizontal shear strength measurements were consistent for all rebar types and the recorded values surpassed the strengths generally reported for GFRP rebars. The bond-to-concrete strength of the tested BFRP rebars were not significantly different from bond-to-concrete strength commonly reported for GFRP rebars because similar surface enhancement techniques are used for either rebar type. Based on the obtained results it was noted that the tested BFRP rebars surpassed the strength related acceptance criteria for GFRP rebars. While the manufacturer reported properties varied and each rebar type performed different, the tested BFRP rebars were generally stronger (higher performance) than GFRP rebars. Ultimately, it was found that BFRP rebars are a suitable and viable alternative for construction in Florida and that those materials should be considered for FDOT Specification 932.

Table of Contents

List of Figures	x
List of Tables	xiv
1 Introduction	1
1.1 Introduction	1
1.2 Problem Statement	4
1.3 Project Objectives	5
1.4 Project Scope	6
1.5 Report Organization	6
2 Background	8
2.1 Igneous Rocks	9
2.2 Fiber Types and Production	10
2.2.1 Basalt Fiber	10
2.2.2 Glass Fiber	11
2.2.3 Carbon Fiber	12
2.2.4 Aramid Fiber	13
2.2.5 Fiber Types Summary	13
2.2.6 Properties of Basalt Fibers	14
2.3 Sizing	14
2.4 Resin Types and Properties	14
2.4.1 Epoxy	16
2.4.2 Polyester	16
2.4.3 Vinylester	17

2.5	BFRP Rebar Production	17
2.5.1	Pultrusion	18
2.5.2	Wet Lay-Up	20
2.6	BFRP Rebar Properties	21
2.7	Test Procedures for FRP Rebar	23
2.7.1	Physical Characteristics	23
2.7.2	Strength Characteristics	25
2.8	Failure Characteristics of FRP Rebars	30
2.9	Durability of FRP Rebars	31
2.10	Concrete Elements Reinforced with BFRP	35
3	BFRP Building Compliance and Market	38
3.1	Regulations for FRP Rebars	38
3.2	Acceptance Criteria for FRP Rebars	41
3.3	Global BFRP Rebar Manufacturer Analysis	43
3.4	BFRP Products Database	48
4	Experimental Program	50
4.1	Introduction	50
4.2	Experimental Concept	50
4.2.1	Acceptance Criteria	52
4.3	Equipment and Test Devices	54
4.3.1	Cutting Saw	54
4.3.2	Precision Saw	55
4.3.3	Caliper	55
4.3.4	Precision Balance	56
4.3.5	Support Frame for Specimen Alignment	56
4.3.6	Test Fixture for Transverse Shear Tests	57
4.3.7	Test Fixture for Apparent Horizontal Shear Tests	60
4.3.8	Test Fixture for Tensile Strength Tests	61
4.3.9	Test Fixture for Bond-to-Concrete Test	62

4.3.10	Load Frame	65
4.3.11	Extensometer	66
4.4	Test Procedures	67
4.4.1	Cross-Sectional Area Test — Specific Gravity (Relative Density)	67
4.4.2	Fiber Content Test — Ignition Loss	68
4.4.3	Moisture Absorption Test	69
4.4.4	Transverse Shear Strength Test	70
4.4.5	Apparent Horizontal Shear Test	70
4.4.6	Tensile Strength and Modulus Test	71
4.4.7	Bond-to-Concrete Strength Test	72
4.5	Data Acquisition and Data Analysis	72
5	Results	74
5.1	Introduction	74
5.2	Cross-Sectional Properties	74
5.3	Fiber Content	75
5.4	Moisture Absorption	78
5.5	Transverse Shear Test	78
5.5.1	Load vs. Displacement	79
5.5.2	Stress vs. Displacement	81
5.6	Modes of Failure	84
5.7	Summary of Transverse Shear Properties	86
5.8	Apparent Horizontal Shear Test	87
5.8.1	Load vs. Displacement	87
5.8.2	Stress vs. Displacement	88
5.9	Modes of Failure	92
5.10	Summary of Horizontal Shear Strength Properties	93
5.11	Tensile Test	94
5.11.1	Load vs. Displacement Behavior	94
5.11.2	Stress vs. Strain Behavior	96
5.12	Modes of Failure	99

5.13	Summary of Tensile Properties	101
5.14	Bond-to-Concrete Strength	102
5.15	Bond Stress vs. Slip at Free End	102
5.16	Modes of Failure	108
5.17	Summary of Bond-to-Concrete Strength	111
5.18	BFRP Rebar Performance	111
6	Discussion	115
6.1	Research Significance	115
6.2	Critical Analysis of Major Findings	116
6.2.1	Cross-Sectional property	116
6.2.2	Fiber Content	117
6.2.3	Moisture Absorption of BFRP rebar	118
6.2.4	Transverse Shear Strength	118
6.2.5	Apparent Horizontal Shear Strength	119
6.2.6	Tensile Properties	120
6.2.7	Bond-to-Concrete Strength	121
6.3	Supplementary Findings	121
6.4	BFRP Design Specifications	122
6.4.1	Design Guide Considerations	126
6.5	Research Limitations	127
6.6	Future and Further Directions	128
7	Conclusions	131
7.1	Summary	131
7.2	Conclusions	132
7.3	Further Recommendations	134
	Appendices	144
A	Individual Specimen Results	145
A.1	Density and Cross-Sectional Dimension Test	145

A.2	Fiber Content Test	147
A.3	Transverse Shear Test	148
A.4	Horizontal Shear Test	149
A.5	Tensile Test	151
A.6	Bond-to-Concrete Test	152

List of Figures

2.1	Continuous basalt fiber production process (Ipbüker et al., 2014)	10
2.2	Thermoset polymeric resin used in FRP rebars	15
2.3	Schematic diagram of FRP rebar pultrusion (Borges et al., 2015)	18
2.4	Obtain position of exothermic peak (Borges et al., 2015)	19
2.5	Basalt FRP rebar production steps	21
2.6	Tensile stress and strain of different types of FRP according to Busel (2016)	22
2.7	Transverse shear fixture — Main body of fixture disassembled	25
2.8	Transverse shear fixture	26
2.9	Tensile strength test load transfer (Schesser et al., 2014)	27
2.10	FRP rebar tensile failure mechanism (Ehrenstein, 2006)	31
3.1	Chronology of documents related to the use of FRP rebar for concrete reinforcement	39
3.2	BFRP manufacturer locations	45
3.3	Production and storage strategies chosen by BFRP manufacturers	47
3.4	BFRP production rates (as reported by manufacturers)	48
4.1	Sample pictures of tested BFRP # 3 Rebars	52
4.2	Sample pictures of tested BFRP # 5 Rebars	52
4.3	Saw and diamond blade for BFRP rebar cutting	54
4.4	Precision saw	55
4.5	Electronic caliper	56
4.6	Precision scale, used to meet ASTM D 792 requirements	57
4.7	Tensile test preparation alignment frame	58
4.8	Transverse shear test concept	58

4.9	Transverse shear test — methodology	59
4.10	Transverse shear box — parts	59
4.11	Horizontal shear test concept	60
4.12	Horizontal shear test — methodology	60
4.13	Horizontal shear test fixture	61
4.14	Bottom unit connected to actuator	62
4.15	Tensile fixture installed in load frame	62
4.16	Bond-to-concrete experimental setup	63
4.17	Schematic of the mold	64
4.18	Fixing the rebar and the plastic tube	64
4.19	Laboratory setup in the HPMI	65
4.20	MTS control panel	66
4.21	MTS extensometer	67
5.1	Fiber content percentage of rebars from all manufacturers	76
5.2	Fiber content specimen of rebar type C #3, 5 after test	77
5.3	Fiber content specimen of rebar #3 after test	77
5.4	Moisture absorption results of rebars from all manufacturers	78
5.5	Extension vs. transverse shear load behavior of type A rebars Lot 1 size 3 and 5	79
5.6	Extension vs. transverse shear load behavior of type B rebars Lot 1 size 3 and 5	80
5.7	Extension vs. transverse shear load behavior of type C rebars Lot 1 size 3 and 5	80
5.8	Extension vs. transverse shear load behavior of type C rebars Lot 2 size 3 and 5	81
5.9	Transverse shear stress vs. extension behavior of rebar type A Lot 1 size 3 and 5	82
5.10	Transverse shear stress vs. extension results of rebar type B Lot 1 size 3 and 5	82
5.11	Transverse shear stress vs. extension behavior of type C Lot 1 size 3 and 5	83
5.12	Transverse shear stress vs. extension behavior of type C Lot 2 size 3 and 5	83
5.13	Failure pattern for tested rebar after transverse shear test	85
5.14	Extension vs. horizontal shear load behavior of rebar type A Lot 1 size 3 and 5	87
5.15	Extension vs. horizontal shear load behavior of rebar type B Lot 1 size 3 and 5	88
5.16	Extension vs. horizontal shear load behavior of type C Lot 1 size 3 and 5	89
5.17	Extension vs. horizontal shear load behavior of type C Lot 2 size 3 and 5	89

5.18	Horizontal shear stress vs. extension behavior of rebar type A Lot 1 size 3 and 5 . . .	90
5.19	Horizontal shear stress vs. extension behavior of rebar type B Lot 1 size 3 and 5 . . .	90
5.20	Horizontal shear stress vs. extension behavior of rebar type C Lot 1 size 3 and 5 . . .	91
5.21	Horizontal shear stress vs. extension behavior of rebar type C Lot 2 size 3 and 5 . . .	91
5.22	Failure pattern for tested rebar after horizontal shear test	92
5.23	Tensile strength vs. displacement behavior of rebar type A Lot 1 size 3 and 5	94
5.24	Tensile strength vs. displacement behavior of rebar type B Lot 1 size 3 and 5	95
5.25	Tensile strength vs. displacement behavior of rebar type C Lot 1 size 3 and 5	95
5.26	Tensile strength vs. displacement behavior of rebar type C Lot 2 size 3 and 5	96
5.27	Tensile stress vs. strain behavior of rebar type A Lot 1 rebar size 3 and 5	97
5.28	Tensile stress vs. strain behavior of rebar type B Lot 1 rebar size 3 and 5	97
5.29	Tensile stress vs. strain behavior of rebar type C Lot 1 rebar size 3 and 5	98
5.30	Tensile stress vs. strain behavior of rebar type C Lot 2 rebar size 3 and 5	98
5.31	# 3 rebar final failure pattern after tensile test	100
5.32	# 5 rebar final failure pattern after tensile test	100
5.33	Free end slip behavior of the tested rebar type A Lot 1 # 3	103
5.34	Free end slip behavior of the tested rebar type A Lot 1 # 5	104
5.35	Free end slip behavior of the tested rebar type A Lot 1 # 3 and # 5	104
5.36	Free end slip behavior of the tested rebars type B Lot 1 # 3	105
5.37	Free end slip behavior of the tested rebars type B Lot 1 # 5	105
5.38	Free end slip behavior of the tested rebars type B Lot 1 # 3 and # 5	106
5.39	Free end slip behavior of the tested rebar type C Lot 1 # 3	106
5.40	Free end slip behavior of the tested rebar type C Lot 1 # 5	107
5.41	Free end slip behavior of the tested rebar type C Lot 1 # 3 and # 5	107
5.42	Overview rebar surface after bond strength test on type A Lot 1 rebar # 3	108
5.43	Overview rebar surface after bond strength test on type A Lot 1 rebar # 5	108
5.44	Overview rebar surface after bond strength test on type B Lot 1 rebar # 3	109
5.45	Overview rebar surface after bond strength test on type B Lot 1 rebar # 5	109
5.46	Overview rebar surface after bond strength test on type C Lot 1 rebar # 3	109
5.47	Overview rebar surface after bond strength test on type C Lot 1 rebar # 5	110

6.1 Gaussian distribution for tensile strength of # 3 rebars 125

6.2 Gaussian distribution for tensile strength of # 5 rebars 125

List of Tables

2.1	Average chemical composition of basaltic rocks based on 3594 analyzed rock samples	9
2.2	Typical properties of resin matrices	16
2.3	Environmental reduction factor for various fibers and exposure conditions	32
3.1	Required test procedures and specimen quantities per acceptance test and production lot	42
3.2	Required sizes and tensile loads of FRP reinforcing bars	43
3.3	Production logistics and rates per manufacturer	46
3.4	BFRP rebars produced by manufacturer	49
4.1	Physical and mechanical tests on BFRP rebars	51
4.2	Physical characteristics of tested BFRP rebars	52
4.3	Acceptance criteria for GFRP rebar # 3	53
4.4	Acceptance criteria for GFRP rebar # 5	53
5.1	Statistical evaluation of diameter measurements for rebar size # 3 and # 5	75
5.2	Transverse Shear test statistical values for each sample group (US Customary Units)	86
5.3	Horizontal Shear test statistical values for each sample group (US Customary Units)	93
5.4	Tensile strength test statistical values for each sample group (US Customary Units)	102
5.5	Bond-to-concrete strength test statistical values for each sample	111
5.6	Acceptance criteria for rebar type A # 3	112
5.7	Acceptance criteria for rebar type A # 5	112
5.8	Acceptance criteria for rebar type B # 3	113
5.9	Acceptance criteria for rebar type B # 5	113
5.10	Acceptance criteria for rebar type C # 3	114

5.11	Acceptance criteria for rebar type C # 5	114
6.1	Guaranteed shear and bond-to-concrete strength of rebars	123
6.2	Guaranteed strength and elastic modulus of rebars	124
6.3	Reduction factors	127
A.1	Diameter measurements for each individual specimen	146
A.2	Fiber content test results for each individual specimen	147
A.2	Fiber content test results for each individual specimen	148
A.3	Transverse shear test results (ultimate values) for each individual specimen	148
A.3	Transverse shear test results (ultimate values) for each individual specimen	149
A.4	Horizontal shear test results (ultimate values) for each individual specimen	150
A.5	Tensile strength test results (ultimate values) for each individual specimen	151
A.5	Tensile strength test results (ultimate values) for each individual specimen	152
A.6	Bond-to-Concrete strength test results for each individual specimen (Imperial Units)	152
A.6	Bond-to-Concrete strength test results for each individual specimen (Imperial Units)	153
A.7	Bond-to-Concrete strength test results for each individual specimen (Metric Units) .	153
A.7	Bond-to-Concrete strength test results for each individual specimen (Metric Units) .	154

Chapter 1

Introduction

1.1 Introduction

The Florida Department of Transportation (FDOT) continues to implement innovative materials to enhance the sustainability and durability of the infrastructure. Because Florida is a coastal state with many structures exposed to saltwater (e.g., the splash zone for bridge piers), the FDOT currently works progressively on research and applications of non-corrosive materials, such as fiber reinforced polymers (FRP) reinforcement bars (rebars), in an effort to replace or substitute traditional steel rebars. Over the last two decades, technological advancements have facilitated the use of glass fiber reinforced polymer (GFRP) and basalt fiber reinforced polymer (BFRP) composites as internal rebars for concrete structures. These emerging materials are a modern, viable alternative to traditional steel reinforcement due to significant advantages (e.g., magnetic transparency, lightness, and — most importantly — corrosion resistance) that can lead to more durable concrete members and extended structural life. Hence, a key initiative for the Florida Department of Transportation is the progressive implementation of FRP technology for concrete reinforcement in infrastructure projects.

In a recently completed FDOT research project, GFRP rebars were evaluated for physio-mechanical and bond-to-concrete properties to properly implement GFRP rebars in concrete for the use in aggressive environments (FDOT research project BDV 30 977-18). The project showed that the material properties of FRP rebars are beneficial for the use in concrete, and that the technology has the potential for standardized use in publicly funded construction projects via im-

plementations in design specifications (FDOT's Standard Specifications for Road and Bridge Construction — Section 932-3). However, the past projects have mostly focused on glass FRP rebars, because glass fibers are more dominant in the US market and Basalt FRP rebars have not yet been thoroughly investigated for public agencies. The activities performed for this project followed similar efforts as conducted for BDV 30 977-18, but target the virgin material characteristics and bond-to-concrete properties of basalt fiber reinforced polymer reinforcement bars (BFRP Rebars) to evaluate a second/additional alternative that can replace traditional rebars.

Basalt is a volcanic rock which can be formed into continuous fibers through melting raw basalt at approximately 1500 °C and using technologies similar to those used for the production of E-Glass and AR-Glass fibers. Only raw basalt rock is necessary to produce the fibers, and the purity of the basalt depends on the source rock only. Because no additional chemical components are needed to produce basalt fibers, they are considered a “greener product” (relative to glass fibers). Basalt filaments are formed by platinum-rhodium bushings (similar as for glass filaments), and a sizing agent is applied during the cooling process, before the fibers are spooled. Due to the inherent properties of basalt and the different chemistry from glass fibers, basalt fibers are more chemically resistant, have a higher tensile strength, and have a modulus of elasticity that exceeds the elasticity of E-glass fibers by about 15 % to 30 % (Rarnalaishnan and Tolmare, 1998). In addition, basalt fibers are more UV-resistant, have a higher fire resistance, and better retain physical characteristics in cold temperatures. Finally, the production of basalt fibers are more environmentally friendly than the production of glass fibers because toxic ingredients can be omitted.

For the production of BFRP reinforcing bars, the basalt fibers are embedded in a polymeric resin matrix, similar to GFRP rebars. In a high quality produced basalt fiber reinforced polymer rebar, the basalt fibers carry the load (primarily in tension), while the resin matrix protects the fibers, binds them, and also transfers the load between them. Matrices are typically thermosetting resins; epoxy resins seem to be preferred for BFRP because of the high mechanical toughness and excellent corrosion resistance; coupled with ease of manufacturing, epoxy resins are ideal for FRP pultruded systems. Drawbacks of epoxy resins include low modulus of elasticity, sensitivity to abrasion, relatively low fatigue resistance, and high cost. The main factors affecting the characteristics of an FRP rebar include fiber volume, dimensional effects, rate of curing, manufacturing process, and quality control measures during manufacturing. The unit weight of BFRP rebars is about one-third

of steel, which reduces transportation costs and makes the rebars easy to handle at the job site, yielding additional benefits to its implementation (Rarnalaishnan and Tolmare, 1998). To ensure proper bond between the the pultruded BFRP rebar and the concrete, a surface treatment is applied to increase the friction at the bond interface or to improve the interlocking effect. Manufacturers have developed different BFRP rebar types, where the surface enhancement varies (sand-coated, helical wrapping, lugs, etc.). Accordingly, various different BFRP rebars exist and their properties are highly dependent on the used raw and the proprietary production techniques.

The American Concrete Institute Committee 440 (ACI440) has led the effort to address the technical implementation for GFRP rebars by developing and publishing test methods, specifications, and design guidelines (ACI Committee 440, 2006, 2012, 2008b, 2013). Previous versions of ACI440 (ACI Committee 440, 2008a) and the 2010 version of the Canadian-CSA Specifications for Fiber Reinforced Polymers (Canadian Standard Association, 2010) were developed to standardize glass, carbon, and aramid FRP bars. The Canadian Standards Association (CSA) has led the western effort for developing specifications and design guidelines for BFRP, and the new CSA S807 (Benmokrane, 2018) standard includes FRP bars made with basalt fibers that emphasize the current importance of this material and the confidence of a commercialized usage in the field (Vincent et al., 2013). Similarly, ASTM Committees D30 and D20 have addressed the emergence of this technology by developing a number of test methods (ASTM-International, 2015a) intended to characterize GFRP rebars. In addition, the FDOT has developed documents to aid the implementation and design of GFRP rebar technology for the built infrastructure, specifically Section 932 for nonmetallic accessory materials for concrete pavement and concrete structures (Ruelke, 2014), and more recently the fiber reinforced polymer guidelines (FRPG) (Florida Department of Transportation, 2015) are important documents in this context. At the national level, AASHTO has also developed guides for the use of FRP technology (AASHTO, 2012) for externally bonded systems. AASHTO (2018) describes the unique material properties of GFRP composite materials and lists provisions for the design and construction of concrete bridge elements reinforced with GFRP reinforcing bars. It is desired to add BFRP specific criteria to these specifications and guidelines as soon as practical to provide redundant supply chains and potentially improved performance expectations. Moreover, the International Code Council Evaluation Service (ICC-ES), which is the industry leader in performing technical evaluations for code compliance as part of the International

Code Council (ICC) that develops model codes and standards, published the Acceptance Criteria for the use of GFRP and BFRP rebars for concrete reinforcement, known as AC454 (International Code Council Evaluation Services, 2017). Hence, today any structure that is to be built according to the requirements of the Florida Building Code, which is based on the model code (International Building Code, IBC), can be realized with BFRP rebar technology.

Unlike carbon and glass fiber reinforced materials, basalt fibers have not been widely used, which results from a lack of research and required testing to establish this material as a serious competitor. The increasing demand on the infrastructure, as well as environmental challenges due to the unique climate and location of the State of Florida, resulting in accelerated degradation of infrastructure, need to be addressed by making progress toward safe and long-term infrastructure solutions.

1.2 Problem Statement

In recent years, the number of reinforced concrete (RC) structures specifying FRP rebars has increased significantly due to a more pronounced need for more resilient structures. In response to these structural trends, the number of BFRP rebar manufacturers has grown quickly. However, compared to other construction materials (and specifically compared to traditional steel rebar manufacturing), the production of BFRP rebars has not been standardized yet. Consequently, different products have been developed by various manufacturers, and these products differ notably in characteristics — dependent on the raw materials, material proportions, production processes, and final geometric features. Accordingly, the most suitable products are yet to be identified and the present state-of-production-practice has to be studied to identify the currently available products and the market trends in an effort to centralize the most important strength and material properties that engineers will need throughout the structural design process. This is important because inferior rebar products are available in the current market, and if these products remain indistinguishable from high-quality BFRP rebars, they may lead to misuse and potential failure. To consistently and safely use or implement BFRP rebar technology for infrastructure projects, the material properties of high-quality rebar products from different manufacturers have to be characterized and evaluated to develop robust acceptance criteria for basalt based FRP rebars in FDOT Specifications Section 932. A strategic approach is needed to better use and improve this technology such that the different products can be categorized and the effect of individual BFRP rebar attributes can be determined.

Minimum criteria specific to Basalt FRP rebars are desirable because such benchmark values will help manufacturers most efficiently target defined quality parameters that FDOT, and ultimately other state DOTs, can rely on. Likewise, threshold values are needed, under the mandatory low-bid procurement system, to guarantee safe and reliable designs of future concrete structures, which are internally reinforced with BFRP rebars.

1.3 Project Objectives

The project objective was to complement existing FRP rebar specifications and to identify non-corrosive BFRP rebar technologies for concrete reinforcement with suitable surface enhancements for the construction of durable, resilient, and potentially more sustainable infrastructure in Florida. It was the goal to provide test data and recommendations to inform the currently ongoing efforts toward a full implementation of this emerging technology by the FDOT, such that special project specific approvals for BFRP rebars may not be necessary in the future. To embrace BFRP rebar technology, a comprehensive literature review and a worldwide state-of-the art summary of currently manufactured BFRP rebars was necessary to provide relevant information for the selection of representative BFRP rebars for the subsequent experimental program. It was the intention of the experimental program to target physical, mechanical, and bond-to-concrete characteristics of BFRP rebars to evaluate the most essential material properties of virgin (or unaged) BFRP rebars in an effort to classify the material performance. These tasks aimed to identify suitable BFRP rebar technologies for use in Florida. Because potential future research projects will focus on refining durability modeling of BFRP rebars, it was an additional goal to obtain benchmark values for subsequent studies — in which BFRP rebars may be exposed to harsh environments for extended times, before they are tested for property retention characteristics. While material characterization was an important objective for this research project, the ultimate goal was to provide experimentation-based recommendations and relevant updates to existing FDOT guidelines and specifications for the use of BFRP rebar in concrete structures. Likewise, recommendations and relevant updates for future updates of the 2nd edition of the AASHTO LRFD Bridge Design Guide Specifications for the GFRP Reinforced Concrete was an additional goal of this research.

1.4 Project Scope

In this research project, the physical characteristics and material properties of three representative but distinct BFRP rebars were evaluated. These three rebar types were produced by different manufacturers (Galen Panamerica, RockRebar[®], Pultrall), and each rebar type had various distinctive features (dissimilar fiber types, various resin types, different surface enhancement properties, etc.). Representative samples (specimen groups) of two commonly used rebar sizes (# 3 and # 5) were exposed to a multitude of experiments in their virgin material state. First, the physical properties of each rebar type and size were studied before the mechanical strength properties were evaluated. Physical tests on rebars included density measurements or measurement of cross-sectional dimensions, percentage of fiber contents, and moisture absorption characteristics. Mechanical tests were conducted to determine the transverse shear strength, horizontal shear strength, tensile strength including elastic modulus properties, as well as the bond-to-concrete characteristics. All test data were statistically reduced and compared to the prevailing material specifications or acceptance criteria for FRP rebars (AC454, ASTM D7957, etc.). Because ASTM acceptance criteria for BFRP rebars in the US are yet to be established, the performance of the tested BFRP rebars was evaluated based on the available acceptance criteria for glass FRP rebars according to FDOT Specification Section 932. Based on the experimental findings, theoretical analysis of the results, and literature reflections, recommendations were provided to supplement FDOT Specifications Section 932 for the implementation of acceptance criteria for BFRP rebars and to develop AASHTO design guide recommendations for BFRP reinforced concrete structures.

1.5 Report Organization

To provide a structured overview of the completed research, this report was divided into seven chapters, which are briefly described here. After the introduction presented in this chapter, the following Chapter 2 presents background information about BFRP rebar technology, historical developments in the basalt fiber and BFRP rebar industry, as well as information about raw constituent materials, and the production processes. In addition, existing literature with a focus on physical and mechanical properties of BFRP rebars are presented. Chapter 3 describes the development of BFRP rebar specifications and the current state-of-the-market (industry profile). A detailed description of

the experimental methodology, the conducted test procedures, and the experimental concepts are detailed in Chapter 4. The relevant test protocols (ASTM, ACI, etc.) that were followed for each individual experiment are described to ensure the repeatability and accuracy of the experimental approach. Likewise, all equipment and test devices are listed and described in detail along with the materials that were needed to prepare the specimens for testing. While Appendix A lists all individual test results for each tested specimen, Chapter 5 concisely presents the obtained test group results for all conducted experiments in the form of graphs and tables; it also documents the typical failure patterns for each conducted test procedure and for each evaluated rebar type. A detailed discussion addressing recommendations for BFRP strength and material properties along with design specifications for FDOT Specifications Section 932 and propose AASHTO design guidance for BFRP reinforced concrete structures is presented in Chapter 6. Finally, in Chapter 7, a summary of this project is followed by a concise list of conclusions that were drawn based on the entirety of this research project.

Chapter 2

Background

After a brief introduction of the research, this chapter provides a detailed description of Basalt Fiber Reinforced Polymer (BFRP) reinforcement bars (rebars) from the production of the fiber over the properties of the composition material of the rebar and its usage. Fibers and composite materials have gained a lot of attention in the recent decades because of their wide availability and special properties like the high strength-to-weight ratio. The first attempts to produce basalt fibers go back to Paul Dhé (from Paris, France), who invented a basalt fiber furnace in the United States in 1923 (Dhé, 1923; Colombo et al., 2012). The technology did not gain a lot of traction in the US due to initial production difficulties and more profitable opportunities with glass fibers. After the manufacturing process for glass fibers was successfully industrialized in Toledo, Ohio, by Games Slayter in 1933 (Slayter, 1938), the major fiber producers in the US abandoned basalt fiber research in favor of their main glass products (Faruk et al., 2017). However, extensive research on basalt fibers was conducted in the former Soviet Union, during the Cold War (Jamshaid and Mishra, 2016), for military purposes in a search for ballistic resistant textiles. After the Soviet Union collapse in 1991, the research projects were declassified (in 1995) and released for civilian applications. In consequence, basalt fibers are a recent development in the construction industry and most basalt fiber producing companies are now located in countries that used to be associated with the Eastern Bloc (Zych and Wojciech, 2012). Nowadays, basalt fibers gain attention from different industry fields all over the world. Before the fibers can be used for composite products, the fiber itself is produced from raw basalt. Therefore, the next section 2.1 introduces the origin of continuous basalt fibers.

2.1 Igneous Rocks

The source material is an important factor in the characterization process for basalt fibers. Igneous rocks are one of the three main classes of rocks, besides sedimentary and metamorphic rocks. Igneous rocks are formed from molten material, mostly classified on the basis of their composition (either mineralogical or chemical) and according to their silica content. Molten rock material below the surface is called magma and then described as lava as soon as it reaches the earth surface. Igneous rocks have to be separated into plutonic rocks (coarse-grained igneous rocks that solidified within the crust), which are usually classified according to their mineralogical composition, or volcanic lava rocks (fine-grained and solidified at or very near the earth crust surface with a faster cooling process), which are classified according to their chemical composition (Best, 2003).

Basalt is the most common volcanic rock on Earth and basaltic rocks (including gabbro, diabase, and their metamorphosed equivalents) are the most common rocks in the Earth's crust. Gabbro is a coarse-grained plutonic equivalent of basalt that solidified within the Earth's crust. Diabase is compositionally equivalent to gabbro and basalt but in its physical structure (grain structure) between them. It forms into basalt when it solidifies rapidly and to gabbro when more time is given for the crystals to grow (Maitre, 2002). Besides the structural differences, the chemical structure is defined for all three types of raw basalt similar to that shown in Table 2.1. Basalt has a strict

Table 2.1: Average chemical composition of basaltic rocks based on 3594 analyzed rock samples

Rock Type	SiO_2	TiO_2	Al_2O_3	Fe_2O_3	FeO	MnO	MgO	CaO	Na_2O	K_2O	P_2O_5
Basalt	50	1.8	16	3.9	7.2	0.2	6.8	9.7	3.0	1.1	0.3

chemical definition that contains more than 45 percent and less than 52% of SiO_2 and less than five percent of total alkalis ($K_2O + Na_2O$). High silica and low iron contents ensure the production of fibers with high strength properties. When meeting the requirements of the chemical composition, any of the described raw materials can be used for the basalt fiber production, which is regulated by different national documents. Russian specifications for basalt fiber are defined as melted basalt or gabbro-diabase (ISC, 2014). After the clarification of the proper source for the fiber production, the next section 2.2 shows the manufacturing process of fibers.

2.2 Fiber Types and Production

The section below summarizes the main fiber types that are in use for structural engineering applications. Additionally, the two production methods for basalt and glass fibers are explained to have a comparison to the most used fiber types.

Fibers commonly used to produce FRP rebars are glass, carbon, and aramid because of their higher tensile strength in comparison to traditional steel. As a drawback compared to steel, tensile failure of FRP rebars show linear-elastic response with sudden breakage. Basalt fibers show better mechanical properties than glass fibers, and they are more widely available and cheaper than carbon fibers (Zych and Wojciech, 2012). Continuous basalt fibers have become commercially available as an alternative to glass fibers. Glass has been the predominant fiber for many civil engineering applications because of an economical balance of cost and specific strength properties. In addition, they were (in exactly the same way becoming available to the international market offering different kinds of fibers (ACI Committee 440, 2007). The following subsections detail the production of different fiber types, starting with basalt based fibers.

2.2.1 Basalt Fiber

According to the Russian specifications for fiber reinforced polymer bars, basalt fibers for polymer composites reinforcement are made from melted basalt or gabbro-diabase (ISC, 2014) as described in Section 2.1. The schematic process of the basalt fiber production is shown in Figure 2.1. Starting

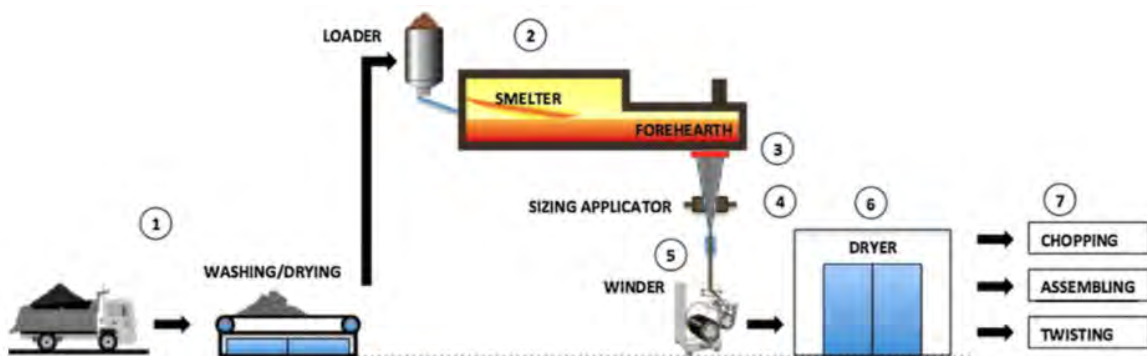


Figure 2.1: Continuous basalt fiber production process (Ipbüker et al., 2014)

on the left side of the figure, the raw basaltic rock is first crushed, washed, and then transported to a furnace. The melting process requires a minimum melting temperature of approximately 1450°C

(2640°F). Unlike glass, infrared energy is absorbed by the opaque basalt, and therefore, it is more difficult to uniformly heat the entire basalt mixture. Molten basalt must be held in the smelter for extended periods of time to ensure a homogeneous temperature. When melting occurs and uniformity is reached by removal of gases, the molten basalt flows into the fore hearth (Ipbüker et al., 2014). The molten material is forced through a platinum/rhodium crucible bushing with 9 to 24 micrometer nozzles to extrude continuous fibers. Basalt fibers are sized during the manufacturing process (in the same way as glass) to protect the fiber and to impart the resin compatibility needed for optimum performance. Sizing such as silences, starch, gelatin, oil, or wax is applied to improve the bond and to minimize degradation of filament strength that would otherwise be caused by filament-to-filament abrasion (Bagherpour, 2012; Zych and Wojciech, 2012). The fibers can be made in the form of chopped fibers (cheaper and lower mechanical properties) or continuous fibers rovings (spinneret method) (Fiore et al., 2015). After the basalt fibers are produced, they are converted (packaged or spooled) into a suitable form for each particular application (Pavlovski et al., 2007).

Only raw basalt is necessary to produce the fibers, and the purity of the raw material for the fibers depends only on the rock source. As a consequence of specific kinds of original rock sources, more than one category of basalt fibers with different chemical compositions may be obtained. Due to these factors, basalt fibers may take on different mechanical or physical properties (Zych and Wojciech, 2012). During the production process no additional chemical components are needed to produce basalt fibers. Toxic ingredients, typically used in glass formulation, can be omitted, therefore, they are considered as a “greener product” (relative to glass fibers) (Zych and Wojciech, 2012). The production of glass fibers requires the addition of several ingredients and a tedious mixing process. The properties and production process are listed in the upcoming subsection 2.2.2.

2.2.2 Glass Fiber

This subsection describes glass fibers and their production for comparison to basalt. The most common types of glass fibers are electrical (E-glass), high strength (S-glass), and alkali-resistance (AR-glass). E-glass is the most common reinforcement material used in civil and industrial structures. Those fibers are named E-Glass because they offer high electrical insulating properties. In addition, they are known for low susceptibility to moisture, and high mechanical strength. It is

produced from lime-alumina-borosilicate, which can be easily obtained from an abundance of raw materials like sand (Bagherpour, 2012). S-glass provides higher tensile strength and modulus of elasticity but is more cost prohibitive and so less preferable than E-glass. AR-glass is resistant in high alkali environments such as in concrete, but at the moment, no compatible sizing is available to use it in the FRP production where the fibers are combined with a thermoplastic resin (Nanni et al., 2014).

The main difference to basalt fibers is that glass is made from a complex batch of materials, whereas basalt filament is made from melting basalt rock with no other additives, which reduces the environmental impact. Major glass ingredients of the batch of materials are silica sand, lime stone, and soda ash. Silica sand is the glass former, while lime stone and soda ash is added for lowering the melting temperature. Additional materials can be mixed in for manipulating certain properties like adding borax for more chemical resistance (Aubourg et al., 1991). Fiberglass furnaces are generally divided into three distinct sections. First, the batch is delivered into the furnace section for melting. Then, the molten glass flows into the refiner section, where the temperature of the glass is lowered from 1370°C (2500°F) to about 1260°C (2300°F). In the last step, the molten glass is transferred into the end section located directly above the fiber-forming stations. The molten mass is rapidly cooled to prevent crystallization and formed into glass fibers by a process also known as fiberization. Nearly all continuous glass fibers are made by a direct draw process and formed by extruding molten glass through a platinum alloy bushing that may contain up to several thousand individual orifices (Wallenberger et al., 2001). Typical glass fiber diameters range from 3 to 20 micrometers. Individual filaments are combined into multifilament strands, which are pulled by mechanical winders at velocities of up to 61 m/s (200 ft/s) and wound onto tubes or forming packages (Wallenberger et al., 2001). After describing the production of glass fibers, carbon fibers are presented in the next subsection.

2.2.3 Carbon Fiber

Primarily, carbon fibers are used for pre-stressed strands (and not as much for regular rebar purposes) in civil structures because of their high tensile strength, high modulus of elasticity, and most importantly, because of its creep resistance, which is significantly higher when compared to glass or basalt fibers. Carbon fibers made from polyacrylonitrile (PAN) are typically classified as

high-modulus carbon fiber. Fibers made from carbon typically have a high fatigue strength, high resistance to alkali or acid attacks, a low coefficient of thermal expansion (CTE), and high electrical conductivity. However, it also has a relatively low impact resistance, can cause galvanic corrosion in contact with metals, and has a significantly higher unit cost. Accordingly, proper sizing must be applied before these fibers can be embedded in resin similar to other fibers on the market. Moreover, carbon fibers have the highest tensile strength (three times the strength of glass fibers) , but they are also the most expensive (about ten times more than glass fibers) (Nanni et al., 2014). Another fiber type used for engineering purposes are aramid fibers (see subsection 2.2.4).

2.2.4 Aramid Fiber

Aramid fibers are organic aromatic polyamide based with high fatigue and creep resistance. In addition, these fibers are good isolators for electricity or heat. However, they are sensitive to ultraviolet (UV) light, high temperature, and moisture, and a good chemical or mechanical bond between the aramid fibers and resin is difficult to achieve (Bagherpour, 2012). Within the wide availability of different grades, Kevlar 29, 49, and 149 are the most common fibers in structural applications. Compared to glass fibers, aramid fibers have a higher tensile strength and also a 50 % higher modulus of elasticity. Nevertheless, the use of these fibers is limited by the high material costs in the production of FRP bars (Nanni et al., 2014).

2.2.5 Fiber Types Summary

Compared to the other fibers, basalt has the highest density and a considerably high ultimate strain. The lowest strain combined with the highest tensile modulus is generally found for carbon fibers (Low- and high-modulus). Glass fibers measure the lowest tensile strength and modulus. Aramid fibers, in addition to carbon fibers, are not suitable for the commercial use of composite rebars because of economical aspects. Therefore, the focus for FRP rebars is on glass and basalt fibers because of a wide availability and cost efficiency. While the most important fiber types are shown in the subsections above, the next section 2.2.6 focuses on the properties of basalt and its comparison to glass fibers.

2.2.6 Properties of Basalt Fibers

The paragraph below is summarizing properties with their advantages and disadvantages of basalt fibers. Basalt is a volcanic rock that can be formed into continuous fibers through melting pure raw basalt and using technologies similar to those used for the production of glass fibers. Due to the inherent properties of basalt, the fibers are more chemically resistant, have a higher tensile strength, and a modulus of elasticity that exceeds the elasticity of glass fibers by about 15% to 30% (Rarnalaishnan and Tolmare, 1998). In addition, basalt fibers are more UV-resistant, have a higher fire resistance, and they better maintain their physical characteristics in cold temperatures. Basalt fibers are reported to withstand temperatures from -260°C to 750°C (Bagherpour, 2012). The variety of advantages is combined in a stiff rod used as reinforcement by adding a resin matrix. The composite system of fibers and resin is combining advantages of two materials to eliminated disadvantages of the individual parts. Therefore, the following section 2.4 details the different resin types, their individual properties, and how the resin is used in the FRP rebar production.

2.3 Sizing

Sizing is a protective coating applied in the fiber manufacturing process. The sizing not only plays a key role in improving rebar properties (due to the load transfer between fiber/matrix inter-phase) but also crucial role in enhancing the durability properties of rebar. Sizing is typically selected and paired based on the type of fiber-resin matrix. Although sizing is an important process, it was observed that no specification or standards exist. Due to the proprietary nature of sizing material and application, it is considered that specifying sizing is not feasible, and durability aging tests must be used to identify adequate sizing, that are compatible with the fiber and matrix.

2.4 Resin Types and Properties

Next to the fibers, the resin is the other important material to produce a high quality FRP rebar. It is used to bond the fibers together a two-component system. The main functions of the resin matrix are to protect the fibers from mechanical and environmental attacks, to maintain the alignment of fibers, and to guarantee proper load transfer between individual fibers. Resins have proven their suitability for use in FRP reinforcing bars by maintaining chemical stability under

harsh environmental conditions and by protecting the fibers from aggressive chemicals that would otherwise damage the filaments (Benmokrane et al., 2002).

Two major groups of resins exist: the thermoset (once cured, they cannot be converted back to their liquid state) and thermoplastic (soft when heated) resins. Thermoplastic resins are typically not used for civil engineering purposes because they melt when heated and solidify when cooled. Thermoset resins cure permanently and irreversibly at elevated temperatures (Bagherpour, 2012). The most common thermosetting resins used in the composites industry are epoxies, unsaturated polyesters, and vinyl esters (ACI Committee 440, 2007). Currently, vinyl esters are predominantly used for the production of FRP rebars followed by epoxy, with polyesters typically excluded from permanent applications due to durability concerns. Initially, in their virgin state, thermoset polymeric resins are usually liquid at room temperature or solid with a low melting point as shown in Figure 2.2. The figure shows an example of a thermoset polymeric resin which is liquid at room



Figure 2.2: Thermoset polymeric resin used in FRP rebars

temperature, poured into a vessel. It can be used in the FRP rebar production process in a heated resin bath. Heat treatment and catalysts (hardeners) are used in the curing process to solidify the resin. After the curing process is completed, the material is permanently solidified through polymerization/cross linking of polymer chains, as it cannot be converted back to its initial liquid stage. The properties of typical resin matrices for FRP composites are listed in Table 2.2. Vinyl ester has the highest minimum tensile strength compared to epoxy and polyester, while polyester has the lowest moisture content and epoxy resin has the highest minimum glass transition temperature in the listed ranges. The density, the Poisson's ratio (transverse strain to axial strain), and the

Table 2.2: Typical properties of resin matrices

Resin Type	Density	Tensile Strength	Longitudinal Modulus	Poissons's Ratio	CTE	Moisture Content	Glass Transition Temperature
	lb/yd^2	ksi	ksi		$10^{-6}/^{\circ}F$	%	$^{\circ}F$
Epoxy	2000–2400	5–15	300–500	0.35–0.39	1.6–3.0	0.15–0.60	203–347
Polyester	2000–2400	7–19	400–600	0.38–0.40	1.3–1.9	0.08–0.15	158–212
Vinyl-ester	1900–2300	10–11	435–500	0.36–0.39	1.5–2.2	0.14–0.30	158–329

Notes : $1lb/yd^3 = 0.593kg/m^3$; $1ksi = 6.89N/mm^2$; $^{\circ}F = (9/5^{\circ}C + 32)$

Coefficient of linear thermal expansion (CTE) are similar for all three types.

The following subsections describe suitable resins for an FRP production, starting with subsection 2.4.1 describing the specific properties of epoxy resin.

2.4.1 Epoxy

Epoxyes are well-established in the civil engineering sector because of their lower shrinkage properties in direct comparison to vinyl ester. Epoxy resins are usually used for high-performance composites with superior mechanical properties, resistance to corrosive liquids and environments, superior electrical properties, good performance at elevated temperatures, and excellent adhesion to a substrate. However, they have a low ultraviolet (UV) resistance and require post-cure (longer time in the die under certain temperatures) because of a higher viscosity than other resins (polyester or vinyl ester) (ACI Committee 440, 2007). Although epoxyes can be more expensive than other resins, they are more suitable for high performance applications. Epoxy resins are compatible with most composite manufacturing processes and are also, at the moment, the predominant adhesive of choice for concrete repair with FRP products. (Bagherpour et al., 2009). The following subsection 2.4.2 provides necessary information about polyester resin.

2.4.2 Polyester

Polyester can be classified as saturated and unsaturated. Thermoset unsaturated polyester resins represent approximately 75% of the composites industry. To initiate curing, the resin is dissolved in a monomer (like styrene) solution so that it can react with the unsaturated ends on the polymer, which then converts to a solid thermoset structure. The advantage is the balance of properties,

which include dimensional stability, cost efficiency, and ease of handling during processing. Because of different required properties such as flexibility, electrical insulation, corrosion, or heat resistance, a wide range of specific performance polyester resins are available (ACI Committee 440, 2007; Bagherpour et al., 2009). The last resin type combines advantages of epoxy and polyester, which are listed in subsection 2.4.3.

2.4.3 Vinylester

Vinyl esters were developed to combine the properties of epoxy resins with the fast curing of polyester resins. In fact, it can have higher physical performance and costs less than epoxies. Due to the combined properties, mechanical toughness, and high corrosion resistance (ACI Committee 440, 2007). These characteristic enhancements do not need complex processing or a special fabricating process like epoxy resins. Vinyl ester resins are most commonly coupled with glass fibers (Nanni et al., 2014). However, in the current market, BFRP rebars are usually a combination of basalt fibers with epoxy resin.

Consequently, the next section 2.5 provides common production methods for BFRP rebars, combining the fibers with the resin in an automated process for mass production.

2.5 BFRP Rebar Production

Different processes have been developed to combine the fibers and the resin for the efficient production of fiber reinforced polymer rebars. Typical production methods for fiber reinforced composite materials are pultrusion, wet-laying, braiding, or weaving. According to the literature and manufacturers, production processes like braiding or weaving are not used for the FRP rebar production. The following section describes the currently common processes to produce basalt FRP rebars: pultrusion and wet lay-up process. Based on cost efficiency, production speed, and product quality, pultrusion is the dominant manufacturing method. However, the production method is not standardized, which may lead to different rebar products from one manufacturer to another, such that each rebar manufacturer may produce entirely different rebars. Different investigations were obtained to verify these processes, identify possible weaknesses, and to make recommendations for standardization requirements. Scanning electron microscope (SEM) analysis has shown that porosity and voids are present with BFRP rebars. Researchers recommend that improvement in the

manufacturing process should be implemented to reduce and/or eliminate these defects (ElSafty et al., 2014). The first process is described in Subsection 2.5.1.

2.5.1 Pultrusion

The pultrusion method is the dominant process to manufacture FRP rebars because of its cost efficient and fast production. A continuous molding process combines fiber reinforcement and thermosetting resin, which produces a constant cross-sectional rebar (Figure 2.3). The figure shows

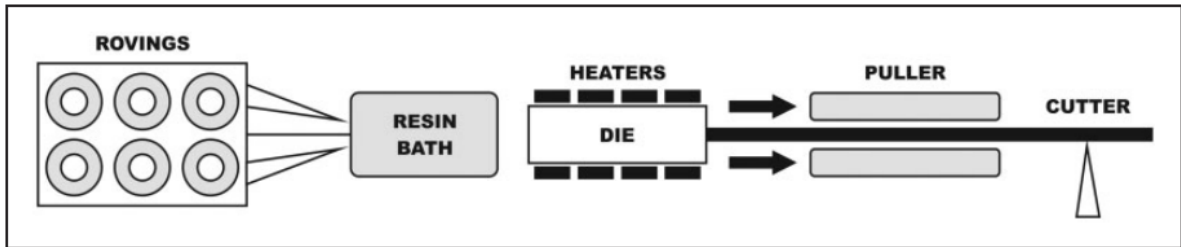


Figure 2.3: Schematic diagram of FRP rebar pultrusion (Borges et al., 2015)

from the left side on, that fibers are continuously pulled from rovings, to be wetted (impregnated) with the desired liquid resin in a resin bath. Borges et al. (2015), investigated the influence of resin bath temperature on the properties of pultruded GFRP rebars with polyester resin. It was shown that temperatures between 30 °C to 50 °C were suitable for the production process. Higher temperatures lead to a low viscosity and an insufficient wetting of the fibers before entering the heating die. The fibers are pulled through a heated metal die (with different heating zones) of the desired diameter, which defines the final shape. The recommended curing temperatures for resins is about 177 °C (Joshi et al., 2003). In the study of Borges et al. (2015) four heating zones were calculated ranging from 90 °C to 110 °C to 130 °C back to 110 °C again. The die was 900 mm long and the pulls speed was set at 0.46 m/min. Inside the pultrusion die, a controlled temperature lets the fibers and the resin harden while the heat activates the curing or polymerization of the thermoset resin until it changes its condition from liquid to solid. Inside the heating die the rebar reacts chemically and solidifies under an exothermic reaction forming from a liquid stage to a gel stage until the solid stage is reached. To set the rate of the manufacturing process, the gel time and the peak exothermic temperature of the thermoset resin need to be evaluated. The gel time is the moment where the mixed components start to solidify and the peak exothermic temperature is the maximum temperature the rebar itself reaches due to the reaction and therefore assigns the time of

the maximum reaction. Figure 2.4 shows a schematic of how the gel time and the position of the exothermic peak is evaluated (according to ASTM D 2471 - “Standard Test Method for Gel Time and Peak Exothermic Temperature of Reacting of Thermosetting Resins”). After the wet-out on the

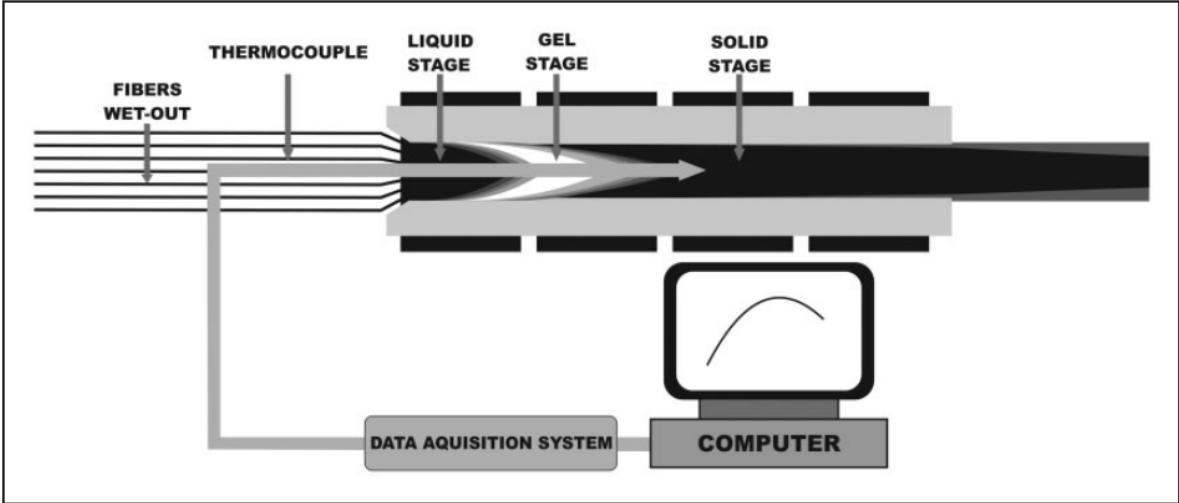


Figure 2.4: Obtain position of exothermic peak (Borges et al., 2015)

left side of the figure, the bundled fibers enter the heating die. A data acquisition system is collecting the data of the different hardening stages of the fibers to measure the exact point of the solid stage to determine the curing time in the die. Internal defects in the cured material, can lead to lower durability and mechanical properties, can be caused by estimating an incorrect rate. Therefore, the production rate is determined by the curing time of the resin. The composite solidifies when cooled and is cut to the desired length after pulling it through the pultrusion machine. Different processing variables can affect the quality and process efficiency such as die temperature, fiber content, pull speed, cure time, or resin viscosity. Accordingly, product availability and company logistics are constrained only by storage and transporting limitations. The pultrusion process has a significant influence on the final properties of FRP rebars, as it affects the rate of resin polymerization, the air void content, and thus, the fiber content. Moreover, to achieve a sufficient bond between concrete and the produced rebar in its final application, an additional process is required to apply the surface enhancement features. (You et al., 2015). These can come in the form of ribs, sand coating, , helical wrap, or combinations of both. Because of the fixed cross section of dies, a tight dimensional control of FRP rebars is assured. The pultrusion is considered to be a relatively simple process for the manufacturing of FRP bars, particularly for the production of straight rods. Coiling is also possible when smaller diameters are produced (ACI Committee 440, 2007; Patnaik, 2009). Because

of limitations of the method, small diameters are also produced with a different production process explained below (see Subsection 2.5.2)

2.5.2 Wet Lay-Up

A newer automated FRP rebar production process is the wet lay-up process, developed by a Norwegian company (ReforceTech AS Norway). Because it is a recent development in the production of FRP rebars, products manufactured with this technique have not been researched widely. The production costs are believed to be reduced in comparison to the traditional pultrusion method because of a simple process with reduced working staff.

Wet lay-up is used to produce simple composites. A programmable arm with controlled movement in three orthogonal directions manufactures the rebars with the desired length and shape. Fibers impregnated with a polymeric resin are automatically laid to form an FRP rebar after curing. The fibers are guided through a funnel-like resin bath where thorough wetting and impregnation of the fiber take place. The wet fiber is then pulled to a working platform. Several layers are laid up one over the other to produce a one-dimensional FRP construct. This new production method is said to be less expensive, but contains several disadvantages such as inconsistent cross-sectional shapes or uneven surfaces due to non-uniform pull on the fiber threads, which leads to a wavy surface. However, this waviness attribute can be beneficial for bond-to-concrete behaviors but also leads to lower tensile strength. Bar diameters of 0.2 in. (5 mm) to 0.6 in. (16 mm) have been successfully produced using this process.

After the production process, tests of physical, mechanical, and durability properties are necessary for quality control and product verification processes. Mechanical testing is important for the specification and certification of FRP rebars. Therefore, the test procedures are described in Section 2.7, with a special focus on the tensile properties in Subsection 2.7.2, because they are the most important characteristic for the rebar classification and structural concrete design. Hence, the next section provides a general overview of the most important characteristics before detailing each test procedure individually.

2.6 BFRP Rebar Properties

This section focuses on the properties of the produced FRP rebar. These material characteristics of the final product are important for the application in civil structures. Figure 2.5 summarizes the process for the production of basalt fiber reinforced polymer (BFRP) reinforcing bars (rebar). Basalt fibers manufactured from molten basaltic rocks are embedded in a polymeric resin matrix,

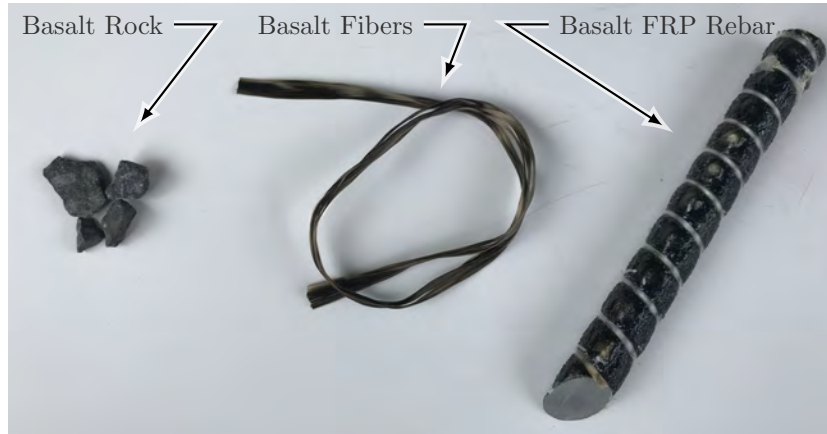


Figure 2.5: Basalt FRP rebar production steps

similar to GFRP rebars (from left to right). Mainly, fibers are known for their high tensile strength-to-weight ratio and — specifically when they form rebars — for corrosion resistance, as compared to carbon-steel (black) reinforcement. The fiber volume is mainly responsible for the tensile strength of the FRP rebar. According to the ASTM D 2584 “Standard Test Method for Ignition Loss of Cured Reinforced Resins,” the fiber content shall not be less than 55 % by volume or 70 % by mass and shall be reported by volume or by mass in accordance with the method used (ASTM-International, 2011). However, a volume fraction of about 80% is common for FRP rebars, and according to Bagherpour et al. (2009), a fiber content beyond that does not allow the fibers to be completely surrounded by the resin matrix. The tensile behavior of FRP rebars is characterized by a linear elastic stress-strain relationship up to failure as shown in Figure 2.6. The graph shows the stress-strain diagrams for different FRP composites compared to the stress-strain curve for steel (dot-dash line). The y-axis shows the tensile stress in MPa on the left and in ksi on the right side. The tensile strain in percent is provided on the x-axis. It can be seen that the incline of the FRP products are smaller than the one for steel (lower E-Modulus) but the point of maximum tensile stress is significantly higher for all FRP products. The biggest incline and highest tensile stress with the lowest strain

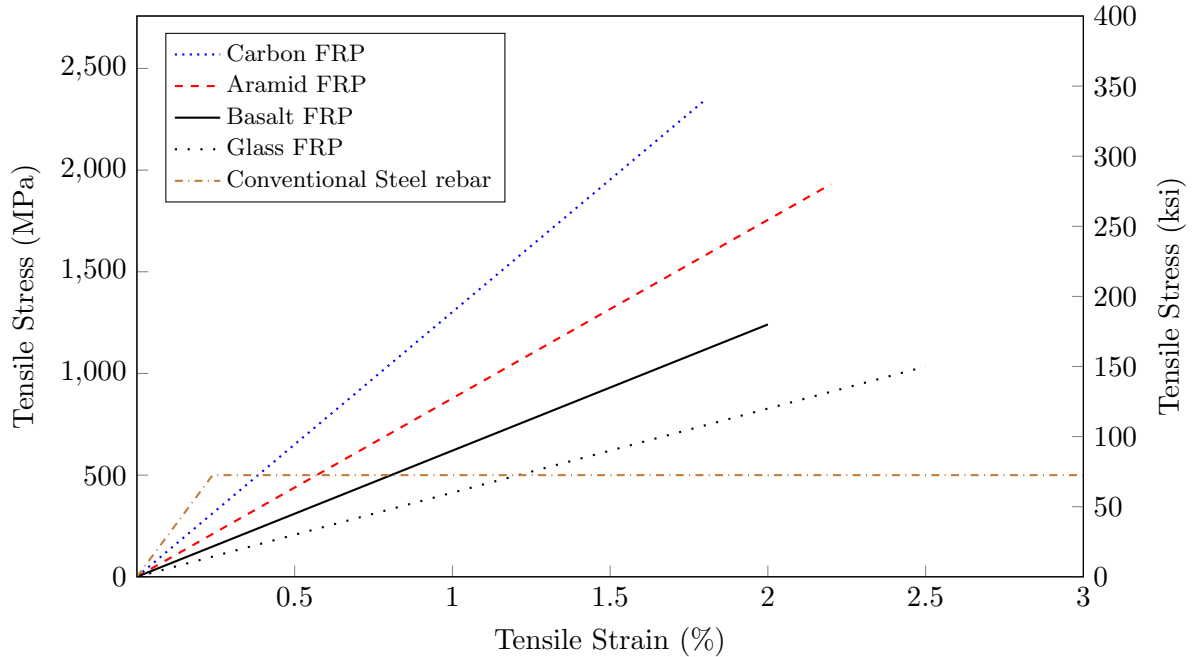


Figure 2.6: Tensile stress and strain of different types of FRP according to Busel (2016)

is reached by carbon FRP (tightly dotted line) followed by aramid FRP (dash line), which has a higher strain than basalt FRP (straight line). Glass FRP (wide dotted line) can be pointed out as the FPR product with the lowest tensile stress and lowest elastic modulus and basalt FRP is situated between aramid and glass. Compared to steel rebars, basalt FRP rebars offer higher tensile strength but lower ultimate tensile strain and lower tensile modulus of elasticity, which results in a more brittle failure for FRP products. Unlike steel, the tensile strength of an FRP rebar varies with its diameter, while the longitudinal modulus does not change appreciably. Based on the ongoing FDOT research project BDV 30 977-18, it is assumed that this phenomenon (known as shear lag) is due to the fact that the tensile force is usually introduced at the outer surface (via anchors) and the outer fibers have to transfer the load to the adjacent (inner) fibers through interface shear stresses in the resin matrix. Therefore, the shear lag effect becomes more significant as the bar diameter increases because the core of the bar is further distanced from the outer surface and more resin must be activated. This leads to lower strength measurements for larger diameter rebars because the inner core do not contribute completely to the load carrying mechanism before the outermost fibers start to fail. The tensile strain (or stretch) in the outermost fiber reaches its limit before the innermost fibers. The reason for the longitudinal modulus to remain almost constant (while the strength reduces with increasing bar diameter) is assumed to be a result of the measurement

technique, in which an extensometer is applied at the outermost surface — at the fiber that is activated to its full potential — independent of the rebar diameter.

2.7 Test Procedures for FRP Rebar

To use any new FRP rebar product in publicly funded infrastructure projects, it has to meet or exceed specific test criteria and must be certified by an FDOT-approved laboratory. Numerous properties, such as the cross-sectional area, fiber content, moisture absorption, tensile strength, horizontal and transverse shear strength, bond strength, durability, etc., have to be evaluated for test groups that include multiple specimens from different production lots. The following subsections detail these tests to provide an overview of the general acceptance process and to provide context for the associated acceptance criteria listed in the next chapter.

2.7.1 Physical Characteristics

Density and Cross-Sectional Area

To monitor physical changes in a sample while testing, and to indicate degree of uniformity in different specimens, the specific gravity of the product is determined through multiple specimens. A clean specimen is conditioned for at least 40 hours prior to testing in a temperature range from 21 °C to 25 °C at a moisture content between 40 % and 60 %, then it is cut to the desired length (while the minimum length is 10 mm and the maximum length is 50 mm) and the weight is recorded to the nearest 0.05 g. The recorded weight of the curtailed specimen should measure a minimum of 5 g and a maximum of 50 g. The density of test specimen is determined via the principle of buoyancy and the cross-sectional dimensions are calculated by dividing the determined volume by the measured specimen length. For the calculation of FRP rebar strength properties, the measured cross-sectional area is an important characteristic because strength values can differ significantly between strength values determined via nominal diameter dimensions and values determined from the experimentally measured area. It is the cross-sectional area per ASTM D 792 (ASTM-International, 2015b) that is used in many of the following test procedures to determine the strength characteristics.

Fiber Content

To obtain the loss of resin in cured reinforced sample when exposed to constant high temperature, and to study the structure of the composite material via the relative material proportions (percentage of fibers vs. percentage of resin by weight), the FRP rebar specimens are tested for fiber content. A clean specimen is first conditioned for at least 40 hours prior to testing in temperature range from 21 °C to 25 °C at moisture content between 40 % and 60 %. Three samples (at minimum) with a known weight of at least 5 g and a maximum size of 25 mm × 25 mm in a crucible (of known mass) are exposed to a minimum of 565 °C in a muffle furnace until all resin is burnt and only the fibers remain. If the rebar product was made with sand on the surface for bond enhancement, this sand must be removed from the crucible before determining the fiber content. The percentage of fibers can be determined through the difference in weight before and after the burning process.

Absorption

The moisture absorption properties of FRP rebars are determined according to ASTM D 5229 test standards. A total of 7 different methods are provided in ASTM D 5229 to find the moisture absorption in different environments. Procedure A is most commonly used, and is therefore, followed and described for this research project as well. At least three specimens per bar type are oven dried, if any moisture is present. Three diameter measurements are taken at 120° intervals perpendicular to the longitudinal axis of the FRP rebar, and those measurements are recorded to the nearest 0.001 mm. Then, each specimen is weighed with a precision of 0.05 g in its dry state. The specimens are then submerged in distilled water at a constant temperature. After two weeks in the water bath, the specimens are removed and the surface is toweled dry so that no free water remains on the surface of the rebar. Weight measurements are taken again with a precision of 0.05 g. This procedure is repeated and weight gains are monitored until three consecutive two-week measurements do not differ significantly from one another.

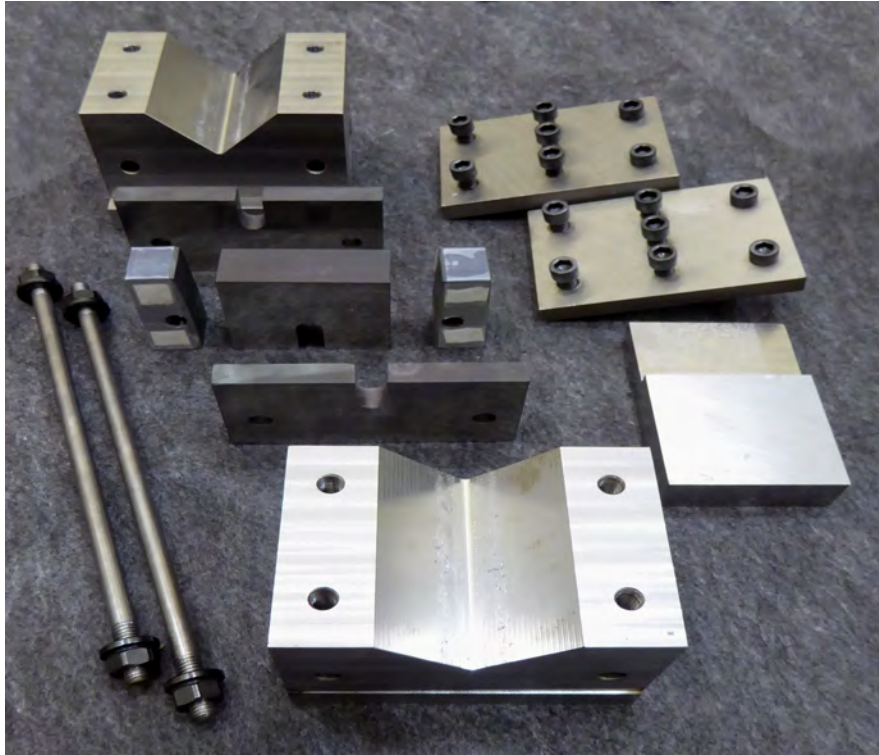


Figure 2.7: Transverse shear fixture — Main body of fixture disassembled

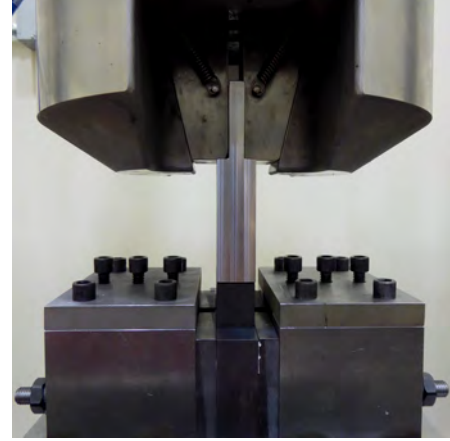
2.7.2 Strength Characteristics

Transverse Shear Strength

The transverse shear strength is an important characteristic if the bars are used as dowels in concrete pavement, stirrups in concrete beams, or as general shear reinforcement elements. ASTM D 7617 (ASTM-International, 2012b) is used in the process of testing and analyzing the data. Before testing, the specimens are conditioned according to the ASTM D 5229 (ASTM, 2014). The conditioned specimen are then cut to length with a minimum length of 225 mm so that they fit in the shear fixture, which is a device that produces double shear on the FRP rebar specimen that is represented in Figure 2.8. This fixture has two bar seats, two lower plates, and two guides machined from steel, which are connected with two threaded rods using bolts and nuts. The conditioned and curtailed bars are placed inside the shear test fixture and tested with a displacement rate such that the test continuous for at least 1 minute and a maximum of 10 minutes until the force reaches 70% of the ultimate load. The transverse shear strength is determined using the ultimate load and the cross-sectional area of the specimen as measured per ASTM D 729 (see above).



(a) Assembled fixture in test frame



(b) Main body of fixture assembled

Figure 2.8: Transverse shear fixture

Horizontal Shear Strength

Next, the FRP rebar product is tested for horizontal shear properties. The horizontal shear test is conducted according to the ASTM D 4475 (ASTM-International, 2012a) standards. This test alone does not suffice for design purposes, but the horizontal shear failure is an indicator for the strength of the resin, and therefore, is a well-suited quality control criteria and used for comparison among multiple specimens from the same manufacturer. First, the diameter at the center of the specimen is recorded and the specimens are conditioned at a temperature range from 21 °C to 25 °C and a moisture content between 40 % and 60 % before they are cut to a length of at least 5 times the diameter. A minimum of 5 specimen are tested per sample. The horizontal shear strength is assessed through a three-point load test over a span length that is short enough to prevent bending failure. The load is applied at the center of specimen with a displacement rate of $1.3 \frac{\text{mm}}{\text{min}}$ until the shear failure is reached via horizontal delamination (failure of the resin). The ultimate load and the break type are recorded and analyzed.

Tensile Properties

The test procedure to measure the tensile strength of FRP rebars is described in ASTM D 7205 (ASTM-International, 2015a). Because of the low shear strength of the FRP rebar, special preparations are required to properly test the rebars and to obtain proper results. A naked FRP rebar, gripped by the testing machine, would fail under high transverse stresses at the grip during the pulling process without reaching the ultimate tensile strength. Therefore, ASTM D 7205 describes

a method in which the FRP rebar has to be anchored on both ends with a steel pipe that is filled with an expansive grout or resin to transfer the loads from the testing machine into the rebar through friction. The grout or epoxy inside the anchor forms a cylindrical shell around the specimen. Because of the high stiffness of the steel tubes, the grout or epoxy exerts pressure on the specimen, which decreases the risk of premature failing in the grip region and clamps the rebar inside the steel tube. The basic idea of this system was to provide lateral pressure on the rebar in a sleeve to prevent slippage of the rebar. Further research work has shown that an internal pressure between 25 MPa (3.6 ksi) and 70 MPa (10 ksi) generated by the expansive cementitious material in the sleeve is enough to grip FRP tendons with different surface treatments (Schesser et al., 2014). The rebar with two anchors on the ends is then installed (after the grout cured one week) into the testing machine or into a fixture which is mounted into a test frame. Figure 2.9 illustrates one end of the prepared FRP sample with the applied anchor system. Normally, such grouts are poured

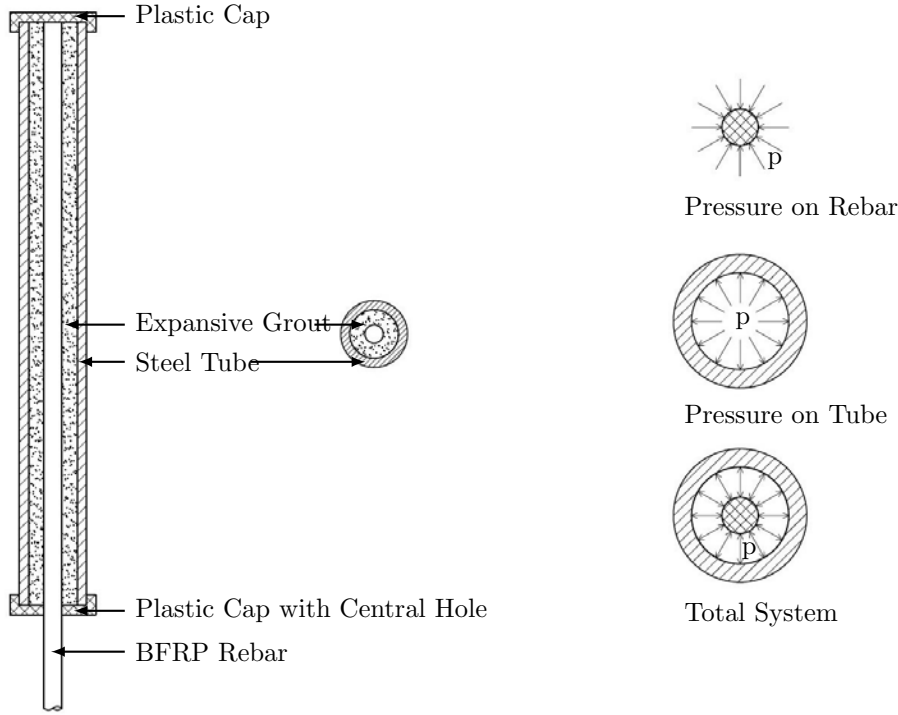


Figure 2.9: Tensile strength test load transfer (Schesser et al., 2014)

into holes drilled in rock or concrete as a non-explosive demolition agent. Because larger diameter rebars fail under higher loads, a longer anchor length (more friction) is required for longer rebars. The rebar diameter dependent anchor length is listed in ASTM for each rebar size.

According to the ASTM, the specimen length is dependent on the tested diameter of the rebar.

The total specimen length consists of two anchors of the both ends of the FRP rebar and the free specimen length in between the anchors. Because of shear lag effects, ASTM D 7205 prescribes the free specimen length with 40 times the diameter. Besides the effect of the gripped part of the FRP rebar test specimen, the free specimen length has not been fully evaluated yet, and only a few researchers have studied the behavior on GFRP rebars. The study of Castro and Carino (1998) dealt with tensile tests on five different GFRP rebar types (Diameter 9 mm to 15 mm) with a free specimen length from 40 to 70 times the diameter. The anchor length was set with 15 times the rebar diameter, which was evaluated in an expeditious approach and found to be the minimum anchorage length to avoid slippage of the FRP rebar. The intention was to evaluate the influence of the free-length-to-bar-diameter ratio on the measured tensile strength. The tested specimen from different manufacturers and different rebar diameters lead to no significant influences on the results. Different than Castro and Carino (1998) approach of longer specimen, the project of Gieben (2017) evaluated tensile tests on GFRP rebars from different sizes and manufacturers with a smaller free specimen length from 20 to 40 times the diameter. Three tensile tests per manufacturer (three in total) occurred. Tests showed no significant impacts on the final results compared to mechanical results according the ASTM D 7205 regardless of the free specimen length. Additionally according to (Gieben, 2017), the elastic modulus, calculated from the standard range between 0.1% and 0.3%, should be calculated between 0.2% and 0.3% for short specimens with a free length of 20 times the rebar diameter. The tensile tests of the short specimen length illustrated a non-linear behavior under reduced loads (low strain range). Instead, all specimens in this research, independent of the free specimen length, measured identical elastic moduli (within each test group) in the higher strain ranges. However, it should be noted that the free test length (between the grips of the test machine) of traditional steel reinforcement bars is merely 15 times the bar diameter (G. and D., 2011).

Aside from the dimensions, ASTM D 7205/ D 7205M-06 ASTM-International (2015a) also prescribes the procedure for determining the elastic modulus of the rebars. The tensile modulus of elasticity should be calculated from the strain range of the lower half of the stress-strain curve, with the starting point at a strain of 0.1% and the end point at a strain of 0.3%. Therefore, the elastic modulus is calculated from deformation measurements at relatively low stress levels. Strain measurements are obtained on the outer fiber of the rebar with an extensometer. The shear lag effect is not considered in this method, underlined by constant values for the modulus of elasticity (Gieben,

2017).

The tensile strength, however, is determined from the ultimate load divided by the cross-sectional area. As a consequence, the test results of the elastic modulus are generally showing a low variance, while the ultimate stress differs widely from one specimen to another. This is because structural effects like local air voids and residual stresses are affecting the tensile properties, while these factors do not have an influence on the material behavior under low stress and thus no influence on the elastic modulus. The ultimate stress, in turn, is not only determined by the properties of the raw materials, but also by their interaction with each other (Ehrenstein, 2006).

These interactions allow the rebar to develop additional properties, which make the product suitable for use as reinforcement in concrete dealing with harsh environments. Accordingly, the properties of the combined materials as a reinforcement bar are described in section 2.6 below.

Bond-to-Concrete Properties

In actual engineering applications where FRP rebars are used for internal concrete reinforcement, the bond-to-concrete behavior is of utmost importance because it defines the uniformity or the composite action of the final concrete element. A surface treatment is applied to the rebars to increase the friction at the bond interface or to improve the interlocking effect and to ensure proper bond between the pultruded BFRP rebar and the concrete. Manufacturers have developed different BFRP rebar types, where the surface enhancement vary. For instance the surface may be sand-coated, ribbed, or helical-wrapped. Ribbed rebars resemble the conventional black steel reinforcement and offer a high bond interaction with the surrounded concrete but another production step is needed to add the surface texture, which complexes the production. Sand coating is a simpler and faster way to treat the surface of a rebar and also offers good bond quality. The main factors affecting the properties of an FRP rebar include fiber volume, dimensional effects, rate of curing, manufacturing process, and quality control measures during manufacturing (Nanni et al., 2014). Therefore the production is decisive for the later properties of the rebar. The nature of the FRP manufacturing pultrusion process requires a marginal investment to set up (compared to traditional steel mills), while strict control measures, which are necessary to assure quality and consistency of the produced BFRP rebar, may not always be fully implemented. Although their initial cost (raw material and manufacturing costs) and environmental impact (CO_2 emission during the manufacturing process)

may be slightly higher than that of conventional steel, the use of FRP rebars in concrete structures subjected to harsh environments generates a significant potential for extending the service life of these structures and lowering their overall life cycle cost.

While the FRP rebar is reacting over the life-period to environmental influences, the durability of a rebar needs to be evaluated. The next Section 2.9 shows the most important aspects to consider when durability of an FRP rebar may be an issue.

2.8 Failure Characteristics of FRP Rebars

The mechanical behavior from FRP rebars differs from steel and has to be considered in the design of reinforced concrete because FRP rebars do not yield and fail suddenly. In addition, the fibers are anisotropic, which means that they have different properties in different directions, and the high tensile strength only exists along the fiber axis. The composite FRP rebar (due to its production) also is an anisotropic material and is significantly weaker in the transverse direction than in its longitudinal direction. This property affects the shear strength as well as the bond behavior (ACI Committee 440, 2015).

The failure mode of the FRP rebar itself is strongly dependent on the bond behavior of the fibers and the surrounded resin. Figure 2.10 shows two different failure modes of the matrix after fiber breakage (in tension). The right failure mechanism is not able to transfer the load to the next fiber due to an insufficient bond and results in fiber breakage with slippage. A composite with such a relative low bonding strength between the fibers shows a brush-like formed failure pattern, because the failed fibers delaminate immediately after breakage. The left failure mechanism shows a transfer of the force from the broken fiber to the next one available, which results out of sufficient bonding strength. Not all the fibers reach their rupture strength at the same time. Individual fibers on the outer side of the rebar break and induce additional tension in the fibers nearby until the brittle failure of the rebar occurs (Ehrenstein, 2006). However, too much bond strength could transfer too much force to the surrounding fibers, which can cause a zip-effect that expands through the whole matrix and leads to an abrupt failure of the composite material. Moreover, a composite with a moderate bond strength is the most advantageous for a high strength material. BFRP rebars are produced to reinforce concrete, especially in harsh environments, where its non-rusting properties compared to conventional black steel reinforcement are advantageous. Therefore, the knowledge of

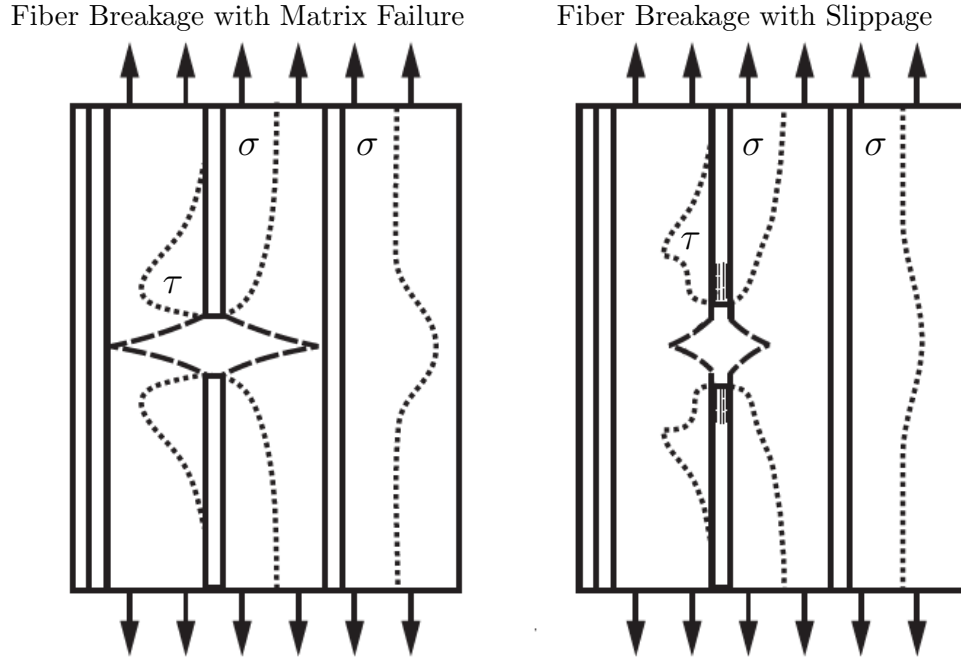


Figure 2.10: FRP rebar tensile failure mechanism (Ehrenstein, 2006)

the interactions of the rebars and concrete is essential. The following subsection 2.10 lists different failure mechanisms of concrete reinforced with FRP rebars.

2.9 Durability of FRP Rebars

Harsh environments have an influence on the properties of an FRP rebar. Because of its reaction to outer influences, the durability of FRP rebars is an important aspect and has to be considered in the designing process before failing suddenly and brittle due to influences occurring over the lifetime. FRP rebars are susceptible to varying amounts of strength and stiffness changes in the presence of environments before, during, and after construction. Environments can include water, ultraviolet exposure, elevated temperatures, or solutions (alkaline, acidic, or saline). Depending on the condition, the strength of the FRP may change (ACI Committee 440, 2015). To consider long-term exposure to the environment ACI 440 provides reduction factors for various fibers and exposure conditions listed in Table 2.3. Currently, the design code includes carbon, glass, and aramid fibers. The table provides two exposure conditions where fibers are exposed to earth and water or not. Due to outer influences, the tensile strength, creep rupture, and fatigue endurance can be reduced. Therefore, after the environmental situation is set, the tensile strength and strain has

Table 2.3: Environmental reduction factor for various fibers and exposure conditions

Exposure condition	Fiber type	Environmental reduction factor, C_E
Concrete not exposed to earth and water	Carbon	1.0
	Glass	0.8
	Aramid	0.9
Concrete exposed to earth and water	Carbon	0.9
	Glass	0.7
	Aramid	0.8

to be multiplied with the reduction factor C_E (last column in table), which reduces the design value or not in the case of carbon fibers in concrete not exposed to earth and water. Nevertheless, FRP composites are resistant in harsh environments; such environments, as well as acidic and alkali ones, could deteriorate the interface of fibers and matrix if they get in contact directly. For instance, acid diffuses into the macromolecule structure of the polymer and degrades the matrix. In addition, heat, moisture, and air pollution influence the mechanisms of degradation and the subsequent results of aging (Bagherpour, 2012). Serviceability criteria or fatigue and creep rupture can control the design of concrete members reinforced with FRP rebars in many cases. Aramid FRP (AFRP) and glass FRP (GFRP) are especially emphasized in the design code because of low stiffness characteristics.

Though FRP rebars made from basalt fibers are established as a promising replacement for CFRP and GFRP, the durability characteristics and their long-term behavior in concrete structures is not fully understood. For concrete elements exposed to harsh environmental conditions such as alkaline, saline, acidic, and de-iodized environments, FRP rebars appear to be the default alternative. But the durability of FRP materials (specifically basalt) in these harsh environments is one of the most important material-specific properties because it is often the primary reason for the use of this technology. While the high pH environment created by the cementitious matrix in concrete provides corrosion protection for conventional black steel rebars, the same high pH environment may attack FRP products and cause load capacity degradation. Accordingly, FRP rebars inside concrete elements situated in harsh environments are often exposed to multiple conditions or to a combination of chemically degrading elements simultaneously. The interaction of these combined conditions on FRP rebars are still not fully understood and research in this area is still needed.

However, initial efforts have been made and some of the completed projects are summarized below.

According to Wu et al. (2014), the durability of BFRP rebars exposed to alkaline solutions is less than the durability in saline, acidic, and de-iodized solutions when tested at 20 °C, 40 °C, and 55 °C. The degradation process of FRP rebars seems to be under control if the sustained load levels are kept below 20 % of ultimate tensile strength, but starts to accelerate beyond the 20 % threshold. According to Wu et al. (2014) findings, it takes 16.1 years for an alkaline solution to reduce the tensile strength of BFRP rebars by 50 %.

A study conducted by Lu et al. (2015) compared virgin to aged, pultruded BFRP plates and rebars to measure the effect of thermal aging (at 135 °C and 300 °C for four hours) on the longitudinal tensile strength and the interlaminar shear properties. At 300 °C, the resin decomposed thermally. As the immersion temperature and thermal aging was increased, the mechanical properties of BFRP plates notably decreased. The degradation process of aged rebars immersed in alkaline solution and distilled water accelerated due to thermal aging. While rebars aged at 135 °C and 300 °C degraded by 62.3 % and 74.1 % when exposed to high alkaline solution, the degradation process for un-aged BFRP bars exposed to high alkaline solution for three months at 60 °C was accelerated by 43.2 %.

Altamas et al. (2015) studied the bond-to-concrete durability properties of sand-coated basalt fiber reinforced polymer (BFRP) rebars and glass fiber reinforced polymer (GFRP) rebars via accelerated conditioning in acidic, saline, and alkaline solutions for 30 days, 60 days, and 90 days. The variations in slip of BFRP and GFRP bars after conditioning were negligible. The results showed that the bond strength of BFRP immersed in acid solution for 90 days was reduced by 14 % compared to bond strength of un-aged BFRP rebars, and the bond strength of rebars immersed in ocean water and alkaline solution for 90 days was reduced by 25 % in comparison with un-aged rebars. While the bond strength of GFRP rebars reduced by 25 % after acidic exposure, it reduced by 17 % after exposure to alkaline and saline environments in comparison with un-aged rebars. All specimens failed in interlaminar shear when tested for pullout strength.

Wang et al. (2017) tested tensile strength and Young's modulus properties of BFRP and GFRP rebars exposed to seawater and sea sand concrete (SWSSC). The rebars were exposed to normal SWSSC (N-SWSSC), and high-performance SWSSC (HP-SWSSC) at room temperature, 40 °C, 48 °C, and 50 °C for 21 days, 42 days, and 63 days. Damaging mechanisms were determined by using scanning electron microscopy (SEM), changes of microstructure were characterized via X-ray

computed tomography (CT), and energy dispersive X-ray spectroscopy (EDS) was used to compute chemical elements after exposure. Sodium Hydroxide (NaOH , $2.4 \frac{\text{g}}{\text{L}}$), potassium hydroxide (KOH , $19.4 \frac{\text{g}}{\text{L}}$), sodium chloride (NaCl , $35 \frac{\text{g}}{\text{L}}$), and calcium hydroxide (Ca(OH)_2 , $2 \frac{\text{g}}{\text{L}}$) were mixed in 1 L of distilled water to prepare N-SWSSC with a pH level of 13.4. In addition, sodium hydroxide (NaOH , $0.6 \frac{\text{g}}{\text{L}}$), potassium hydroxide (KOH , $1.4 \frac{\text{g}}{\text{L}}$), sodium chloride (NaCl , $35 \frac{\text{g}}{\text{L}}$), and calcium hydroxide (Ca(OH)_2 , $0.037 \frac{\text{g}}{\text{L}}$) were mixed in 1 L of distilled water to prepare N-SWSSC with a pH level of 12.7. Two BFRP rebar specimens and two GFRP rebar specimens per test group (conditioned vs. unconditioned), with a total length of 760 mm — including steel tube anchors with a length of 250 mm on both ends — were tested for ultimate tensile load. The rebars were embedded in the steel pipe anchors using an epoxy resin, and load rates for these experiments were set to $2 \frac{\text{mm}}{\text{min}}$. The ultimate tensile strength of BFRP specimen exposed to N-SWSSC in 32°C varied from 1317 MPa to 1253 MPa, whereas the ultimate tensile strength of BFRP specimen exposed to N-SWSSC in 40°C varied from 1273 MPa to 1103 MPa, while the ultimate tensile strength of BFRP specimen exposed to N-SWSSC in 48°C varied from 1257 MPa to 799 MPa, and the ultimate tensile strength of BFRP specimen exposed to N-SWSSC in 55°C varied from 908 MPa to 352 MPa. The ultimate tensile strength of BFRP specimen exposed to HP-SWSSC in 32°C varied from 1341 MPa to 1323 MPa, whereas the ultimate tensile strength of BFRP specimen exposed to HP-SWSSC in 40°C varied from 1288 MPa to 1219 MPa, and the ultimate tensile strength of BFRP specimen exposed to HP-SWSSC in 55°C varied from 1212 MPa to 1046 MPa. The ultimate tensile strength of GFRP specimen exposed to N-SWSSC in 32°C varied from 952 MPa to 925 MPa, whereas the ultimate tensile strength of GFRP specimen exposed to N-SWSSC in 40°C varied from 903 MPa to 961 MPa, and the ultimate tensile strength of GFRP specimen exposed to N-SWSSC in 55°C varied from 855 MPa to 848 MPa. The ultimate tensile strength of GFRP specimen exposed to HP-SWSSC in 32°C varied from 1031 MPa to 1036 MPa, whereas the ultimate tensile strength of GFRP specimen exposed to HP-SWSSC in 40°C varied from 959 MPa to 996 MPa, and the ultimate tensile strength of GFRP specimen exposed to HP-SWSSC in 55°C varied from 966 MPa to 948 MPa. Nearly no change was found in Young's Modulus for GFRP and BFRP bars after exposure to SWSSC solutions, mainly because this property depends on the Young's Modulus of the (basalt and glass) fibers, and because the modulus degradation for fibers in SWSSC solutions may not be significant. When compared to HP-SWSSC, N-SWSSC was more aggressive on both

BFRP and GFRP bars due to the high alkali ion concentration. In high-temperature environments, the GFRP rebars were more durable than the BFRP rebars because of the different resins. Based on the SEM, 3D X-ray, and CT-results, the resin properties of GFRP bars were more stable in SWSSC conditions than the resin used for the tested BFRP rebars.

Patnaik (2009) studied the mechanical properties of BFRP rebars and moment strength of concrete beams reinforced with BFRP rebars made by the wet lay-up process (see Section 2.5.2) and compared the results with beams reinforced by traditional pultruded BFRP rebars (see Section 2.5.1). The size of the rebars used in this study ranged from #1 rebars to #3 rebars. But more precisely, the rebar diameters for these tests included 4.3 mm, 7.1 mm, 9.8 mm. The average tensile strength of 4.3 mm rebars was 1110 MPa, the average tensile strength of 7.1 mm rebars was noted with 1084 MPa, and the average tensile strength of 9.8 mm rebar measured 1067 MPa. The average modulus of elasticity of 4.3 mm rebars was recorded with 41.1 GPa, while the average modulus of elasticity of 7.1 mm rebar was determined to be 41.4 GPa, and the average modulus of elasticity for 9.8 mm rebars was noted at 45.1 GPa. A total of 13 beams with a cross section of 203 mm \times 203 mm, longitudinally reinforced with BFRP rebars, were tested. The beam measured a length of 2135 mm, while the span length was set to 1520 mm. All beams failed in a ductile manner, showing large mid-span deflections. The measured failure loads were greater than, or within the 3% range predicted by ACI 440.1R06 (ACI Committee 440, 2006). The results showed that the BFRP bars produced by wet lay-up were as strong as pultruded FRP rebars, but it was noted that the durability characteristics of the BFRP rebars via wet lay-up methods require additional research.

2.10 Concrete Elements Reinforced with BFRP

Basalt FRP rebars are generally suitable alternatives to steel, epoxy-coated steel, or stainless steel bars in reinforced concrete structures, especially for durability or electromagnetic transparency purposes (Nanni et al., 2014). The occurring failure modes in FRP-reinforced structures are concrete crushing or FRP tensile rupture (Ehrenstein, 2006). In comparison to steel reinforced concrete with its three stages from the uncracked section, to the cracked section of linear-elastic yield up to the post-yield of reinforcement failure, FRP-reinforced concrete passes only through the first two stages without a post-yielding process (ACI Committee 440, 2007).

Due to the high alkalinity of the concrete (approximately pH 13), the steel is protected against

corrosion. For structures in aggressive environments, such as marine structures and bridges exposed to seawater or parking garages exposed to deicing salts, the alkalinity will be reduced. If the alkalinity reduces to a certain pH (approximately 9), the steel depassivates and corrosion can initiate, which causes concrete deterioration and loss of serviceability (ACI Committee 440, 2015). Due to their advantages in durability aspects, FRP rebars are embedded in concrete for civil engineer applications such as highway barriers, offshore structures, and bridge decks, which are exposed to harsh environments where traditional black steel might corrode during the estimated service time (Brik, 2003). Mainly beams or flexural concrete members are reinforced by FRP rebars at this point. Concrete beams reinforced with BFRP bars achieved moment strengths that are consistent with the relevant properties of the constituent materials and are comparable to those predicted using ACI 440.1R-06 (Patnaik, 2009). However, a lack of experience exists in the use of FRP reinforcement in compression members (columns) and for moment frames or zones where moment redistribution is required (Nanni et al., 2014). Performed SEM analysis by ElSafty et al. (2014) of samples immersed in alkaline solution at elevated temperature for 1000 hours did not show significant signs of degradation. Only the outermost covering of the bar had been affected by the conditioning. Reductions of transverse and horizontal interlaminar shear strength due to conditioning in alkaline solution for 1000 and 3000 hours were detected. A reduction of flexure strength due to conditioning in alkaline solution was recorded after conditioning for 3000 hours with exposure to alkaline solution at 60 °C. Further tests should be required to gather sufficient information for a standardized usage to establish degradation factors for design purposes like they already exist in different codes for other FRP rebars.

Next to the durability factors, environmental impacts of the BFRP rebar production have to be considered to reduce pollution. Because of the high temperature required for production, steel reinforcement has a higher carbon footprint than FRP reinforcement. Recycling instead is not as easy as reproducing steel. Without corrosion, the life cycle costs associated with FRP-reinforced structures are likely lower where steel corrosion should be a concern. A comparison between FRP-reinforced pavement and steel-reinforced pavement over the lifetime determined that FRP reinforcement had a significantly smaller environmental impact than the version with steel (ACI Committee 440, 2015).

While the general properties and components of BFRP rebars are described above, the following chapter offers details about the certification process of FRP rebars and their implementation into

national and international codes. Moreover, an analysis of the current BFRP market was conducted to collect information about availability and production processes around the world. The gathered information about the available products shall help to provide recommendations for an implementation of BFRP rebars into the national design codes and for the use of these construction materials in public infrastructure projects. The next chapter deals with BFRP specifications and market.

Chapter 3

BFRP Building Compliance and Market

This chapter provides details about current regulations for FRP rebars with the focus on basalt fibers and the international BFRP market situation and the available products. The standardization progress in the FRP industry is described in Section 3.1. In addition, Section 3.2 provides a comparison of the different acceptance criteria for the mechanical properties on national and international levels followed by Section 3.3 and 3.4, which summarize the state of the art in the BFRP industry.

3.1 Regulations for FRP Rebars

This section describes the national and international regulations for FRP rebars and its historical development. Several global activities have been completed to implement FRP rebars into design codes and guidelines since the 1980s. In the United States, the initiatives and vision of the National Science Foundation and the Federal Highway Administration promoted the development of this technology to support research at different universities and research institutions.

In 1991, the American Concrete Institute (ACI) established Committee 440 — FRP Reinforcement. The objective of the committee was to provide the construction industry with science-based design guidelines, construction specifications, and inspection and quality control recommendations related to the use of FRP rebars for concrete structures. In 2001, Committee 440 published the first version of the document “Guide for the Design and Construction of Structural Concrete Rein-

forced with FRP Bars.” The availability of this document further expedited the adoption of FRP rebars (Nanni et al., 2014). Around the start of the millennium, research projects on fiber reinforced polymers were conducted in many countries (e.g., Japan, Europe, China, Canada, and America), which led to the development of standard documents and national design codes for the use and implementation of FRPs as illustrated in Figure 3.1. The first document that introduced test methods

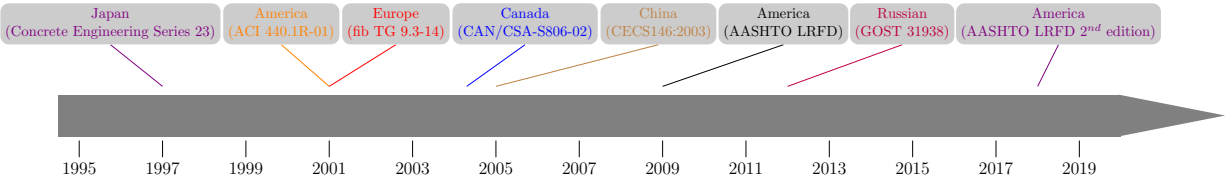


Figure 3.1: Chronology of documents related to the use of FRP rebar for concrete reinforcement

for FRP rebars was “Recommendation for Design and Construction of Concrete Structures Using Continuous Fiber Reinforcing Materials”, which was published in 1997 by the Japan Society for Civil Engineering (JSCE). ASTM International and the Organization for Standards (ISO) developed standardized test methods related to the use of FRP composites in structural engineering. Model test methods for FRP bars are recommended by the ACI document 440.3R, “Guide Test Methods for Fiber-Reinforced Polymers (FRPs) for Reinforcing or Strengthening Concrete and Masonry Structures,” effective since 2004, while earlier documents like ACI 440.2R introduced first design recommendations in 2002. Test procedures have also been developed by the Canadian Standards Association (CSA) or the European International Federation for Structural Concrete (fib) (Nanni et al., 2014).

The American Concrete Institute Committee 440 (ACI440) has led the effort to address the technical implementation for GFRP rebars by developing and publishing test methods, specifications, and design guidelines (ACI Committee 440, 2006, 2008a,b, 2012, 2013, 2015). The 2008 version of ACI440 (ACI Committee 440, 2008b) and the 2010 version of the Canadian-CSA Specifications for Fiber Reinforced Polymers (Canadian Standard Association, 2010) were developed to standardize glass, carbon, and aramid FRP bars. The Canadian Standards Association (CSA) has led the western effort for developing specifications and design guidelines for BFRP. The new CSA S807 (Benmokrane, 2018) standard includes FRP bars made from basalt fibers, which emphasize the current importance of this material and the confidence of a commercialized usage in the field (Vincent et al., 2013). Similarly, ASTM Committees D30 and D20 have addressed the

emergence of this technology by developing a number of test methods (ASTM-International, 2015a) intended to characterize GFRP rebars, while BFRP rebars do not have specifications in the US. Recently, in 2017, ASTM D 7957 specific guidelines for solid round glass fiber reinforced polymer bars for concrete reinforcement was adopted (ASTM-International, 2017). In addition, the FDOT has developed documents to aid the implementation and design of GFRP rebar technology in the built infrastructure, specifically the expanded Section 932 for nonmetallic accessory materials for concrete pavement and concrete structures (Ruelke, 2014), and more recently the fiber reinforced polymer guidelines (FRPG) (Florida Department of Transportation, 2015; Hurtado, 2018). At the national level, the American Association of State Highway and Transportation Officials (AASHTO) has also developed guides for the use of FRP technology (AASHTO, 2012) for externally bonded systems. It is desired to add BFRP-specific criteria to these specifications and guidelines as soon as practical to provide redundant supply chains and additional alternatives. Agencies are interested in BFRP composites because the technology has improved recently (as explained in Chapter 2). The variability of the raw source still presents uncertainty for its adoption in infrastructure applications, where fiber manufactures are working on providing solutions. Further reasons are properties such as a higher elastic modulus, higher tensile strength, and, for example, the consideration of a more environmentally friendly product.

In general, for a design guidelines to become official, it must be adopted by a model building code or by a regulatory agency. In the United States (and other parts of the world, including the United Nations), the International Building Code (IBC) part of the family of International Codes (I-Codes) is the predominant model code (adopted by all 50 states, Puerto Rico, and the US Virgin Islands) and covers the design and construction of new buildings. (Nanni et al., 2014) Moreover, the International Code Council Evaluation Service (ICC-ES), which is the industry leader in performing technical evaluations for code compliance as part of the International Code Council (ICC) that develops model codes and standards, published the “Acceptance Criteria for the use of GFRP and BFRP rebars for concrete reinforcement,” known as AC454 (International Code Council Evaluation Services, 2017). Hence, today any structure that is to be built according to the requirements of the Florida building code, which is based on the model code (International Building Code, IBC), can be realized with BFRP rebar technology.

For the implementation process of a product, the existence of a set of protocols and provi-

sions is necessary. Therefore, tests, analysis of the results, and the design have to be conducted. Moreover, ICC Evaluation Services (ICC-ES) develops in partnership with the proposers of new technology-specific documents called “acceptance criteria (AC)” for the purpose of issuing evaluation (research) reports. After it is demonstrated that the product is manufactured under an approved quality control program, the experimental program outlined in the AC is conducted by a certified independent laboratory, its outcomes are evaluated by ICC-ES, and, assuming compliance, a evaluation service report (ESR) is issued. Thus, the alternative material/technology now has official recognition (Nanni et al., 2014).

Through the development of standardized test procedures and available design documents, it became feasible to compare and evaluate standardized material performances, which lead to the development of acceptance criteria for different products. These acceptance criteria are described in Section 3.2 below.

3.2 Acceptance Criteria for FRP Rebars

This section lists the acceptance criteria for the most important certification documents for FRP rebars. Acceptance criteria for FRP rebars include mechanical, physical, and durability requirements for implementation and usage in civil structures on a state, national, or international level. Physical requirements include testings of FRP properties such as the fiber content, glass transition temperature, measured cross-sectional, and durability tests that consider the moisture absorption, the resistance to alkaline environments, and the void content (International Code Council Evaluation Services, 2016). This section provides mechanical acceptance criteria for FRP rebars because this research project focuses on the mechanical tensile strength of BFRP rebars. Required criteria are listed in Table 3.1 for Section 932 in the State of Florida for FRP rebars, ASTM D 7957 on a national level for glass FRP rebars, and on the bottom for AC454 on an international level for glass or basalt FRP rebars. It can be seen that the table matches the required mechanical properties according to the official test procedure (ASTM and ACI) with the different available documents (FDOT Section 932 and AC454) that require these tests. The table details how many specimens per lot and how many lots have to be considered for each test and bar size. The different certification documents require testing of three to five to ten samples per production lot. In summary, each certification document requires a comparable amount of specimens and test repetitions per

Table 3.1: Required test procedures and specimen quantities per acceptance test and production lot

		Tensile		Shear		Bond
		Ultimate Load ASTM D7205	Elastic Modulus ASTM D7205	Transverse ASTM D7617	Apparent Horizontal ASTM D4475	Strength ACI 440.3R
FDOT 932-3	Bar Size	each	each	each	each	smallest (5), median (5), largest (5)
	Specimen per Lot	10	10	5	5	15
	Lots	3	3	3	3	3
ASTM D7957	Bar Size	each	each	each	each	each
	Specimen per Lot	8	8	8	8	8
	Lots	3	3	3	3	3
AC454	Bar Size	each	each	each	each	smallest (5), median (5), largest (5)
	Specimen per Lot	5	5	5	5	15
	Lots	5	5	5	5	1

specimens to gather sufficient data for a general use in the field.

According to the normal (Gaussian) distribution to estimate the mean strength with a 95% confidence level, within 5% margin of error, a sample size of at least five rebars are needed as stated in ACI 440.1R-01. To obtain a 99% level of confidence at the same margin of error, at least nine rebars are needed. To determine guaranteed values of strengths and strains at a 99.87% probability requires testing of 25 specimens (Kocaoza et al., 2004). The guaranteed strength or strain is to be derived based on statistical analysis if fewer test specimens are tested, or the distribution is not a normal distribution (ACI Committee 440, 2006). Additionally, to the required amount of test specimen, the certification documents (FDOT, ASTM, and AC454) present rebar size and tensile load requirements for FRP rebars. All three specifications define the minimum and maximum cross-sectional dimensions and the minimum guaranteed tensile strength values per rebar size as shown in Table 3.2. It can be seen that information for the rebar sizes and corresponding limits for the measured cross-sectional area and the minimum strength values for tensile capacities are listed. The span between the min. and max. cross section is included because of differences in surface enhancements and production processes. The last column lists minimum guaranteed tensile loads for each rebar size for GFRP and CFRP bars. The only difference between the FDOT Section 932,

Table 3.2: Required sizes and tensile loads of FRP reinforcing bars

Bar Size Designation	Nominal Bar Diameter	Nominal Cross-Sectional Area	Measured Cross Section		Minimum Guaranteed Tensile Load	
			Minimum	Maximum	GFRP Bars	CFRP Bars
#	in.	in. ²	in. ²	in. ²	kip	kip
2	0.250	0.049	0.046	0.085	6.1	10.3
3	0.375	0.11	0.104	0.161	13.2	20.9
4	0.500	0.20	0.185	0.263	21.6	33.3
5	0.625	0.31	0.288	0.388	29.1	49.1
6	0.750	0.44	0.415	0.539	40.9	70.7
7	0.875	0.60	0.565	0.713	54.1	-
8	1.000	0.79	0.738	0.913	66.8	-
9	1.128	1.00	0.934	0.388	29.1	-
10	1.270	1.27	1.154	1.385	98.2	-

the ASTM D 7957, and the AC454 is that the AC454 provides additional minimum tensile loads for the measured diameters, which are a little higher than the minimum loads calculated by using the nominal diameter.

While different production techniques and processes exist in the FRP rebar market, these established acceptance criteria allow manufacturers to target specific properties. Nevertheless, BFRP rebars were produced before these acceptance criteria were available and manufacturers followed individual and proprietary production sequences. Accordingly, the market is diverse with various products, and new manufacturers enter the market quickly. However, an overview of the current BFRP rebar industry follows below.

3.3 Global BFRP Rebar Manufacturer Analysis

This section provides information about the BFRP rebar manufacturers, their production logistics, and the available products. The first FRP rebar became commercially available in the late 1980s, when the market demand for electromagnetic-transparent reinforcing systems increased. At that time, the technology was developed enough to provide a viable solution as internal reinforcement for concrete structures (Nanni et al., 2014). Afterwards, the technology gained traction and different BFRP rebar manufacturers were established around the world with a majority of the early companies

in Russia. European and Northern American companies followed the trend of manufacturing FRP rebars, while the basalt fiber was imported from areas with an easier access to basalt rock sources, such as Asia or parts of Europe. In the text below, the current BFRP rebar manufacturers are analyzed; first based on general data provided in the literature, and then based on market data gathered directly from manufacturers.

Markets and Markets (2016) conducted a study that projected the market growth up to \$91 million until 2021. This growth is fueled by the increasing demand for the renovation and strengthening of new and existing structurally deficient bridges, especially in harsh environments near the coast or connecting islands to the mainland. For instance, according to the National Bridge Inventory (NBI), more than 146,000 bridges are structurally deficient or functionally obsolete in the US as of 2010. From February 2003 to December 2013, FDOT District 7 conducted a study that evaluated the current status and the required repair costs of 54 (20 steel and 34 concrete) bridges. It concluded that 76% of all repair costs would be necessary to alleviate damages due to corrosion (Fallaha et al., 2017). Thus, the use of FRP rebars in these applications has the potential to reduce the life cycle costs, thereby enhancing service life and safety.

The Floodway Bridge (Canada) is one of the largest bridges constructed with FRP rebars. In addition, The Florida Keys Bridges (US) is one of the prominent examples for the use of CFRP rebars to strengthen structurally deficient bridges and bridge elements. Many similar projects, in which FRP rebars are used as internal concrete reinforcements, are executed in the US and Canada (Markets and Markets, 2016). Nevertheless, the lack of confidence in durability in aggressive environments (for 75 to 100 years of service life), limitations on strength due to low design resistance factors related to lack of ductility or due to degradation of properties over time, are challenges for the implementation. Moreover, creep-rupture mechanisms limit the service limit state design, and the comparatively low elastic modulus (relative to conventional black steel) leads to greater deflection and larger crack openings (Fallaha et al., 2017). Accordingly, a new challenge will be the development and implementation of new inspections and repair methods.

North America is one of the main leaders in the world market for FRP rebars and has the fastest-growing demand worldwide because of its high economic growth rate, numerous construction projects, and capacity expansion, although the basalt fibers are mostly produced in Russia and China and have to be imported. In 2018, the first basalt fiber production plant in North America

is being commissioned in North Carolina. Raw basalt rock is melted and shaped into basalt fibers. The produced fibers are combined with a resin in one process to produce the final FRP rebar shape. At this time, seven manufacturers produce BFRP rebars in the US either exclusively or in combination with other FRP rebar. Figure 3.2 provides a visualization of BFRP rebar manufacturer density worldwide, and it can be seen that (to this date and to the knowledge of the author) 23 manufacturers commercially produce BFRP rebar products year round. It is reported by Galen Panamerica that there are hundreds of “garage BFRP operations” that pultrude products in Russia and Ukraine during the warmer months. The circles on the map indicate number (per country)



Figure 3.2: BFRP manufacturer locations

and location of manufacturers. The highest density can be found in North America with nine manufacturers (seven in USA and two in Canada). A total of six BFRP rebar producers are located in Europe (two in Germany, one in Norway, one in Ukraine, one in Austria, and one in England), while eight Asian manufacturers exist (four in China, three in Russia, and one in India).

As part of this research project, 23 BFRP manufacturers from ten different countries were contacted to participate in a survey with the aim to collect manufacturer-specific data about production logistics, the produced BFRP rebar product types, their physical features, and the manufacturer guaranteed material properties. All manufacturers in these 23 countries were contacted via email, phone calls, or personal meetings. These initial conversations were followed by surveys with a BFRP rebar production-specific questionnaire. Details about the contacted BFRP rebar manufacturers and a copy of the survey that was shared with them can be found in Appendix A. Based

on the provided information, the state of the market was analyzed and the data is presented below to provide additional context for the technology, within a national and international framework. Table 3.3 lists the production and rates per manufacturer. The leftmost column in the table lists

Table 3.3: Production logistics and rates per manufacturer

Manufacturer	First BFRP bar Year	Production Logistic [†]	Production Rate	
			<i>m/d</i>	<i>ft/d</i>
No Rust Rebar Inc.	Before 1990	Stock in large quantities	4,600	15,000
Smarter Building System	2000	Stock in large quantities	6,000	19,700
Neuvokas Corp.	-	-	-	-
KODIAK Fiberglass Rebar	2014	Stock in large quantities	9,200	30,000
Advanced Filament Technologies	1998	Stock in large quantities	3,000	9,800
US Basalt	-	-	-	-
Proven Performance Chemicals	-	-	-	-
Pultrall Inc.	2010	Production on demand	8,800	28,800
Armkar Inc.	-	-	-	-
Incotology GmbH	-	-	-	-
Deutsche Basalt Faser GmbH	2017	Stock in small quantities	14,000	45,900
ASA.TEC GmbH	2012	Production on demand	960	3,150
Basalt Technologies UK Limited	-	-	-	-
ReforceTech AS	-	-	-	-
Technobasalt-Invest	2010	Stock in small quantities	16,000	52,500
Galen Panamerica	2001	Stock in large quantities	20,000	65,600
Rusnano (TBM)	-	-	-	-
Armastek	2007	Production on demand	50,000	164,000
GMV	-	-	-	-
Phoenix New Material Co., Ltd.	-	-	-	-
GBF Basalt Fiber Co., Ltd	-	-	-	-
Huabin General Machinery Co.,Ltd.	-	-	-	-
Flips India Engineering	-	-	-	-

[†] Small quantities below 500m (1640ft.); Large quantities over 500m (1640ft.)

the contacted manufacturers in this survey. Data about their first BFRP rebar production stocking quantities and the production rates are listed in the table (for those manufacturers who responded to the survey). Based on the received data from ten manufacturers, it can be inferred that just two manufacturers started their BFRP production before the year 2000. Furthermore, over 50% of the manufacturers started the production of BFRP rebars after 2007. The majority stock their products in large quantities and it can be seen that the production rates are significantly higher in the Asian and European countries compared to the United States. Kodiak Fiberglass Rebar is the company that (currently) provides the largest production capacity on the North American

continent for BFRP rebars with a production output of 4,600 m/d. In comparison the Russian company Armastek is able to produce 50,000 m/d, which is about 11 times more. Figure 3.3 shows a diagram that compares the different stocking options used by the various manufacturers in the industry. The part of the pie chart with solid diagonal lines identifies 50% of the companies that

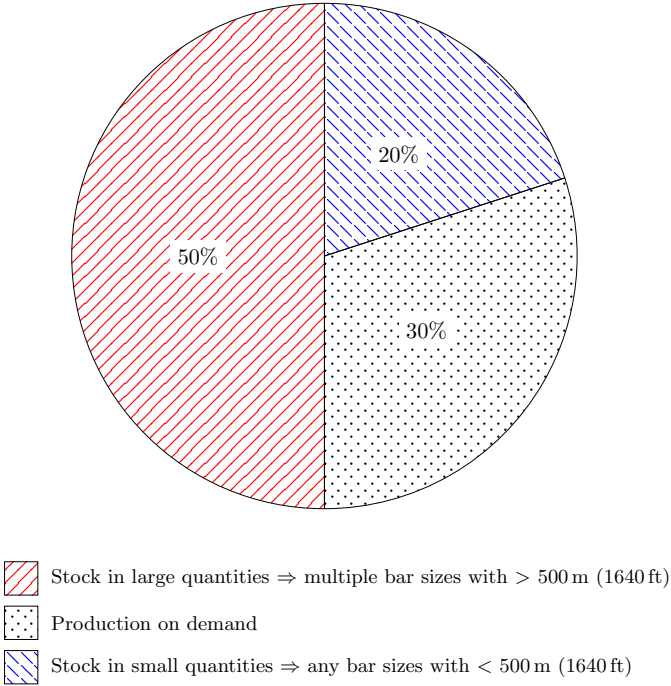


Figure 3.3: Production and storage strategies chosen by BFRP manufacturers

stock rebars in large quantities [> 500 m(1640 ft)], while the area with the dashed diagonal lines, signifies with 20% the stocking of small quantities [< 500 m(1640 ft)], and the dotted part represents manufacturers, who produce rebar on demand (30%). The next Figure visualizes the production rates of the manufacturers. The production rates are listed on the y-axis in ft/d (left axis) and m/d (right axis). Three character IDs (see Table reftab:BFRP rebars produced by manufacturer) for each manufacturer (which participated in the survey) are listed along the x-axis. The bars visualize the lowest production rate for ASA TEC GmbH (ASA) with 960 m/d (3150 ft/d) and the highest production rate for Armastek with 50 000 m/d (164 000 ft/d). The average production of all listed BFRP rebar producers is 13 000 m/d (42 650 ft/d).

17 questions about the chosen production logistics made up the first part of the BFRP rebar manufacturer survey; the second part was aimed at specific product properties and the following Section 3.4 summarizes the findings from part two.

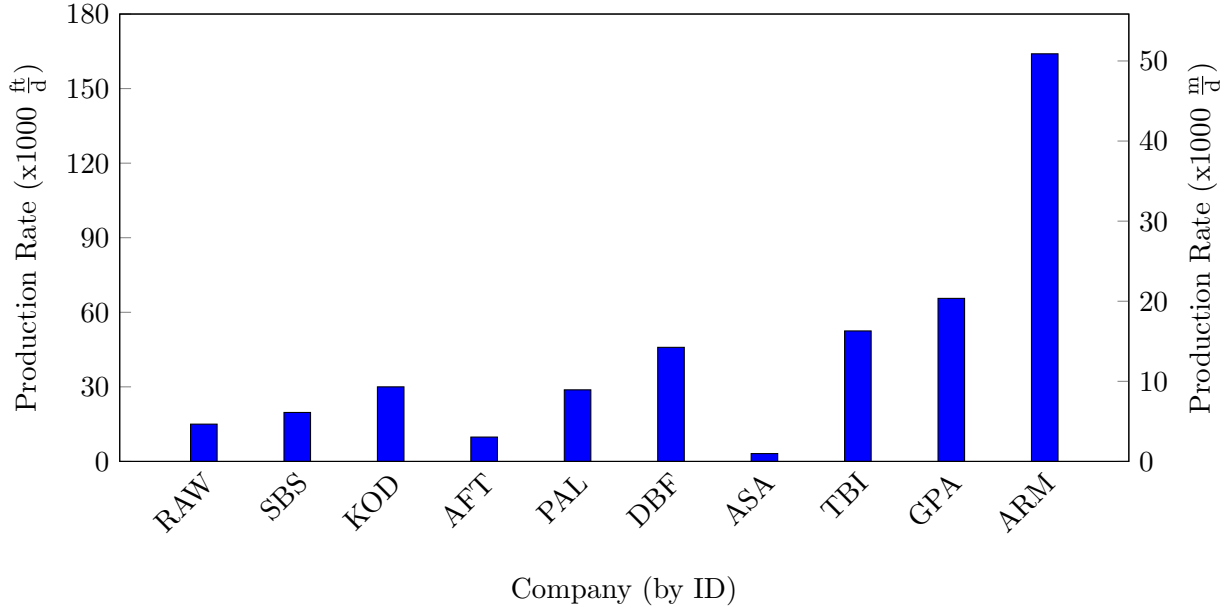


Figure 3.4: BFRP production rates (as reported by manufacturers)

3.4 BFRP Products Database

The data collected through the second part of the survey provides centralized information about parameters such as cross-sectional shape, resin type, surface enhancement, and produced diameters. The answers to all survey questions reflect the currently available products and the related parameters, cross-sectional shape, resin type, surface enhancement, and produced diameters. The acquired data are shown in Table 3.4. Based on the manufacturers who shared their company-specific data, the dominant cross-sectional shape is round and solid. The only exception is the German company Deutsche Basalt Faser GmbH, which produces round hollow rebars instead. In addition, the majority of the BFRP rebar producers focus exclusively on the production of basalt FRP rebars. However, four companies also produce rebars with other fiber types like glass or add basalt fibers afterward to their portfolio because the production sequences and processes for these rebars are similar. Besides vinyl ester, the most used resin type is epoxy: it is one of the more expensive types with a long curing time. The surface enhancement is the feature that varies the most between the listed manufacturers. The use of helical wrap, sand coat, or a combination of both is applied based on the manufacturer. The various produced rebar diameters differ in quantities/availability between manufacturers. Based on the preferred measurement system in the production country (metric vs. imperial), the available nominal rebar diameters differ. Some rebar producers only pro-

Table 3.4: BFRP rebars produced by manufacturer

Manufacturer	Cross-Sectional Shape	Fiber Type	Resin Type	Surface Enhancement	Produced Diameters
RAW	Round (solid)	Basalt	Epoxy	Helical wrap & Sand coat	#1, 2, 3, 4, 5, 6, 7, 8, 9, 10, 11
SBS	Round (solid)	Basalt	Epoxy / Vinyl Ester	Helical wrap	#1, 2, 3, 4, 5, 8
NVC	Round (solid)	Basalt	Epoxy	-	#3
KOD	Round (solid)	Basalt/Glass	Epoxy / Vinyl Ester	Helical wrap/rib & Sand coat	#2, 3, 4, 5, 6, 7,8
AFT	Round (solid)	Basalt	Epoxy	Helical wrap	#1, 2, 3, 4, 5, 6, 7, 8, 9, 10, 11
USB	-	Basalt	-	-	-
PPC	-	Basalt	-	-	-
PAL	Round (solid)	Basalt/Glass	Epoxy	Sand coat	#2, 3, 4, 5, 6, 7, 8, 9, 10, 11
AKI	-	Basalt	-	-	-
ICT	-	Basalt	-	-	-
DBF	Round (hollow)	Basalt	Thermoset	Sand coat	#1, 2, 3, 4, 5
ASA	Round (solid)	Basalt	Vinyl Ester	Helical rib	#2, 3, 4, 5, 6, 8
BTL	-	Basalt	-	-	-
RAS	-	Basalt	-	-	-
TBI	Round (solid)	Basalt	Epoxy	Helical rib	#1, 2, 3, 4
GPA	Round (solid)	Basalt/Glass	Epoxy	Sand coat	#1, 2, 3, 4, 5, 6, 7, 8, 9, 10, 11
RSN	-	Basalt	-	-	-
ARM	Round (solid)	Basalt/Glass	Epoxy	Helical wrap & Sand coat	#1, 2, 3, 4, 5, 6, 7, 8, 9, 10, 11
GMV	-	Basalt	-	-	-
PNM	-	Basalt	-	-	-
GBF	-	Basalt	-	-	-
HGM	-	Basalt	-	-	-
FIE	-	Basalt	-	-	-

duce a single size, while other producers have the capacity to supply a wide array of rebars (# 1 to # 12 or higher). Rebar # 3 with a diameter of 3/8 inch (10 mm) and rebar # 5 with a diameter of 5/8 inch (16mm) are the two most commonly available, and therefore, most used diameters in civil applications.

Chapter 4

Experimental Program

4.1 Introduction

The experimental program chapter details how the performance of three different BFRP rebar products was evaluated. The experimental concept and the general research approach as well as an overview of the different test procedures and a brief description of tested rebar material are described in the following Section 4.2. The equipment and test devices that were used to perform the experiments, including special test fixtures that were needed to test the strength properties of BFRP rebars, are described in Section 4.3. Finally, the test procedures based on the relevant and applicable ASTM standard documents are outlined in Section 4.4.

4.2 Experimental Concept

To properly evaluate a new material, such as BFRP rebars, for use in infrastructure projects, the physical and mechanical properties of the material must be evaluated and compared to acceptance criteria, if such criteria are available. Accordingly, the experimental approach aimed to fully characterize strategically chosen representative BFRP rebar samples for physical and strength characteristics. The relevant physical properties included the cross-sectional dimensions, fiber content, and moisture absorption characteristics, while the physical properties including the transverse shear strength, the apparent horizontal shear strength, the tensile properties, and the bond-to-concrete characteristics. Table 4.1 lists all these tests and references the applicable ASTM standards that were followed throughout the experimental program. In addition, the table shows how many speci-

Table 4.1: Physical and mechanical tests on BFRP rebars

		Test type	Test method	Specimen count	
				Per sample	Total
Physical		Cross-sectional area	ASTM D792	5	40
		Fiber content	ASTM D2584	5	40
		Moisture absorption	ASTM D570	5	40
Mechanical		Tensile strength	ASTM D7205	5	40
		Transverse shear strength	ASTM D7617	5	40
		Apparent horizontal shear strength	ASTM D4475	5	40
		Bond-to-concrete	ACI440.3R,B.3	5	30

mens (per sample group) were needed to reliably measure the materials' performance. Because # 3 rebar of lot 1 from manufacturer C had high moisture absorption property, manufacturers developed a new technology and provided a second lot. But two other producers were still developing the production line and could only provide prototype rebars (hence only one lot was tested).

In line with the previously described state-of-the-market situation (c.f. Section 3.1), and based on availability in the local market, representative rebar samples from three distinct BFRP rebar manufacturers were chosen. All materials that were tested for the purpose of this research project were provided by No Rust Rebar, Pultrall, and Galen Panamerica. These manufacturers provided specific products, which in the following will be referred to as Rebar Type A, Rebar Type B, and Rebar Type C (or simply Type A, Type B, and Type C), respectively. Because this research targeted the most commonly available and often used FRP rebar sizes, the manufacturer supplied # 3 and # 5 rebars, such that each Rebar Type had two sub-variants (e.g.; Type A # 3 and Type B # 3). All specimen types that were characterized throughout this research are shown in the following Figures 4.1 and 4.2. It can be seen that (at minimum) all rebar types featured a sand coat at the outer surface to improve the bond-to-concrete properties. In addition to surface sand, one product (Type A) also had helical fibers made from polyethylene terephthalate, produced by Dacron. The makeup and the surface enhancement properties of the tested rebars are described in Table 4.2. Because the precise material compositions are proprietary manufacturer information, no more data can be supplied here.

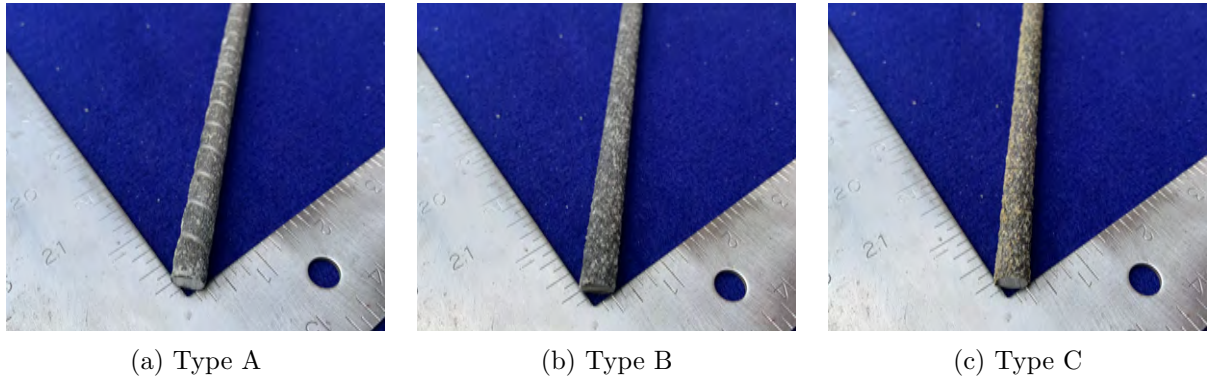


Figure 4.1: Sample pictures of tested BFRP # 3 Rebars

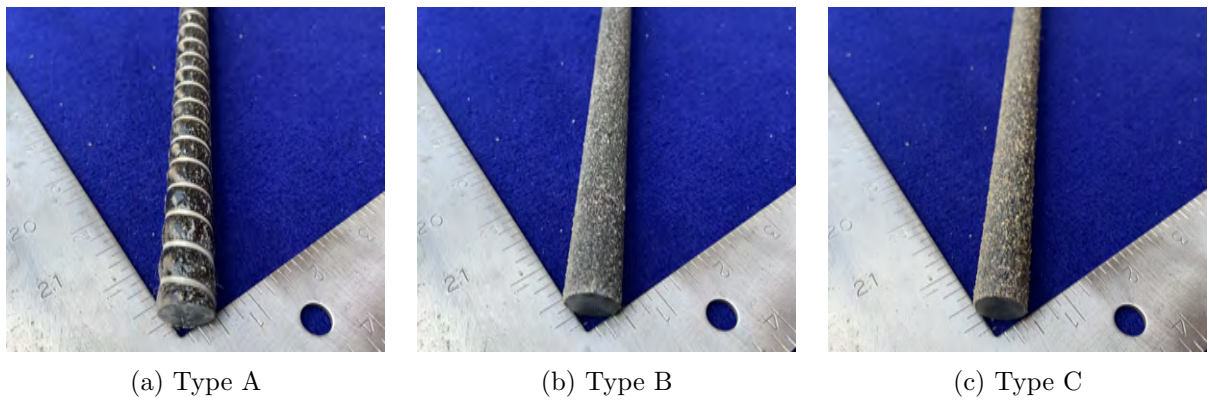


Figure 4.2: Sample pictures of tested BFRP # 5 Rebars

Table 4.2: Physical characteristics of tested BFRP rebars

Name	Cross Section	Surface Enhancement	Resin Type
A	Round (solid)	Sand coat and helical wrap	Epoxy
B	Round (solid)	Sand coat	Epoxy
C	Round (solid)	Sand coat	Vinyl-ester

4.2.1 Acceptance Criteria

While acceptance criteria for basalt FRP rebars are not fully established yet, criteria for other fiber based rebars have been adopted. One of the most established composite rebar materials is the glass fiber reinforced polymer (GFRP) rebar, which is known to possess a lower ultimate tensile strength and a lower elastic modulus — compared to basalt FRP rebars. For reference, the data in the Tables 4.3 and 4.4 show common acceptance criteria for (GFRP) rebars. For the purpose of this research, the results obtained by testing BFRP rebars were compared to GFRP rebar acceptance

Table 4.3: Acceptance criteria for GFRP rebar # 3

Test Method	Test Description	Unit	FDOT 932-3/2017	AC454	ASTM D 7957
			Criteria	Criteria	Criteria
ASTM D 792	Measured Cross-Sectional Area	in. ²	0.104 – 0.161	0.104 – 0.161	0.104 – 0.161
ASTM D 2584	Fiber Content	% wt.	≥ 70	≥ 70	≥ 70
ASTM D 570	Moist. Absorption short term @50 °C	%	≤ 0.25	≤ 0.25	≤ 0.25
ASTM D 570	Moist. Absorption long term @50 °C	%	≤ 1.0	n/a	≤ 1.0
ASTM D 7205	Min. Guaranteed Tensile Load	kip	≥ 13.2	≥ 13.2	≥ 13.2
ASTM D 7205	Min. Guaranteed Tensile Strength	ksi	n/a	n/a	n/a
ASTM D 7205	Tensile Modulus	ksi	≥ 6,500	≥ 6,500	≥ 6,500
ASTM D 7205	Max. Strain	%	n/a	n/a	n/a
ASTM D 7617	Min. Guaranteed Transverse Shear	ksi	≥ 22	≥ 22	≥ 19
ASTM D 4475	Horizontal Shear Stress	ksi	n/a	≥ 5.5	n/a
ACI440. 3R,B.3	Bond-to-concrete strength	ksi	≥ 1.1	≥ 1.1	≥ 1.1

Table 4.4: Acceptance criteria for GFRP rebar # 5

Test Method	Test Description	Unit	FDOT 932-3/2017	AC454	ASTM D 7957
			Criteria	Criteria	Criteria
ASTM D 792	Measured Cross-Sectional Area	in. ²	0.288 – 0.388	0.288 – 0.388	0.288 – 0.388
ASTM D 2584	Fiber Content	% wt.	≥ 70	≥ 70	≥ 70
ASTM D 570	Moist. Absorption short term @50 °C	%	≤ 0.25	≤ 0.25	≤ 0.25
ASTM D 570	Moist. Absorption long term @50 °C	%	≤ 1.0	n/a	≤ 1.0
ASTM D 7205	Min. Guaranteed Tensile Load	kip	≥ 29.1	≥ 32.2	≥ 29.1
ASTM D 7205	Min. Guaranteed Tensile Strength	ksi	n/a	n/a	n/a
ASTM D 7205	Tensile Modulus	ksi	≥ 6,500	≥ 6,500	≥ 6,500
ASTM D 7205	Max. Strain	%	n/a	n/a	n/a
ASTM D 7617	Min. Guaranteed Transverse Shear	ksi	≥ 22	≥ 22	≥ 19
ASTM D 4475	Horizontal Shear Stress	ksi	n/a	≥ 5.5	n/a
ACI440. 3R,B.3	Bond-to-concrete strength	ksi	≥ 1.1	≥ 1.1	≥ 1.1

criteria because BFRP acceptance criteria in the US are yet to be established. Accordingly, the listed criteria (while established for glass) serve as reference points and are used for comparison and initial benchmark data only.

4.3 Equipment and Test Devices

All equipment and tools that were needed for sample preparation and to conduct the individual tests are listed in this section.

4.3.1 Cutting Saw

The BFRP rebar samples that were provided by the manufacturers had a length between 2.30 m (90 in.) and 2.50 m (98 in.). According to the ASTM, the tested samples have to be tested in a desired length according to their diameter. To cut the samples, a heavy-duty single-bevel compound miter saw with a diamond cutting wheel was used. It featured a machine-based frame to ensure a straight cut. The saw was placed on a stable and leveled working table for a safe working space. A wooden template was designed to ensure a fast workflow and a properly angled cut with 90° relative to the longitudinal axis of the rebar (Figure 4.3). The round blade that was used to cut the BFRP rebars



Figure 4.3: Saw and diamond blade for BFRP rebar cutting

was a Diamond Montage Y1-2 Series diamond disk, which was designed for general purpose cutting and to ensure a precise and clean cut of the sample. Because the saw dust caused by the cutting process can be dangerous for human health (especially when cutting fibers), protective equipment (respiratory masks, eye wear, and ear protection) was worn at any time the saw was used. While this kind of cut was sufficient to prepare the BFRP rebars for tensile strength testing, the specimens that were prepared for the evaluation of the cross-sectional properties had to be further cut with a

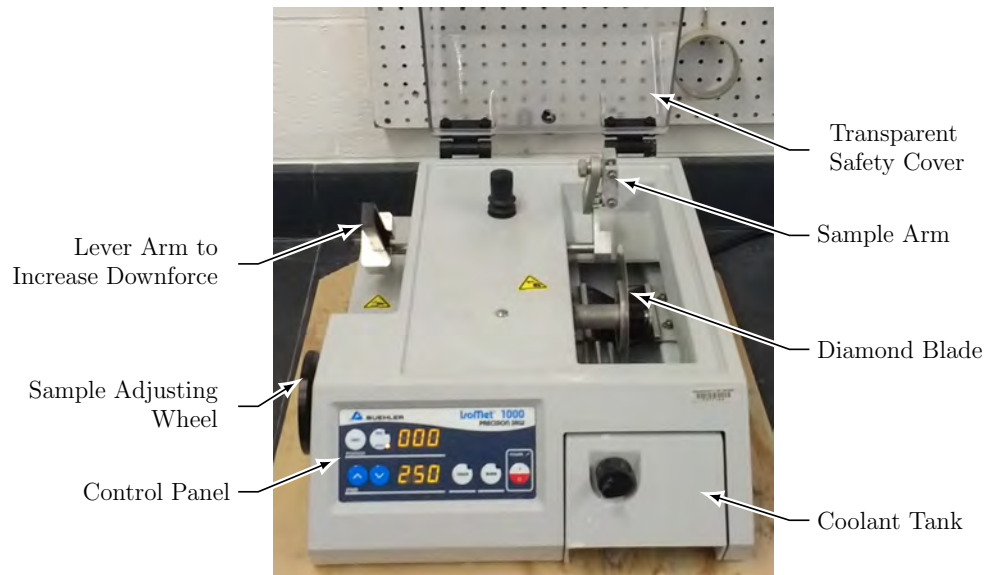


Figure 4.4: Precision saw

more precise instrument (cf. Subsection 4.3.2).

4.3.2 Precision Saw

According to ASTM D 792, a precision saw is necessary to cut the specimen for the determination of the cross-sectional area of the BFRP rebar via the water displacement method. For a proper cut of the BFRP material, the saw shown in Figure 4.4 was equipped with a 127 mm (5 in.) diameter diamond blade. The model used for this research was an IsoMet 1000 Precision Cutter¹ produced by Buehler. The machine was equipped with a Sample Arm to support the sample during the cutting process. The samples were guided over the blade — the specimen fell onto the blade, and not vice versa — through a gravity-fed system. Thereby, deformations throughout the cutting process were reduced. However, the contact pressure was adjustable and could be increased through the addition of load to the lever arm that was connected to the sample arm. After precision cuts, the exact specimen's length had to be recorded as explained next.

4.3.3 Caliper

A digital caliper was used to measure the exact length of each BFRP rebar specimen for the cross-sectional evaluation according to ASTM D 792 (ASTM-International, 2015b). The caliper had to fulfill the requirements of ASTM D 7205 (ASTM-International, 2015a) for the cross-sectional

¹ Information retrieved on June 13, 2018 from: www.buehler.com

area determination. Therefore, the electronic caliper shown in Figure 4.5 was used with a precision of 0.01 mm (0.001 in.). Before every use, the caliper was zeroed.



Figure 4.5: Electronic caliper

4.3.4 Precision Balance

After the rebars were cut with the precision saw, different measurements for the water displacement method had to be obtained. The used precision balance, which was needed to determine the cross-sectional area, was a Nimbus Precision Balance NBL 623e² produced by Adam Equipment Inc (see Figure 4.6). Its readability of 0.001 g (2.205×10^{-6} lbs.) and its operation with a repeatability of 0.002 g (4.409×10^{-6} lbs.) matches the requirements for ASTM D 792 (ASTM-International, 2015b). For a balanced setup, the scale was equipped with a bubble level indicator for optimal results. Furthermore, this scale was equipped with a transparent and removable draft shield to reduce erroneous readings that may result from air flow. Because the included shield was not sufficient to accommodate the desired applications for this project, a customized extension was produced with 3D-printing technology.

4.3.5 Support Frame for Specimen Alignment

For the installation of the steel tube anchors on specimens, a designated frame was provided to assure adequate alignment. As mentioned in Chapter 2, FRP rebars are anisotropic and have to be anchored according to the ASTM 7205 before their tensile properties can be evaluated. Therefore, an adjustable alignment frame made from aluminum was used, as shown in Figure 4.7. Two vertical supports were installed to hold the three horizontal supports, to which the rebars were fixed via movable pipe clamps. The frame was constructed with extruded aluminum profiles to guarantee a

² Information retrieved on June 14, 2018 from: www.adamequipment.com/nbl-623e



Figure 4.6: Precision scale, used to meet ASTM D 792 requirements

high stiffness while maintaining its adjustability to adapt to different rebar sizes and lengths. The rebars were fixed in the plastic plug, which fitted precisely into one end of the steel tube. The rebar specimens were placed on the melamine-coated particleboard on the bottom and positioned along the horizontal supports to ensure a 90° angle before potting the anchors. After the grout was poured into the bottom-plugged steel tube, the upper end was sealed with a red plastic cup. The other end of the rebar was potted after a curing time of 24 hours, and after seven days — when the expansive grout reached its peak pressure — the specimens were ready to be tested and move to the test site.

4.3.6 Test Fixture for Transverse Shear Tests

The fixture for the transverse shear test was built at the FAMU-FSU College of Engineering Machine Shop according to ASTM D7617 (ASTM-International, 2012b). The concept of the transverse shear test and the mechanics of the test can be seen in the Figure 4.8 and Figure 4.9. It can be seen that the top pusher was able to pass through the gap in the middle of the fixture, to cut the rebar — producing a localized shear force. The force was increased until the rebar failed in shear, in both the



Figure 4.7: Tensile test preparation alignment frame

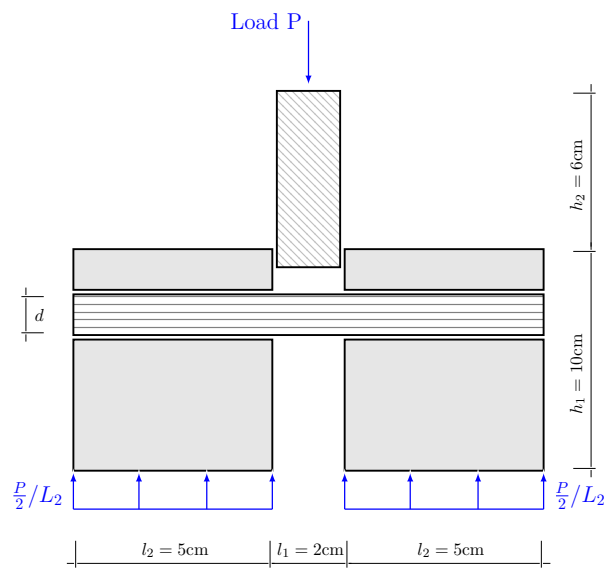


Figure 4.8: Transverse shear test concept

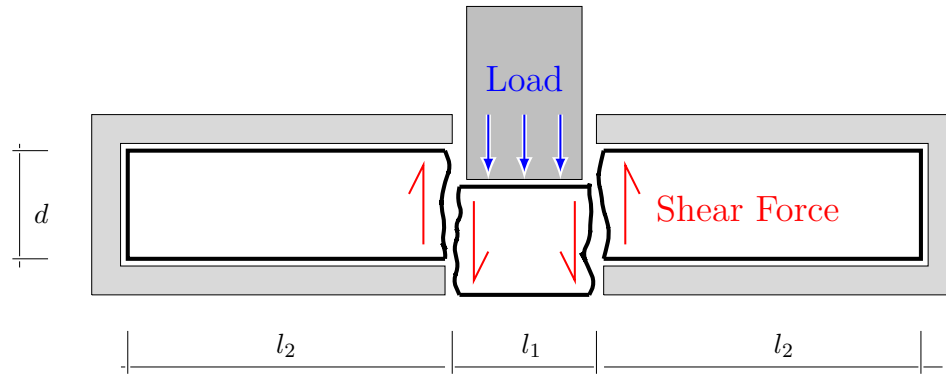


Figure 4.9: Transverse shear test — methodology

cutting planes (between both the surfaces of the top pusher and the fixture). Figure 4.10 shows the built transverse shear fixture that was used to conduct all transverse shear tests. The test fixture consisted of two V-form bar seats, two straps, two lower blades, an upper blade, and two guides machined from steel. The bar seats, the two lower blades, and the two guides were transversely bolted together with two threaded rods and nuts with washers. Between the lower blades and the

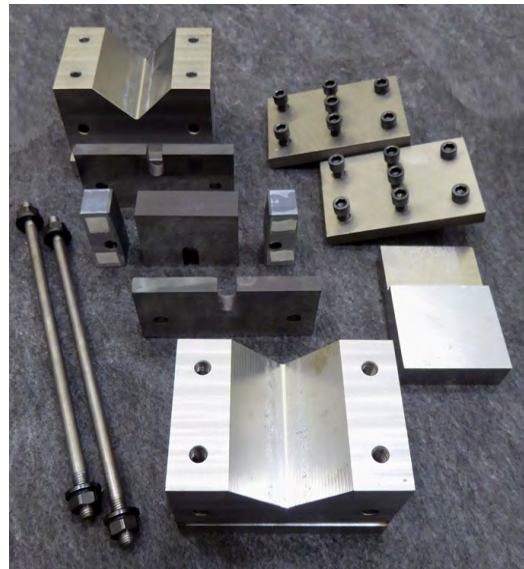


Figure 4.10: Transverse shear box — parts

guides, thin shims were placed to ensure that the upper blade fitted properly between the two lower blades (Kampmann et al., 2018).

4.3.7 Test Fixture for Apparent Horizontal Shear Tests

The apparent horizontal shear test fixture was built according to ASTM D4475 (ASTM-International, 2012a). The concept of this test is similar to a typical three-point bending test but with a short span to diameter ratio (5 to 1) (c.f. 4.11) which produces a inter-laminar shear force along the longitudinal axis of the bar leading it to failure in shear (c.f. 4.12) rather than in flexure. Accordingly,

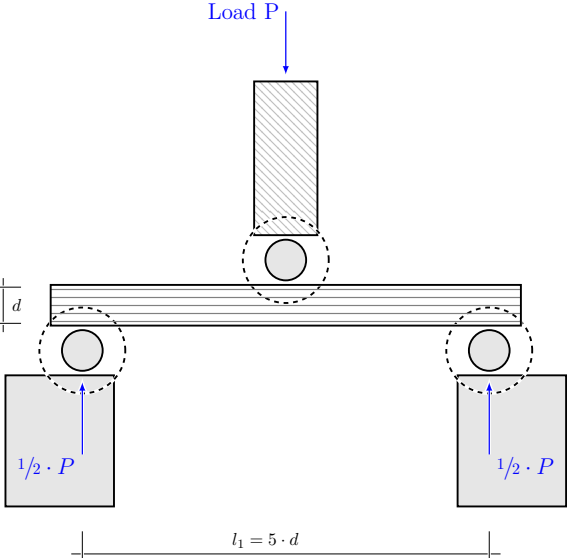


Figure 4.11: Horizontal shear test concept

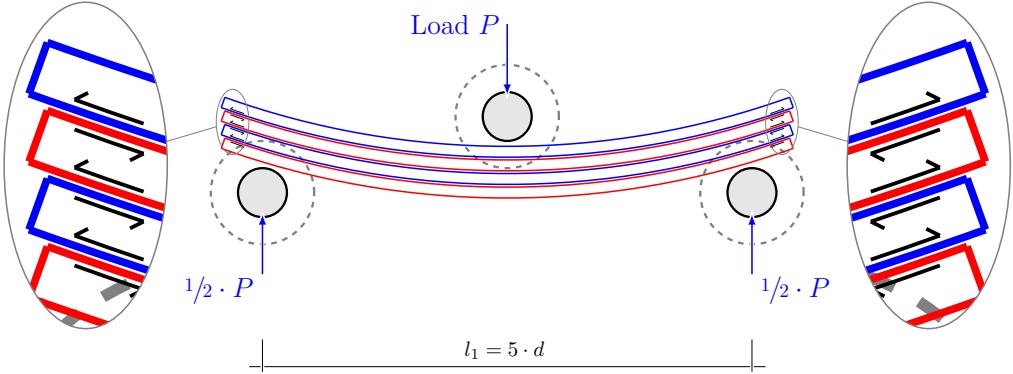


Figure 4.12: Horizontal shear test — methodology

the built fixture for horizontal shear test shown in Figure 4.13 was used. The fixture consisted of two bar supports and a loading nose built on a steel beam. Both the loading nose as well as the two bottom supports were made from suitable hardened steel rods with a groove in the middle to fit the individual rebar sizes. These steel rods were held in place, with the help of a spring on each side of the rod (Kampmann et al., 2018). This setup was used for all conducted apparent horizontal

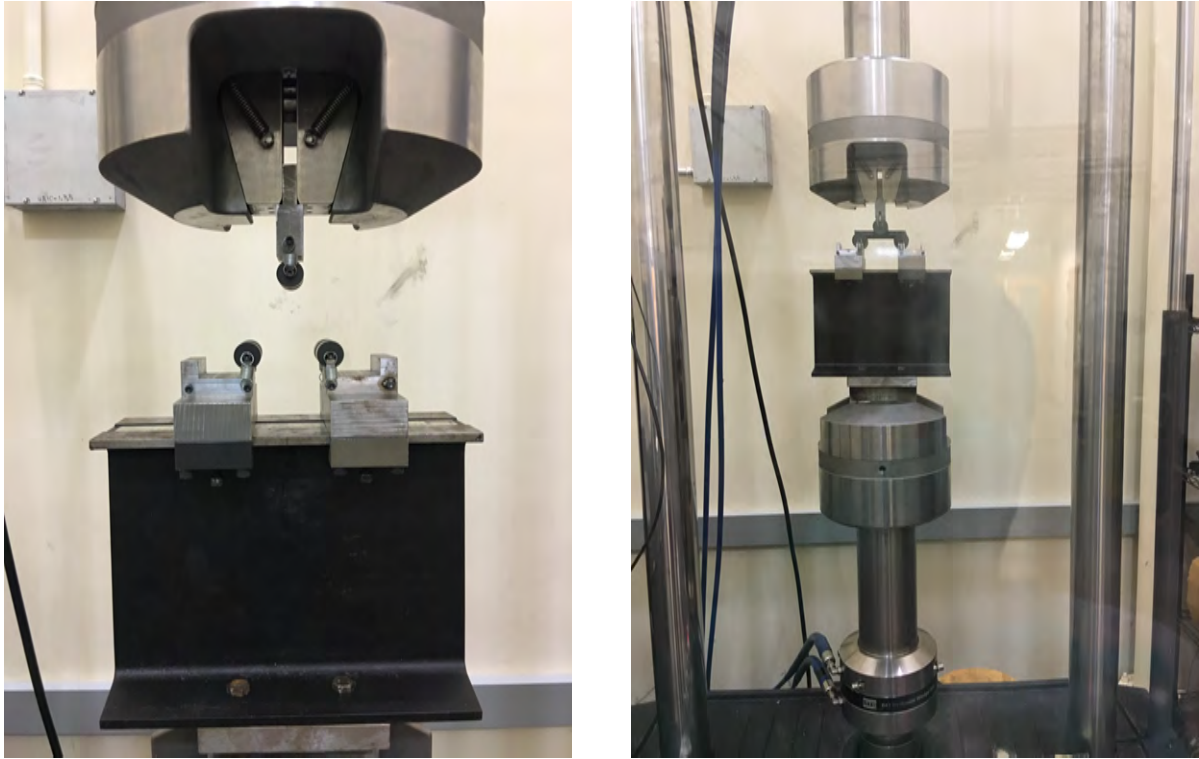
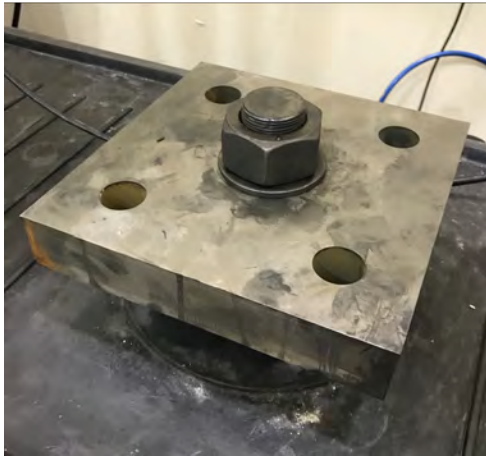


Figure 4.13: Horizontal shear test fixture

shear test, while the distance between the supports was adjusted, dependent on the tested rebar size/diameter.

4.3.8 Test Fixture for Tensile Strength Tests

As mentioned above, an additional test fixture was needed to install the tensile specimens for proper load transfer. The standard load frame grips were not suitable for the tensile test experiments, and therefore, removed to directly attach the fixture to the load mechanism via threaded rod as shown in Figure 4.14. After installing the test fixtures at the bottom and at the upper cross-head, the tensile samples were installed by leading them through the slot of the bearing plates. Afterwards, the rebar was centered with locking plates to fix the specimen and to ensure proper alignment. The fixtures then transfer the load from the bearing plates to the cross section of the steel tube without touching the free portion of the BFRP rebar specimen. Due to this mechanism, the full load was transferred to the FRP rebars via friction between the cured expansive grout and the steel tube anchors. Figure 4.15 shows the installed fixture and the entire test setup. This setup was used to properly test all rebar types and sizes for tensile strength and elastic modulus.



(a) Bottom Plate



(b) Bottom Fixture

Figure 4.14: Bottom unit connected to actuator



Figure 4.15: Tensile fixture installed in load frame

4.3.9 Test Fixture for Bond-to-Concrete Test

The test fixture for the bond-to-concrete test was designed to accommodate the requirements listed in ASTM D7913 (ASTM International, 2014). As seen in Figure 4.16, the fixture was divided into two sub fixtures: an upper and a lower fixture component. The upper fixture was designed to slide the concrete cube into place and to hold it in line with the thrust of the test frame. The lower part of the fixture was attached to the bottom of the test frame and designed to accommodate the steel tube anchor. Both the top and bottom parts of the fixture consisted of four uniformly threaded

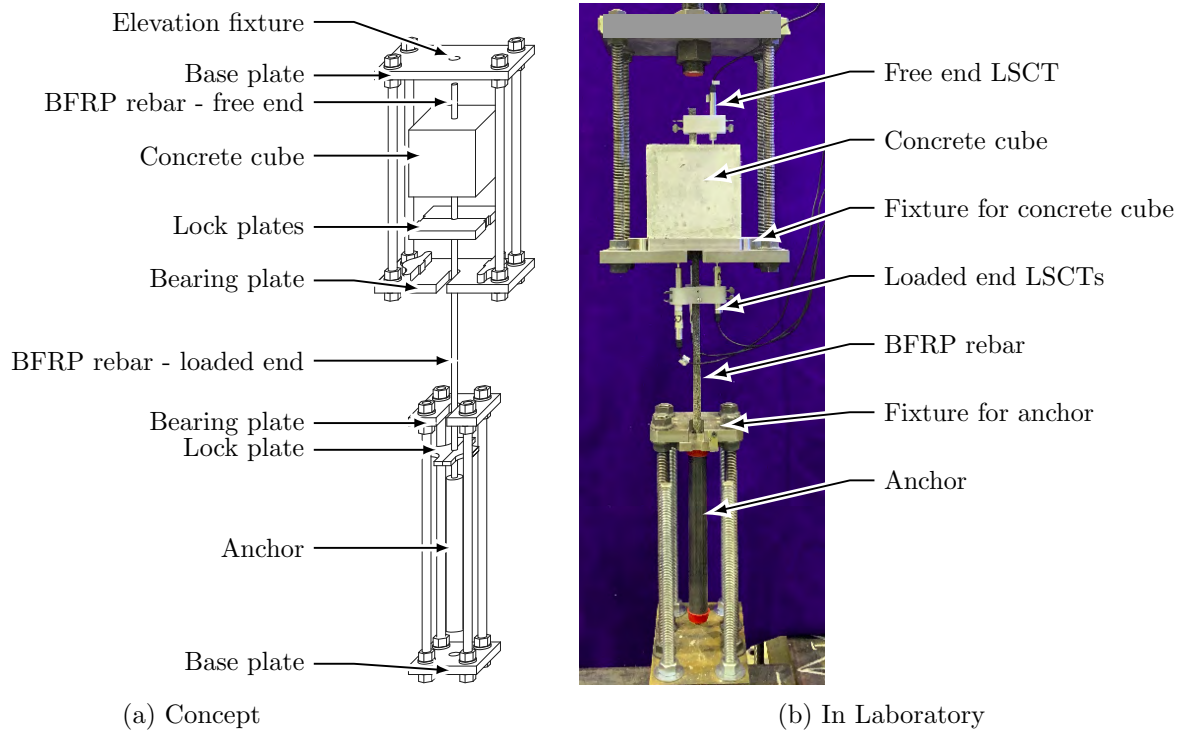


Figure 4.16: Bond-to-concrete experimental setup

rods connecting the top and bottom plates of the fixtures as seen in Figure 4.16. This design was used to conduct all pullout experiments.

Casting Concrete Cubes for Bond-to-Concrete Tests

According to ASTM D7913 (ASTM International, 2014), the test specimen for pullout testing can either be single casted (vertical or horizontal), or two FRP bars casted into one horizontal prism (ganged horizontal specimens). The horizontal prism has to be separated into two halves before conducting the pullout test. This test setup is primarily used to evaluate the “top bar effect,” which occurs due to moisture migration in curing concrete and which can negatively affect bond strength in concrete reinforcing bars. Because the top bar effect was not part of this research project, the specimen were single casted. For this study, 30 pullout specimens embedded with #3 and #5 rebars were prepared via horizontal casting with combined molds using form dividers according ASTM D7913 (ASTM International, 2014), as shown in Figure 4.17. For easy removal without disturbing the embedded bars, melamine-coated particle boards were used and the edges of each mold were sealed with silicon to guarantee a watertight mold. Because the embedment length is given by the mold, the bond length had to be controlled by bond breakers made from plastic tubing

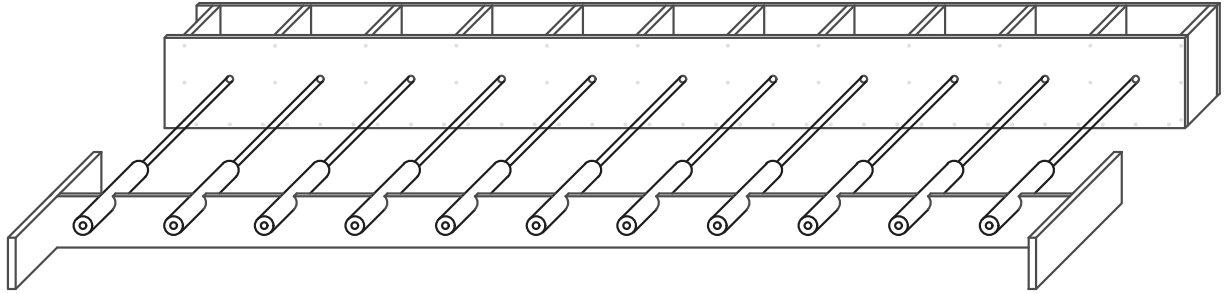


Figure 4.17: Schematic of the mold



Figure 4.18: Fixing the rebar and the plastic tube

with an inner diameter that was large enough to just accommodate the individual rebar size. To prevent the BFRP rebar and the plastic tubes from moving, the rebars were held in place with a screw (at the free end) and the tubes were taped to the mold (c.f. 4.18) before the concrete was poured into the molds. Each BFRP rebar was cut to a length that provided enough space for the measurement system and to prevent the rebar from unnecessary bending while installing the steel anchor at the opposite end. For consistency, one single operator placed the concrete in three layers of approximately equal thickness, while a different single operator rodded each layer 25 times with a 16 mm 5/8 in. diameter tamping rod. After each layer was consolidated, a third operator tapped the mold for each specimen with a rubber mallet 5 times. As soon as the top layer was completely consolidated, the free surface was struck off and leveled with a trowel, before it was covered to prevent evaporation according to ASTM C192 (ASTM International, 2018). For curing, the specimens remained covered in the molds for 17 days, but were removed thereafter to install the anchors at the load end (around the BFRP rebars) according to ASTM D7205 (ASTM-International, 2015a). In line with test procedure ASTM C39 (ASTM-International, 2004), the

compressive strength of five test cylinders (152.4 mm × 304.8 mm or 6 in. × 12 in.) was obtained at the day of pullout testing (≥ 28 days) with a mean compressive strength of 51 MPa (7396 psi), a standard deviation of 1.39 MPa (201.38 psi), and a coefficient of variation of less than 2.7%.

4.3.10 Load Frame

To properly determine the tensile strength of BFRP rebars, a displacement-controlled testing machine with a large enough working space and load capacity was required. The High Performance Material Institute (HPMI) in Tallahassee is provided an MTS Landmark testing system (floor sanding) with a model 370 Load Frame, which was manufactured in 2009 and had a maximum work space capacity of approximately 2002 mm (78.8 in.) and a maximum load capacity of 500 kN (110 kip) (MTS Landmark Testing Solutions, 2015). The used Model 647.50A grips — which were used for the shear strength tests — could apply a clamping pressure up to 69 MPa (10 ksi) with wedges inside the grip mechanism of a 4 in. (101.6 mm) width. Figure 4.19 shows an overview of the testing machine and the laboratory setup. In the foreground, the computer with the MTS process-

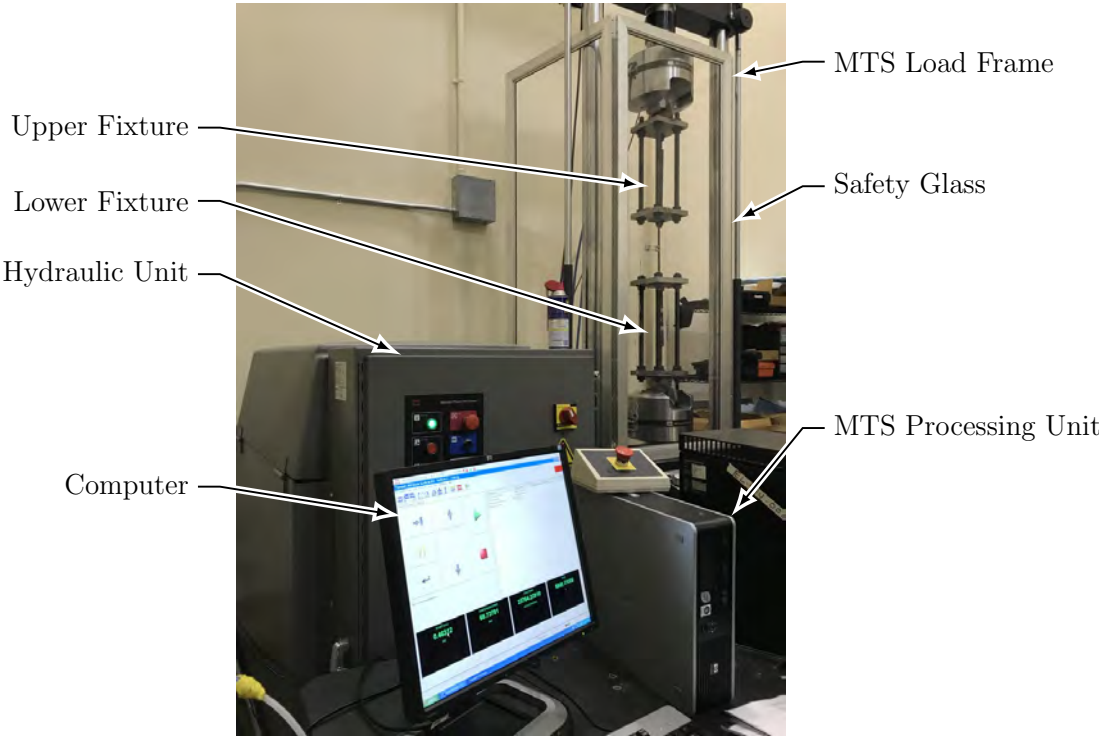


Figure 4.19: Laboratory setup in the HPMI

ing unit is shown. Behind the computer, the hydraulic unit is set to run the MTS load frame. As

shown, the tensile test fixture is installed in the test frame, which was located behind safety glass. The properly calibrated machine had a load measuring system (load cell) with a precision of $\pm 1\%$ of the measured load. The provided hydraulic pressure to drive the actuator, which applied the load to the gripped specimens, was a detached system next to the testing frame. The load and/or displacement applications for the system were controlled via the MTS FlexTest 60 Controller, which was connected to all sensors, hydraulic, and electrical components, to properly drive the test and to collect the raw data. Furthermore, the controller was connected to the computer and to the MTS control panel (shown in Figure 4.20) to operate the machine and to monitor the test procedure. With the control panel, it was possible to adjust the position of the cross bar and to open or close



Figure 4.20: MTS control panel

the grips with the desired pressure. For fine adjustments, a handset was provided next to the control panel. To control the load and displacement settings, the computer system featured the “MTS TestWorks 4” software. The software interface allowed a proper operation of the machine, including the definition of test parameters and live monitoring of the test results. In addition, the program had an export function to retrieve the gathered raw test data.

4.3.11 Extensometer

To accurately record the stretch of the outermost rebar fibers while testing the ultimate tensile strength, an extensometer was used to determine the localized specimen strains. Figure 4.21 shows the used MTS model 634.12-25 extensometer which has a gauge length of 1.00 in. (25.4 mm). After an initial load of about 1 kN was applied, the extensometer was installed in the middle section of the free specimen length with rubber bands ensuring proper contact between the measuring parts of the extensometer and the surface of the rebar.

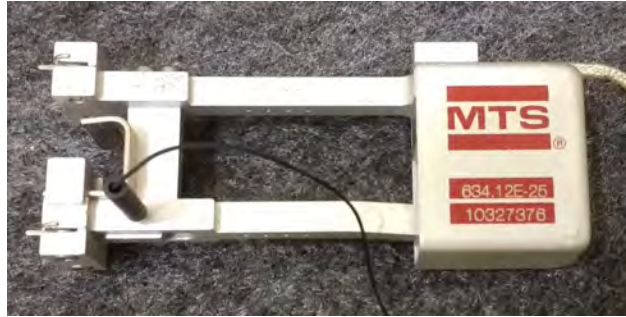


Figure 4.21: MTS extensometer

4.4 Test Procedures

This section details how each specific test procedure was conducted and which standard test method was followed to evaluate the individual rebar property.

4.4.1 Cross-Sectional Area Test — Specific Gravity (Relative Density)

The test procedure to determine the density and specific gravity (relative density) of plastics by displacement methods is described to explain how the rebar diameter (or cross section) was specified for each product. The cross-sectional properties were measured according to ASTM D 792 (ASTM-International, 2015b), while the density of each specimen was calculated via the buoyancy principle. A clean specimen was conditioned for 40 h prior to testing in a temperature range from 21 °C to 25 °C (70 °F to 74 °F) at a relative humidity between 40 % and 60 %. The specimen was then cut to the desired length of 25 mm (1 in.) using an electric precision saw. The length of each curtailed specimen was measured 3 times, at 120° intervals perpendicular to the longitudinal axis of the FRP rebar, and the average value was noted for density calculations. Afterwards, the weight of dry and conditioned specimen was measured using an electronic balance and recorded to the nearest 0.05 g (0.0017 oz.). The recorded weight of the curtailed specimen was measured to be no less than 10 g (0.352 oz.) and the value was used as the initial specimen weight, (W_i), needed for density calculations. A glass beaker of known volume was used as an immersion vessel to hold the water in which the sample was submerged. However, the immersion vessel was tared to obtain the weight of the sample under buoyancy only. The temperature of the water bath was monitored for each test and constant water temperatures of 21 °C to 25 °C (70 °F to 74 °F) were maintained throughout all experiments. A corrosion-resistant copper wire was used as a sample holder and attached to the

fixture that was independent of the water bath/vessel but introduced the forces to the scale, the specimen was carefully attached to one end of the copper wire. Then, the weight of the specimen along with the copper wire was measured and recorded (Specimen + wire, W_{s+w}). The immersion vessel was placed on the support (independent of the weighing mechanism), and the specimen was completely submerged in the water with the help of the copper wire. To remove any entrapped air or air bubbles at the surface of the FRP rebar, the specimen was carefully rubbed with the wire across the surface and submerged in a rotating motion. Any water that was displaced onto the scale was wiped without disturbing the immersion vessel. The weight of the submerged specimen was measured and recorded as final weight (W_f). Density measurements were determined via the buoyancy principle and the cross-sectional dimensions were calculated by dividing the determined volume by the measured specimen length. For reliability of test results and to obtain representative values for the BFRP rebar product as a whole, the test was repeated five times for specimens taken from different sections of the production lot and the average value was assigned.

4.4.2 Fiber Content Test — Ignition Loss

The procedure for ignition loss test for cured reinforced resins is explained here to describe how the fiber content for the tested basalt FRP rebars was determined. ASTM D 2584 -11 (ASTM-International, 2011) outlines this procedure and details the required conditions. Similar to the specimen preparation for the cross-sectional dimension experiments, the specimens for this procedure were also conditioned in a temperature range from 21 °C to 25 °C (70 °F to 74 °F) at a relative humidity between 40 % and 60 %, for at least 40 hours prior to testing. The conditioned sample was then cut to the desired length of 25 mm (1 in.) with a precision of 0.05 mm (0.0019 in.). The weight of the conditioned sample (W_s), was then recorded to the nearest 0.05 g (0.0017 oz.) using an electronic balance. This weight was used as the 100 % reference value for calculating the fiber and resin contents (relative to the initial weight). Likewise, a clean and oven-dried crucible was weighed (W_c) to the nearest 0.05 g (0.0017 oz.) to obtain the initial weight of the sample holder. The FRP rebar specimen was transferred to the crucible and the total weight of the specimen and the crucible (W_i) was recorded to the nearest 0.05 g (0.0017 oz.). To burn off all resin, the crucible (of known mass) along with the specimen were exposed to a temperature of 542 °C to 593 °C (1000 °F to 1100 °F) in a muffle furnace until the specimens reached a constant weight. The crucible was then

carefully removed from the muffle furnace and allowed to cool down to room temperature, before the cooled crucible including the remaining material was weighed using a precision electronic balance. This weight was recorded as final weight (W_f). Because the rebar products were made with sand at the surface for bond enhancement, the weight of the sand (W_s) was recorded and subtracted from the initial weight of the crucible and the specimen to obtain comparable and absolute fiber content percentages. Because fibers (and sand) are not susceptible to loss on ignition, the reduction in weight due to the burning process is equivalent to the weight of resin, and hence, the percentage of fibers was determined through the difference in weight before and after the burning process. For reliability of test results and to obtain representative values for the BFRP rebar product as a whole, the test was repeated five times for specimens taken from different sections of the production lot and the average value was assigned.

4.4.3 Moisture Absorption Test

The test procedure described in ASTM D 5229 (ASTM, 2014) defines the standard method for determining the moisture absorption characteristics of FRP and is an indicator of porosity. This paragraph explains how the porosity of the tested rebars was determined and calculated. ASTM D 5229 offers seven different test procedures (A through E, Y, and Z) to assign moisture absorption properties for FRP in different environments. Procedure A is most commonly used, and was used for this research project. Each specimen was first oven dried for 48 h to eliminate moisture entrapped in the pores or at the surface. The dried and conditioned specimens were placed in storage bags to ensure that no moisture contaminated the specimens. Three diameter measurements were taken at 120° intervals, perpendicular to the longitudinal axis of the FRP rebar, and those measurements were recorded to the nearest 0.001 mm ($\frac{4}{10\,000}$ in.). Then, each specimen was weighed with a precision of 0.05 g (0.0017 oz.) in its dry state and recorded as W_i . The specimens were then submerged in distilled water. The water along with the submerged specimens were stored in an air-circulated oven to maintain a temperature of 50 °C (122 °F) throughout the entire duration of the conditioning. First weight measurements to record W_1 after water conditioning were taken after two weeks. To obtain additional measurements, the specimens were removed from the water bath in two-week intervals (continuous conditioning) and surface dried with a fresh paper towel until no free water remained on the surface of the FRP rebar. All intermediate measurements and the final weight of each specimen

(W_f) were measured and recorded to the nearest 0.05 g (0.0017 oz.). This procedure was repeated and weight gains were monitored until three consecutive two-week measurements did not differ by more than 0.02 % from one another. For reliability of test results and to obtain representative values for the BFRP rebar product as a whole, the test was repeated five times for specimens taken from different sections of the production lot and the average value was assigned.

4.4.4 Transverse Shear Strength Test

ASTM D 7617 (ASTM-International, 2012b) was used in the process of testing and analyzing the transverse shear strength data. Before testing, the specimens were conditioned according to the ASTM D 5229 (ASTM, 2014). The conditioned specimen were then cut to a minimum length of 225 mm (8.85 in.) so that they fit in the shearing apparatus, which is a device that produces double shear on the FRP rebar specimen. The conditioned and curtailed bars were placed inside the shear test device and loaded with a displacement rate such that the test continued for at least 1 minute, but not more than 10 minutes until the force reached 70 % of the ultimate load. The transverse shear strength was determined using the ultimate load and the nominal cross-sectional area of the specimen.

4.4.5 Apparent Horizontal Shear Test

The FRP rebar products were tested for the apparent horizontal shear properties and this test was conducted according to ASTM D 4475 (ASTM-International, 2012a) standards. First, the diameter at the center of the specimen was recorded and the specimens were conditioned at a temperature range from 21 °C to 25 °C (69.8 °F to 77 °F) and a moisture content between 40 % and 60 % before they were cut to a length of approximately five times the diameter. The horizontal shear strength was assessed through a three-point load test over a span length that was short enough to avoid bending failure. The load was applied at the center of specimen with a displacement rate of $1.3 \frac{\text{mm}}{\text{min}}$ ($0.05 \frac{\text{in.}}{\text{min}}$) until the shear failure was reached via horizontal delamination (failure of the resin or resin-fiber interface). The ultimate load and the break type (number of fracture surfaces) were recorded and analyzed. For reliability of test results and to meet the requirements listed in FDOT Specifications, Section 932, a minimum of five specimen per sample were tested.

4.4.6 Tensile Strength and Modulus Test

The rebars were tested according to the ASTM D7205, which describes a specific test method for specimen preparation and testing of FRP rebars. It details how to anchor and grip the rebar specimen via steel pipe anchors at both ends, which is necessary because of the low shear and crushing strength of FRP rebars as such anchors prevent the rebar from failing in shear before reaching the ultimate tensile strength. Otherwise, the grip mechanism of standard test machines would lead to a premature (transverse) failure of the specimen. The anchors for this research project were potted with expansive grout to transfer the force from the testing machine into the rebar through compression and friction between the rebar surface and the grout. The dimensions of the anchors relate to the rebar diameter and the free specimen length between the anchors was set to 40 times the rebar diameter. After the grout in the anchors was cured for a minimum of seven days, the specimens were fixed in the MTS test frame. After the specimen was placed into the fixture and aligned properly by the locking plates, the crossbar of the machine was locked for safety purposes. Subsequently, the handset was used for the fine adjustment. An initial load of 1 kN (0.225 kip) was applied to the bar by using the setting wheel of the handset. The next step was to place the extensometer with two little rubber bands in the middle of the free specimen length of the rebar. When the extensometer was fixed, the safety pin was pulled out and the extensometer connected to the computer was ready to measure the displacement. Then, safety glass was placed on the top of the table of the load frame to protect the laboratory staff from chipping fibers caused by the failure of the rebars. The specimen was installed in the MTS Load Frame and the test was set up and configured with the program MTS TestWorks 4 to control and start the tests. The load had been zeroed before the samples were hung into the fixture to gain proper results without additional forces of the fixtures' dead weight. The rates were chosen to target a failure time between 60 s (1 min) and 600 s (10 min) as defined by ASTM D 7205 / D 7205 (ASTM-International, 2015a). To test the setup, some test specimens were produced in addition to the experimental program. After starting the test program, the force versus displacement and the strain data were monitored continuously at a 10 Hz frequency. According to ASTM D 7205, the tensile chord modulus of elasticity should be calculated from the strain range of the lower half of the stress-strain curve, with the start point being a strain of 0.1% and the end point being a strain of 0.3%. To protect the extensometer, it was removed around 10% displacement before the sample failed and possibly

damaged the extensometer. The testing machine stopped automatically when the force dropped by 85 %. This procedure was performed on 40 specimens.

4.4.7 Bond-to-Concrete Strength Test

The bond-to-concrete properties of the rebars were evaluated via pullout testing according to ASTM D7913 (ASTM International, 2014). The bond strength experiments were conducted under standard laboratory conditions within $(23 \pm 2)^\circ\text{C}$ [$(73 \pm 5)^\circ\text{F}$] and $(50 \pm 10)\%$ relative humidity, using a 300 kN (66 kip) hydraulically controlled load frame. First, the specimens were cleaned and installed in the test frame and an initial seating load of 272 kN (600 lbs.) was applied to generate sufficient stiffness in the system. Then the LSCTs, which were needed to measure the rebar slip at both ends (the so-called free and load ends). Once the setup was made safe, a static force was continuously applied via a displacement rate of $0.75 \frac{\text{mm}}{\text{min}}$ ($0.03 \frac{\text{in.}}{\text{min}}$) and the raw data was recorded with 1000 Hz until the measured force decreased significantly (more than 50 %) and the slippage at the free end of the bar measured at least 2.5 mm (0.1 in.). After each test was completed, the concrete block was split open to analyze the failure mode and to measure the precise bond length of each specimen. For repeatability, a minimum of five specimen per sample group were tested.

4.5 Data Acquisition and Data Analysis

All raw data for tensile strength and shear strength tests were recorded with MTS TestWorks software, and the raw data for the bond-to-concrete experiments were recorded using LabView software with high data rates. For all experiments, the measurements were written to file at 10 Hz (using appropriate filters). For efficient data analysis and data presentation, the high-speed data was filtered and reduced using R-statistics³ and R-Studio⁴ software packages. However, all reported numerical maximum and minimum values are based on the raw data and were calculated before any filter was applied.

To properly analyze and evaluate the BFRP rebar samples (specimen groups), the individual specimen results were determined and categorized, before statistical values (minimum, maximum, average, standard deviation and coefficient of variation) for the relevant specimen groups were

³R.app GUI 1.70 (7434 El Capitan build), S. Urbanek & H.-J. Bibiko, R Foundation for Statistical Computing, 2016

⁴Version 1.1.383 2009-2017 RStudio, Inc.

individually calculated using R-static software. The mean and other statistical values for each BFRP rebar sample were calculated based on a minimum of five individual specimen results.

Chapter 5

Results

5.1 Introduction

The performance evaluation of basalt fiber reinforced polymer (BFRP) rebars is summarized in this chapter. The following results were obtained at the FAMU-FSU College of Engineering in the High Performance Materials Institute (HPMI). All tests were conducted in accordance with the relevant American Society for Testing and Materials (ASTM) test protocol. The collected raw data were analyzed with the engineering software R-statistics¹ and R-Studio². The results are presented throughout this chapter in tables and graphs for visual representation. For clarity, each property was individually studied and presented separately. At the end of the chapter, a summary of the test results is provided to comprehensively present each specific product, document its performance, and to compare it to the acceptance criteria in FDOT 932, AC 454, and ASTM D 7957 (for glass based FRP rebars).

5.2 Cross-Sectional Properties

The effective rebar diameter was measured according to the ASTM D 792-13. Due to the variety of FRP rebars on the market and depending on the proprietary production methods, rebars from different manufacturers with different surface enhancement may vary significantly and deviate from the given nominal diameter. Table 5.1 below lists the results of water displacement method according

¹R.app GUI 1.70 (7434 El Capitan build), S. Urbanek & H.-J. Bibiko, R Foundation for Statistical Computing, 2016

²Version 1.1.383 2009-2017 RStudio, Inc.

to the ASTM D 792-13 of all the rebar products.

Table 5.1: Statistical evaluation of diameter measurements for rebar size # 3 and # 5

Rebar		Min Value	Max Value	Mean Value	Standard Deviation	CoV †
Type	Size	mm	mm	mm	mm	%
A	#3	10.23	10.24	10.28	0.02	0.22
B	#3	10.78	10.87	10.94	0.06	0.58
C-1	#3	9.92	9.95	9.99	0.03	0.32
C-2	#3	10.16	10.18	10.25	0.02	0.23
A	#5	16.64	16.71	16.78	0.05	0.31
B	#5	17.51	17.65	17.98	0.18	1.05
C-1	#5	17.05	17.14	17.40	0.14	0.86
C-2	#5	16.90	17.26	17.64	0.23	1.73

† Coefficient of Variation

5.3 Fiber Content

The fiber content by weight of the rebars was calculated according to ASTM D 2584 -11 (ASTM-International, 2011). The measured fiber content results are plotted in the Figure 5.1. The bar chart was generated to compare the different rebar types against each other and to compare the different rebar sizes. Each row in the plot indicates a specific rebar size, while each column represents a different rebar type. The bars represent individual specimens. The red hatched part of the bars indicates the fiber content in percentage, the blue crosshatched part represents the percentage of resin, and the black part represents the amount of sand that was applied to the rebar surface to increase the bond-to-concrete performance. Since the weight of the sand surface enhancement has a relative higher contribution (percentage wise) on smaller specimens, the percentage weight on # 3 rebars is higher than # 5 rebars as presented in bar chart. The 100 % values for these rebars are based on total specimen weight minus the sand content. The dashed line at the 70 % mark shows the currently accepted minimum fiber content for FRP rebars. It can be seen that all individual rebar specimens met the minimum requirement for the fiber content. The only marginal exception was specimen d of rebar Type A, # 3, however, that specimen still passed the acceptance criteria. Overall, the measured fiber content results show that the production quality was consistent for all rebar types and sizes (within each rebar product).

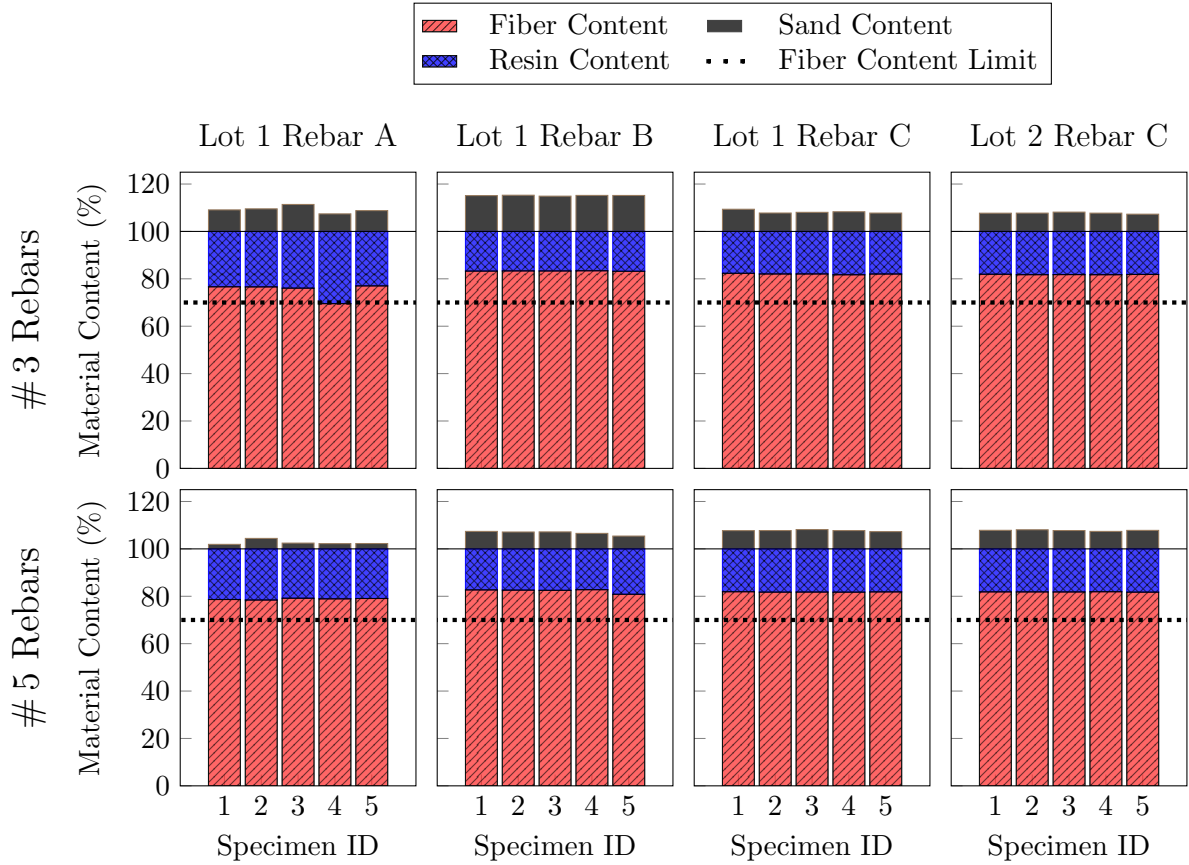


Figure 5.1: Fiber content percentage of rebars from all manufacturers

The following Figure 5.2 and 5.3 exemplify the rebar appearance after the loss on ignition test procedure. While the specimens shown in the figure were type C rebar materials, the appearance of the rebars after the test were similar for all rebar types. The following Figure 5.3 presents exemplary closeup pictures for individual test specimens of rebar types A through C. These pictures show # 3 rebars, but # 5 rebars were similar in appearance after completion of the lost on ignition experiments.

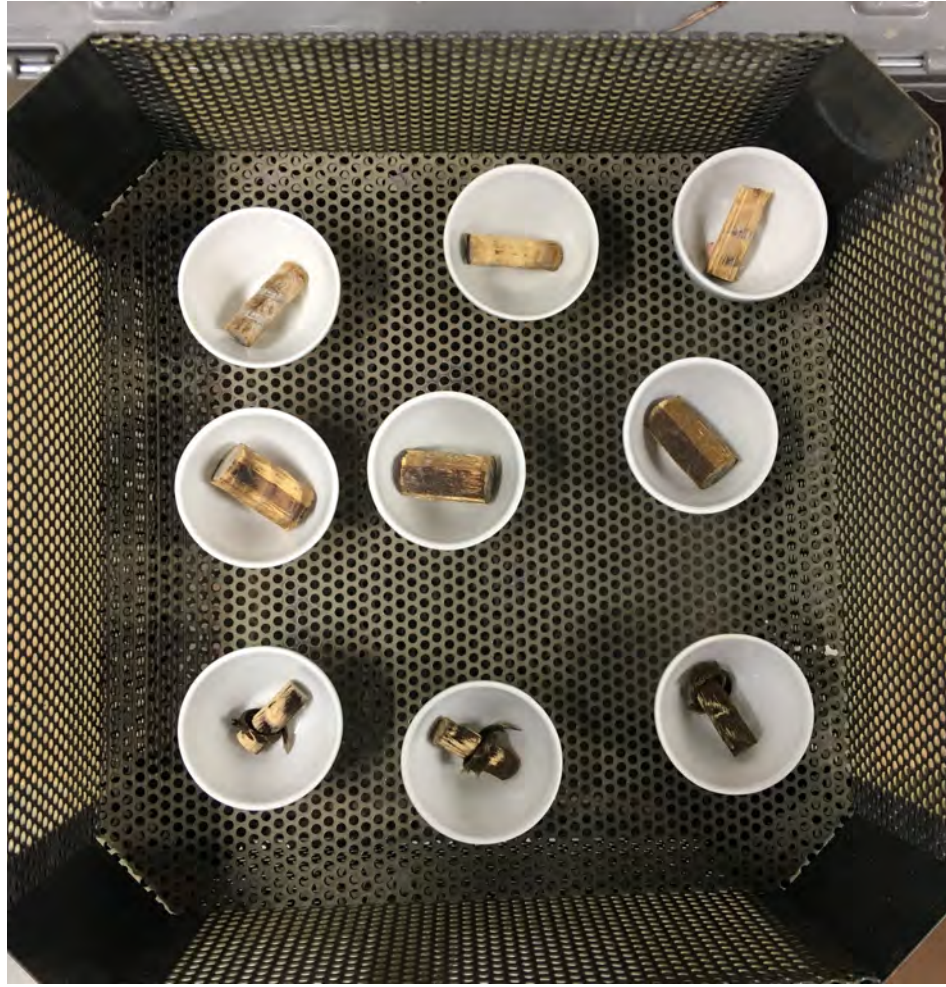


Figure 5.2: Fiber content specimen of rebar type C # 3, 5 after test



(a) Type A

(b) Type B

(c) Type C

Figure 5.3: Fiber content specimen of rebar # 3 after test

5.4 Moisture Absorption

The moisture absorption property of rebars was tested in accordance with ASTM D 5229 (ASTM, 2014). The graph plotted in Figure 5.4 represents weight change of the rebar specimen stored in distilled water over a test period of 98 d. It can be seen in the graph that all rebar types showed comparable moisture absorption behavior, except # 5 rebar from type C with epoxy resin. All the rebar types satisfied the AC454 limitations for the absorption limit of 0.25 % in first 24 hours of exposure except # 5 rebar from type C.

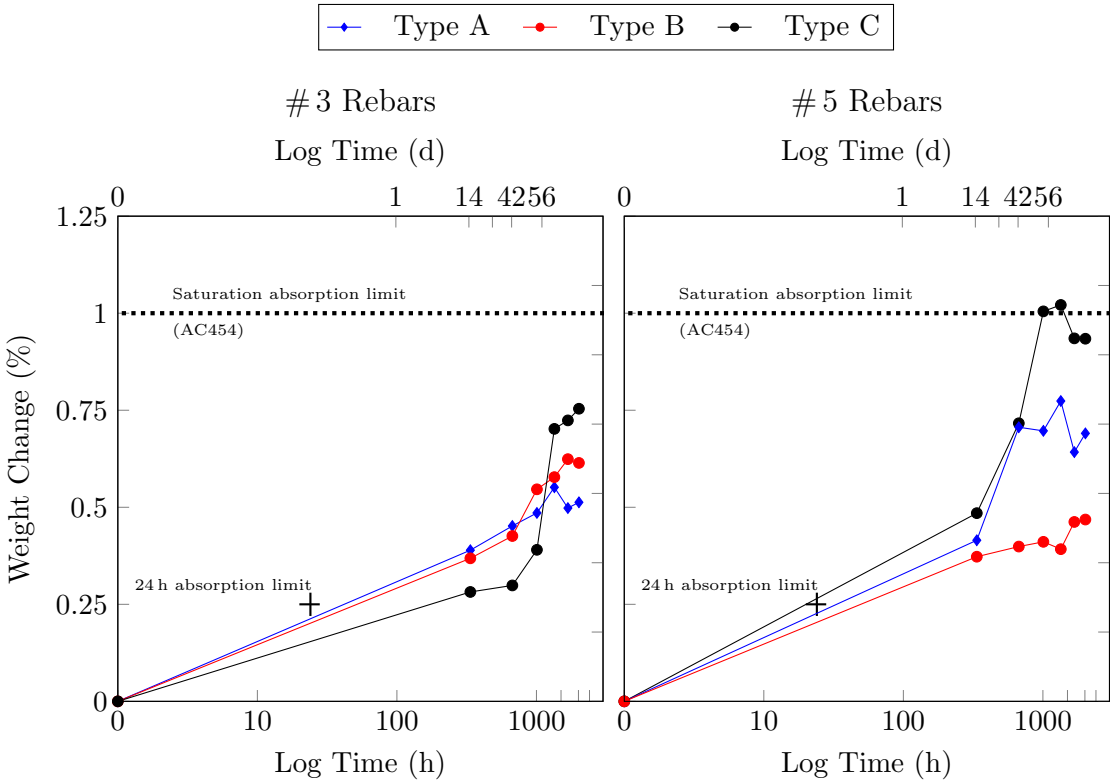


Figure 5.4: Moisture absorption results of rebars from all manufacturers

5.5 Transverse Shear Test

ASTM D 7617 (ASTM-International, 2012b) was used in the process of testing and analyzing the transverse shear strength of the rebars. Tested and processed data are plotted in the following sections 5.5.1 and 5.5.2.

5.5.1 Load vs. Displacement

The graphs plotted in Figures 5.5, 5.6, 5.7, and 5.8 show the load vs. displacement behavior of transverse shear behavior of #3 and #5 rebars from all manufacturers. The x-axis of the graph represents the cross-head extension or the relative displacement between the edges of the directly sheared specimen, while the y-axis shows the measured force throughout the load application period.

The Graph in figure 5.5 shows a linear behavior until it reaches the ultimate failure load. It

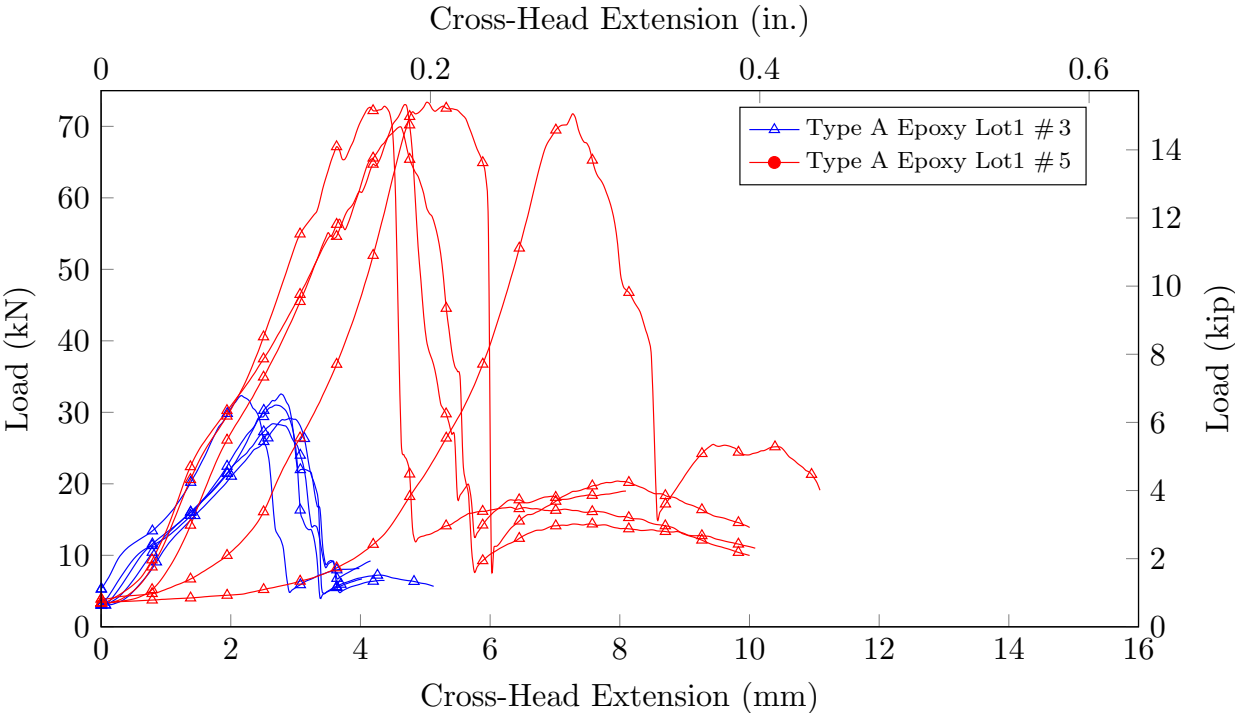


Figure 5.5: Extension vs. transverse shear load behavior of type A rebars Lot 1 size 3 and 5

can be seen that #5 sized rebar sustained higher load in comparison with #3 rebars. All the #3 rebars sustained a consistent load while #5 rebars sustained same peak load but the extension of the rebars varied. The graph in Figure 5.6 shows a comparison between the load and the displacement for transverse shear strength of #3 and #5 rebars lot 1 from type B rebar. It can be seen that the graph had a linear behavior until it reached the ultimate failure load. All the rebars sizes sustained a consistent load with similar extension. The graph in Figure 5.7 presents a comparison between the load and the displacement for of transverse shear strength of #3 and #5 rebars lot 1 from type C rebar. The graph shows a linear behavior until it reached 90% of the ultimate failure load.

The visualized data in Figure 5.8 show the load vs. displacement behavior for transverse shear

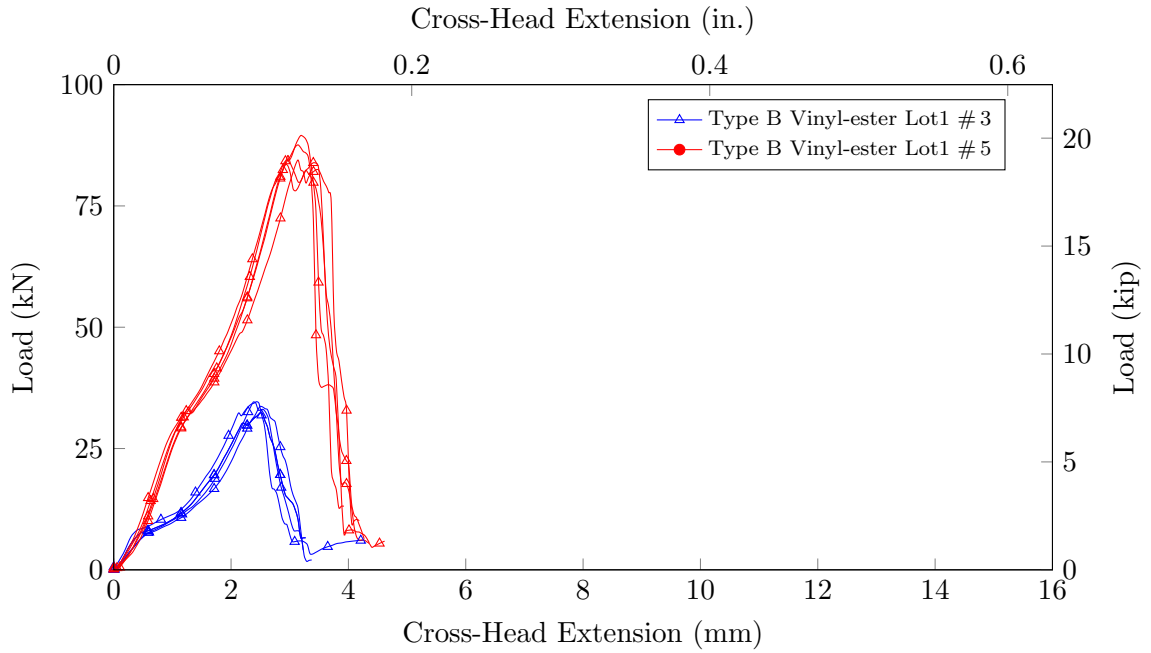


Figure 5.6: Extension vs. transverse shear load behavior of type B rebars Lot 1 size 3 and 5

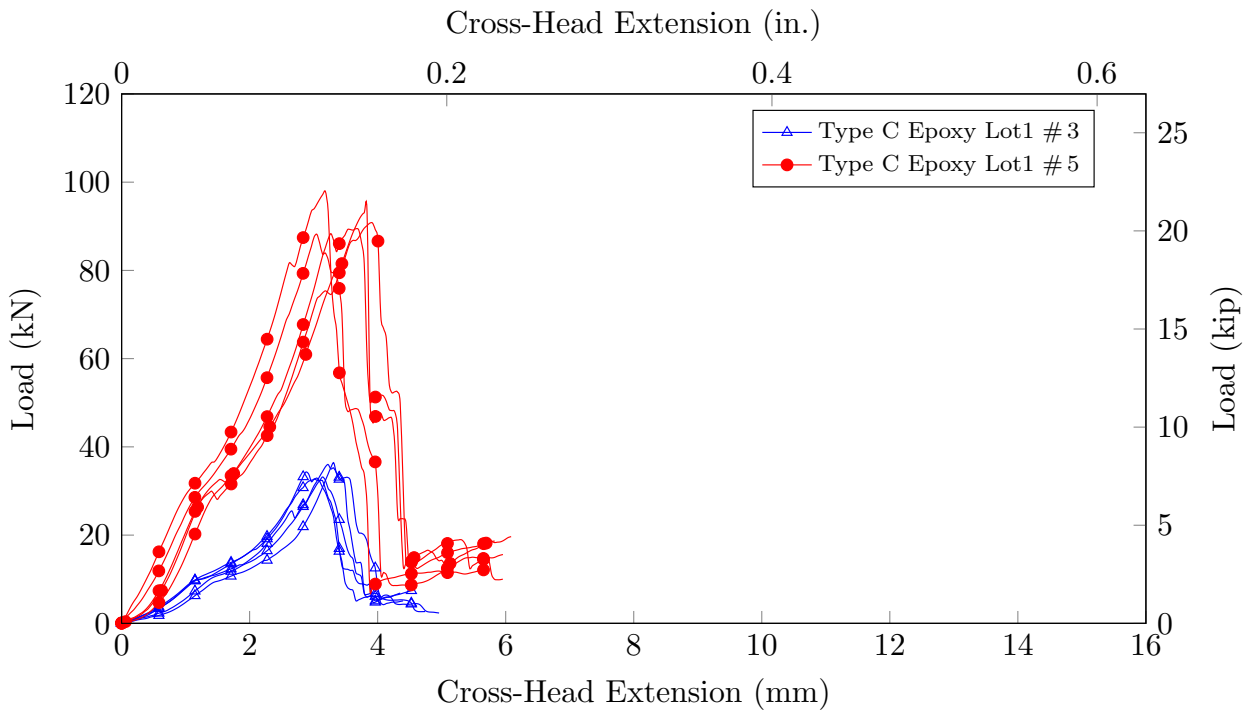


Figure 5.7: Extension vs. transverse shear load behavior of type C rebars Lot 1 size 3 and 5

strength of #3 and #5 rebars lot 2 from type C rebar. It can be seen that the material behaved linearly until 90% of the ultimate failure load was reached.

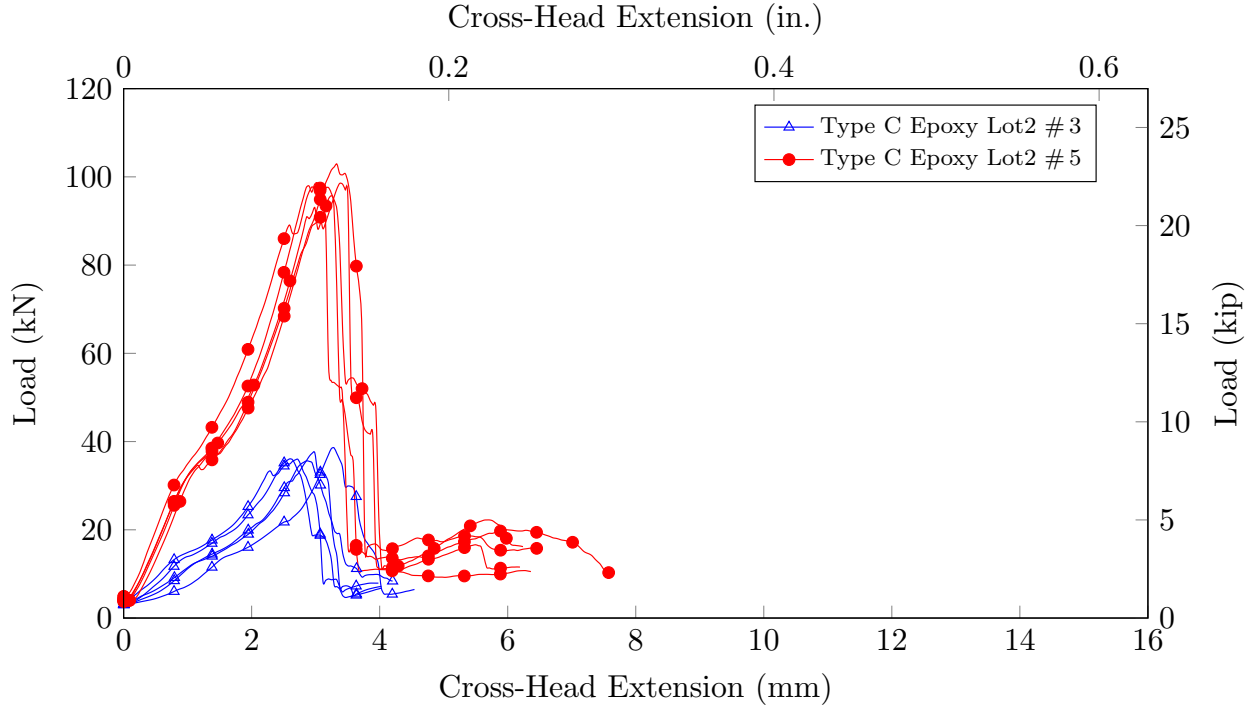


Figure 5.8: Extension vs. transverse shear load behavior of type C rebars Lot 2 size 3 and 5

5.5.2 Stress vs. Displacement

Transverse shear results are presented in Figures 5.9, 5.10, 5.11, and 5.12 compare the stress vs. displacement behavior of transverse shear test of # 3 and # 5 rebars from all rebar manufacturer. The data along the x-axis represents the cross-head extension or the direct shear displacement, while the y-axis signifies the measured shear stress.

The data in Figure 5.9 show that the material behaved nearly linearly until the ultimate failure load was reached. It can be seen in Figure 5.9 that the stress vs. strain behavior of both the rebars is close but not identical-especially because it varied significantly for rebar number # 5.

The graph in Figure 5.10 presents the stress vs. displacement behavior of transverse shear test of rebar type C lot 1. From the post failure stress vs. strain behavior of rebar type C as shown in Figure 5.10, it can be seen that the rebars underwent similar failure behavior.

The graph in Figure 5.11 presents the stress vs. displacement behavior of transverse shear test of rebar type C lot 1. The graphs display a mostly linear behavior until the ultimate failure load was reached. Figure 5.12 shows the stress vs. displacement behavior of transverse shear test of rebar type C lot 2. It can be seen that the data represented a nearly linear behavior until the ultimate

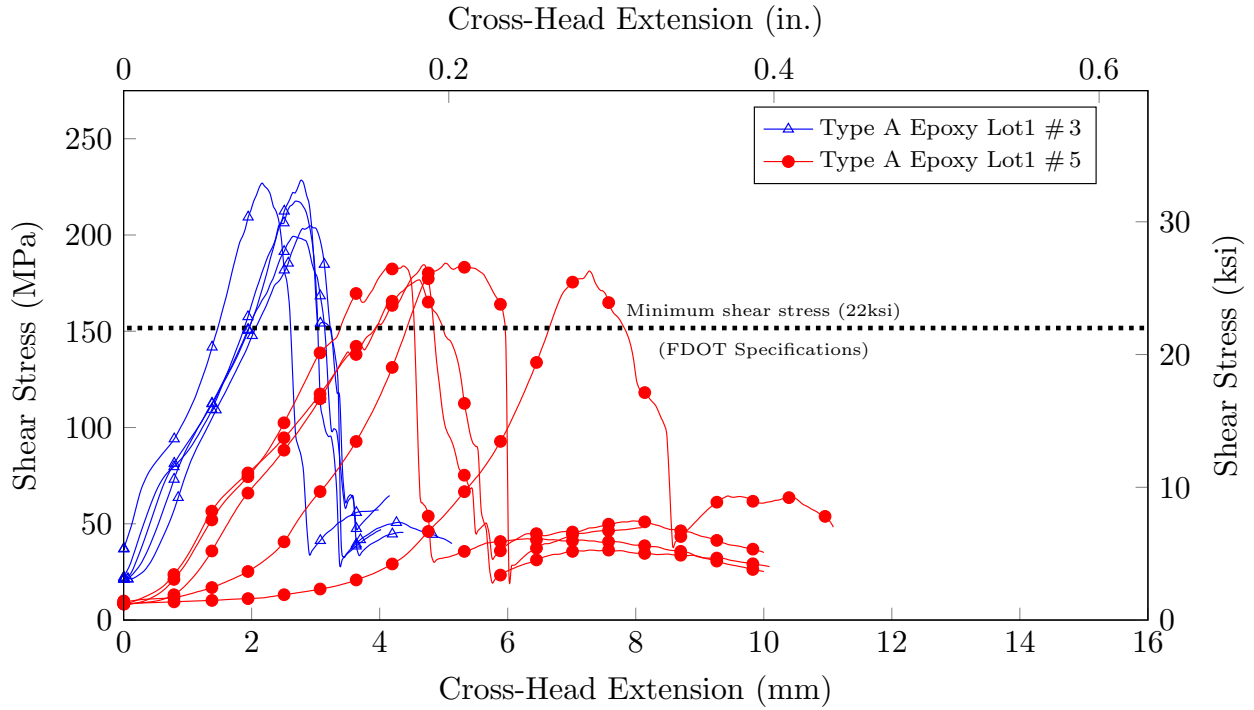


Figure 5.9: Transverse shear stress vs. extension behavior of rebar type A Lot 1 size 3 and 5

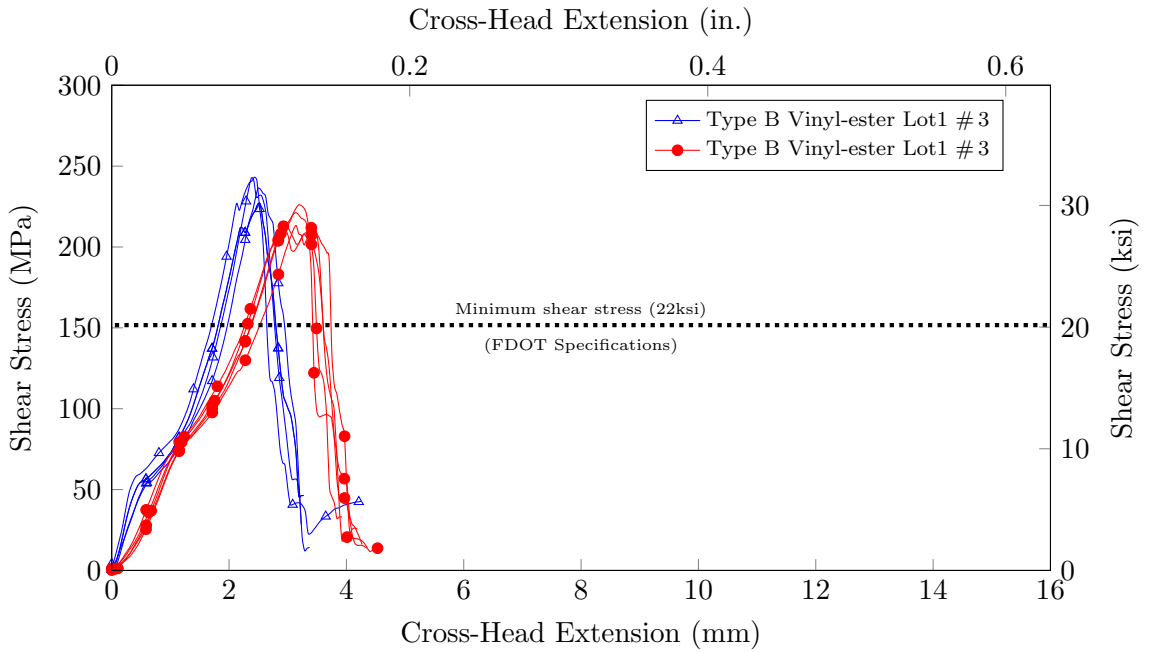


Figure 5.10: Transverse shear stress vs. extension results of rebar type B Lot 1 size 3 and 5

failure load was attained. The stress vs. strain behavior of failed rebar specimen from both lots of type C in Figures 5.11 and 5.12 show that, although the ultimate failure capacity of the rebars varied significantly, all the rebar samples failed in an identical manner.

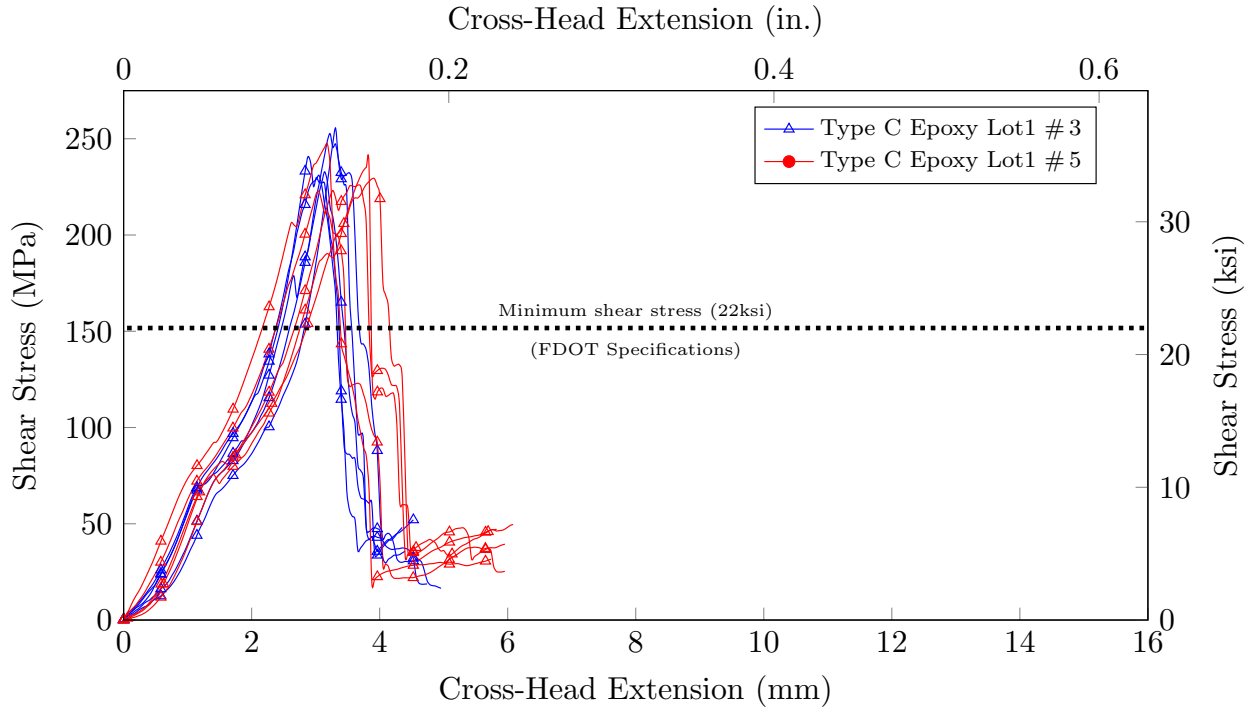


Figure 5.11: Transverse shear stress vs. extension behavior of type C Lot 1 size 3 and 5

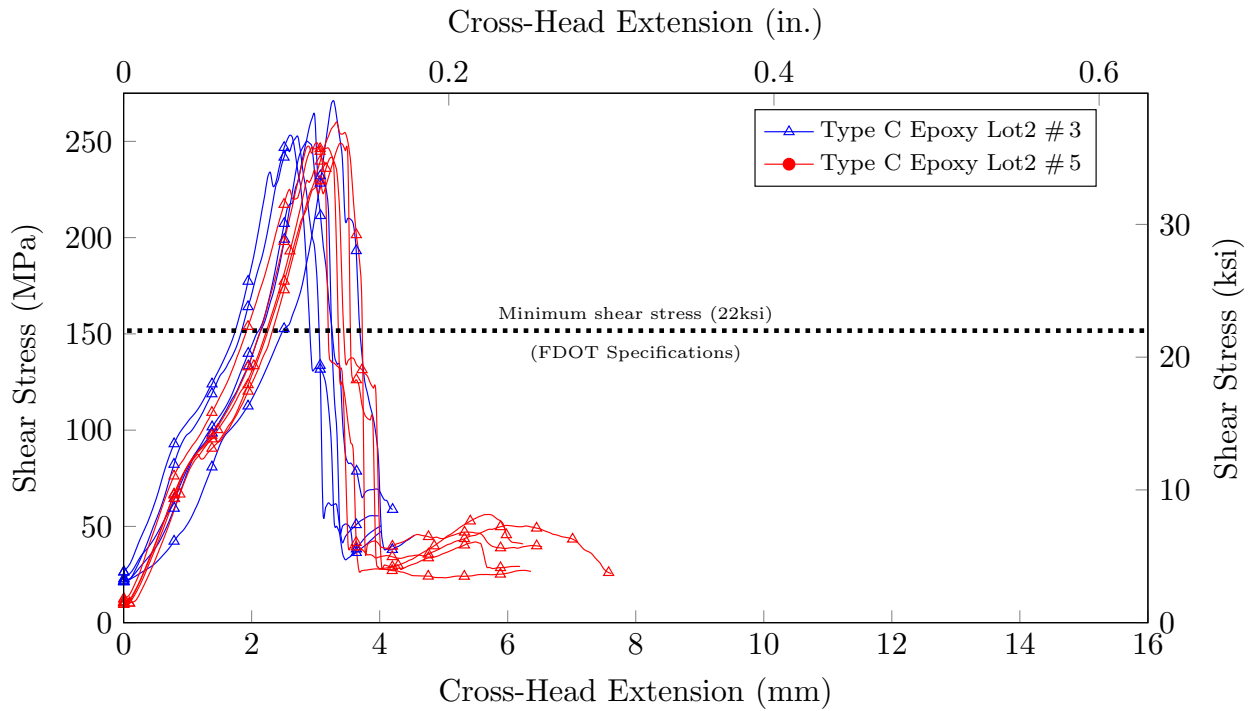


Figure 5.12: Transverse shear stress vs. extension behavior of type C Lot 2 size 3 and 5

5.6 Modes of Failure

To study the failure process, the failed BFRP rebars were analyzed in detail to observe the failure pattern of outer fibers and inner fibers. Therefore Figure 5.13 exemplifies the failure patterns of the tested BFRP specimen in response to the applied transverse shear loads. Figure 5.13 shows that the failure mode for all the rebars was identical irrespective of the sizes and types. The test fixture was designed so that direct shear stresses are applied perpendicular to the longitudinal axis of the rebars and a “scissor-like” failure occurs at the center of the specimen as dictated in ASTM standards. After a detailed analysis of failed specimens, it was seen that similar to GFRP rebars, BFRP rebar samples also tried to bend throughout the test, although fibers were aligned in the longitudinal direction.



(a) Type A #3



(b) Type A #5



(c) Type B #3



(d) Type B #5



(e) Type C #3



(f) Type C #5

Figure 5.13: Failure pattern for tested rebar after transverse shear test

5.7 Summary of Transverse Shear Properties

The results of the statistical evaluation for the transverse shear strength properties of the tested products are listed in the following Table 5.2. A total of 30 specimen, five for each rebar type and size, were tested. The average and all other statistical values were calculated based on a sample size of five specimen, and the corresponding results are shown in the table. For numerical comparison and concluding values, Table 5.2 lists the minimum shear stress (\wedge), the maximum shear stress (\vee), the average shear stress (μ), the standard deviation (σ), and the coefficient of variation (CV) for each individual test sample.

Table 5.2: Transverse Shear test statistical values for each sample group (US Customary Units)

Sample Group				Statistical Values				
Manuf. Type	Resin Type	Size #	Lot No.	Shear Stress				
				\wedge ksi	\vee ksi	μ ksi	σ ksi	CV %
Rebar A	Epoxy	3	1	29.1	33.2	31.4	1.9	6.00
Rebar A	Epoxy	5	1	25.7	26.9	26.5	0.5	1.94
Rebar B	Vinyl-ester	3	1	33.3	35.8	34.5	1.2	3.51
Rebar B	Vinyl-ester	5	1	30.8	32.9	31.7	0.8	2.62
Rebar C	Epoxy	3	1	33.6	37.5	35.2	1.6	4.64
Rebar C	Epoxy	3	2	36.5	39.8	37.7	1.4	3.71
Rebar C	Epoxy	5	1	32.4	35.9	33.7	1.4	4.14
Rebar C	Epoxy	5	2	35.3	38.0	36.5	1.0	2.71

It can be seen in Tables 4.3 and 4.4 that all the BFRP rebar samples are satisfying the minimum required criteria for GFRP transverse shear stress.

5.8 Apparent Horizontal Shear Test

The FRP rebar products were tested for horizontal shear properties. The horizontal shear test was conducted according to the ASTM D 4475 (ASTM-International, 2012a) standards.

5.8.1 Load vs. Displacement

The graphs in Figures 5.14, 5.15, 5.16, and 5.17 plot the load vs. displacement behavior of short span 3 point bending. Each rebar type is shown individually — and every specimen within the relevant sample is displayed — to compare # 3 and # 5 from the same manufacturer. The x-axis of the graph represents the cross-head frame displacement, and the y-axis represents the applied load.

The graph in Figure 5.14 shows a nearly linear behavior until it reached the ultimate failure load. Following the peak load, a descending branch proceeds with individual peaks and falls. The

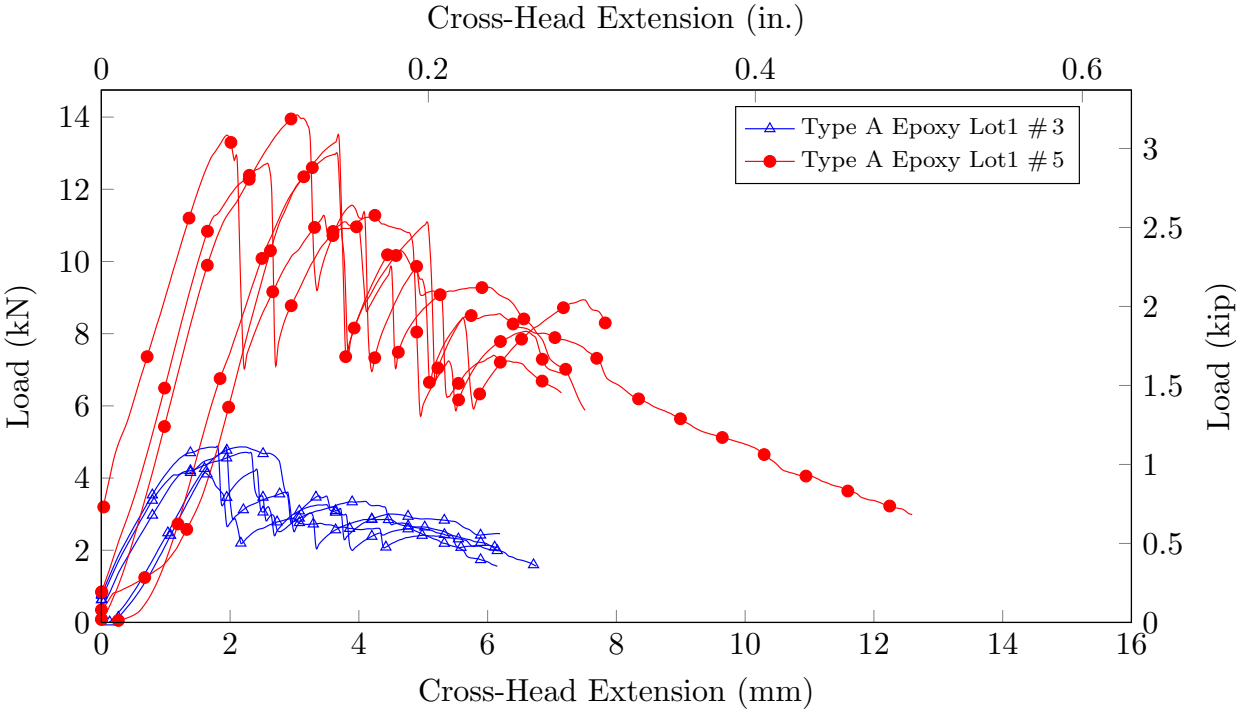


Figure 5.14: Extension vs. horizontal shear load behavior of rebar type A Lot 1 size 3 and 5

peaks and falls represent individual layers of fibers engaged and failing in tension located in the lower part of the specimen experiencing pure tension, while the upper part is in compression.

Extension vs. Horizontal shear behavior of rebar type B can be seen in the graph in Figure 5.15. Similar to type A, # 5 type B rebar sustained more load in comparison with # 3 rebars. The failure

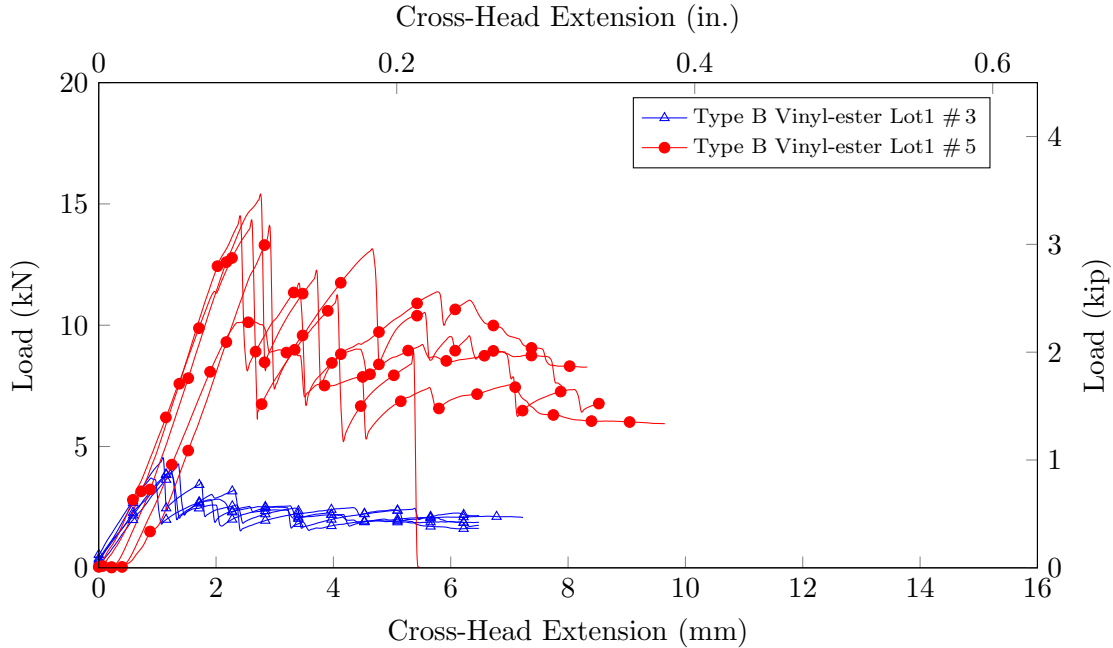


Figure 5.15: Extension vs. horizontal shear load behavior of rebar type B Lot 1 size 3 and 5

pattern of both rebars was similar and identical to type A rebar failure pattern.

The graphs shown in Figures 5.16 and 5.17 show the load vs. displacement behavior of rebar type C Lot 1 and 2. The graphs show a linear behavior until it reached 90 % of the ultimate failure load. It can be seen in Figures 5.16 and 5.17 that the failure behavior of type C rebar is identical irrespective of production lot and rebar size. After a detailed analysis, we can see the shear lag effect in the rebars similar to other two types.

5.8.2 Stress vs. Displacement

To provide clarity and to compare the transverse shear strength performance of the two rebar sizes, stress vs. strain behavior of rebar is shown in this section via graphs. The following graphs in Figures 5.18, 5.20, and 5.21 show the comparison of the stress vs. cross-head behavior for the tested BFRP rebars. The x-axis of graph represents the cross-head extension, while the y-axis signifies the measured shear stresses. As expected, there is a significant difference in peak load between rebar sizes of type A rebar. Nevertheless, the resultant horizontal shear stress is approximately the same regardless of the rebar size. The stress vs. strain behavior of rebar type B shows that the failure pattern was identical for both the sizes but #5 rebars sustained more stress in comparison with #3 rebars.

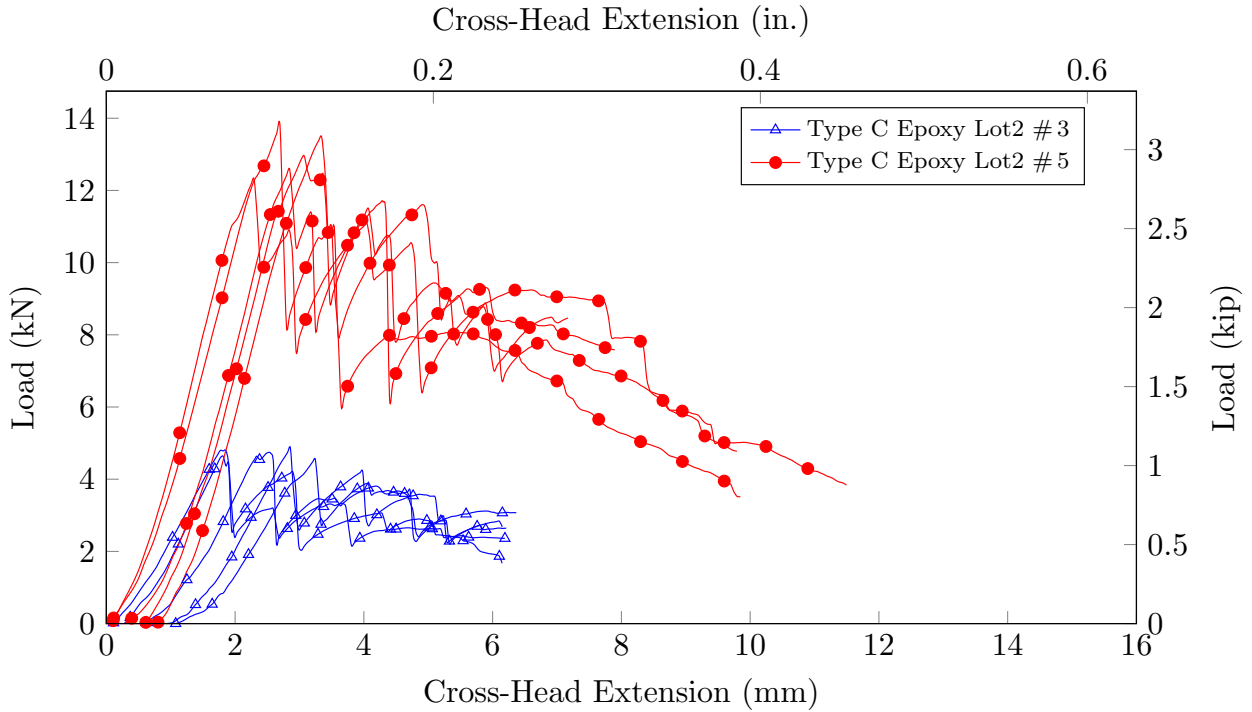


Figure 5.16: Extension vs. horizontal shear load behavior of type C Lot 1 size 3 and 5

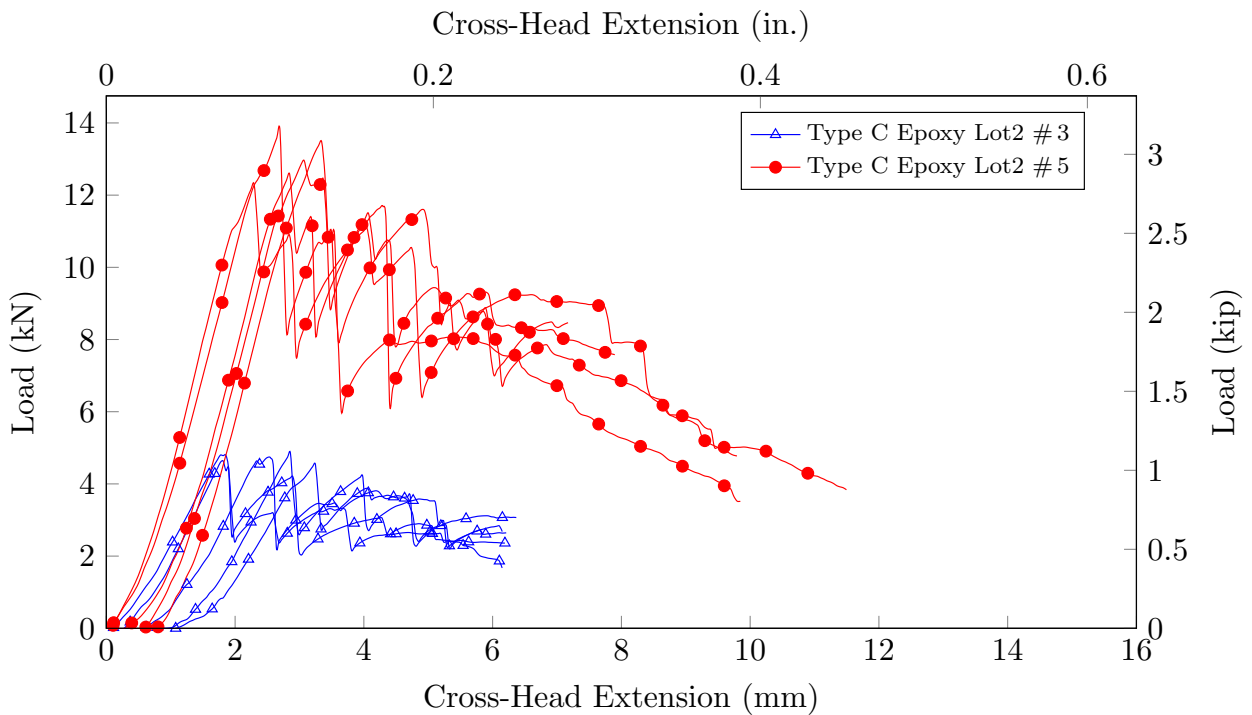


Figure 5.17: Extension vs. horizontal shear load behavior of type C Lot 2 size 3 and 5

The graphs in Figures 5.20 and 5.21 compare the stress vs. displacement behavior of horizontal shear test of #3 and #5 rebars from lot 1 and 2 of type C rebars. Figures 5.20 and 5.21 show

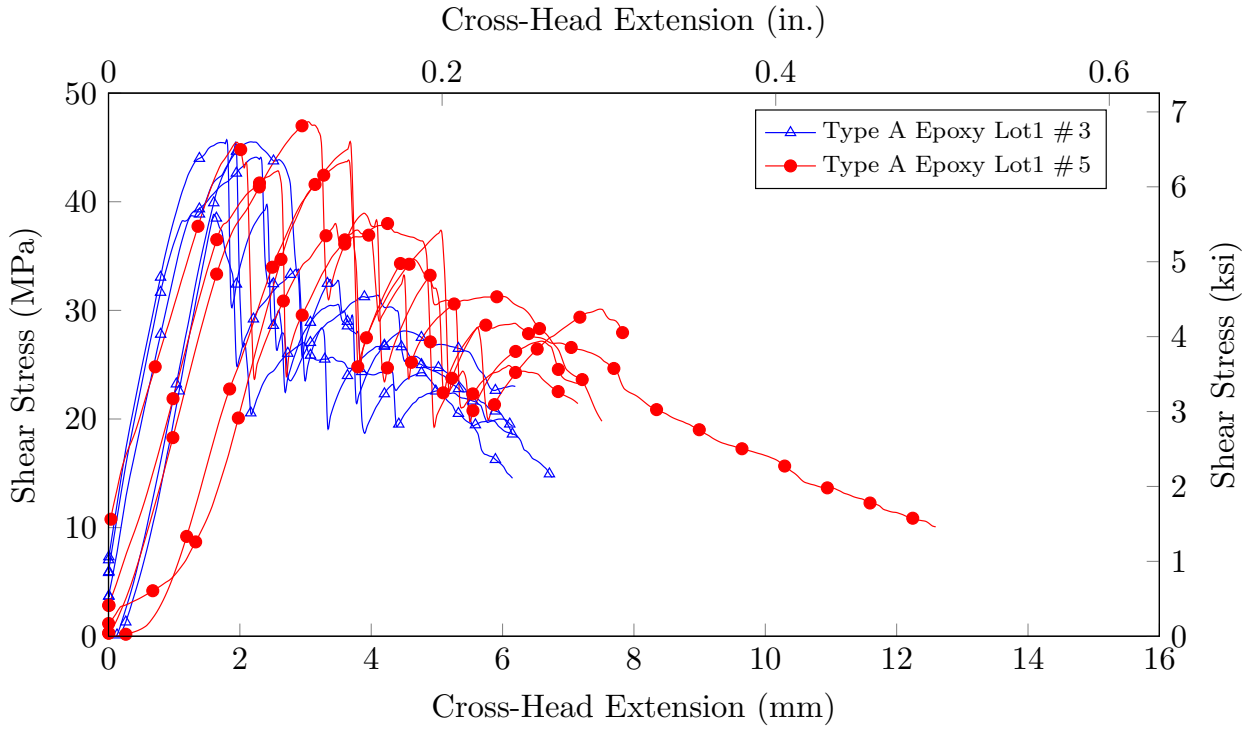


Figure 5.18: Horizontal shear stress vs. extension behavior of rebar type A Lot 1 size 3 and 5

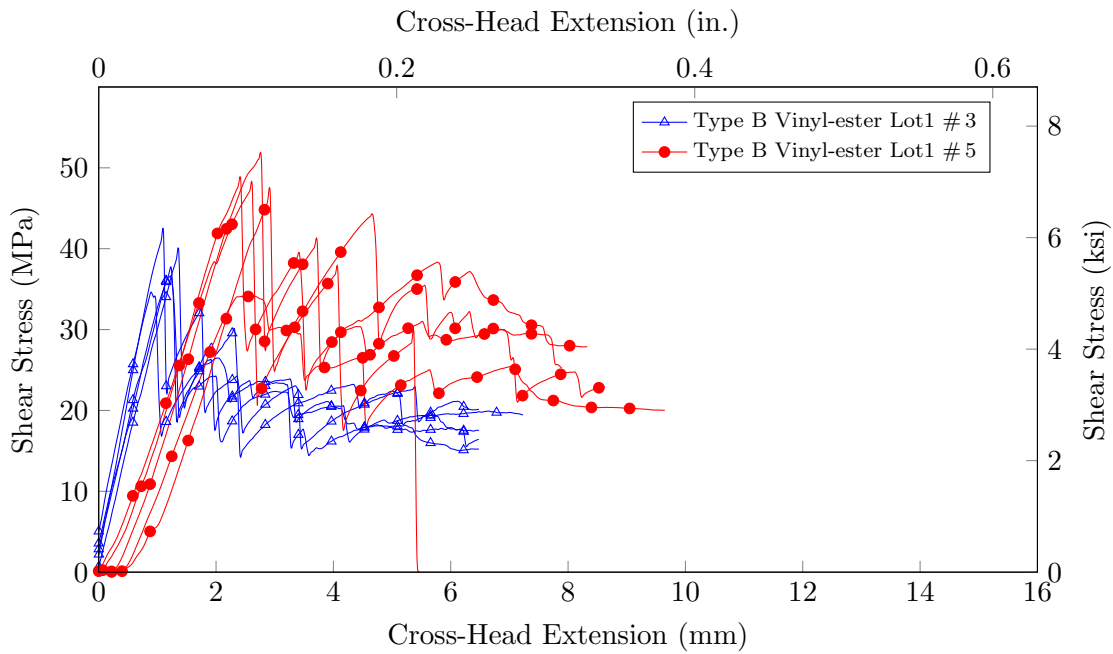


Figure 5.19: Horizontal shear stress vs. extension behavior of rebar type B Lot 1 size 3 and 5

that all the rebars of type C underwent similar stress and strain irrespective of lot and size.

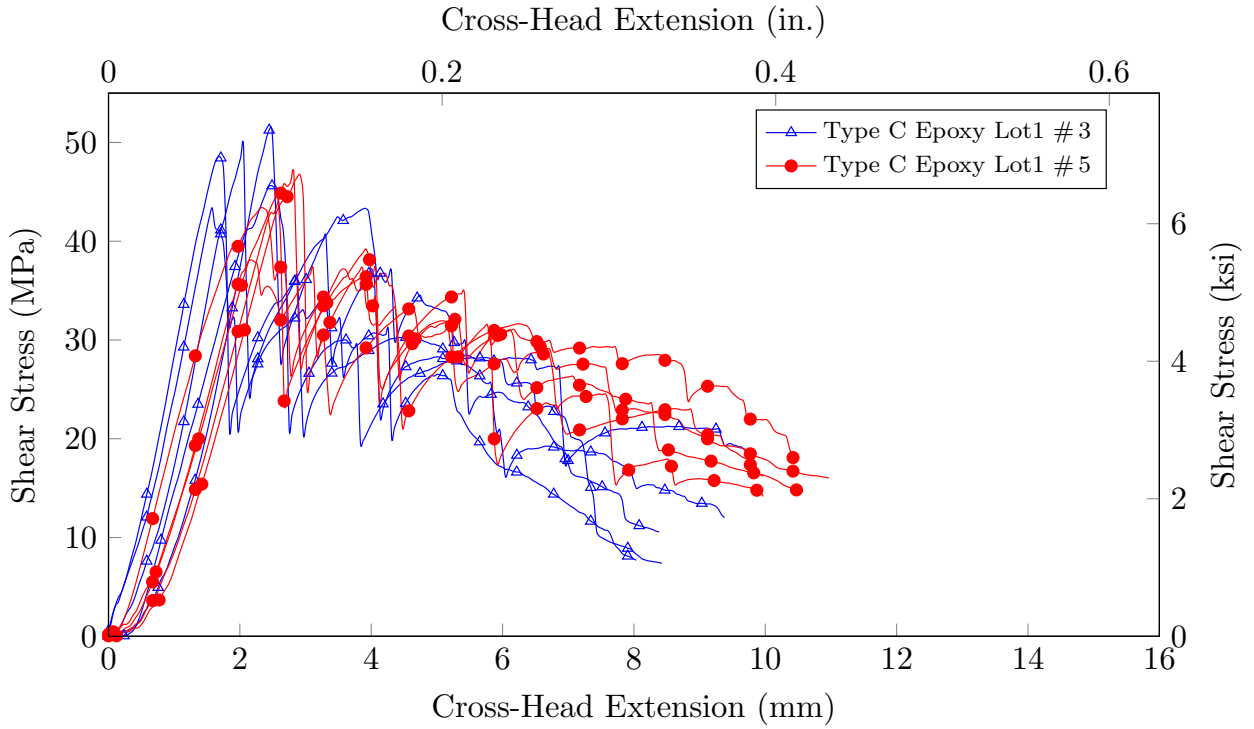


Figure 5.20: Horizontal shear stress vs. extension behavior of rebar type C Lot 1 size 3 and 5

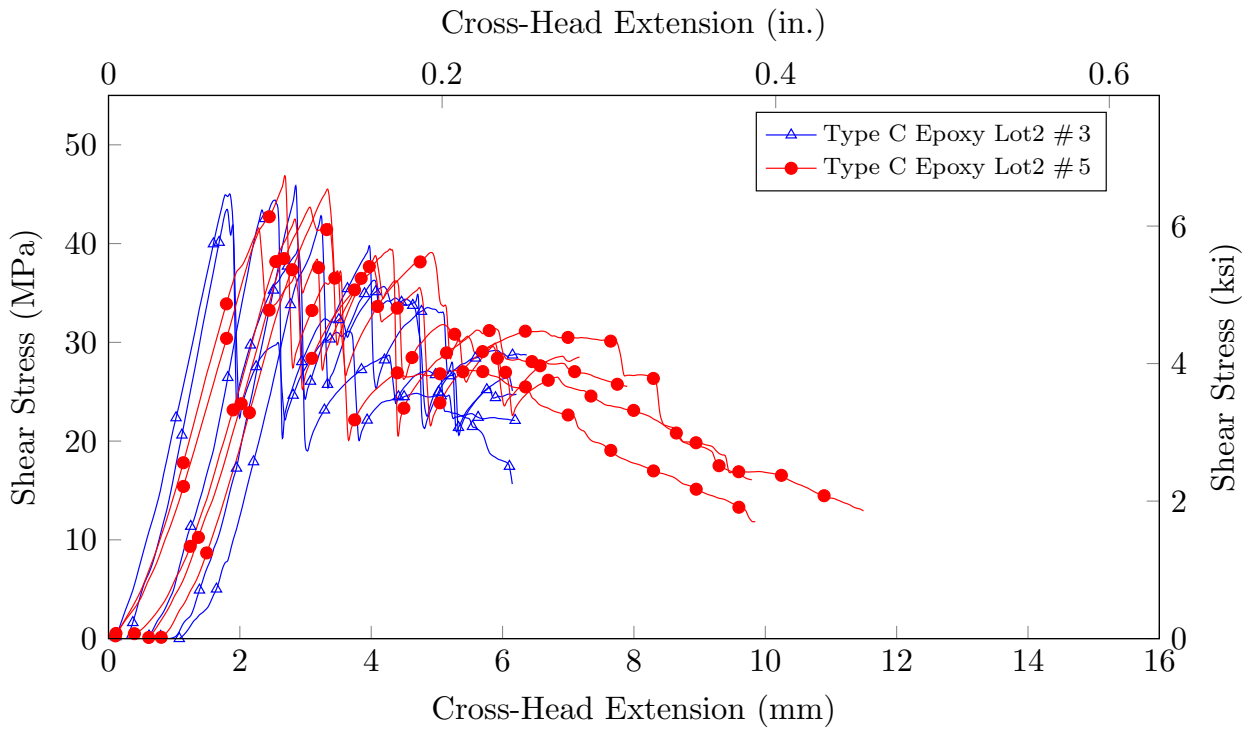


Figure 5.21: Horizontal shear stress vs. extension behavior of rebar type C Lot 2 size 3 and 5

5.9 Modes of Failure

To study the shear lag effect of BFRP rebars, failure modes of the tested rebars were analyzed. Figure 5.22 shows the failed BFRP specimen after completion of the horizontal shear test. All the



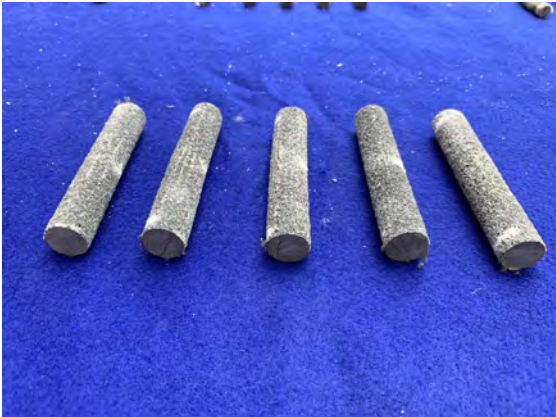
(a) Type A #3



(b) Type A #5



(c) Type B #3



(d) Type B #5



(e) Type C #3,



(f) Type C #5

Figure 5.22: Failure pattern for tested rebar after horizontal shear test

tested specimens failed due to the apparent horizontal shear force, resulting in horizontal failure planes as observed from the perpendicular cracks to the applied load, through the depth of the cross section. After the peak load, secondary cracks were generated representing the horizontal shear failure plane as each inter-laminar layer of fibers is engaged in tension and then failing in fiber-matrix interface.

5.10 Summary of Horizontal Shear Strength Properties

The statistical values for the horizontal shear strength properties of the tested products are listed in the following Table 5.3. A total of 30 specimens, five for each type and each size, were tested in total. The average of five specimens was assigned to each sample (specimen group) as shown in the table. All BFRP rebar samples satisfied the minimum acceptance criteria for the horizontal shear strength of glass FRP rebars according to FDOT Specifications 932, with the ultimate values shown in Tables 4.3 and 4.4.

Table 5.3: Horizontal Shear test statistical values for each sample group (US Customary Units)

Sample Group				Statistical Values				
Manuf. Type	Resin Type	Size #	Lot No.	Shear Stress				
				\wedge ksi	\vee ksi	μ ksi	σ ksi	CV %
Rebar A	Epoxy	3	1	5.8	6.7	6.4	0.4	5.90
Rebar A	Epoxy	5	1	6.2	6.9	6.5	0.3	3.89
Rebar B	Vinyl-ester	3	1	5.1	6.1	5.6	0.4	6.80
Rebar B	Vinyl-ester	5	1	5.0	7.5	6.6	1.0	14.46
Rebar C	Epoxy	3	1	6.4	7.5	7.0	0.5	6.57
Rebar C	Epoxy	3	2	6.2	6.7	6.5	0.2	2.79
Rebar C	Epoxy	5	1	5.6	6.8	6.4	0.5	7.98
Rebar C	Epoxy	5	2	6.0	6.8	6.4	0.3	4.99

For numerical comparison and concluding values, Table 5.3 lists the minimum shear stress (\wedge),

the maximum shear stress (\wedge), the average shear stress (μ), the standard deviation (σ), and the coefficient of variation (CV) for each individual test sample.

5.11 Tensile Test

The rebars were tested according to the ASTM D 7205 (ASTM-International, 2015a) to evaluate the tensile properties. The obtained and processed data of the tensile strength test are shown in this section via graphs and table.

5.11.1 Load vs. Displacement Behavior

To compare the load vs. displacement behavior of the different rebar samples and specimens, the graphs in the Figure 5.23, 5.24, 5.29, and 5.30 plot the recorded test data. As shown, the x-axis of the graph represents the cross-head extension — which has to be interpreted with care because it includes the elastic deformation of the load frame and the test fixtures — and the y-axis indicates the applied and measured load. Figure 5.23 shows that # 5 rebar type A sustained higher failure

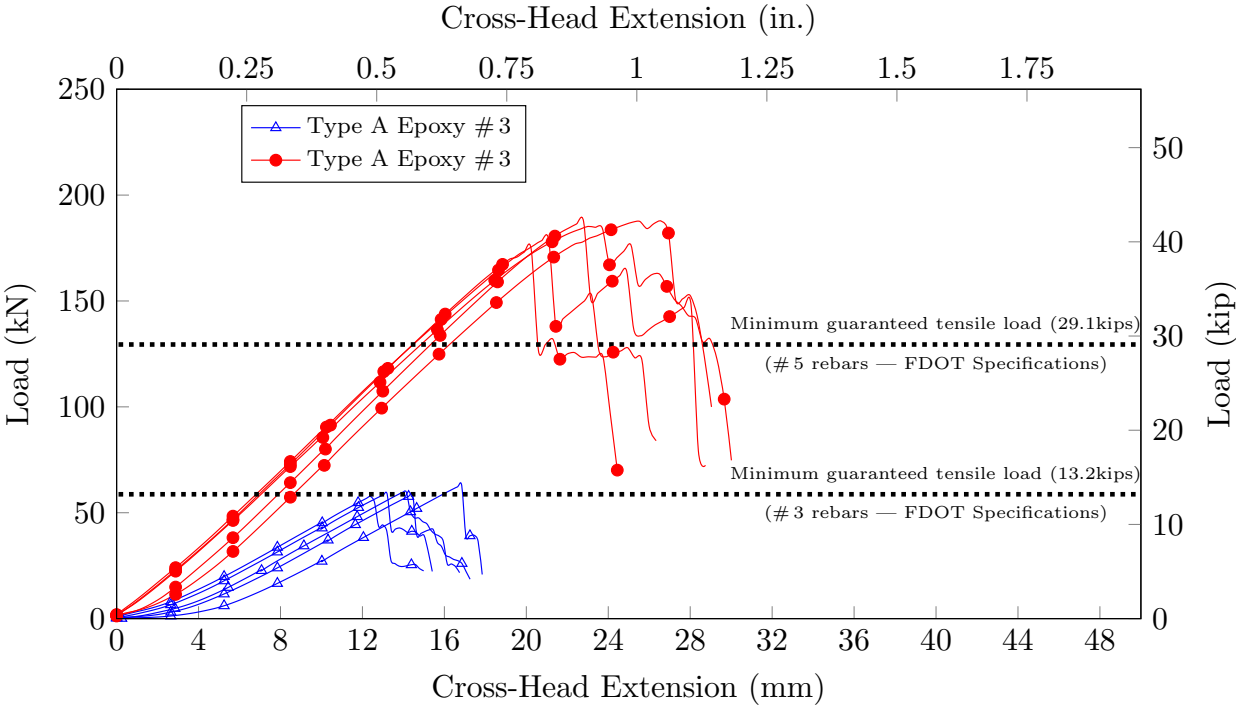


Figure 5.23: Tensile strength vs. displacement behavior of rebar type A Lot 1 size 3 and 5

load in comparison with # 3 rebars. And the extension of rebar # 5 was almost twice that of the # 3

rebars extension. Figure 5.24 shows that the extension of # 5 was more than twice in comparison

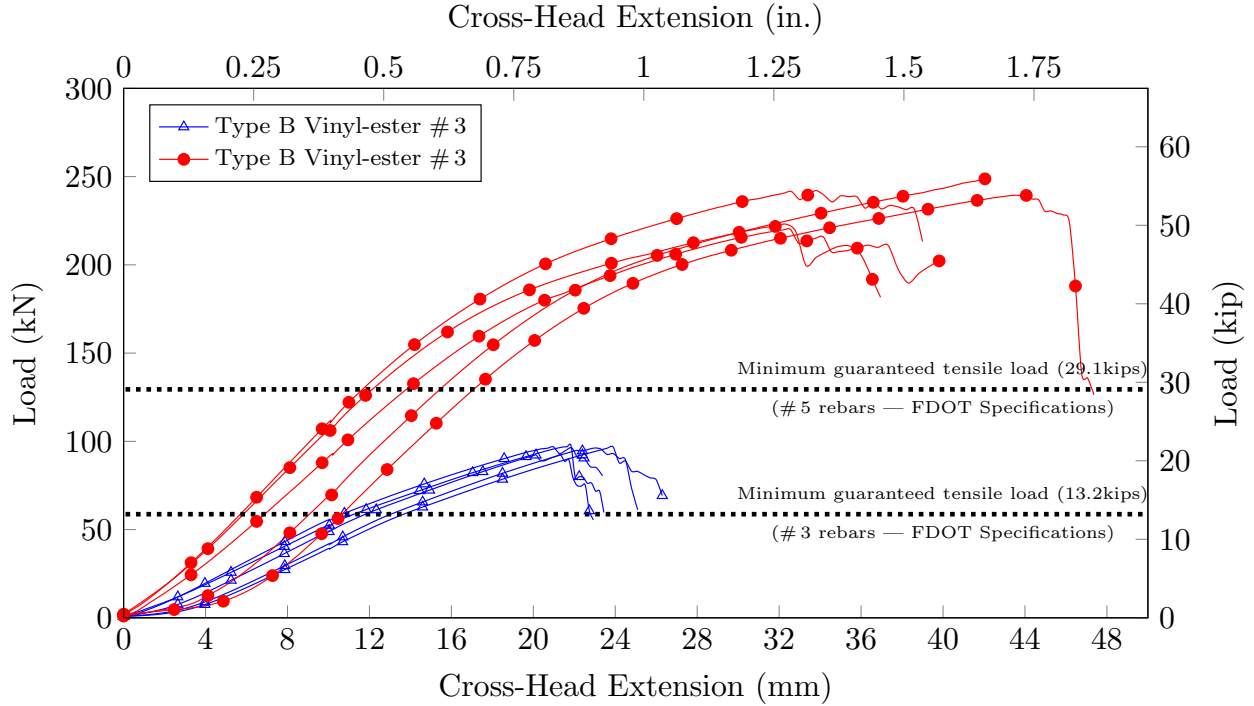


Figure 5.24: Tensile strength vs. displacement behavior of rebar type B Lot 1 size 3 and 5

with # 3 rebar and the peak load was much higher. All the rebar failed in similar fashion. After

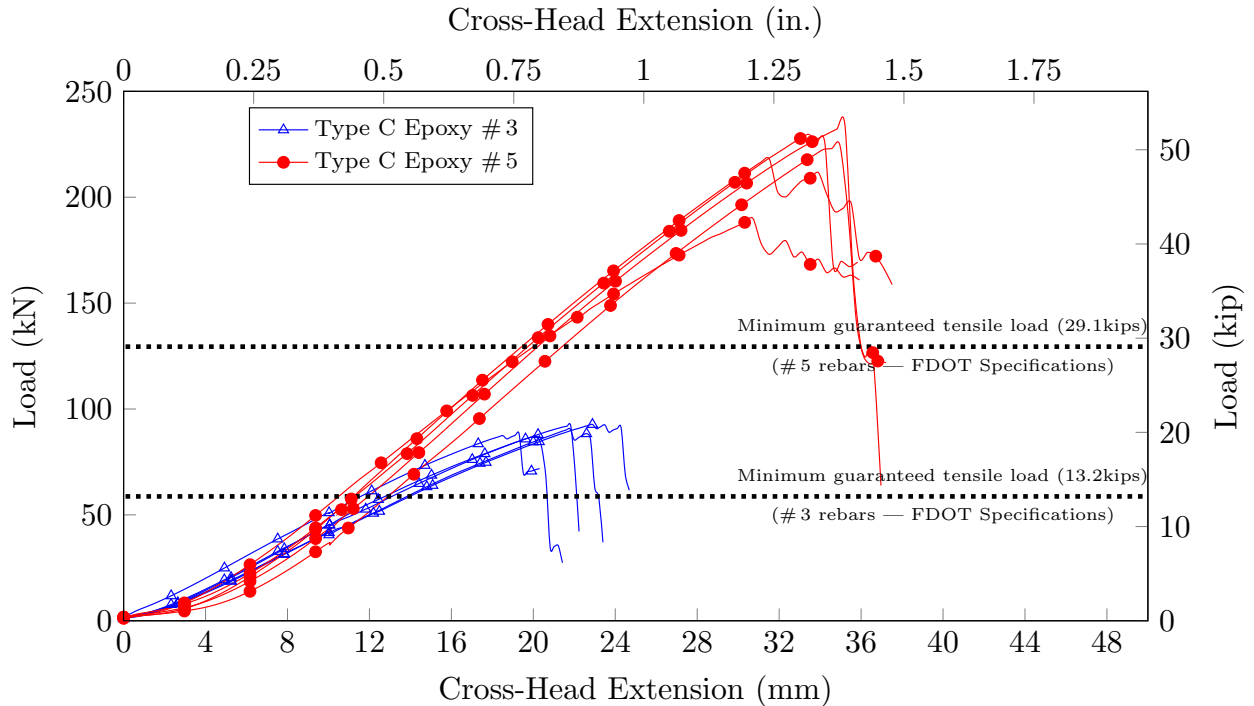


Figure 5.25: Tensile strength vs. displacement behavior of rebar type C Lot 1 size 3 and 5

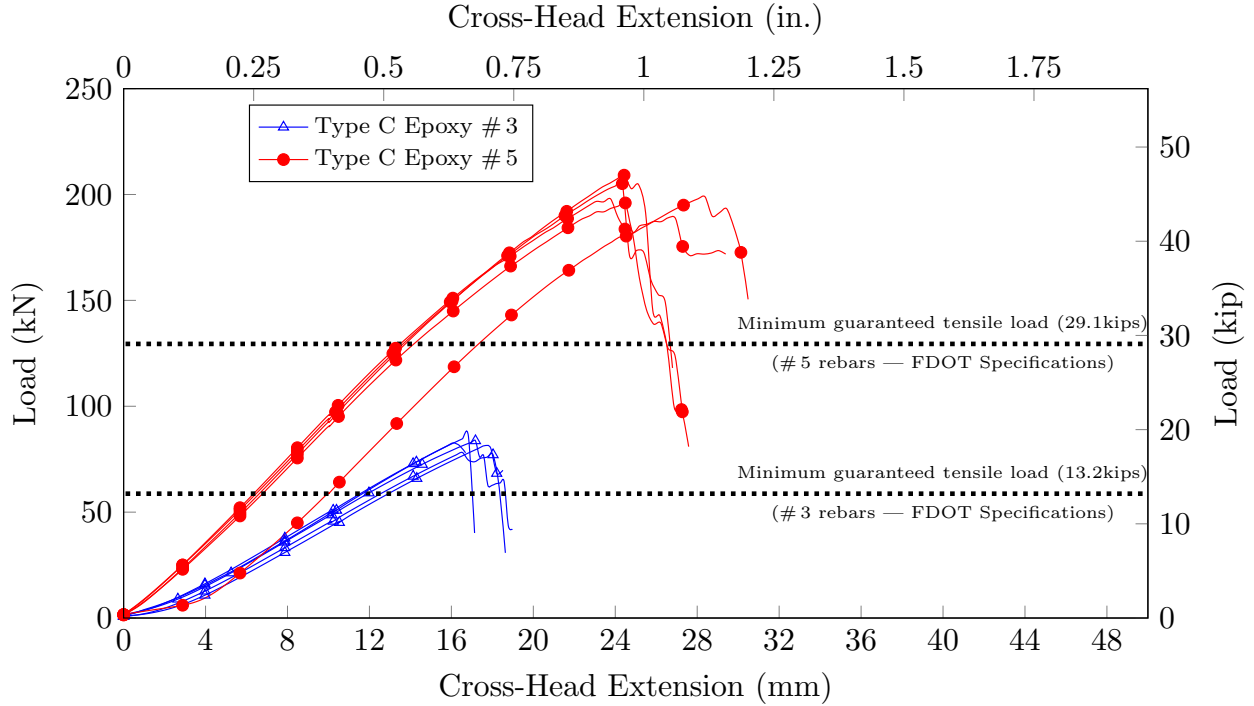


Figure 5.26: Tensile strength vs. displacement behavior of rebar type C Lot 2 size 3 and 5

comparing Figures 5.25 and 5.26, it can be seen that the rebars of the same size from both the lots of type C sustained the same peak load and failed in the same mode. Post failure extension of #5 rebars was almost twice in comparison with #3 rebars.

5.11.2 Stress vs. Strain Behavior

The stress-strain behavior of the failed rebars of all types was plotted to quantify and compare the elastic moduli of the tested BFRP rebars. The data in the Figures 5.27, 5.28, 5.29, and 5.30 were plotted to compare the stress vs. strain behavior of the different rebar types. Accordingly, the x-axis shows the applied stress while the y-axis represents the outermost surface strain that was measured with an external extensometer (c.f. Chapter 4, section 4.3). The post failure results plotted in the graph in Figure 5.27 show that although the load capacities of the different sized rebars vary in large scale, the slope of the stress-strain curve is identical for all the rebars.

It can be seen in Figure 5.28 that the post failure results, also known as stress-strain behavior of rebar type B are nonidentical for both the rebar sizes.

The post failure stress-strain behavior of rebar type C as shown in Figures 5.29 and 5.30 show that the slopes of #3 bars from different lots are identical but slopes of #5 bars are not identical.

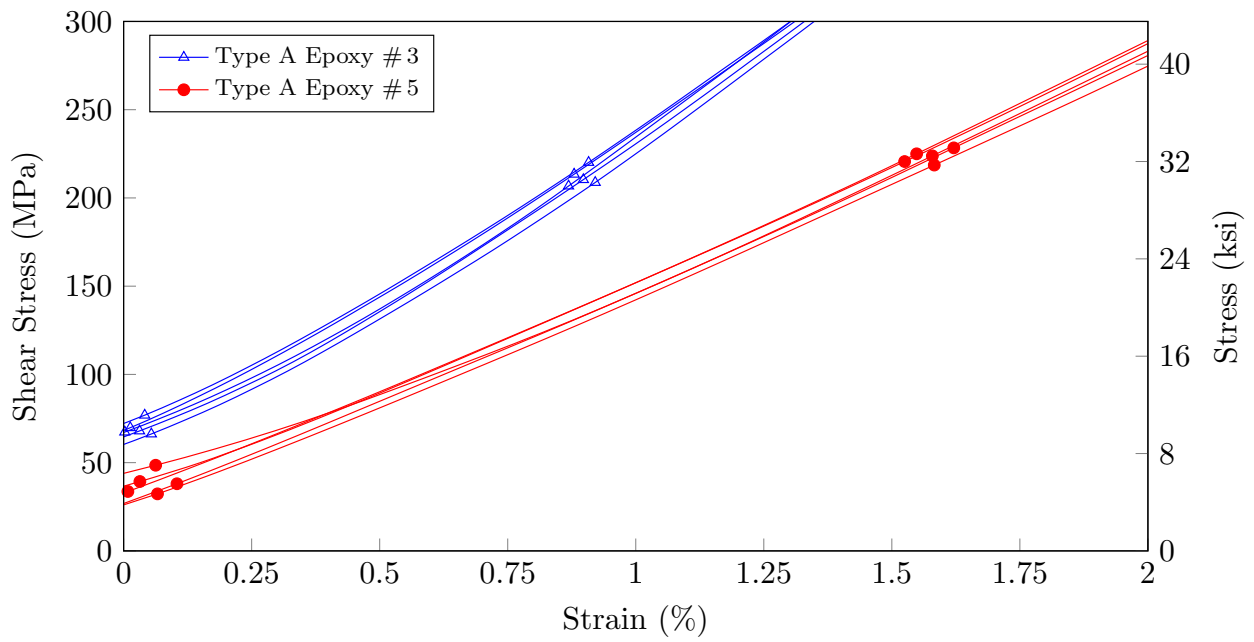


Figure 5.27: Tensile stress vs. strain behavior of rebar type A Lot 1 rebar size 3 and 5

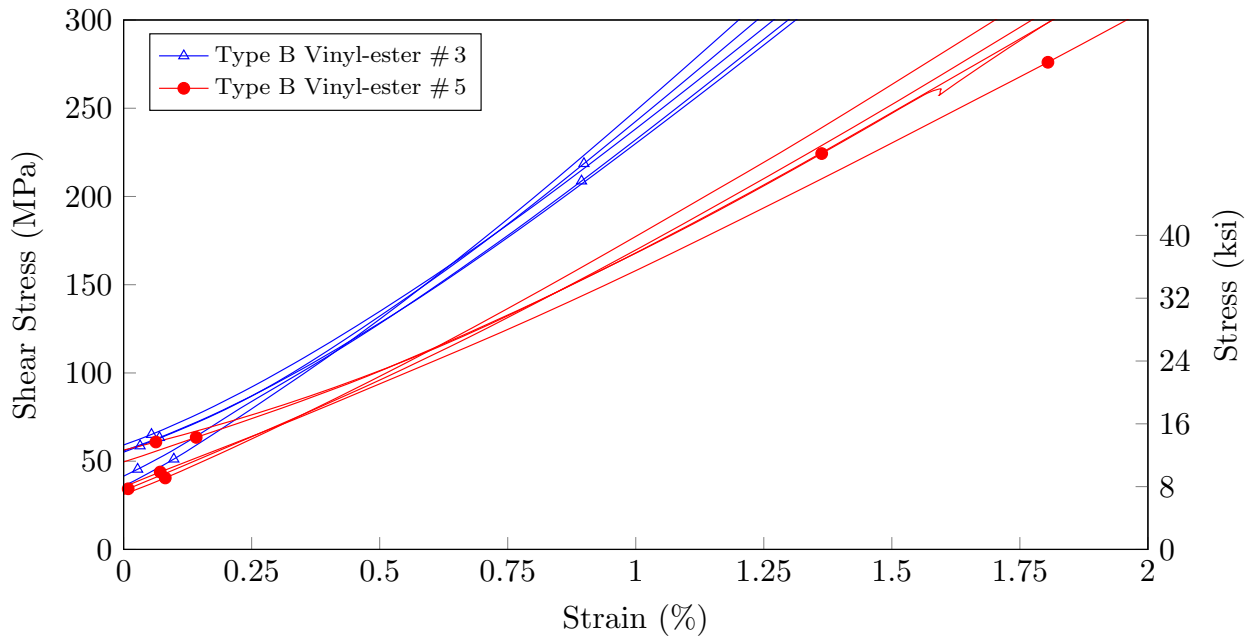


Figure 5.28: Tensile stress vs. strain behavior of rebar type B Lot 1 rebar size 3 and 5

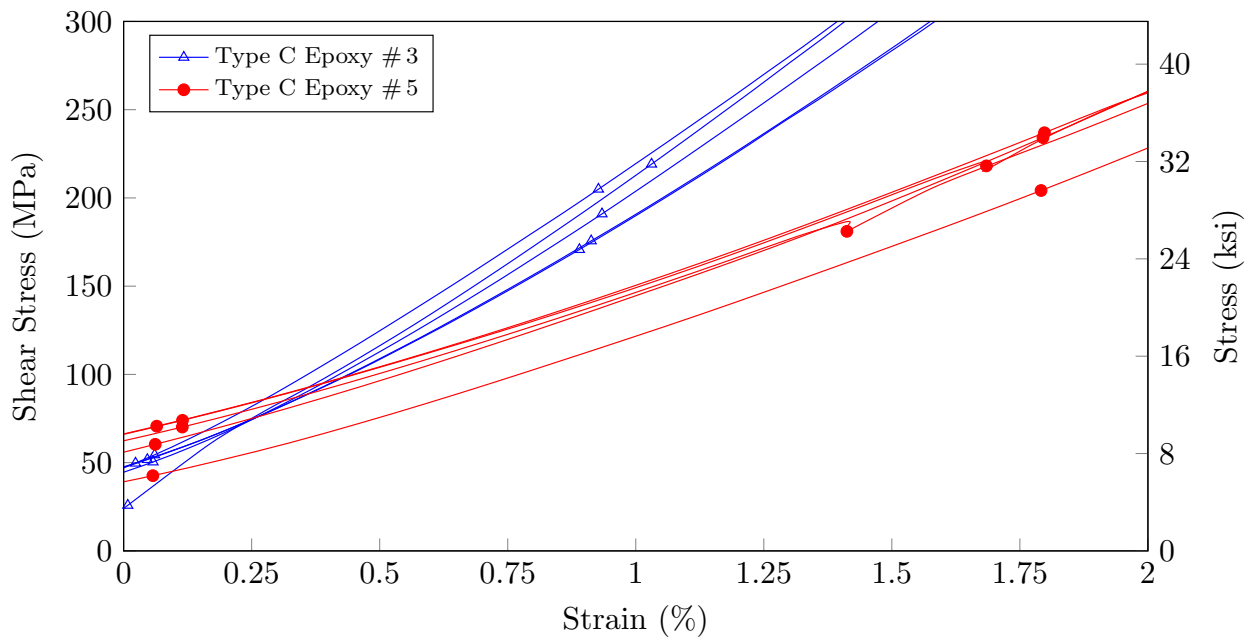


Figure 5.29: Tensile stress vs. strain behavior of rebar type C Lot 1 rebar size 3 and 5

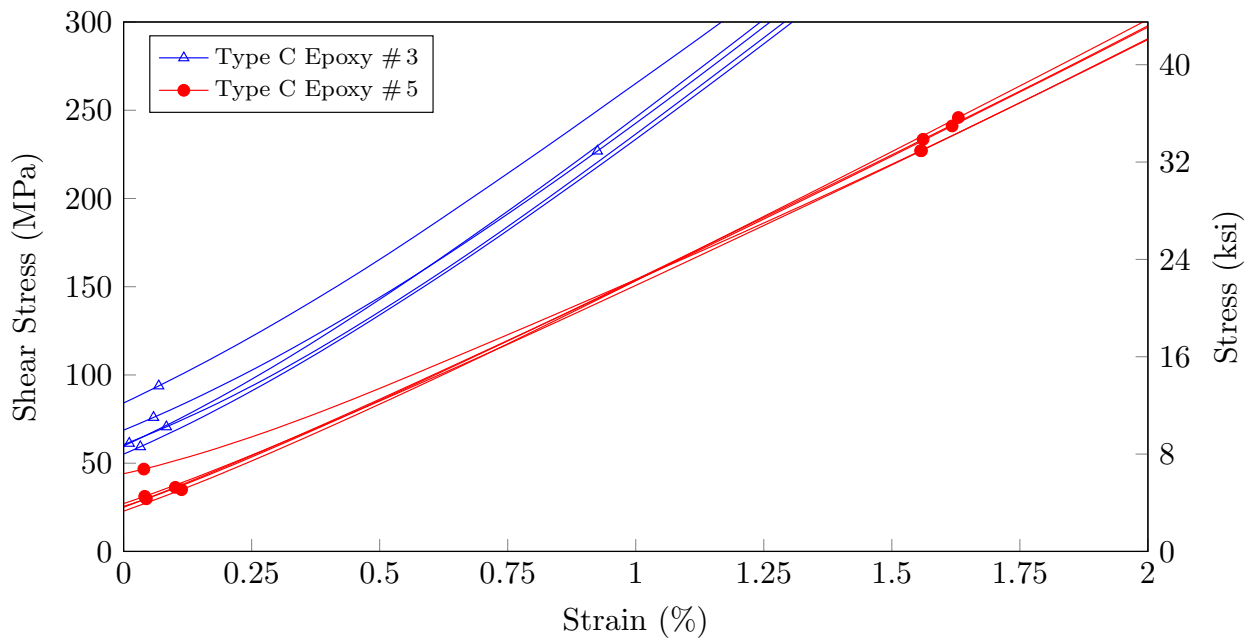


Figure 5.30: Tensile stress vs. strain behavior of rebar type C Lot 2 rebar size 3 and 5

5.12 Modes of Failure

According to ASTM D 7205, three different failure modes may occur during a tensile strength test. The first and expected one is the tensile rupture outside of the anchor pipes. Due to insufficient sample preparation or test procedure issues, two more failure modes may occur. The rebar could slip within the grouted anchor (rebar slippage) or the anchor could slip out of the fixture/grips (anchor slippage). Therefore, the last two described failure modes lead to unusable results when defining the material characteristics. However, for this research project, no specimen failed due to rebar or anchor slippage. Hence, tensile rupture of the BFRP rebar was the recorded failure mode for each bar that was tested.

Figure 5.31a and 5.32a show the failed specimens of type A rebars. It can be seen that all specimens, regardless of their diameter, displayed similar failure pattern. The fibers formed a brush type of failure and all specimens suffered fiber delamination throughout the entire free specimen length. Figure 5.31b and 5.32b present the post failure pattern of type B rebar specimens. It is shown that all the rebar sizes had an identical failure. The fibers were delaminated and a distinct brush-like failure was observed. Similarly, Figure 5.31c and 5.32c # 5 rebars exemplify the failure mode of type C rebars. All the specimens from two lots failed in a similar manner. After the peak load was reached, a bundle of outer fibers failed and brushed out over the entire free specimen length. After the first load drop, this behavior continued at each additional sudden load drop until delamination reached the center of the rebar, and the specimen eventually separated into two parts along the rebar axis.



(a) Type A



(b) Type B



(c) Type C

Figure 5.31: # 3 rebar final failure pattern after tensile test



(a) Type A



(b) Type B



(c) Type C

Figure 5.32: # 5 rebar final failure pattern after tensile test

5.13 Summary of Tensile Properties

The results of the statistical evaluation for the measured tensile properties of all products along with the elastic modulus property are listed in the following Table 5.4. A total of 40 specimen, 5 per rebar size and type, were tested and analyzed to determine the results shown in the table. For numerical comparison and concluding values, Table 5.4 lists the minimum tensile stress (\wedge), the maximum tensile stress (\wedge), the average tensile stress (μ), the standard deviation (σ), and the coefficient of variation (CV) for each individual test sample.

Table 5.4: Tensile strength test statistical values for each sample group (US Customary Units)

Sample group				Statistical values									
Manf. Type	Resin Type	Size #	Lot No.	Tensile Strength					Elastic Modulus				
				\wedge ksi	\vee ksi	μ ksi	σ ksi	CV %	\wedge ksi	\vee ksi	μ ksi	σ ksi	CV %
Rebar A	Epoxy	3	1	118.8	128.1	121.7	3.8	3.14	6742	7735	7238	3145	57.37
Rebar A	Epoxy	5	1	127.8	137.9	134.2	4.3	3.23	7639	7990	7753	147	1.90
Rebar B	Vinyl-ester	3	1	188.8	198.8	196.3	4.2	2.15	7542	7999	7808	179	2.29
Rebar B	Vinyl-ester	5	1	161.9	183.2	172.5	9.2	5.32	7810	8301	7946	201	2.53
Rebar C	Epoxy	3	1	178.2	189.3	183.9	4.8	2.61	5385	7659	7154	990	13.84
Rebar C	Epoxy	5	1	139.6	171.8	161.2	12.9	7.97	7346	7933	7640	3312	62.88
Rebar C	Epoxy	3	2	161.3	175.0	169.2	5.0	2.97	6531	7881	7200	516	7.16
Rebar C	Epoxy	5	2	143.9	153.4	147.7	4.0	2.73	7065	8138	7479	410	5.48

5.14 Bond-to-Concrete Strength

The bond stress τ_{max} (MPa or lbs./in.²) for a circular bar diameter d (mm or in.) is given by Equation 5.1, in which F represents the recorded pullout load (N or lbs.) and L is the accurately measured bond length (mm or in.).

$$\tau_{max} = \frac{F}{d\pi L} \quad [inMPa \text{ or } psi] \quad (5.1)$$

This formula was used to determine the bond behavior development and is the basis for the following graphs; Figures 5.39, 5.40, 5.33, 5.34, 5.36, and 5.37 depict the measured bond stresses along the rebar surfaces relative to the rebar slip at the free end. For clarity, the post failure measurements (at the onset of a 50% load drop) were removed from these graphs. All tested specimens failed at the rebar-concrete interface in bond slip, without splitting the concrete open or without tensile failure. The bond capacity and the failure behavior of the BFRP rebar-concrete interface were affected by the surface enhancement features.

5.15 Bond Stress vs. Slip at Free End

The graphs in this section compare the bond stress vs. slip at free end of rebar. Graphs in Figure 5.41, 5.35, and 5.38 portray bond stresses vs slip at free end of the rebars of both the sizes.

The x-axis of the graph signifies the measured bond stress, while the y-axis represents the slip of rebar at the free end.

Generally, from the graphs in Figures 5.33 to 5.41, it can be seen that each rebar type resulted in a consistent but distinct failure mode with ultimate stresses that were characteristic for each rebar type. All of the sand-coated rebars (Type-A and B) showed a soft failure while the rebars with a deformed surface (Type-C) failed suddenly with abrupt pullout.

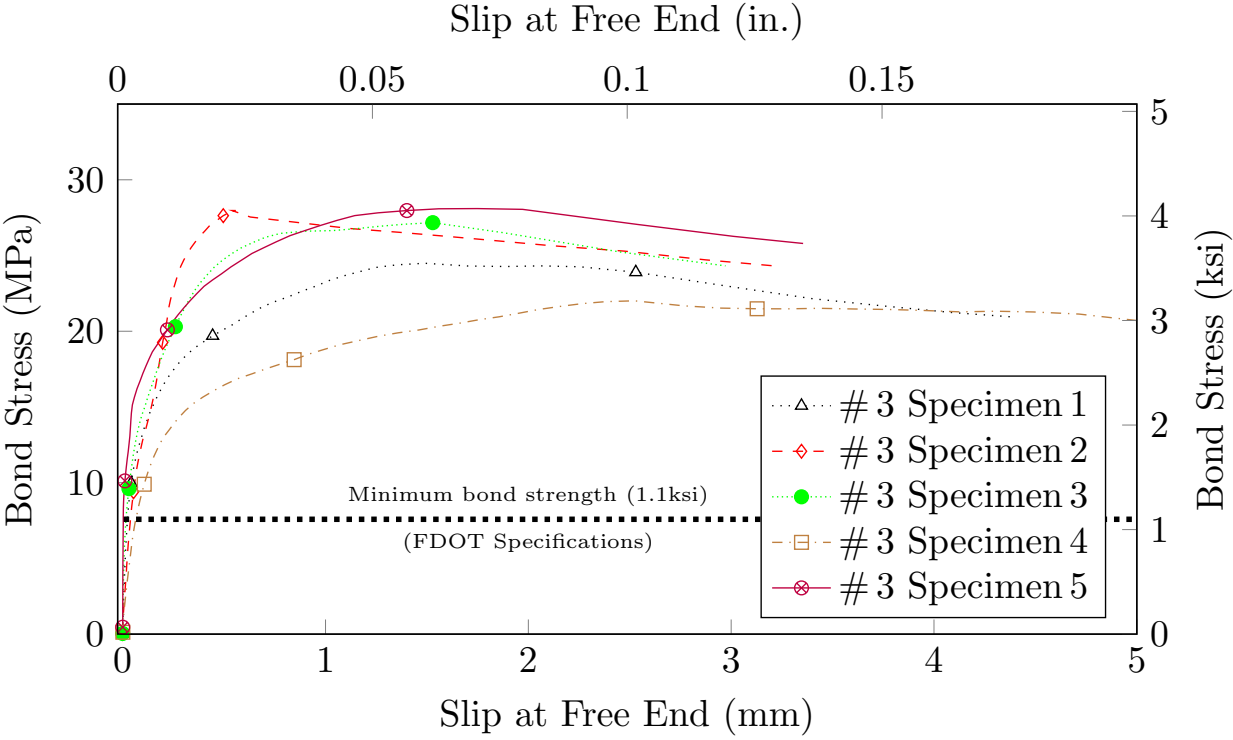


Figure 5.33: Free end slip behavior of the tested rebar type A Lot 1 #3

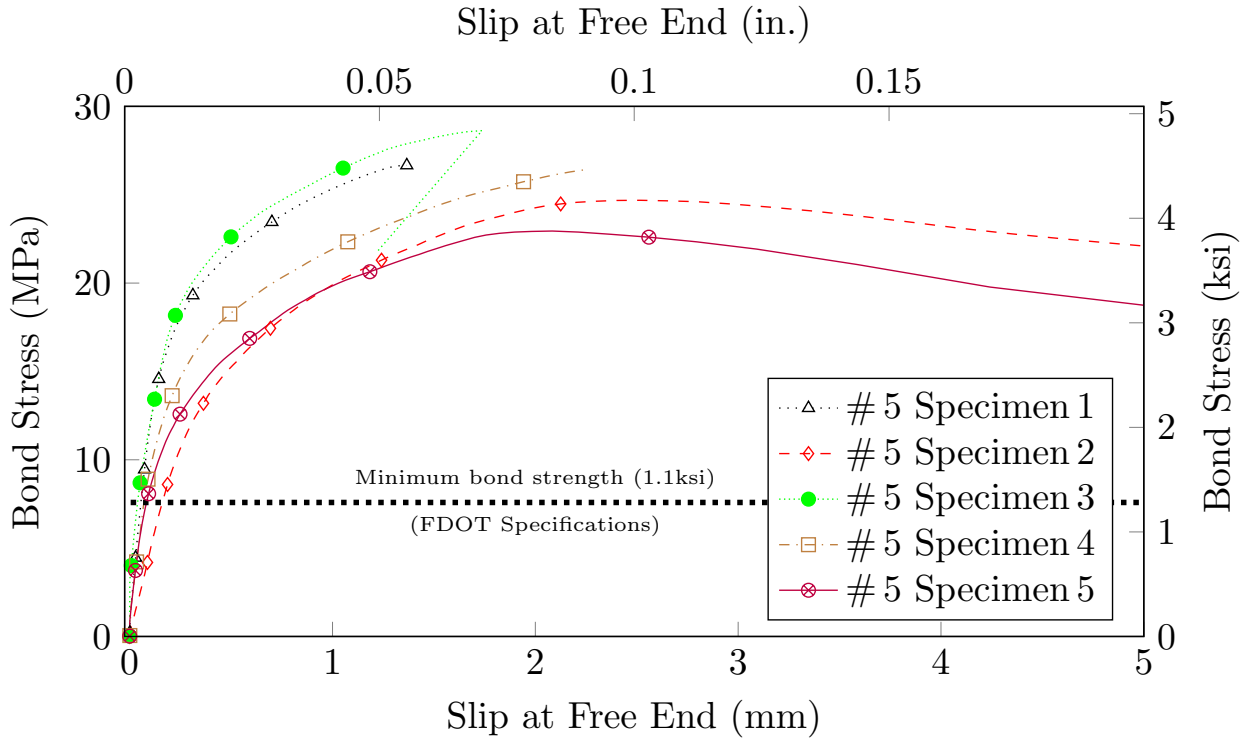


Figure 5.34: Free end slip behavior of the tested rebar type A Lot 1 #5

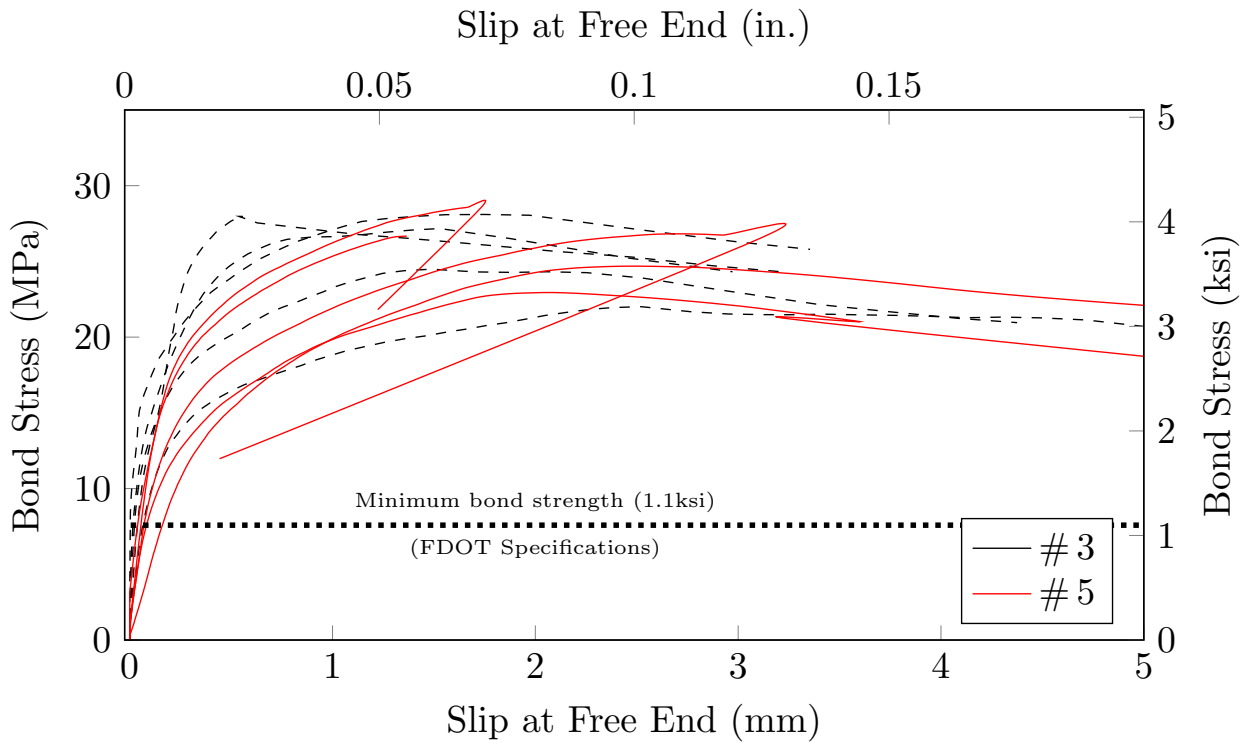


Figure 5.35: Free end slip behavior of the tested rebar type A Lot 1 #3 and #5

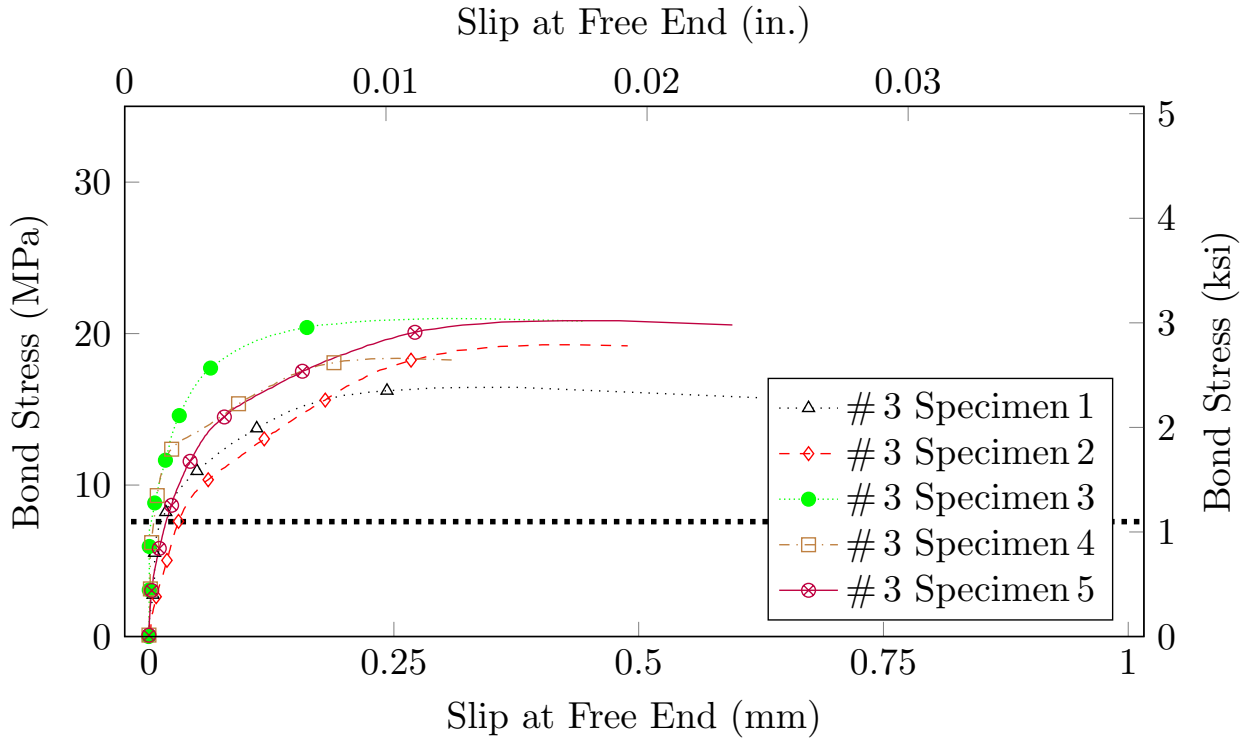


Figure 5.36: Free end slip behavior of the tested rebars type B Lot 1 # 3

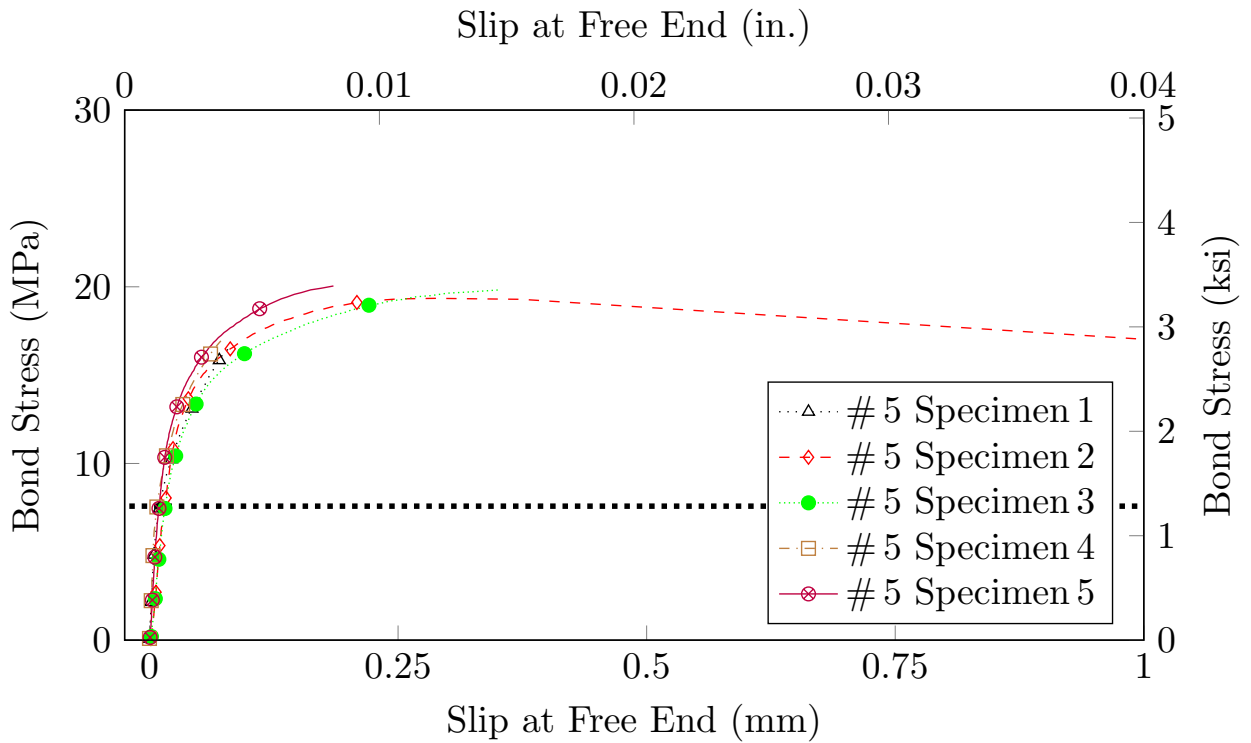


Figure 5.37: Free end slip behavior of the tested rebars type B Lot 1 # 5

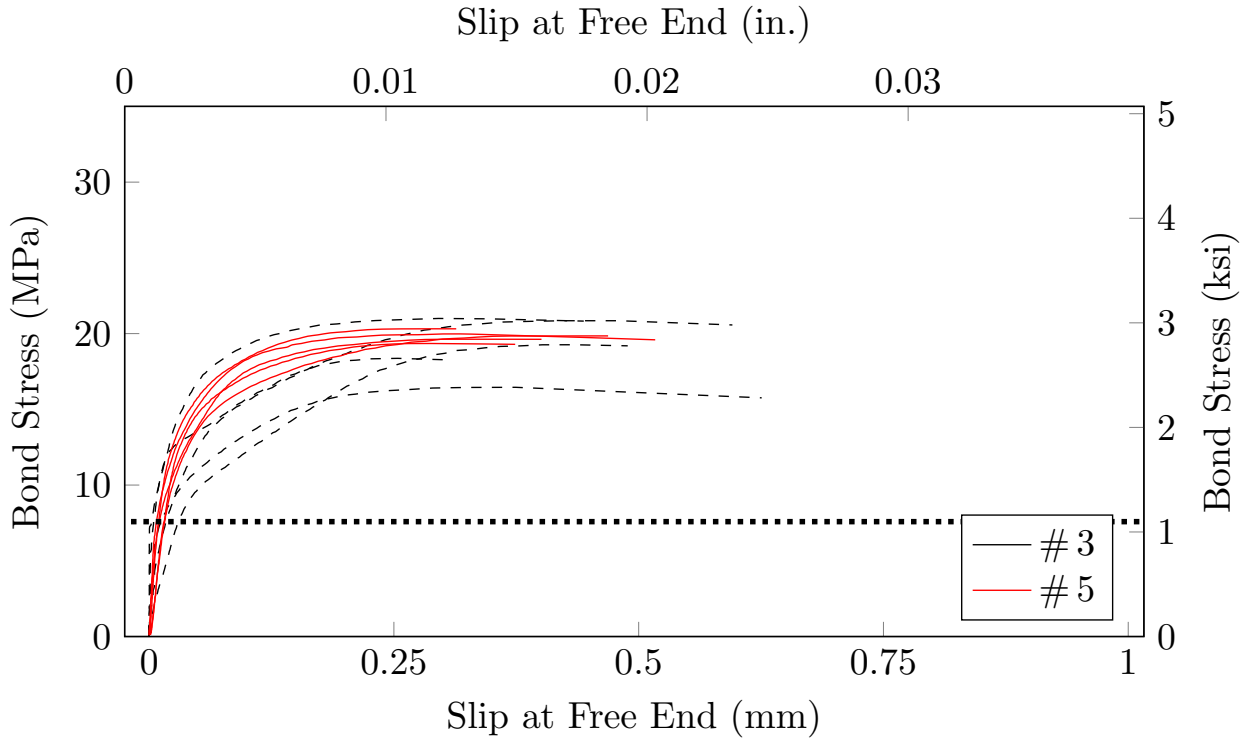


Figure 5.38: Free end slip behavior of the tested rebar type B Lot 1 #3 and #5

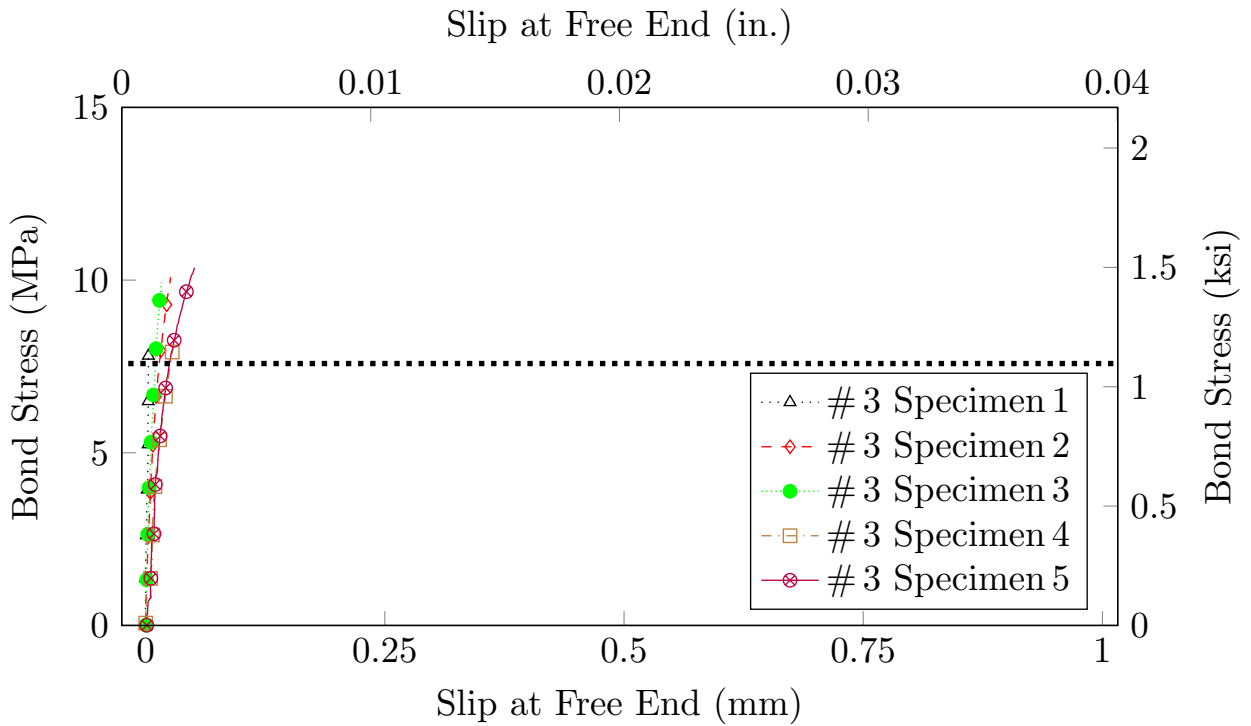


Figure 5.39: Free end slip behavior of the tested rebar type C Lot 1 #3

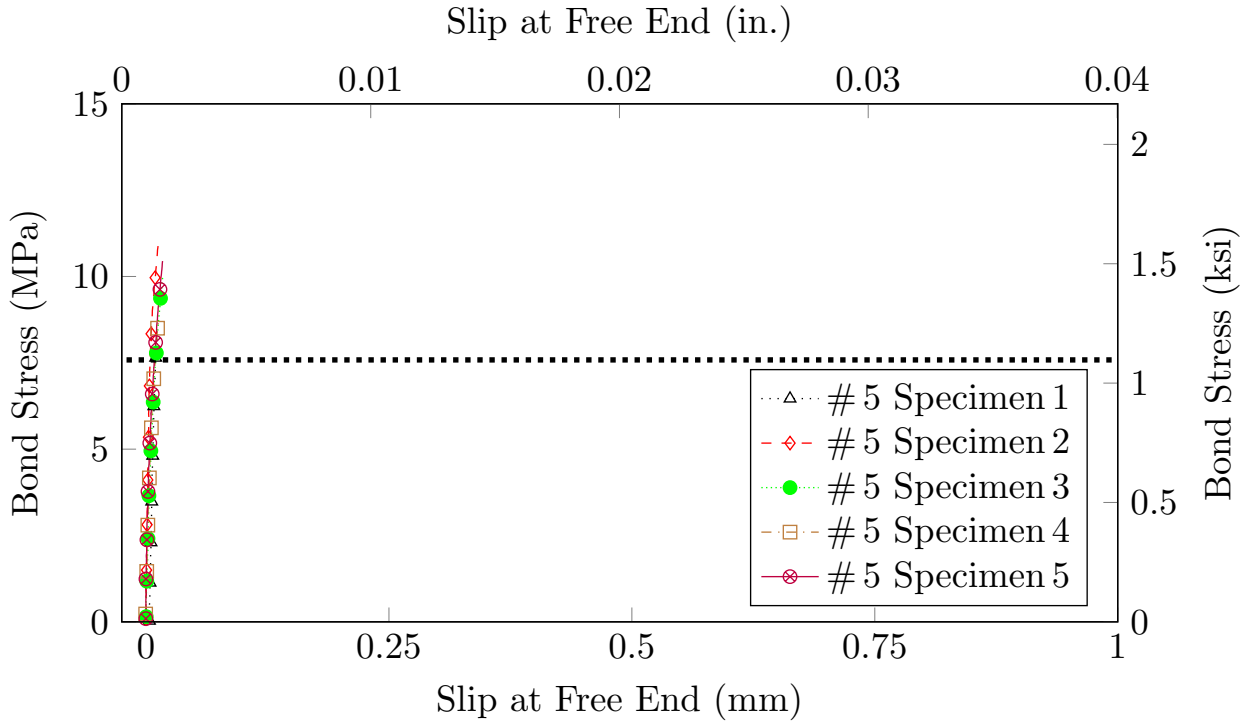


Figure 5.40: Free end slip behavior of the tested rebar type C Lot 1 #5

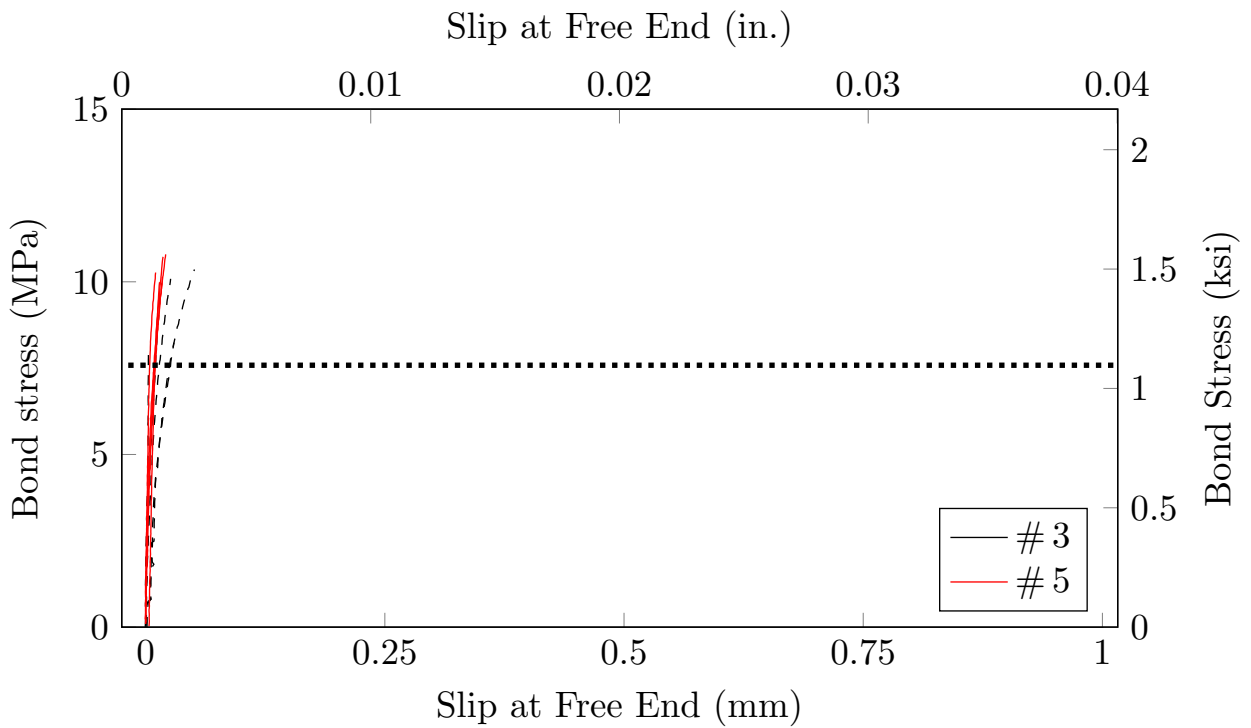


Figure 5.41: Free end slip behavior of the tested rebar type C Lot 1 #3 and #5

5.16 Modes of Failure

After the pullout tests were completed, the concrete blocks were split in half to further evaluate the failure mode by analyzing the surface of the rebar and the concrete. Figures 5.42, 5.43, 5.44, 5.45, 5.46, and 5.47 depict the different failure modes as they were observed after pullout testing. It

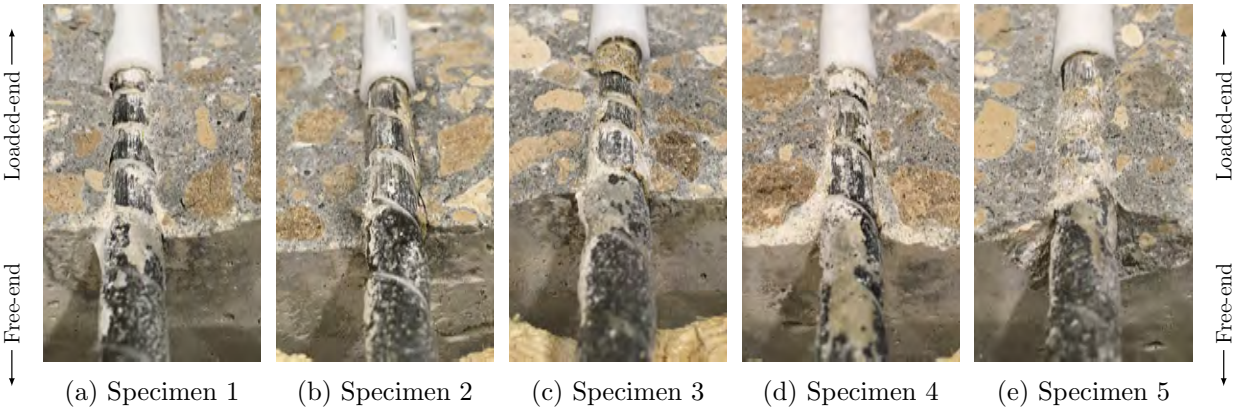


Figure 5.42: Overview rebar surface after bond strength test on type A Lot 1 rebar # 3

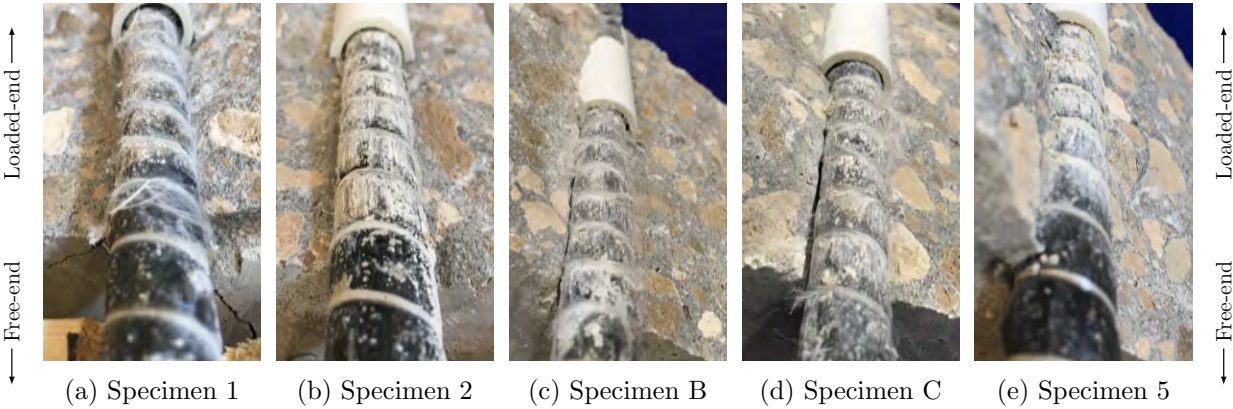


Figure 5.43: Overview rebar surface after bond strength test on type A Lot 1 rebar # 5

was noted that the rebar surface of all manufacturers was significantly damaged at the loaded end. For rebar type A only the sand layer was pulled off from the concrete and the surface deformed slightly, but the helical wraps remained in place. For rebar type B the layer between rebar and sand coat, which was made of fiber mesh, was entirely peeled off from the rest of the rebar. For rebar type C, de-bonding of the entire sand coat was observed (sand delamination). Close to the unloaded end, the surface layer of the rebar did not peel off, and most parts of the sand-coated layer remained well-adhered to the bar.

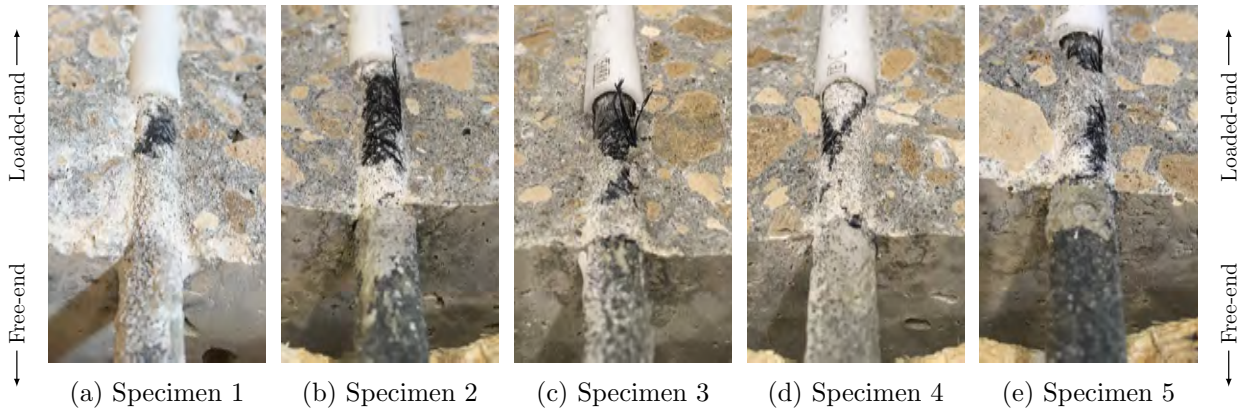


Figure 5.44: Overview rebar surface after bond strength test on type B Lot 1 rebar # 3

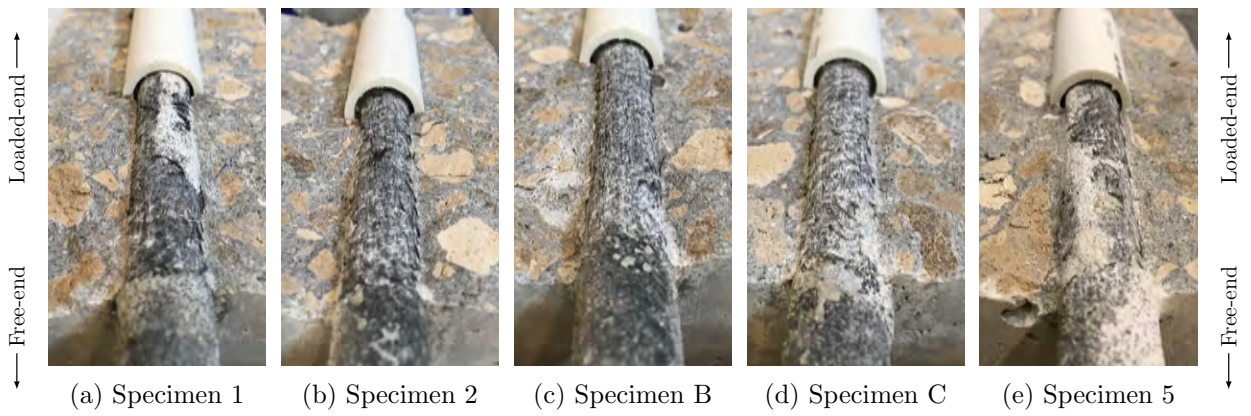


Figure 5.45: Overview rebar surface after bond strength test on type B Lot 1 rebar # 5

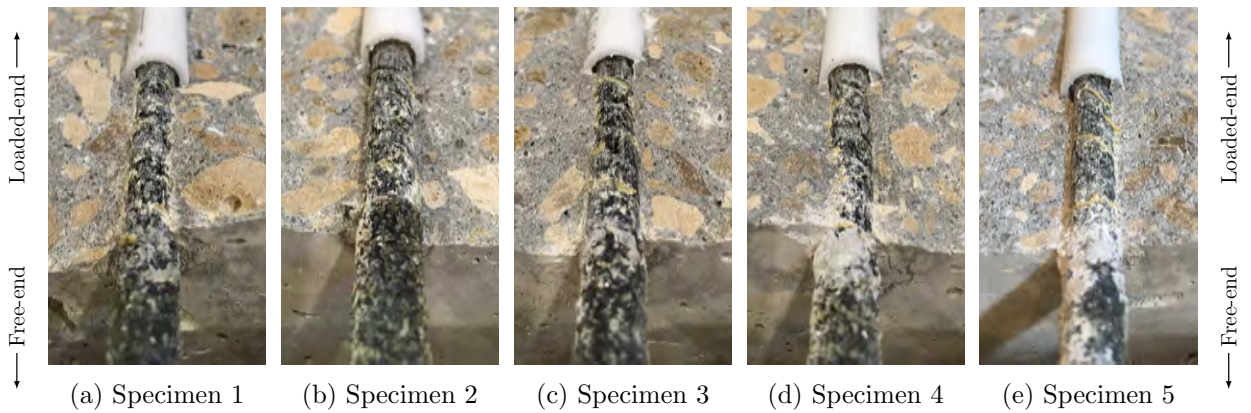


Figure 5.46: Overview rebar surface after bond strength test on type C Lot 1 rebar # 3

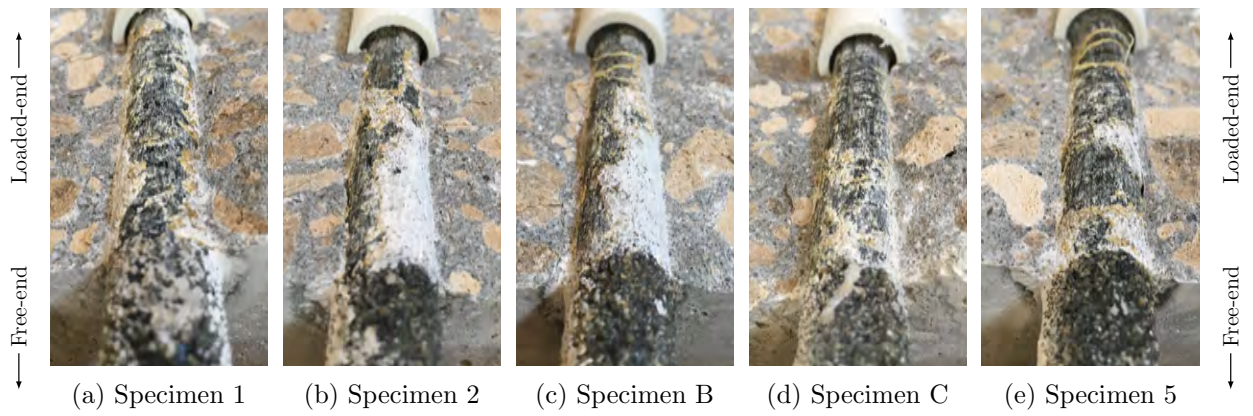


Figure 5.47: Overview rebar surface after bond strength test on type C Lot 1 rebar # 5

5.17 Summary of Bond-to-Concrete Strength

The statistical values for the bond strength properties of the tested products are listed in the following Table 5.5. A total of 30 specimens, five for each type and each size, were tested in total. The average of five specimens was assigned to each sample (specimen group) as shown in the table. All BFRP rebar samples satisfied the minimum acceptance criteria for the bond strength of glass FRP rebars according to FDOT Specifications 932, with the ultimate values shown in Tables 4.3, and 4.4. For numerical comparison and concluding values, Table 5.5 lists the minimum bond stress (\wedge), the maximum bond stress (\vee), the average bond stress (μ), the standard deviation (σ), and the coefficient of variation (CV) for each individual test sample.

Table 5.5: Bond-to-concrete strength test statistical values for each sample

Sample Group				Statistical Values				
Manuf. Type	Resin Type	Size #	Lot No.	\wedge ksi	\vee ksi	μ ksi	σ ksi	CV %
Type A	Epoxy	3	1	3.20	4.08	3.77	0.38	0.10
Type A	Epoxy	5	1	3.33	4.16	3.77	0.32	0.08
Type B	Vinyl-ester	3	1	2.39	3.05	2.79	0.27	0.10
Type B	Vinyl-ester	5	1	2.81	2.95	2.88	0.05	0.02
Type C	Epoxy	3	1	2.24	2.43	2.33	0.08	0.03
Type C	Epoxy	5	1	2.89	3.01	2.96	0.04	0.02

5.18 BFRP Rebar Performance

This section summarizes the material performance of the evaluated BFRP rebar samples based on the available acceptance criteria for glass FRP rebars, as shown in Tables 4.3, and 4.4, based on three different specifications. Tables 5.6 and 5.7 summarizes and compares the results for the type A rebar met or exceeded the acceptance criteria. The acceptance criteria for fiber content properties of #3 and #5 rebar samples of type B are shown in Table 5.8 and Table 5.9 respectively.

Table 5.10 details the obtained results and the acceptance criteria for #3 of type C rebar. It can be seen that the cross section properties and fiber content properties of the rebar fell within

Table 5.6: Acceptance criteria for rebar type A #3

Test Method	Test Description	Unit	Per diameter		FDOT 932-3/2017		AC454		ASTM D7957	
			Nom.	Exp.	Criteria	✓/✗	Criteria	✓/✗	Criteria	✓/✗
ASTM D 792	Measured Cross-Sectional Area	in. ²	0.11	0.15	0.104 – 0.161	✓	0.104 – 0.161	✓	0.104 – 0.161	✓
ASTM D 2584	Fiber Content	% wt.	75.17	75.17	≥ 70	✓	≥ 70	✓	≥ 70	✓
ASTM D 570	Moist. Absorption Short Term @50 °C	%	0.2	0.2	≤ 0.25	✓	≤ 0.25	✓	≤ 0.25	✓
ASTM D 570	Moist. Absorption Long Term @50 °C	%	0.55	0.55	≤ 1.0	✓	n/a	n/a	≤ 1.0	✓
ASTM D 7617	Min. Guaranteed Transverse Shear	ksi	29.1	n/a	≥ 22	✓	≥ 22	✓	≥ 19	✓
ASTM D 4475	Horizontal Shear Stress	ksi	5.75	n/a	n/a	n/a	≥ 5.5	✓	n/a	n/a
ASTM D 7205	Min. Guaranteed Tensile Load	kip	13.4	13.4	≥ 13.2	✓	≥ 13.2	✓	≥ 13.2	✓
ASTM D 7205	Min. Guaranteed Tensile Strength	ksi	121.7	105.2	n/a	n/a	n/a	n/a	n/a	n/a
ASTM D 7205	Tensile Modulus	ksi	7306	6313	≥ 6,500	✓	≥ 6,500	✓	≥ 6,500	✓
ASTM D 7205	Max. Strain	%	1.66	1.66	n/a	n/a	n/a	n/a	n/a	n/a
ACI440. 3R,B.3	Bond-to-Concrete Strength	ksi	3.20	2.64	≥ 1.1	✓	≥ 1.1	✓	≥ 1.1	✓

Table 5.7: Acceptance criteria for rebar type A #5

Test Method	Test Description	Unit	Per diameter		FDOT 932-3/2017		AC454		ASTM D7957	
			Nom.	Exp.	Criteria	✓/✗	Criteria	✓/✗	Criteria	✓/✗
ASTM D 792	Measured Cross-Sectional Area	in. ²	0.307	0.25	0.288 – 0.388	✓	0.288 – 0.388	✓	0.288 – 0.388	✓
ASTM D 2584	Fiber Content	% wt.	78.4	78.4	≥ 70	✓	≥ 70	✓	≥ 70	✓
ASTM D 570	Moist. Absorption Short Term @50 °C	%	0.18	0.18	≤ 0.25	✓	≤ 0.25	✓	≤ 0.25	✓
ASTM D 570	Moist. Absorption Long Term @50 °C	%	0.77	0.77	≤ 1.0	✓	n/a	n/a	≤ 1.0	✓
ASTM D 7617	Min. Guaranteed Transverse Shear	ksi	25.7	n/a	≥ 22	✓	≥ 22	✓	≥ 19	✓
ASTM D 4475	Horizontal Shear Stress	ksi	6.22	n/a	n/a	n/a	≥ 5.5	✓	n/a	n/a
ASTM D 7205	Min. Guaranteed Tensile Load	kip	41.2	41.2	≥ 29.1	✓	≥ 32.2	✓	≥ 29.1	✓
ASTM D 7205	Min. Guaranteed Tensile Strength	ksi	137.9	121.0	n/a	n/a	n/a	n/a	n/a	n/a
ASTM D 7205	Tensile Modulus	ksi	7749	6989	≥ 6,500	✓	≥ 6,500	✓	≥ 6,500	✓
ASTM D 7205	Max. Strain	%	1.78	1.78	n/a	n/a	n/a	n/a	n/a	n/a
ACI440. 3R,B.3	Bond-to-Concrete Strength	ksi	3.33	2.89	≥ 1.1	✓	≥ 1.1	✓	≥ 1.1	✓

the acceptance ranges, whereas the moisture absorption of the rebar exceeded specifications. The rebar met and exceeded all acceptance ranges for all evaluated strength parameters. The following Table 5.11 shows that #5 rebar of type C were within the acceptance range for cross section, fiber content, and shear properties, whereas the modulus of elasticity was lower than the required minimum.

Table 5.8: Acceptance criteria for rebar type B # 3

Test Method	Test Description	Unit	Per diameter		FDOT 932-3/2017		AC454		ASTM D 7957	
			Nom.	Exp.	Criteria	✓/✗	Criteria	✓/✗	Criteria	✓/✗
ASTM D 792	Measured Cross-Sectional Area	in. ²	0.110	0.14	0.104 – 0.161	✓	0.104 – 0.161	✓	0.104 – 0.161	✓
ASTM D 2584	Fiber Content	% wt.	83.3	83.3	≥ 70	✓	≥ 70	✓	≥ 70	✓
ASTM D 570	Moist. Absorption Short Term @50 °C	%	0.2	0.2	≤ 0.25	✓	≤ 0.25	✓	≤ 0.25	✓
ASTM D 570	Moist. Absorption Long Term @50 °C	%	0.644	0.644	≤ 1.0	✓	n/a	n/a	≤ 1.0	✓
ASTM D 7617	Min. Guaranteed Transverse Shear	ksi	33.3	26.0	≥ 22	✓	≥ 22	✓	≥ 19	✓
ASTM D 4475	Horizontal Shear Stress	ksi	5.1	3.98	n/a	n/a	≥ 5.5	n/a	n/a	n/a
ASTM D 7205	Min. Guaranteed Tensile Load	kip	20.9	20.9	≥ 13.2	✓	≥ 13.2	✓	≥ 13.2	✓
ASTM D 7205	Min. Guaranteed Tensile Strength	ksi	183.6	148.9	n/a	n/a	n/a	n/a	n/a	n/a
ASTM D 7205	Tensile Modulus	ksi	7542	5957	≥ 6,500	✓	≥ 6,500	✓	≥ 6,500	✓
ASTM D 7205	Max. Strain	%	2.5	2.5	n/a	n/a	n/a	n/a	n/a	n/a
ACI440. 3R,B.3	Bond-to-Concrete Strength	ksi	2.39	2.02	≥ 1.1	✓	≥ 1.1	✓	≥ 1.1	✓

Table 5.9: Acceptance criteria for rebar type B # 5

Test Method	Test Description	Unit	Per diameter		FDOT 932-3/2017		AC454		ASTM D 7957	
			Nom.	Exp.	Criteria	✓/✗	Criteria	✓/✗	Criteria	✓/✗
ASTM D 792	Measured Cross-Sectional Area	in. ²	0.307	0.372	0.288 – 0.388	✓	0.288 – 0.388	✓	0.288 – 0.388	✓
ASTM D 2584	Fiber Content	% wt.	82.28	82.28	≥ 70	✓	≥ 70	✓	≥ 70	✓
ASTM D 570	Moist. Absorption Short Term @50 °C	%	0.18	0.18	≤ 0.25	✓	≤ 0.25	✓	≤ 0.25	✓
ASTM D 570	Moist. Absorption Long Term @50 °C	%	0.501	0.501	≤ 1.0	✓	n/a	n/a	≤ 1.0	✓
ASTM D 7617	Min. Guaranteed Transverse Shear	ksi	30.8	25.3	≥ 22	✓	≥ 22	✓	≥ 19	✓
ASTM D 4475	Horizontal Shear Stress	ksi	5.0	4.09	n/a	n/a	≥ 5.5	n/a	n/a	n/a
ASTM D 7205	Min. Guaranteed Tensile Load	kip	49.7	49.7	≥ 29.1	✓	≥ 32.2	✓	≥ 29.1	✓
ASTM D 7205	Min. Guaranteed Tensile Strength	ksi	144.9	133.6	n/a	n/a	n/a	n/a	n/a	n/a
ASTM D 7205	Tensile Modulus	ksi	7819	6448	≥ 6,500	✓	≥ 6,500	✓	≥ 6,500	✓
ASTM D 7205	Max. Strain	%	2.07	2.07	n/a	n/a	n/a	n/a	n/a	n/a
ACI440. 3R,B.3	Bond-to-Concrete Strength	ksi	2.81	2.34	≥ 1.1	✓	≥ 1.1	✓	≥ 1.1	✓

Table 5.10: Acceptance criteria for rebar type C # 3

Test Method	Test Description	Unit	Per diameter		FDOT 932-3/2017		AC454		ASTM D 7957	
			Nom.	Exp.	Criteria	✓/✗	Criteria	✓/✗	Criteria	✓/✗
ASTM D 792	Measured Cross-Sectional Area	in. ²	0.110	0.109	0.104 – 0.161	✓	0.104 – 0.161	✓	0.104 – 0.161	✓
ASTM D 2584	Fiber Content	% wt.	82.035	82.035	≥ 70	✓	≥ 70	✓	≥ 70	✓
ASTM D 570	Moist. Absorption Short Term @50 °C	%	0.20	0.20	≤ 0.25	✓	≤ 0.25	✓	≤ 0.25	✓
ASTM D 570	Moist. Absorption Long Term @50 °C	%	0.75	0.75	≤ 1.0	✓	n/a	n/a	≤ 1.0	✓
ASTM D 7617	Min. Guaranteed Transverse Shear	ksi	33.59	33.59	≥ 22	✓	≥ 22	✓	≥ 19	✓
ASTM D 4475	Horizontal Shear Stress	ksi	6.38	6.38	n/a	n/a	≥ 5.5	✓	n/a	n/a
ASTM D 7205	Min. Guaranteed Tensile Load	kip	19.68	19.68	≥ 13.2	✓	≥ 13.2	✓	≥ 13.2	✓
ASTM D 7205	Min. Guaranteed Tensile Strength	ksi	163.38	163.38	n/a	n/a	n/a	n/a	n/a	n/a
ASTM D 7205	Tensile Modulus	ksi	6.933	6.933	≥ 6,500	✓	≥ 6,500	✓	≥ 6,500	✓
ASTM D 7205	Max. Strain	%	2.34	2.34	n/a	n/a	n/a	n/a	n/a	n/a
ACI440. 3 R,B.3	Bond-to-Concrete Strength	ksi	2.24	1.98	≥ 1.1	✓	≥ 1.1	✓	≥ 1.1	✓

Table 5.11: Acceptance criteria for rebar type C # 5

Test Method	Test Description	Unit	Per diameter		FDOT 932-7/2017		AC454		ASTM D 7957	
			Nom.	Exp.	Criteria	✓/✗	Criteria	✓/✗	Criteria	✓/✗
ASTM D 792	Measured Cross-Sectional Area	in. ²	0.307	0.353	0.288 – 0.388	✓	0.288 – 0.388	✓	0.288 – 0.388	✓
ASTM D 2584	Fiber Content	% wt.	81.8	81.8	≥ 70	✓	≥ 70	✓	≥ 70	✓
ASTM D 570	Moist. Absorption Short Term @50 °C	%	0.25	0.25	≤ 0.25	✓	≤ 0.25	✓	≤ 0.25	✓
ASTM D 570	Moist. Absorption Long Term @50 °C	%	1.17	1.17	≤ 1.0	✗	n/a	n/a	≤ 1.0	✗
ASTM D 7617	Min. Guaranteed Transverse Shear	ksi	32.38	28.115	≥ 22	✓	≥ 22	✓	≥ 19	✓
ASTM D 4475	Horizontal Shear Stress	ksi	5.56	4.826	n/a	n/a	≥ 5.5	✗	n/a	n/a
ASTM D 7205	Min. Guaranteed Tensile Load	kip	42.82	42.82	≥ 29.1	✓	≥ 32.2	✓	≥ 29.1	✓
ASTM D 7205	Min. Guaranteed Tensile Strength	ksi	119.6	121.16	n/a	n/a	n/a	n/a	n/a	n/a
ASTM D 7205	Modulus	ksi	5710	5836	≥ 6,500	✗	≥ 6,500	✗	≥ 6,500	✗
ASTM D 7205	Max. Strain	%	2.12	2.07	n/a	n/a	n/a	n/a	n/a	n/a
ACI440. 3 R,B.3	Bond-to-Concrete Strength	ksi	2.89	2.37	≥ 1.1	✓	≥ 1.1	✓	≥ 1.1	✓

Chapter 6

Discussion

To support the development of basalt-specific acceptance criteria for FDOT Specifications Section 932, this research was conducted with a focus on the biomechanical properties of readily available BFRP rebars. A test matrix — to address the cross-sectional properties, fiber content, moisture absorption, transverse shear strength, horizontal shear strength, tensile properties, and bond-to-concrete characteristics for three dissimilar rebars including two sizes (# 3 and # 5) — was developed to evaluate the essential material properties for BFRP rebar characterization. Based on established test standards and acceptance criteria for glass FRP (GFRP) rebars, BFRP rebars were classified for performance, and it was found that all test samples (specimen groups) from rebar types A, B, and # 3 rebar samples from type C satisfied the minimum requirements for GFRP rebars. Rebar # 5 of type C satisfied all criteria except the maximum moisture absorption and minimum elastic modulus criteria. In the following, these findings are discussed in further detail and studied in context of the available and relevant literature to provide BFRP rebar implementation recommendations and suggestions for future design specifications.

6.1 Research Significance

BFRP rebars are still considered new in civil engineering construction in the United States, but it has been successfully used around the world in demonstration and low-risk projects (Singha, 2012; Patnaik, 2009; Elgabbas et al., 2016). Before using new or emerging materials for infrastructure projects, the physical and mechanical properties must be evaluated and compared to acceptance criteria. In the case of emerging materials, acceptance criteria might not have been fully established

yet and research is needed to characterize a variety of products to determine general market quality and to define adequate limiting values. In this report, recommendations for physical properties such as cross-sectional dimensions, fiber content, and moisture absorption properties for BFRP rebars are proposed. In addition, recommendations for minimum mechanical properties, including the apparent horizontal shear strength, the transverse shear strength, the tensile properties, and the bond-to-concrete characteristics are suggested. These suggestions are based on experimental material evaluations, the above presented analyses, and the accompanying literature. These efforts were necessary because acceptance criteria for the specific use of BFRP rebars in the U.S. are still missing. More specifically, FDOT Specifications Section 932 provides defined minimum criteria for glass and carbon based FRP rebars, but values for BFRP rebars have not been implemented yet. Likewise, while some design codes like international building code AC454 (International Code Council, 2017) generally allow the use of BFRP rebars for engineering structures, some design guidelines in the USA, such as AASHTO LRFD guidelines (AASHTO, 2012, 2018), already provide specific procedures for the structural design with glass and carbon FRP rebars — using defined adjustment factors — explicit values for basalt have not been proposed yet. Accordingly, this research project was needed to initiate the development of BFRP rebar specific acceptance criteria and to open the discussion about adjustment factors for another rebar alternative.

6.2 Critical Analysis of Major Findings

Because various material properties were experimentally evaluated throughout this research project and each property has its one specific relevance, these properties are individually discussed in the following subsections.

6.2.1 Cross-Sectional property

The cross-sectional properties were measured according to ASTM D 792 (ASTM-International, 2015b), and it is an important characteristic because rebars are classified based on that diametric size and the strength requirements are dependent on the actual rebar size (in form of the nominal diameter). For traditional steel rebars, the tensile strength of rebar is directly related to effective area. While this is not ultimately true for FRP rebars — as only the fibers carry the tensile loads — it is a measurement that is needed due to design and detailing needs of reinforcement in con-

crete elements to this end, and in order to implement the use of FRP rebars, the same nominal geometry used in steel rebar is specified for FRP rebars with the exception of a range to account for different surface treatments, which for # 3 GFRP rebar is 0.11 in.², with a minimum measured area of 0.104 in.² and a maximum measured area of 0.161 in.² For # 5 rebars, the nominal cross-sectional area is given as 0.31 in.², with a minimum measured cross-sectional area of 0.228 in.² and a maximum of 0.338 in.². All rebars shall be within that range to avoid errors in assumed centroid position for structural resistance calculations, any fit up errors in detailing such as spacing, cover or clearance, and consistency in product approval (Hurtado, 2018; AASHTO, 2018). Likewise, the production sequence for BFRP rebars and the load transfer is similar to glass fiber based rebars, which allows similar definitions for both rebar types (Kampmann et al., 2018).

6.2.2 Fiber Content

The experiments and the accompanying mathematical procedures to determine the fiber content percentage for FRP rebars are specified in material standard ASTM D 2584 -11 (ASTM-International, 2011). Fiber content (given in percent) plays a key role in the tensile behavior and load capacity of FRP rebars because induced stresses are mostly carried by the fibers, while the resin matrix must be stiff and elastic enough to transfer the loads between the individual fibers. The minimum fiber content percentage required for GFRP rebars according to FDOT Specifications Section 932, AC454 (International Code Council, 2017), and ASTM D7957 (ASTM-International, 2017) which follows ASTM D 2584 -11 (ASTM-International, 2011), is 70%. After careful evaluation on the tested samples, it was seen that two of the three BFRP rebar products exceeded the required minimum criteria by at least 10%. The third manufactured product exceeded the criteria by 5% on average. Further decrease in the fiber content percentage may affect the stress transfer capacity of the rebar. However, it appears reasonable to suggest a minimum fiber content percentage for BFRP rebars that is similar to that for GFRP products because the observed load carrying and stiffness behaviors were acceptable in the context of the measured fiber contents. As mentioned by You et al. (2015); ACI Committee 440 (2015), fiber contents less than 70% are not acceptable because the fiber-volume fraction significantly affects the tensile strength and quality of FRP rebars. Additional research and analyses are required to establish a precise correlation between fiber content percentage and its effects on the rebar strength to support any modifications of the GFRP specifications

for a BFRP specific minimum. For now, the 70 % minimum criteria seems to be appropriate for BFRP rebars as well and should be adopted in FDOT Specifications Section 932.

6.2.3 Moisture Absorption of BFRP rebar

ASTM D 5229 (ASTM, 2014) details seven different test procedures (A through E, Y, and Z) for estimating moisture absorption properties for FRPs in different environments. Procedure A is most commonly used, and therefore, was followed for this research project. It is considered that the moisture absorption correlates to durability and the corresponding strength retention, where high moisture absorption values are indicative of a porous rebar that is more prone to degradation. According to FDOT Specifications Section 932, which follows ASTM D 5229 (ASTM, 2014) section 7.1, AC454 (International Code Council, 2017), and ASTM D 7957 (ASTM-International, 2017), the maximum short-term moisture absorption limit for GFRP rebars is 0.25 % by weight. In addition, the long-term moisture absorption specified by FDOT Specifications Section 932 and ASTM D 7957 (ASTM-International, 2017) is less than 1 %. After proper evaluation of the tested specimens, it was found that the long-term moisture absorption of BFRP rebars was less than 1 %. Kampmann et al. (2019) discussed the long term behavior of GFRP rebars, and it was found that the rebar strength and the micro structure durability is severely affected by an increased moisture absorption property. As increased moisture absorption affects the strength and strength retention of FRP rebars, it is reasonable to suggest that the BFRP rebar should follow the criteria established for GFRP moisture absorption properties (Kampmann et al., 2018). Nevertheless, it must be emphasized that basalt fibers contain approximately 7 % iron oxide, which makes them potentially more vulnerable in alkaline-chloride (concrete-saltwater) environments (Stekloplastics, 2014; Toni Schneider, 2015; Kochergin et al., 2013). Accordingly, a more critical moisture absorption value may eventually be necessary for BFRP rebars, but more research will be needed to support this claim. Until then, it is not advisable to use BFRP rebars in salty or submerged environments.

6.2.4 Transverse Shear Strength

ASTM D 7617 (ASTM-International, 2012b) was followed to test and analyze the transverse shear data obtained from BFRP rebar testing. FRP rebars are weak in the transverse direction or perpendicular to the rebar longitudinal axis due to the unidirectionality of the fibers and the corresponding

low shear strength of the fibers. According to FDOT Specification Section 932, which is in agreement with AC454 (International Code Council, 2017), GFRP rebars are required to reach a minimum shear strength of 22 ksi before rupture. These values are more critical than the 19 ksi minimum transverse shear strength required by ASTM D 7957 (ASTM-International, 2017). After careful testing and analyses, the evaluated #3 BFRP rebars sustained shear stresses before ultimate failure ranging from 30 ksi to 36 ksi and #5 rebars sustained stresses between 26 ksi and 33 ksi. Based on the results obtained in this study, in comparison to other studies (Kampmann et al., 2018; Chen et al., 2007; ElSafty et al., 2014), BFRP rebars have a higher strength compared to GFRP rebars. This research suggests that the minimum transverse shear strength criteria for BFRP rebars can be equal to the specification for GFRP rebars, given that other rebar sizes have not been evaluated and the specification should remain equal regardless of the rebar size. The Authors suggest that with additional test data the specification for transverse shear strength may be increased up to 20%. This specification needs to be validated both for the average value as well as the guaranteed value, if BFRP products are considered for dowel applications as well, the higher shear strength of BFRP in comparison to GFRP can be beneficial (Brown and Bartholomew, 1993; Eddie, 1999).

6.2.5 Apparent Horizontal Shear Strength

The horizontal shear test was conducted according to ASTM D 4475 (ASTM-International, 2012a) standards. AC454 (International Code Council, 2017) specifies a minimum of 5.5 ksi horizontal shear strength for GFRP bars. It has been noted that the FDOT Specifications and ASTM D 7957 (ASTM-International, 2017) currently does not include minimum horizontal shear strength requirements for rebars made from any fiber material. The horizontal shear failure, however, is an indicator of the resin strength and the resin-to-sizing-to-fiber interface and as such important for the load transfer mechanism. Ultimately, this mechanical property is a suitable quality control measure. After a manufacturer survey was conducted — as part of the literature review process, c.f. Section 3.3 — to identify common practices in the FRP rebar industry, it was noted that horizontal shear tests are one of the most common quality control methods that manufacturers use to ensure production consistency (because it is a mechanical test that can be conducted quickly). Accordingly, FDOT Specifications Section 932 would benefit from limiting minimum values for the acceptance of FRP rebars because it would provide a direct benefit to the manufacturing community and the inter-

section between FDOT and technology implementation; this quality control parameter could be directly targeted during production — and quickly evaluated. The horizontal shear strength of # 3, and # 5 GFRP rebars appears to range around 6 ksi (c.f. Kampmann et al. (2018)) with a minimum average of 5.2 ksi. Based on the experimental results obtained for this study, basalt FRP rebars with a size of # 3 and # 5 measure a minimum average apparent horizontal shear strength of 5.6 ksi and an absolute minimum value of 5.0 ksi. According to AC454 (International Code Council, 2017) and Canadian Standard Association (2018), the minimum horizontal shear strength of BFRP rebars should be 5.5 ksi. Hence, for now, a minimum requirement of 5.5 ksi for the apparent horizontal shear strength, tested on at least five specimens, appears to be an adequate addition to FDOT Specifications Section 932.

6.2.6 Tensile Properties

The tensile strength and elastic modulus of BFRP rebars were evaluated based on procedures and methods detailed in ASTM D 7205 (ASTM-International, 2015a). Minimum guaranteed tensile load requirements for # 3 and # 5 GFRP rebars according to FDOT Specifications Section 932, AC454 (International Code Council, 2017), and ASTM D 7957 (ASTM-International, 2017) are 13.2 kip and 29.1 kip, respectively. Based on the findings from this research project and projects targeting glass fiber based rebars (Kampmann et al., 2018), on average BFRP rebars provide a relatively higher ultimate tensile load capacity and modulus — as compared to GFRP rebars (Benmokrane et al., 2015). It was noted that the minimum tensile load sustained by # 3 BFRP rebars is 19.7 kip and that of # 5 rebars was 42.8 kip . In addition, the elastic moduli of BFRP rebars were measured with a minimum of 8000 ksi (c.f. Table 5.4). The elastic moduli of GFRP rebar according to Kampmann et al. (2018) reached average values of approximately 7 ksi. All tested BFRP rebar types superseded the minimum strength criteria for GFRP rebars. According to research done by Patnaik (2009), BFRP rebars are stronger in tension and Wang et al. (2017) proved that long-term durability of BFRP rebars in harsh environments is higher in comparison to GFRP rebars. Wei et al. (2010) tested chemical durability of GFRP and BFRP rebars and found that BFRP rebars are durable and stronger in tension. Further detailed testing of a wide range of rebars from several manufacturers is required to fully study the strength properties of rebar and to properly define a minimum required criteria that is more critical than the one given for glass based FRP

rebars. However, if basalt fiber specific criteria are desirable for the tensile properties, the data in this research suggests that the minimum strength and elastic modulus should be similar for GFRP rebars.

6.2.7 Bond-to-Concrete Strength

The bond-to-concrete strength of the rebar specimen was tested according to procedure described in ASTM D 7913 (ASTM International, 2014). The minimum guaranteed bond strength required for GFRP rebars according to FDOT Specifications Section 932, AC454 (International Code Council, 2017) and ASTM D 7957 (ASTM-International, 2017) is 1.1 ksi. Based on the measurements obtained in this research and a careful analyses of the results, the bond-to-concrete strength of # 3 rebars ranged from 2.2 ksi to 3.2 ksi and it varied between 2.8 ksi and 3.3 ksi for # 5 BFRP rebars. These results, in comparison to other studies (Kampmann et al., 2018; Chen et al., 2007; Brik, 2003; Li et al., 2017; Hassan et al., 2016), show that the bond-to-concrete strength of basalt FRP rebars is similar to the recorded bond strength of GFRP rebars. The bond strength of FRP rebars is a function of the geometric and surface enhancement features. As the surface for FRP rebars is either deformed or sand coated (or possibly both), it is reasonable to assume that the bond behavior of basalt FRP rebars is similar to the bond behavior of glass or other FRP rebars since equivalent friction is generated, irrespective of the fiber type. To this end, this research suggests that the minimum bond-to-concrete strength criteria for BFRP rebars should remain consistent with GFRP available specifications at a minimum guaranteed bond strength of 1.1 ksi.

6.3 Supplementary Findings

Two of the three tested rebar types for this research included rebars made with epoxy resins. The mechanical performance of the rebars made from epoxy resin was higher than the rebars made from other resin. Through the state-of-the-production-practice review, it was noted that many/most basalt rebar producers across the globe uses epoxy resin in the manufacturing processes. It appears that epoxy resins are suitable for the production of basalt FRP rebars and that such constituent materials should be considered in future updates of FDOT Specifications Section 932. However, additional research with a focus on physical and mechanical properties in response to chemical durability for rebars made with different resins should be considered.

Comparing the findings from this research to the findings made in a previous study with a focus on GFRP (Kampmann et al., 2018), it can be seen that the maximum strain and elongation of BFRP rebars surpasses the maximum strains of glass fiber based rebars. The research completed by Wang et al. (2014) has also shown that the tensile strength retention of BFRP rebars is higher than the tensile strength retention of GFRP rebars. In addition, the maximum strain of BFRP is higher. Likewise, the elastic lengthening of BFRP tendons is higher than that of steel (Thorhallsson and Jonsson, 2012; Pearson et al., 2013) and it might be beneficial to evaluate basalt fiber materials for the use of prestressing tendons to make additional alternatives available that can be used for prestressed concrete elements that are completely steel- or corrosion-free.

6.4 BFRP Design Specifications

AASHTO-LRFD specifications for the design of concrete bridges reinforced with BFRP rebars are yet to be developed. Only ICC-ES Acceptance Criteria AC454 (International Code Council, 2017) provides referenced design recommendations and a method of acceptance for BFRP reinforcing under US building codes for alternative materials. The current FDOT Standard Specifications for Road and Bridge Construction Section 932, which details FRP internal reinforcement for concrete structures, does not include or address requirements or minimum criteria for basalt fiber rebars. This research project aims at addressing this knowledge gap by providing recommendations for BFRP rebar specifications. To this end, four different tests were conducted. The assigned guaranteed shear strengths and bond-to-concrete strengths of the tested rebars is the average value for the individual test sample (specimen group). In other words, the mean sample shear strength of the rebars is considered as guaranteed shear strength and mean bond-to-concrete strength is considered as the guaranteed bond-to-concrete strength (ASTM-International, 2012a,b; ASTM International, 2014). To summarize the guaranteed mechanical strength values for all rebar types evaluated in this study, the following Tables 6.1 and 6.2 list the shear and bond-to-concrete characteristics, as well as the tensile properties, respectively. Table 6.1 highlights the transverse shear strength, the horizontal shear strength, and the bond-to-concrete strength for the three different BFRP rebar types (A, B, C). The final results (per test group) were compared to the acceptance criteria for GFRP rebars as given in FDOT Specifications Section 932, such that the prevalent value for the GFRP acceptance criteria represent 100% and a value above 100% indicates a performance above the minimum

Table 6.1: Guaranteed shear and bond-to-concrete strength of rebars

		Transverse Shear			Horizontal Shear			Bond-to-Concrete			
		Strength			Strength			Strength			
Rebar size	Lot	ksi	MPa	% [†]	ksi	MPa	% [†]	ksi	MPa	% [†]	
Rebar A	# 3	1	35.20	242.7	160	7.00	48.31	n/a	2.33	16.09	212
	# 5	1	33.74	232.7	153	6.41	44.16	n/a	2.96	20.41	269
	# 3	2	37.67	259.7	171	6.49	44.71	n/a	1.92	13.22	174
	# 5	2	36.48	251.6	166	6.41	44.15	n/a	1.65	11.41	150
Rebar B	# 3	1	31.39	216.3	143	6.42	44.22	n/a	2.79	19.23	254
	# 5	1	26.51	182.8	120	6.53	45.00	n/a	2.88	19.85	262
Rebar C	# 3	1	34.48	237.2	157	5.56	38.38	n/a	3.77	26.00	343
	# 5	1	31.69	218.5	144	6.64	45.77	n/a	3.77	26.01	343

[†] Percentage comparison based on FDOT specifications section 932, where 100% is GFRP rebar acceptance criteria .

requirement (for GFRP rebars). According to ACI Committee 440 (2015), the guaranteed strength, f_{fu}^* , of GFRP rebars is defined as the experimentally obtained average tensile strength minus three times the measured standard deviation, as shown in equation 6.1, while the guaranteed elastic modulus, $E_f = E_{f,ave}$, is defined as the mean elastic modulus of a test sample (specimen group).

$$f_{fu}^* = f_{fu_{average}} - 3\sigma \quad (6.1)$$

Accordingly, the calculated value for f_{fu}^* corresponds to the 99th percentile (Rossini et al., 2018), such that the chance for material failure (before any design factors are applied) remains below 1%. The strength of commercially available GFRP rebars differs based on the fiber content and manufacturing techniques (Emparanza et al., 2017), and the guaranteed strength is typically experimentally determined at the time of (concrete) design. If a specific rebar product strength is not defined experimentally at that time, the manufacturer specified rebar strength (f'_{fu}) is to be used (ACI Committee 440, 2015; Rossini et al., 2018). This specified design strength, f'_{fu} , is always less

than the guaranteed strength (c.f. equation 6.2) of the particular rebar lot that is to be used for construction.

$$f'_{fu} < f_{fu}^* \quad (6.2)$$

While most strength values for the basalt FRP rebars tested in this research showed that basalt rebars have a higher performance, the general material behavior appeared to be similar to the behavior of GFRP bars, and it is reasonable to assume that Equation 6.2 applies and can be used to calculate the guaranteed strength of basalt rebars. Accordingly, Table 6.2 lists the guaranteed strength values and elastic moduli for the three different BFRP rebar types (A, B, C) tested in this study, and the results are compared to criteria for GFRP rebar according to FDOT Specifications Section 932. The results in Table 6.2 show that both # 3 and # 5 type B rebars were the strongest

Table 6.2: Guaranteed strength and elastic modulus of rebars

	Rebar size	Lot	Tensile Strength							Elastic		
			Mean		Sta. Deviation		Guaranteed			Modulus		
			μ		σ		$\mu - 3\sigma$			E		
			ksi	MPa	ksi	MPa	ksi	MPa	% [†]	ksi	GPa	% [†]
Rebar A	# 3	1	121.7	839	3.82	26.36	110.2	760	92	5482	37.80	84
	# 5	1	134.2	925	4.34	29.92	121.3	836	129	7735	53.46	119
Rebar B	# 3	1	196.3	1353	4.21	29.03	183.6	1266	153	7808	53.83	120
	# 5	1	172.5	1189	9.19	63.33	145.0	999	155	7946	54.79	122
Rebar C	# 3	1	183.9	1268	4.80	33.12	169.5	1168	141	7154	49.32	110
	# 5	1	161.2	1112	12.85	88.63	122.7	1074	131	5267	36.31	81
	# 3	2	169.2	1166	5.03	34.69	154.1	1062	128	7200	49.64	111
	# 5	2	147.8	1019	4.04	27.86	135.6	935	145	7480	51.57	115

[†] Percentage comparison based on FDOT specifications section 932, where 100% is GFRP rebar acceptance criteria.

among all tested rebar samples. But the standard deviation of # 3 type A rebars was the smallest, while the type C # 5 rebars measure the highest standard deviation. The graphs in Figures 6.1 and 6.2 visualize the Gaussian distribution for the measured tensile strength results for # 3 and # 5 rebar, respectively. The mean value and guaranteed tensile strength ($\mu - 3\sigma$) are indicated on the

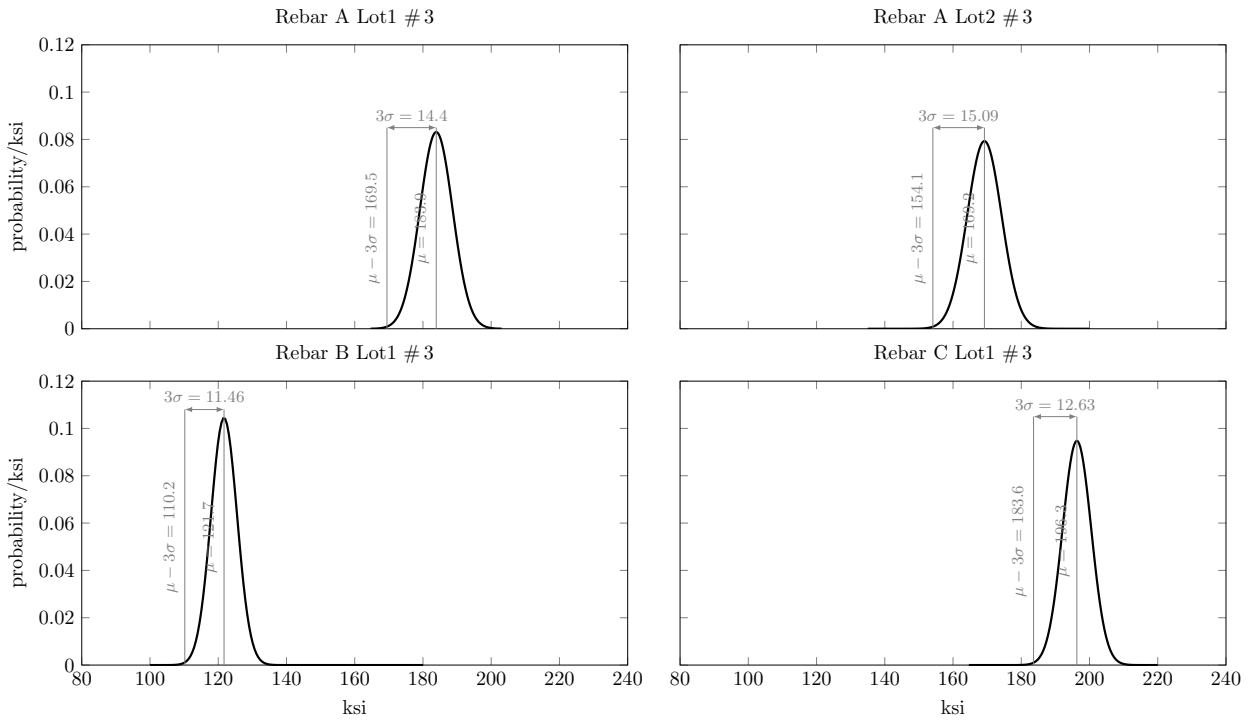


Figure 6.1: Gaussian distribution for tensile strength of #3 rebar

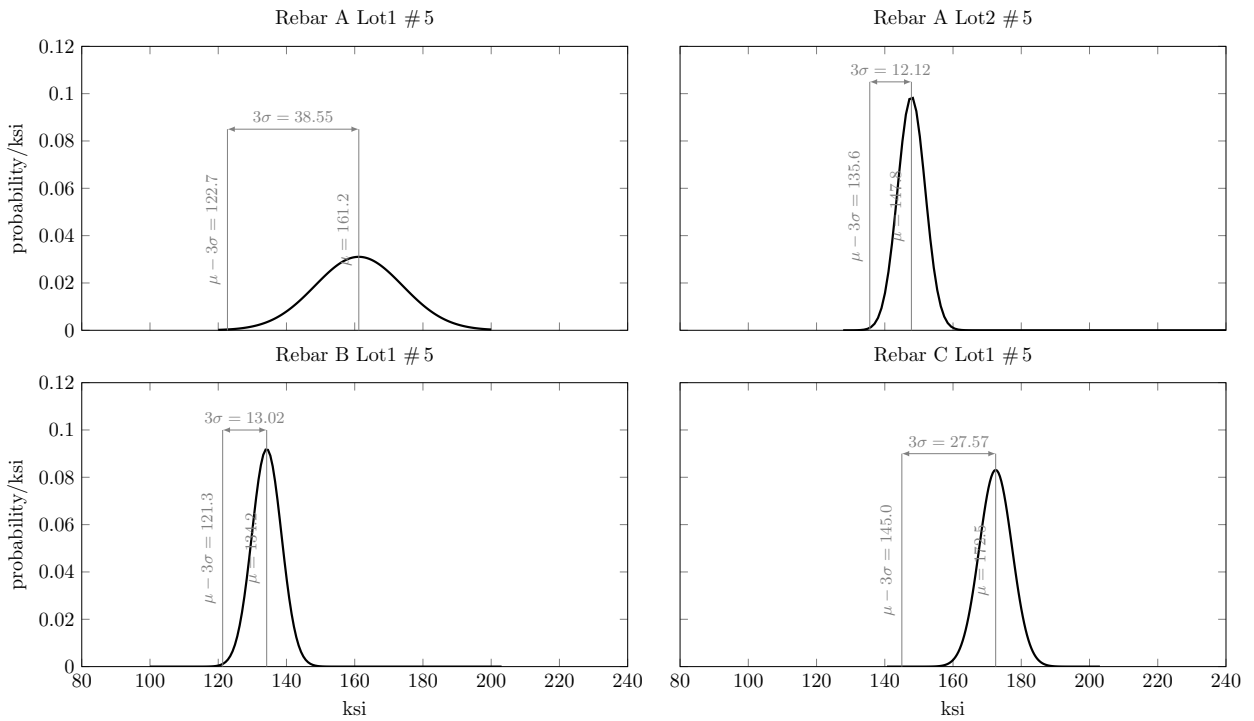


Figure 6.2: Gaussian distribution for tensile strength of #5 rebar

curves. It can be concluded that the guaranteed tensile strength of BFRP rebars can be derived similar to GFRP rebars.

6.4.1 Design Guide Considerations

According to AASHTO-LRFD Bridge Design Guide Specifications for GFRP Reinforced Concrete and ACI 440.1R Guide for the Design and Construction of Structural Concrete Reinforced with Fiber-Reinforced Polymer (FRP) Bars, strength reduction factors must be applied to decrease the design strength of FRP to overcome strength degradations (c.f. Table 6.3). The guaranteed strength of FRP rebars must be reduced by applying the environmental factor (C_E) (ACI Committee 440, 2015) to account for the strength loss due to exposure conditions. Likewise, the design strength for FRP rebars under sustained load must be reduced via the creep rupture factor (C_c) to avoid premature failure due to creep (ACI Committee 440, 2015; du Béton, 2007). The fatigue reduction factor (C_f) must be applied to properly define the strength of FRP rebars under cyclic loading. For the design of FRP rebar reinforced concrete structures, a reduction factor (C_b) has to be applied to the bond-to-concrete strength values listed in Table 6.1 to account for the different surface enhancement properties, which may differ significantly in comparison to steel rebars (ACI Committee 440, 2015). ACI Committee 440 (2015) defines the bond reduction factor as the inverse of the bond coefficient (k_b), which is larger than 1.0 for FRP rebars with a bond strength that is inferior to the bond strength for traditional steel rebars and less than 1.0 for FRP rebars with superior bond strength.

The brittle nature of FRPs implies a possibility of over-reinforced flexural members, which leads to concrete failure in the compression zone or to under-reinforced compression members, which may cause reinforcement rupture in the tension zone (ACI Committee 440, 2015; Rossini et al., 2018). The two failure modes — failure in the compression zone and rupture in the tension zone — are characterized by two different strength factors ϕ_c and ϕ_t respectively (ACI Committee 440, 2015; Rossini et al., 2018). As flexural members can sometimes undergo shear failure, the strength reduction factor ϕ_s is incorporated in the design; in other words, the nominal shear resistance of the designed member shall be reduced to factored shear resistance (Rossini et al., 2018). These factors are applied during the design phase to reduce the estimated nominal moment of a reinforced concrete member. Table 6.3 provides an overview of these factor and exemplifies how each factors

is applied in the design procedures according to ACI Committee 440 (2015); AASHTO (2018). The

Table 6.3: Reduction factors

Reduction factor	Equation used in design
Environmental factor (C_E)	$f_{fd} = C_E f'_{fu}$
Creep rupture factor (C_c)	$f_{f,c} = C_c f_{fd} = C_E C_c f'_{fu}$
Fatigue rupture factor (C_f)	$f_{f,f} = C_f f_{fd} = C_E C_f f'_{fu}$
Bond reduction factor (C_b)	$(C_b) = 1/k_b$
Factor for compression-controlled failures (ϕ_c)	$M_r = \phi_c M_n$
Factor for tension-controlled failures (ϕ_t)	$M_r = \phi_t M_n$
Factor for shear-controlled failures (ϕ_s)	$V_r = \phi_s V_n$

results obtained through this research can be used to initiate the development of the bond factor for BFRP rebars in concrete structures. A detailed research focusing on the reduction factors and long-term durability of BFRP rebars in harsh environments is suggested because this would inform future iterations of the AASHTO LRFD bridge specifications for BFRP rebars and also helps with updates to ACI 440 codes for the implementation of BFRP design specifications.

6.5 Research Limitations

This research project was focused toward a BFRP rebar market analysis and the performance evaluation of three different BFRP rebar products. It was found that numerous readily available rebar types exist, with a range of strength properties, and that those properties are dependent on the different raw materials and surface enhancement features (chosen by the manufacturer). While an effort was made to evaluate representative and commonly available BFRP rebar products, this study was limited to the specific material compositions used by the three selected manufacturers. Likewise, for economical considerations, only the two most common rebar sizes were tested. Only one manufacturer was able to supply material from two lots, while the other two manufacturers were still developing their production lines and only supplied materials from their pilot productions. The results obtained from this research are currently used by the manufacturers to improve the quality of production of the rebars. Accordingly, it must be noted that the presented conclusions have to

be interpreted with care when using other products or different material compositions. While the findings seem adequate and applicable in the context of the BFRP rebar technology, it is emphasized that the derived conclusions are not universal. Because acceptance criteria for BFRP rebar are still under development for FDOT Specifications Section 932, all obtained results were benchmarked relative to the existing acceptance criteria for GFRP rebars.

BFRP rebars are intended for use in harsh environments. Therefore, a long-term durability analysis of these rebars must be done because those aspects could not be addressed through this research project. Only BFRP rebar material properties were tested, while the application behavior of these rebars in concrete elements such as beams, columns, and slabs was not studied here. The presented findings provide insight and initial guidance for the adoption of BFRP rebars in FDOT Specifications and suggestions for future iterations of design guidelines. But the authors explicitly advise acting with caution when extrapolating the findings and conclusions to other or future FRP rebar materials.

6.6 Future and Further Directions

It is noted that no long-term tests were performed throughout this project and that additional durability analyses for BFRP rebars in extreme environments shall be conducted. It appears vital because of the unique chemical composition of basalt fibers and the interaction they can potentially undergo in saline-rich environments heterodyned with high pH concentrations. This may be one of the most important aspects for a proper life cycle of concrete structures reinforced with BFRP rebars in aggressive environments (e.g.; coastal bridges) because of the highly basic conditions of the rebar surrounding cementitious paste.

Lu et al. (2015) compared virgin to aged, pultruded BFRP plates and rebars to measure the effect of thermal aging (at 135 °C and 300 °C for four hours) on the longitudinal tensile strength and the interlaminar shear properties. It was found that the degradation process of aged rebars immersed in alkaline solution and distilled water accelerated due to thermal aging. Similarly, Altamas et al. (2015) studied the bond-to-concrete durability properties of sand coated basalt fiber reinforced polymer (BFRP) rebars and glass fiber reinforced polymer (GFRP) rebars via accelerated conditioning in acidic, saline, and alkaline solutions for 30 days, 60 days, and 90 days. The results showed that the bond strength retention was reduced for rebars immersed in acid solution, alkaline,

and saline environments, as compared to un-aged rebars; all rebars failed in interlaminar shear. Wang et al. (2017) tested tensile strength and Young's modulus properties of BFRP and GFRP rebars exposed to seawater and sea sand concrete (SWSSC). The rebars were exposed to normal SWSSC (N-SWSSC), and high performance SWSSC (HP-SWSSC) at room temperature, 40 °C, 48 °C, and 50 °C for 21 days, 42 days, and 63 days. When compared to HP-SWSSC, N-SWSSC was more aggressive on both BFRP and GFRP bars due to the high alkali ion concentration. In high temperature environments, the GFRP rebars were more durable than the BFRP rebars because of the different resins. Based on the SEM, 3D X-ray, and CT-results, the resin properties of GFRP bars were more stable in SWSSC conditions than the resin used for the tested BFRP rebars. In research projects conducted by Benmokrane et al. (2017) and Kajorncheappunngam et al. (2002), the long-term durability in alkali environments at accelerated temperatures for rebars made with different resins was evaluated. It was seen that the performance of epoxy resins was comparably good and acceptable.

Wei et al. (2011) studied degradation of basalt fiber-epoxy resin and glass fiber-epoxy resin composites in seawater, and it was found that the bending and tensile strength decreased with increased immersion times. This study also emphasized that the chemical stability of BFRP rebars can be improved by lowering the Fe^{+2} ions in basalt rock and durability of rebar in seawater can be increased.

As mentioned before and based on the above listed research studies, it is suggested to conduct degradation analyses of BFRP rebars in harsh environments. Furthermore, because the microstructure porosity and the moisture absorption of FRP rebars are closely related, SEM analysis of basalt fiber rebar specimens after long-term moisture absorption tests should be performed to evaluate the rebar properties at the micro level and to define its vulnerability to degradation. New products should be characterized via SEM technology, such that the findings and images can be stored for comparison to future iterations of specific product lines. The development of a product database is highly suggested. It appears that long-term durability performance of BFRP rebars in concrete structures has not been sufficiently studied yet. To fully embrace this technology, it is important to study the flexural and shear properties of BFRP rebar reinforced concrete beams after exposing them to aggressive environments for extended periods. Therefore, it is suggested to evaluate the performance of BFRP rebars and strength retention in concrete elements exposed to

different environmental conditions.

Chapter 7

Conclusions

To provide a concise overview of the tasks performed for this research project, a brief summary of the experimental work and the analysis is provided in this chapter, before the final conclusion and future recommendations — based on the overall findings and the discussion presented in Chapter 6 — are listed here.

7.1 Summary

This project was conducted to evaluate the performance of three commercially available BFRP rebar products to assist the Florida Department of Transportation in the development of acceptance criteria for basalt based fiber reinforced polymer (BFRP) reinforcing bars for the extension of FDOT Specifications Section 932 — Nonmetallic Accessory Materials for Concrete Pavement and Concrete Structures. Three high-quality rebar products from different established FRP rebar producers were selected to evaluate two of the most commonly used rebar sizes (# 3 and # 5) and to fully characterize the relevant material properties. It was the goal to study the effects of different material constituents and surface enhancement properties. For the purpose of this research, a total of three different physical properties (cross-sectional dimensions, moisture absorption, and fiber content) and four mechanical strength characteristics (transverse shear strength, apparent horizontal shear strength, tensile strength and elastic modulus, and bond-to-concrete strength) were experimentally quantified for virgin state BFRP rebars. Because acceptance criteria for basalt FRP rebars does not yet exist in the US, the findings were compared to the prevalent minimum criteria for glass FRP rebars. The measured and analyzed data showed that two of the three re-

bar products (Type A and B), irrespective of their size, met the GFRP rebar criteria defined in FDOT Specifications Section 932. The other rebar Type C met all performance criteria for the #3 rebar size, but rebar size #5 did not meet the acceptance criteria for moisture absorption or elastic modulus properties. Performance differences were noted for rebar products from different manufacturers because of dissimilarities in material production and surface enhancement properties. However, basalt fiber rebar products appear to be a viable alternative as a non-corrosive rebar option for future FDOT construction projects, and the data gathered throughout this research showed that high-quality BFRP rebars are available in the American market. A standardized use of such rebars seem feasible based on appropriate acceptance criteria because BFRP rebars outperform the already accepted/established GFRP rebars. While the development of acceptance criteria for BFRP rebars has been initiated through this project, and an implementation of this alternative reinforcing technology should be strongly considered by the FDOT, more critical BFRP-specific performance criteria — beyond GFRP performance criteria — can be developed in future projects to further differentiate the various fiber types and to take full advantage of the available material characteristics.

7.2 Conclusions

Based on the research findings which were obtained through a comprehensive literature review, a BFRP rebar market analysis, material characterization, and the discussion points presented throughout this report, the following conclusions were drawn:

- A variety of BFRP rebar types and sizes, with dissimilar physical and strength properties, are currently available in the market. The strength properties of different types of rebars vary vastly based on the manufacturer type, raw materials, and surface enhancement property. While manufacturer reported properties vary, BFRP rebars appear to be [notably] stronger than GFRP rebars.
- The fiber content of BFRP rebars appears to be well-controlled throughout the manufacturing process, and it is nearly identical between various products (or the tested rebar types). This property was notably consistent with minimal coefficients of variations, which indicates high-quality products.

- Differences in performance of rebars were observed based on the moisture absorption property, specifically for the material that did not satisfy the maximum absorption criteria. It appears that the rebar strength is inversely proportional to moisture absorption property because of the related porosity that potentially leads to material imperfections.
- The transverse shear strength of BFRP rebars appears to be measurably stronger than the the transverse shear strength of GFRP rebars. The data showed that BFRP outperformed the minimum GFRP criteria by at least 116 %.
- Because the apparent horizontal shear strength is dependent on the quality of the resin and the resin-fiber interface — and less influenced by the fiber itself — this property was not significantly different from measurements usually obtained for GFRP products. Nevertheless, this property is a valuable quality control parameter that is used by many manufacturers around the world to quickly recognize/address production inconsistencies. As such, FDOT Specifications Section 932 should adopt a minimum threshold value.
- The size effect or shear lag for BFRP rebars with sizes between # 3 and # 5 is notably higher. These phenomenon occurred because BFRP rebars are a product of composite materials and they are produced in multiple layers. Due to the test procedure, the external fibers are stretched the most, while the inner layers stretch less towards the rebar core and can only be fully utilized after the outer fibers fail.
- Similar to GFRP rebars, for BFRP rebars which were manufactured with helical wraps — as surface enhancement property — the helically wrapped fibers ruptured before the longitudinal fibers failed in tension.
- The bond-to-concrete property of BFRP rebars is highly dependent on the surface enhancement features and the rebar geometry. Due to the geometric interlocking effect, helically wrapped rebars (in addition to being sand coated) measured the highest absolute bond-to-concrete strength, while the rebar slip was significantly minimized — in comparison to the measured slip for sand coated rebars.
- The minimum criteria for bond-to-concrete of ≥ 1.1 ksi appears to be at the lower limit, because all rebars tested in this study outperformed this criteria by more than 200 %, with

individual rebar types beyond 300 %.

- Based on the performance analysis of the tested BFRP rebars and an evaluation of all obtained results in context of FDOT Specifications Section 932, AC454, and ASTM 7957, it can be concluded that the tested materials are generally stronger than comparable GFRP rebars.
- The elastic modulus and tensile strength criteria for BFRP rebars can be set higher than the existing criteria for GFRP rebars in FDOT Specifications Section 932.

7.3 Further Recommendations

Because FRP rebars are desirable for use in harsh environments and material properties generally degrade in aggressive media (ACI Committee 440, 2015; du Béton, 2007), the long-term chemical durability performance of BFRP rebars, including their raw material components, have to be studied and evaluated in various alkaline and saline environments before minimum material and design criteria can be ultimately defined. As discussed in Section 6.4.1, for the implementation of BFRP rebar technology in future design codes, such as AASHTO design guidelines, ACI, or state design requirements, the following suggestions are made.

- The bond strength results obtained through this research project can be used in the development of a bond factor (C_b) for BFRP rebars, and this factor can be directly implemented in ACI 440 and AASHTO-bridge design guide specifications.
- Additional studies with a focus on bond-to-concrete properties of BFRP rebars and the bond degradation over time in harsh environments is recommended to full development of a suitable bond reduction factor (C_b) that is specific to BFRP rebars.
- Because BFRP rebars are thought of as a preferable alternative in harsh environments, it is important to study the long-term chemical durability properties of such rebars before the environmental reduction factor (C_E) for BFRP rebars can be independently defined.

References

- AASHTO (2012). *Guide Specifications for Design of Bonded FRP Systems for Repair and Strengthening of Concrete Bridge Elements*. American Association of State Highway and Transportation Officials.
- AASHTO (2018). *AASHTO LRFD Bridge Design Guide Specifications for GFRP-Reinforced Concrete Bridge Decks and Traffic Railings*. American Association of State Highway and Transportation Officials.
- ACI Committee 440 (2006). *Guide for the Design and Construction of Structural Concrete Reinforced with FRP Bars*, (440.1R). American Concrete Institute.
- ACI Committee 440 (2007). *Report on Fiber-Reinforced Polymer (FRP) Reinforcement for Concrete Structures*, (440R). American Concrete Institute.
- ACI Committee 440 (2008a). *Guide for the Design and Construction of Externally Bonded FRP Systems for Strengthening Concrete Structures*, (440.2R). American Concrete Institute.
- ACI Committee 440 (2008b). *Specification for Carbon and Glass Fiber-Reinforced Polymer Bar Materials for Concrete Reinforcement*, (440.6). American Concrete Institute.
- ACI Committee 440 (2012). *Guide Test Methods for Fiber-Reinforced Polymer (FRP) Composites for Reinforcing or Strengthening Concrete and Masonry Structures*, (440.3R). American Concrete Institute.
- ACI Committee 440 (2013). *Specification for Carbon and Glass Fiber-Reinforced Polymer (FRP) Materials Made by Wet Layup for External Strengthening of Concrete and Masonry Structures*, (440.8-13). American Concrete Institute.

- ACI Committee 440 (2015). “*Guide for the design and construction of structural concrete reinforced with fiber-reinforced polymer (frp) bars.*” Report No. ACI 440.1R-15, American Concrete Institute.
- Altalmas, A., Refai, A. E., and Abed, F. (2015). “Bond degradation of basalt fiber-reinforced polymer (bfrp) bars exposed to accelerated aging conditions.” *Construction and Building Materials*, 81, 162–171.
- ASTM (2014). *Standard Test Method for Moisture Absorption Properties and Equilibrium Conditioning of Polymer Matrix Composite Materials*, (D5229). ASTM International, West Conshohocken, PA.
- ASTM-International (2004). *Standard Test Method for Compressive Strength of Cylindrical Concrete Specimens*, (C 39/C 39 M). West Conshohocken, PA.
- ASTM-International (2011). *Standard Test Method for Ignition Loss of Cured Reinforced Resins*, (D2584-11). West Conshohocken, PA.
- ASTM-International (2012a). *Standard Test Method for Apparent Horizontal Shear Strength of Pultruded Reinforced Plastic Rods By the Short-Beam Method*, (D4475 - 02 (REAPPROVED 2008)). West Conshohocken, PA.
- ASTM-International (2012b). *Standard Test Method for Transverse Shear Strength of Fiber-reinforced Polymer Matrix Composite Bars*, (D7617/D7617M - 11). West Conshohocken, PA.
- ASTM International (2014). *Standard Test Method for Bond Strength of Fiber-Reinforced Polymer Matrix Composite Bars to Concrete by Pullout Testing*, (D7913/D7913M). West Conshohocken, PA.
- ASTM International (2014). *Standard Test Method for Bond Strength of Fiber-Reinforced Polymer Matrix Composite Bars to Concrete by Pullout Testing*, (D7913/D7913M). ASTM International, West Conshohocken, PA.
- ASTM-International (2015a). *Standard Test Method for Tensile Properties of Fiber Reinforced Polymer Matrix Composite Bars*, (D7205/D7205M – 06 Reapproved 2011). West Conshohocken, PA.

- ASTM-International (2015b). *Standard Test Methods for Density and Specific Gravity (Relative Density) of Plastics by Displacement*, (D792-13). West Conshohocken, PA.
- ASTM-International (2017). *Standard Specification for Solid Round Glass Fiber Reinforced Polymer Bars for Concrete Reinforcement*, (ASTM D7957 / D7957M – 17). West Conshohocken, PA.
- ASTM International (2018). *Standard Practice for Making and Curing Concrete Test Specimens in the Laboratory*, (C192/C192M). West Conshohocken, PA.
- Aubourg, P., Crall, C., Hadley, J., Kaverman, R., and Miller, D. (1991). *Engineered Materials Handbook*, (Vol. 4). ASM International.
- Bagherpour, S. (2012). (*Polyester*). InTech.
- Bagherpour, S., Bagheri, R., and Saatchi, A. (2009). “Effects of concentrated hcl on the mechanical properties of storage aged fiber glass polyester composite.” *Materials and Design*, 30(2), 271–274.
- Benmokrane, B. (2018). “*Development of New Edition of CSA S807 Standard — Specifications for Fiber Reinforced Polymers.*” Report No. to be assigned, Canadian-CSA Specifications for Fiber Reinforced Polymers.
- Benmokrane, B., Ali, A. H., Mohamed, H. M., ElSafty, A., and Manalo, A. (2017). “Laboratory assessment and durability performance of vinyl-ester, polyester, and epoxy glass-frp bars for concrete structures.” *Composites Part B: Engineering*, 114, 163–174.
- Benmokrane, B., Elgabbas, F., Ahmed, E. A., and Cousin, P. (2015). “Characterization and comparative durability study of glass/vinylester, basalt/vinylester, and basalt/epoxy frp bars.” *Journal of Composites for Construction*, 19(6), 04015008.
- Benmokrane, B., Wang, P., Ton-That, T. M., Rahman, H., and Robert, J.-F. (2002). “Durability of glass fiber-reinforced polymer reinforcing bars in concrete environment.” *Journal of Composites for Construction*, 6(3), 143–153.
- Best, M. G. (2003). *Igneous and metamorphic petrology*, (2nd Edition). Wiley-Blackwell.
- Borges, S. G., Ferreira, C. A., Andrade, J. M., and Prevedello, A. L. (2015). “The influence of bath temperature on the properties of pultruded glass fiber reinforced rods.” *Journal of Reinforced Plastics and Composites*, 34(15), 1221–1230.

- Brik, V. B. (2003). “*Advanced concept concrete using basalt fiber/bf composite rebar reinforcement.*”
Final report for highway-idea project 86, Innovations Deserving Exploratory Analysis Programs.
- Brown, V. and Bartholomew, C. (1993). “Frp dowel bars in reinforced concrete pavements.” *Special Publication, 138*, 813–830.
- Busel, J. P. (2016). “*Introduction to fiber reinforced polymer (frp) composites in infrastructure.*”
Report no., American Composites Manufacturers Association.
- Canadian Standard Association (2010). *Specifications for Fibre Reinforced Polymers*, (CAN/CSA-S807).
- Canadian Standard Association (2018). *Specifications for Fibre Reinforced Polymers*, (CAN/CSA-S807).
- Castro, F. and Carino, N. J. (1998). “Tensile and nondestructive testing of frp bars.” *Journal of Composites for Construction*.
- Chen, Y., Davalos, J. F., Ray, I., and Kim, H. Y. (2007). “Accelerated aging tests for evaluations of durability performance of FRP reinforcing bars for concrete structures.” *Composite Structures*, 78(1), 101–111.
- Colombo, C., Vergani, L., and Burman, M. (2012). “Static and fatigue characterisation of new basalt fibre reinforced composites.” *Composite Structures*, 94, 1165–1174.
- Dhé, P. (1923). “*Tipping crucible for basalt furnaces.*” Patent 1,462,446, United States Patent Office.
- du Béton, F. I. (2007). “Frp reinforcement in rc structures.” *Task Group*, 9, 151.
- Eddie, D. (1999). “Frp dowels for concrete pavements. Master’s thesis, University of Manitoba.
- Ehrenstein, G. W. (2006). *Faserverbund-Kunststoffe: Werkstoffe - Verarbeitung - Eigenschaften*, (2. Edition). Carl Hanser Verlag GmbH and Co. KG.
- Elgabbas, F., Vincent, P., Ahmeda, E. A., and Benmokrane, B. (2016). “Experimental testing of basalt-fiber-reinforced polymer bars in concrete beams.” *Composites Part B*, 91, 205–218.

- ElSafty, A., Benmokrane, B., Rizkalla, S., Mohamed, H., and Hassan, M. (2014). “*Degradation assessment of internal continuous fiber reinforcement in concrete environment.*” Report no., Florida Department of Transportation.
- Empananza, A. R., Kampmann, R., and y Basalo, F. D. C. (2017). “State-of-the-practice of global manufacturing of frp rebar and specifications.” *The 13th International Symposium on Fiber-Reinforced Polymer Reinforcement for Concrete Structures (FRPRCS-13)*, American Concrete Institute Anaheim, CA.
- Fallaha, S., Knight, C., and Nolan, S. (2017). “FDOT GFRP-RC implementation - current status, projects and challenges. First International Workshop on Glass Fibre Reinforced Polymer (GFRP) Bar for Concrete Structures (IWGFRP-1), July 18, 2017.
- Faruk, O., Tjong, J., and Sain, M. (2017). (*Lightweight and Sustainable Materials for Automotive Applications*). Tyler & Francis Group, LCC.
- Fiore, V., Scalici, T., Bella, G. D., and Valenza, A. (2015). “A review on basalt fibre and its composites.” *Composites Part B*, 74, 74–94.
- Florida Department of Transportation (2015). “*Fiber reinforced polymer guidelines (frpg).*” Structural Manual Topic No. 625-020-018 Volume 4, FDOT.
- G., N. and D., V. (2011). *Wendehorst Baustoffkunde Grundlagen - Baustoffe - Oberflächenschutz*, (Vol. 27). Vieweg+Teubner Verlag.
- Gieben, N. (2017). “An analysis of the free specimen length for tensile testing of glass fiber reinforced polymer (gfrp) reinforcement bars according to astm 7205. Master’s thesis, FH Münster University of Applied Sciences.
- Hassan, M., Benmokrane, B., ElSafty, A., and Fam, A. (2016). “Bond durability of basalt-fiber-reinforced-polymer (bfrp) bars embedded in concrete in aggressive environments.” *Composites Part B*, 106, 262–272.
- Hurtado, D. (2018). “*Fdot standard specification for road and bridge construction.*” Report no., Florida Department of Transportation.

- International Code Council (2017). *Fiber-reinforced Polymer (FRP) Bars for Internal Reinforcement of Concrete Members*. 500 New Jersey Avenue, NW.
- International Code Council Evaluation Services (2016). “Acceptance criteria for glass fiber-reinforced polymer (GFRP) bars for internal reinforcement of concrete members.” Acceptance criteria 454, ICCES.
- International Code Council Evaluation Services (2017). “Acceptance criteria for glass fiber-reinforced polymer (GFRP) bars for internal reinforcement of concrete members.” Acceptance criteria 454, ICCES.
- Ipbüker, C., Nulk, H., Gulik, V., Biland, A., and Tkaczyk, A. H. (2014). “Radiation shielding properties of a novel cement-basalt mixture for nuclear energy applications.” *Nuclear Engineering and Design*, 284, 27–37.
- ISC (2014). *Fibre-Reinforced polymer bar for concrete reinforcement general specifications*, (GOST 31938-2012). Interstate Council for Standardization, Metrology and Certification (ISC).
- Jamshaid, H. and Mishra, R. (2016). “A green material from rock: basalt fiber — a review.” *The Journal of The Textile Institute*, 107(7), 923–937.
- Joshi, S. C., Lam, Y., and Tun, U. W. (2003). “Improved cure optimization in pultrusion with pre-heating and die-cooler temperature.” *Composites Part A*, 34, 1151–1159.
- Kajorncheappunngam, S., Gupta, R. K., and GangaRao, H. V. (2002). “Effect of aging environment on degradation of glass-reinforced epoxy.” *Journal of composites for construction*, 6(1), 61–69.
- Kampmann, R., De Caso Y Basalo, F., and Ruiz Emparanza, A. (2018). “Performance evaluation of glass fiber reinforced polymer (gfrp) reinforcing bars embedded in concrete under aggressive environments.” Technical Report BDV30 TWO 977-18, Florida Department of Transportation.
- Kampmann, R., Ruiz Emparanza, A., Telikapalli, S., Suhrheinrich, J., and De Caso Y Basalo, F. (2019). “The correlation between moisture absorption and tensile strength retention of glass fiber reinforced polymer rebars.” *2nd International Workshop on Glass Fibre Reinforced Polymer (GFRP) Bars for Concrete Structures*.

- Kocaoza, S., Samaranayakeb, V., and Nanni, A. (2004). “Tensile characterization of glass frp bars.” *Composites Part B*, 36, 127–134.
- Kochergin, A., Granovskaya, N., Kochergin, D., Savchenko, V., and Galimov, N. (2013). “Ways to supply gabbro-basalt raw materials to mineral fiber producers.” *Glass and Ceramics*, 69(11-12), 405–408.
- Li, C., Gao, D., Wang, Y., and Tang, J. (2017). “Effect of high temperature on the bond performance between basalt fibre reinforced polymer (bfrp) bars and concrete.” *Construction and Building Materials*, 141, 44–51.
- Lu, Z., Xian, G., and Li, H. (2015). “Effects of exposure to elevated temperatures and subsequent immersion in water or alkaline solution on the mechanical properties of pultruded bfrp plates.” *Composites Part B: Engineering*, 77, 421–430.
- Maitre, R. W. L. (2002). (*Igneous Rocks: A Classification and Glossary of Terms: Recommendations of the International Union of Geological Sciences Subcommittee on the Systematics of Igneous Rocks*). 2nd. Cambridge University Press.
- Markets and Markets (2016). “Frp rebar market by resin type, by fiber type, by application — global forecasts to 2021.” *PR Newswire Association LLC*.
- MTS Landmark Testing Solutions (2015). *Versatile, high-performance servohydraulic systems for static and dynamic material and component testing*, (12/15). MTS Systems Corporation, 14000 Technology Drive Eden Prairie, MN 55344-2290 USA.
- Nanni, A., De Luca, A., and Jawaheri Zadeh, H. (2014). (*FRP Reinforced Concrete Structures – Theory, Design and Practice*). CRC Press.
- Patnaik, A. (2009). “*Applications of basalt fiber reinforced polymer (bfrp) reinforcement for transportation infrastructure*.” Report no., The University of Akron.
- Pavlovski, D., Mislavsky, B., and Antonov, A. (2007). “Cng cylinder manufacturers test basalt fibre.” *REINFORCEDplastics*, 36–39.
- Pearson, M., Donchev, T., and Salazar, J. (2013). “Long-term behaviour of prestressed basalt fibre reinforced polymer bars.” *Procedia Engineering*, 54, 261–269.

- Rarnalaishnan, V. and Tolmare, N. S. (1998). “*Performance evaluation of 3-d basalt fiber reinforced concrete & basalt rod reinforced concrete.*” IDEA Program Final Report, Contract No. NCHRP-45, Transportation Research Board National Research Council.
- Rossini, M., Matta, F., Nolan, S., Potter, W., and Nanni, A. (2018). “Aashto design specifications for gfrp-rc bridges.” *Italian Concrete Days*, Associazione Italiana Calcestruzzo Armato e Precompresso (AICAP) & Collegio .
- Ruelke, T. (2014). “*Non metallic accessory materials for concrete pavement and concrete structures.*” Section 932, Florida Department of Transportation.
- Schesser, D., Yang, Q. D., Nanni, A., and Giancaspro, J. W. (2014). “Expansive grout-based gripping systems for tensile testing of large-diameter composite bars.” *Journal of Materials in Civil Engineering*, 26(2), 250–258.
- Singha, K. (2012). “A short review on basalt fiber.” *International Journal of Textile Science*, 1(4), 19–28.
- Slyter, G. (1938). “*Method and apparatus for making glass wool.*” Patent 2,133,235, United States Patent Office.
- Stekloplastics, D. (2014). “Stekloplastic visit to iceland.” *Communication with Stekloplastics Boris Gromkov and Natalya Demenia with Birgir Jóhannesson.*
- Thorhallsson, E. and Jonsson, B. S. (2012). “Test of prestressed concrete beams with bfrp tendons.” *Reykjavik University.*
- Toni Schneider, G. L. (2015). “Lipex gmbh, germany.” *Communication with Toni Schneider, Gert Lichblau with Birgir Jóhannesson.*
- Vincent, P., Ahmed, E., and Benmokrane, B. (2013). “Characterization of basalt fiber-reinforced polymer (bfrp) reinforcing bars for concrete structures.” *Specialty Conference on Material Engineering & Applied Mechanics, 3rd*, MEC–111–1 – MEC–111–10.
- Wallenberger, F. T., Watson, J. C., Li, H., and PPG Industries Inc. (2001). “*Glass fibers.*” ASM Handbook 21, ASM International.

- Wang, X., Wang, Z., Wu, Z., and Cheng, F. (2014). “Shear behavior of basalt fiber reinforced polymer (frp) and hybrid frp rods as shear resistance members.” *Construction and Building Materials*, 73, 781–789.
- Wang, Z., Zhao, X.-L., Xian, G., Wu, G., Raman, R. S., Al-Saadi, S., and Haque, A. (2017). “Long-term durability of basalt- and glass-fibre reinforced polymer (bfrp/gfrp) bars in seawater and sea sand concrete environment.” *Construction and Building Materials*, 139, 467–489.
- Wei, B., Cao, H., and Song, S. (2010). “Tensile behavior contrast of basalt and glass fibers after chemical treatment.” *Materials and Design*, 31, 4244–4250.
- Wei, B., Cao, H., and Song, S. (2011). “Degradation of basalt fibre and glass fibre/epoxy resin composites in seawater.” *Corrosion Science*, 53(1), 426–431.
- Wu, G., Dong, Z.-Q., Wang, X., Zhu, Y., and Wu, Z.-S. (2014). “Prediction of long-term performance and durability of bfrp bars under the combined effect of sustained load and corrosive solutions.” *Journal of Composites for Construction*, 19(3), 04014058.
- You, Y.-J., Kim, J.-H. J., Kim, S.-J., and Park, Y.-H. (2015). “Methods to enhance the guaranteed tensile strength of gfrp rebar to 900 mpa with general fiber volume fraction.” *Construction and Building Materials*, 75, 54 – 62.
- Zych, T. and Wojciech, K. (2012). “Study on the properties of cement mortars with basalt fibres.” *Brittle Matrix Composites 10*, 155–166.

Appendices

Appendix A

Individual Specimen Results

This appendix supplements the results chapter to present the individual test results for every tested specimen and the corresponding statistical results that were determined for each control and test group (of relevant specimen sets). The tables with individual specimen results are sorted by rebar type, size, lot, and specimen count. Dependent on the test procedure, the tables for the individual test results list the most essential (e.g. maximum specimen strength, displacement at maximum strength, etc.) data, while the statistical tables present the minimum (\wedge), maximum (\wedge), mean (μ), standard deviation (σ), and coefficient of variation (CV) values. For the purpose of this research project, a wide variety of physical and mechanical tests were conducted on five specimens per sample of BFRP rebar materials. All statistical results that are presented in the main text above are based on those five individual specimen results.

A.1 Density and Cross-Sectional Dimension Test

The following Table A.1 lists all specimen measurements and results that were determined to derive the BFRP rebar diameters according to ASTM D792 (ASTM-International, 2015b). The diameter and the cross-sectional area of the rebars were calculated from the measured density and the individual specimen volume and lengths.

Table A.1: Diameter measurements for each individual specimen

Specimen				Specimen Length				Weight				
Manuf. Type	Lot No.	Size #	Specimen No.	L1 mm	L2 mm	L3 mm	Average mm	a g	a+s g	b g	s g	δ M g
A	1	3	1	31.30	31.30	31.40	31.30	5.22	13.01	10.36	7.80	2.57
A	1	3	2	32.10	32.10	31.90	32.10	5.32	13.13	10.44	7.81	2.63
A	1	3	3	30.00	30.00	30.00	30.00	5.00	12.81	10.27	7.81	2.46
A	1	3	4	32.30	32.30	32.40	32.30	5.37	13.17	10.48	7.80	2.67
A	1	3	5	31.20	31.10	31.20	31.20	5.18	12.99	10.37	7.81	2.57
A	1	5	1	31.20	31.40	31.20	31.20	13.60	21.40	14.61	7.80	6.80
A	1	5	2	31.20	31.20	31.20	31.20	13.73	21.54	14.69	7.81	6.88
A	1	5	3	31.10	31.00	31.10	31.10	13.64	21.45	14.62	7.81	6.81
A	1	5	4	33.00	33.20	32.90	33.00	14.43	22.24	15.06	7.81	7.26
A	1	5	5	31.00	30.80	30.80	31.00	13.49	21.30	14.51	7.81	6.70
B	1	3	1	27.90	28.10	28.00	27.90	5.02	12.82	10.40	7.79	2.61
B	1	3	2	29.90	29.70	29.70	29.90	5.39	13.21	10.61	7.82	2.79
B	1	3	3	30.20	30.40	30.30	30.20	5.46	13.26	10.63	7.80	2.83
B	1	3	4	28.90	29.00	29.00	28.90	5.17	12.97	10.47	7.80	2.67
B	1	3	5	29.00	29.00	29.00	29.00	5.22	13.03	10.45	7.81	2.63
B	1	5	1	30.50	30.50	30.80	30.50	14.35	22.16	15.56	7.81	7.75
B	1	5	2	30.40	30.50	30.30	30.40	14.26	22.07	15.17	7.81	7.36
B	1	5	3	30.80	30.70	30.70	30.80	14.42	22.22	15.26	7.79	7.46
B	1	5	4	31.00	30.90	30.90	31.00	14.55	22.37	15.33	7.82	7.51
B	1	5	5	29.70	29.70	29.80	29.70	13.87	21.67	14.94	7.80	7.14
C	1	3	1	25.50	25.27	25.12	25.30	3.98	11.77	9.77	7.80	1.97
C	1	3	2	25.14	25.19	25.27	25.20	3.98	11.78	9.76	7.80	1.96
C	1	3	3	25.58	25.33	25.21	25.37	3.98	11.78	9.77	7.81	1.96
C	1	3	4	25.13	25.12	25.27	25.17	3.94	11.74	9.74	7.80	1.95
C	1	3	5	25.70	25.36	25.23	25.43	3.93	11.73	9.76	7.80	1.96
C	1	5	1	25.57	25.35	25.38	25.43	11.41	19.02	13.64	7.61	6.03
C	1	5	2	25.30	25.47	25.69	25.49	11.15	18.94	13.59	7.80	5.79
C	1	5	3	25.39	25.58	25.49	25.49	11.17	18.97	13.60	7.79	5.81
C	1	5	4	25.35	25.36	25.41	25.37	11.25	19.05	13.65	7.80	5.86
C	1	5	5	25.34	25.48	25.34	25.39	11.15	18.95	13.60	7.80	5.80
C	2	3	1	30.80	30.80	30.70	30.80	4.85	12.65	10.30	7.80	2.50
C	2	3	2	31.00	30.90	30.80	31.00	4.90	12.69	10.32	7.80	2.53
C	2	3	3	31.10	31.10	31.10	31.10	4.93	12.74	10.34	7.81	2.53
C	2	3	4	30.30	30.10	30.30	30.30	4.75	12.55	10.25	7.80	2.45
C	2	3	5	31.80	31.80	31.70	31.80	5.00	12.80	10.37	7.80	2.57
C	2	5	1	31.00	30.90	31.00	31.00	9.00	16.79	15.34	7.79	7.54
C	2	5	2	31.40	31.60	31.40	31.40	9.15	16.95	14.84	7.80	7.04
C	2	5	3	30.50	30.60	30.60	30.50	8.81	16.61	14.73	7.80	6.93
C	2	5	4	30.40	30.40	30.70	30.40	8.87	16.67	15.01	7.80	7.21
C	2	5	5	30.30	30.30	30.40	30.30	8.79	16.59	14.96	7.80	7.16

The specific gravity was calculated by dividing the measured dry mass of the sample by the weight of the submerged specimen. Subsequently, the density of the samples was determined by multiplying the specific gravity and the density of the water in which the specimen was submerged. Because the density of every substance depends on its temperature, the water temperature was monitored as described in ASTM. The water temperature measured 19.8° (67.6 °F) for this project, and hence, the distilled water had a density of 998.25 kg/m³ (62.319 lbs./ft³). Then, the volume of the submerged

rebar section was determined by dividing the dry mass of the sample by the density of the water. Afterwards, the volume of the rebar sample was divided by the average length of the sample to calculate the cross-sectional area. Finally, the diameter was calculated based on the assumption that the shape of the rebars was round.

A.2 Fiber Content Test

The relative amount of constituent materials were determined based on weight measurements after lost on ignition tests. The percentage of fiber content is listed in Table A.2 along with the relative resin and sand (surface coating) quantities.

c

Table A.2: Fiber content test results for each individual specimen

Specimen				Contents		
Manuf. Type	Lot No.	Size #	Spec No.	Fiber %	Resin %	Sand %
A	1	3	1	76.6	23.4	9.1
A	1	3	2	76.6	23.4	9.5
A	1	3	3	76.1	23.9	11.4
A	1	3	4	69.5	30.5	7.4
A	1	3	5	77.0	23.0	8.8
A	1	5	1	78.6	21.4	1.9
A	1	5	2	78.4	21.6	4.4
A	1	5	3	79.2	20.8	2.4
A	1	5	4	78.9	21.1	2.2
A	1	5	5	79.1	20.9	2.3
B	1	3	1	83.3	16.7	15.1
B	1	3	2	83.3	16.7	15.3
B	1	3	3	83.3	16.7	14.9
B	1	3	4	83.4	16.6	15.2
B	1	3	5	83.2	16.8	15.2
B	1	5	1	82.7	17.3	7.4
B	1	5	2	82.6	17.4	7.1
B	1	5	3	82.5	17.5	7.2
B	1	5	4	82.8	17.2	6.5
B	1	5	5	80.8	19.2	5.4
C	1	3	1	82.3	17.7	9.4
C	1	3	2	82.1	18.0	7.8
C	1	3	3	82.1	17.9	8.1
C	1	3	4	81.7	18.3	8.3
C	1	3	5	82.0	18.0	7.8
C	1	5	1	81.9	18.1	7.7
C	1	5	2	81.8	18.3	7.7
C	1	5	3	81.8	18.2	8.2

Continued on next page ...

Table A.2: Fiber content test results for each individual specimen

Specimen				Contents		
Manuf. Type	Lot No.	Size #	Spec No.	Fiber %	Resin %	Sand %
C	1	5	4	81.7	18.3	7.7
C	1	5	5	81.9	18.2	7.3
C	2	3	1	82.4	17.6	8.3
C	2	3	2	82.6	17.4	8.8
C	2	3	3	82.4	17.6	7.8
C	2	3	4	82.1	17.9	7.7
C	2	3	5	82.2	17.8	7.7
C	2	5	1	81.9	18.1	7.8
C	2	5	2	81.9	18.2	8.1
C	2	5	3	81.8	18.2	7.7
C	2	5	4	81.9	18.1	7.4
C	2	5	5	81.7	18.3	7.8

For rebar types that included sand as part of the surface enhancement, the weight of sand was subtracted before the fiber and resin content percentage were calculated to achieve comparable results throughout all tested rebar types, independent on the surface enhancement.

A.3 Transverse Shear Test

The following Table A.3 displays the most important measurements and results related to the transverse shear strength test for every individual rebar specimen.

Table A.3: Transverse shear test results (ultimate values) for each individual specimen

Specimen				Transverse		Displacement	
Manuf. Type	Lot No.	Size #	Spec No.	Shear Strength		at Shear Strength	
				ksi	MPa	in.	mm
A	1	3	1	29.77	205	0.115	2.92
A	1	3	2	33.01	228	0.085	2.16
A	1	3	3	29.07	200	0.110	2.79
A	1	3	4	31.87	220	0.107	2.72
A	1	3	5	33.22	229	0.110	2.80
A	1	5	1	26.95	186	0.198	5.04
A	1	5	2	26.73	184	0.172	4.38
A	1	5	3	26.38	182	0.287	7.29
A	1	5	4	25.68	177	0.182	4.62
A	1	5	5	26.84	185	0.185	4.69
B	1	3	1	35.58	245	0.097	2.46

Continued on next page ...

Table A.3: Transverse shear test results (ultimate values) for each individual specimen

Specimen				Transverse		Displacement	
Manuf.	Lot	Size	Spec	Shear Strength		at Shear Strength	
Type	No.	#	No.	ksi	MPa	in.	mm
B	1	3	2	33.26	229	0.099	2.51
B	1	3	3	33.26	229	0.099	2.51
B	1	3	4	35.78	247	0.095	2.42
B	1	3	5	34.52	238	0.099	2.51
B	1	5	1	31.13	215	0.124	3.14
B	1	5	2	32.85	226	0.126	3.19
B	1	5	3	30.79	212	0.116	2.96
B	1	5	4	31.50	217	0.118	2.99
B	1	5	5	32.17	222	0.124	3.14
C	1	3	1	34.08	235	0.125	3.17
C	1	3	2	35.39	244	0.114	2.91
C	1	3	3	33.59	232	0.121	3.07
C	1	3	4	37.47	258	0.130	3.31
C	1	3	5	36.79	254	0.127	3.22
C	1	3	6	33.87	234	0.132	3.36
C	2	3	1	36.95	255	0.103	2.61
C	2	3	2	36.74	253	0.107	2.72
C	2	3	3	39.82	275	0.129	3.27
C	2	3	4	38.35	264	0.118	2.99
C	2	3	5	36.49	252	0.113	2.86
C	2	5	1	36.17	249	0.120	3.04
C	2	5	2	37.99	262	0.132	3.35
C	2	5	3	36.71	253	0.119	3.03
C	2	5	4	35.29	243	0.128	3.26
C	2	5	5	36.26	250	0.134	3.40

The shear strength results (based on the nominal diameter) and the corresponding cross-head displacements — measured at the same moment at which the maximum test load was reached and recorded — are provided.

A.4 Horizontal Shear Test

Similar to the previous section, the following Table A.4 lists the maximum measured data for all specimens that were tested for horizontal shear strength.

Table A.4: Horizontal shear test results (ultimate values) for each individual specimen

Specimen				Horizontal		Displacement	
Manuf.	Lot	Size	Spec	Shear Strength		at Shear Strength	
Type	No.	#	No.	ksi	MPa	in.	mm
A	1	3	1	6.66	45.9	0.086	2.18
A	1	3	2	6.64	45.8	0.066	1.68
A	1	3	3	5.75	39.7	0.064	1.62
A	1	3	4	6.45	44.5	0.088	2.25
A	1	3	5	6.57	45.3	0.078	1.97
A	1	5	1	6.62	45.6	0.076	1.94
A	1	5	2	6.54	45.1	0.147	3.72
A	1	5	3	6.23	42.9	0.101	2.56
A	1	5	4	6.89	47.5	0.120	3.05
A	1	5	5	6.36	43.8	0.142	3.62
B	1	3	1	6.07	41.9	0.044	1.11
B	1	3	2	5.35	36.9	0.049	1.24
B	1	3	3	5.11	35.2	0.036	0.90
B	1	3	4	5.49	37.9	0.049	1.25
B	1	3	5	5.81	40.0	0.055	1.39
B	1	5	1	6.91	47.7	0.104	2.65
B	1	5	2	4.98	34.4	0.094	2.38
B	1	5	3	7.00	48.2	0.095	2.42
B	1	5	4	6.81	47.0	0.116	2.95
B	1	5	5	7.49	51.6	0.110	2.78
C	1	3	1	6.70	46.2	0.098	2.48
C	1	3	2	7.15	49.3	0.067	1.69
C	1	3	3	6.38	44.0	0.063	1.59
C	1	3	4	7.52	51.9	0.098	2.48
C	1	3	5	7.29	50.2	0.082	2.08
C	1	5	1	6.35	43.8	0.092	2.35
C	1	5	2	6.82	47.0	0.112	2.84
C	1	5	3	6.78	46.7	0.116	2.96
C	1	5	4	6.52	44.9	0.101	2.58
C	1	5	5	5.56	38.3	0.084	2.14
C	2	3	1	6.20	42.8	0.128	3.24
C	2	3	2	6.62	45.7	0.071	1.80
C	2	3	3	6.66	45.9	0.113	2.87
C	2	3	4	6.45	44.5	0.072	1.82
C	2	3	5	6.48	44.7	0.100	2.53
C	2	5	1	6.36	43.8	0.121	3.06
C	2	5	2	6.18	42.6	0.113	2.87
C	2	5	3	6.62	45.6	0.132	3.35
C	2	5	4	6.82	47.0	0.108	2.74
C	2	5	5	6.04	41.6	0.091	2.31

The given strength values were determined based on the measured maximum loads and the nominal (not measured) cross-sectional dimensions. The displacement at shear strength represents the cross-head extension that was measured at the instant in time at which the maximum failure load was

recorded. Accordingly, this value is indicative of the ultimate defection of the shear specimen that lead to resin failure and slip between the fibers.

A.5 Tensile Test

The longitudinal tensile properties for all tested specimens are listed in Table A.5.

Table A.5: Tensile strength test results (ultimate values) for each individual specimen

Manuf. Type	Specimen			Tensile		Elastic	
	Lot	Size	Spec	Strength		Modulus	
	No.	#	No.	ksi	MPa	ksi	GPa
A	1	3	1	122	844	5760	39.72
A	1	3	2	120	828	6996	48.24
A	1	3	3	119	819	6917	47.69
A	1	3	4	128	883	6812	46.72
A	1	3	5	119	822	7735	53.33
A	1	5	1	128	881	7800	53.78
A	1	5	2	132	908	7645	52.71
A	1	5	3	138	949	7692	53.04
A	1	5	4	136	938	7639	52.67
A	1	5	5	138	951	7990	55.09
B	1	3	1	189	1302	7735	53.33
B	1	3	2	199	1371	7928	54.66
B	1	3	3	198	1365	7542	52.00
B	1	3	4	197	1361	7837	54.03
B	1	3	5	198	1367	7999	55.15
B	1	5	1	176	1211	7868	54.25
B	1	5	2	162	1116	7819	53.91
B	1	5	3	178	1226	8301	57.23
B	1	5	4	183	1263	7837	54.03
B	1	5	5	164	1131	7907	54.52
C	1	3	1	189	1306	7630	52.61
C	1	3	2	187	1290	7659	52.81
C	1	3	3	180	1238	7535	51.95
C	1	3	4	178	1229	5385	37.13
C	1	3	5	185	1276	7559	52.12
C	1	5	1	172	1184	4126	28.45
C	1	5	2	160	1107	6834	53.45
C	1	5	3	169	1168	7933	54.70
C	1	5	4	165	1137	6534	45.05
C	1	5	5	140	962	7739	53.36
C	2	3	1	171	1178	6990	48.19
C	2	3	2	170	1175	7509	51.78
C	2	3	3	168	1159	6531	45.03
C	2	3	4	175	1207	7881	54.34
C	2	3	5	161	1112	7088	48.87

Continued on next page ...

Table A.5: Tensile strength test results (ultimate values) for each individual specimen

Specimen				Tensile		Elastic	
Manuf.	Lot	Size	Spec	Strength		Modulus	
Type	No.	#	No.	ksi	MPa	ksi	GPa
C	2	5	1	153	1058	8138	56.11
C	2	5	2	146	1006	7242	49.93
C	2	5	3	145	1001	7404	51.05
C	2	5	4	150	1037	7065	48.71
C	2	5	5	144	992	7549	52.05

Specifically, the table presents the maximum tensile stresses and the corresponding elastic moduli, both based on the nominal cross-sectional dimensions.

A.6 Bond-to-Concrete Test

The individual measured bond strength test results are listed in Table A.6 to report both the bond stresses and the rebar bond slippage for each specimen.

Table A.6: Bond-to-Concrete strength test results for each individual specimen (Imperial Units)

Specimen				Bond Stress			Bond Slippage		
Manuf. Type	Lot No.	Size #	Spec No.	at Specific Slippage			Ult. ksi	at Maximum Stress	
				$\frac{2}{1000}$ in. ksi	$\frac{4}{1000}$ in. ksi	$\frac{1}{100}$ in. ksi		Free End in.	Load End in.
A	1	3	1	1.55	1.93	2.54	3.56	0.059	0.080
A	1	3	2	1.31	1.87	3.30	4.07	0.022	0.070
A	1	3	3	1.68	2.12	2.90	3.95	0.060	0.085
A	1	3	4	0.94	1.39	2.01	3.20	0.100	0.123
A	1	3	5	2.21	2.50	3.01	4.08	0.067	0.082
A	1	5	1	1.01	1.71	2.62	3.89	0.054	0.074
A	1	5	2	0.36	0.70	1.55	3.59	0.097	0.119
A	1	5	3	1.24	1.75	2.73	4.16	0.070	0.092
A	1	5	4	0.82	1.37	2.13	3.89	0.105	0.110
A	1	5	5	0.82	1.22	1.83	3.33	0.083	0.106
B	1	3	1	1.60	1.94	2.35	2.39	0.015	0.020
B	1	3	2	1.42	1.77	2.60	2.80	0.017	0.023
B	1	3	3	2.45	2.79	3.03	3.05	0.013	0.018
B	1	3	4	1.96	2.28	2.66	2.67	0.010	0.017
B	1	3	5	1.81	2.26	2.86	3.03	0.018	0.021
B	1	5	1	2.01	2.54	2.83	2.85	0.014	0.026

Continued on next page . . .

Table A.6: Bond-to-Concrete strength test results for each individual specimen (Imperial Units)

Specimen				Bond Stress				Bond Slippage	
Manuf. Type	Lot No.	Size #	Spec No.	at Specific Slippage			Ult. ksi	at Maximum Stress	
				$\frac{2}{1000}$ in. ksi	$\frac{4}{1000}$ in. ksi	$\frac{1}{100}$ in. ksi		Free End in.	Load End in.
B	1	5	2	2.14	2.49	2.80	2.81	0.012	0.024
B	1	5	3	1.98	2.37	2.79	2.88	0.017	0.027
B	1	5	4	2.21	2.66	2.89	2.90	0.013	0.023
B	1	5	5	2.29	2.66	2.94	2.95	0.012	0.035
C	1	3	1	2.06	2.28	2.42	2.43	0.009	0.016
C	1	3	2	1.90	2.22	2.34	2.35	0.008	0.011
C	1	3	3	2.04	2.28	2.38	2.39	0.009	0.016
C	1	3	4	1.62	2.21	2.27	2.27	0.008	0.013
C	1	3	5	1.49	1.89	2.23	2.24	0.010	0.012
C	1	5	1	2.43	2.78	3.00	3.01	0.011	0.038
C	1	5	2	2.30	2.59	2.94	2.96	0.011	0.027
C	1	5	3	2.30	2.59	2.95	2.98	0.013	0.030
C	1	5	4	2.29	2.71	2.96	2.97	0.012	0.028
C	1	5	5	2.18	2.45	2.84	2.89	0.015	0.024

Because ACI 440.3R suggests documenting the slippage behavior through the bond stress measurements at specific rebar slip instances, the table presents not just the ultimate bond stress (strength) but also the bond stresses that corresponded to slip values of $\frac{2}{1000}$ in., $\frac{4}{1000}$ in., and $\frac{1}{100}$ in. For clarity, the table lists all results in imperial units only.

Similar to the previous table, Table A.7 documents the bond-to-concrete measurement results for all tested specimens per ASTM requirements.

Table A.7: Bond-to-Concrete strength test results for each individual specimen (Metric Units)

Specimen				Bond Stress				Bond Slippage	
Manuf. Type	Lot No.	Size #	Spec No.	at Specific Slippage			Ult. MPa	at Maximum Stress	
				$\frac{5}{100}$ mm MPa	$\frac{1}{10}$ mm MPa	$\frac{1}{4}$ mm MPa		Free End mm	Load End mm
A	1	3	1	10.7	13.3	17.5	24.5	1.49	2.02
A	1	3	2	9.1	12.9	22.8	28.0	0.56	1.77
A	1	3	3	11.6	14.6	20.0	27.2	1.53	2.16
A	1	3	4	6.5	9.6	13.9	22.1	2.54	3.13
A	1	3	5	15.3	17.3	20.7	28.2	1.69	2.09
A	1	5	1	6.9	11.8	18.0	26.8	1.38	1.89
A	1	5	2	2.5	4.8	10.7	24.7	2.48	3.02

Continued on next page ...

Table A.7: Bond-to-Concrete strength test results for each individual specimen (Metric Units)

Specimen				Bond Stress			Bond Slippage		
Manuf. Type	Lot No.	Size #	Spec No.	at Specific Slippage			Ult. MPa	at Maximum Stress	
				$\frac{5}{100}$ mm MPa	$\frac{1}{10}$ mm MPa	$\frac{1}{4}$ mm MPa		Free End mm	Load End mm
A	1	5	3	8.6	12.1	18.8	28.7	1.78	2.34
A	1	5	4	5.7	9.4	14.7	26.9	2.67	2.79
A	1	5	5	5.6	8.4	12.6	23.0	2.11	2.70
B	1	3	1	11.0	13.4	16.2	16.5	0.37	0.50
B	1	3	2	9.8	12.2	17.9	19.3	0.42	0.58
B	1	3	3	16.9	19.3	20.9	21.0	0.32	0.45
B	1	3	4	13.5	15.7	18.4	18.4	0.25	0.44
B	1	3	5	12.5	15.6	19.7	20.9	0.45	0.54
B	1	5	1	13.9	17.5	19.5	19.7	0.36	0.65
B	1	5	2	14.7	17.2	19.3	19.4	0.31	0.62
B	1	5	3	13.7	16.4	19.3	19.9	0.43	0.68
B	1	5	4	15.2	18.3	19.9	20.0	0.32	0.59
B	1	5	5	15.8	18.4	20.3	20.4	0.30	0.88
C	1	3	1	14.2	15.7	16.7	16.7	0.24	0.40
C	1	3	2	13.1	15.3	16.1	16.2	0.20	0.29
C	1	3	3	14.0	15.7	16.4	16.4	0.24	0.40
C	1	3	4	11.2	15.2	15.6	15.7	0.21	0.32
C	1	3	5	10.3	13.1	15.4	15.4	0.24	0.30
C	1	5	1	16.8	19.2	20.7	20.8	0.28	0.96
C	1	5	2	15.8	17.9	20.2	20.4	0.28	0.68
C	1	5	3	15.9	17.8	20.3	20.5	0.34	0.75
C	1	5	4	15.8	18.7	20.4	20.5	0.29	0.71
C	1	5	5	15.1	16.9	19.6	19.9	0.37	0.62

However, other than the previous table, Table A.7 offers the test results in metric units. Accordingly, the relevant bond stresses are tabulated for measurements corresponding to 0.05 mm, 0.10 mm, and 0.25 mm of rebar slip.

Appendix B

BDV34-986-02 Final Report – “Instrumentation and Monitoring of FRP bars in Bridge Deck Link-Slab”

(93 pages)

Project Title: “**Instrumentation and Monitoring of FRP bars in Bridge Deck Link-Slab for FPID 435390-1-52-01**”

Contract Number: BDV34 986-02

Final Report

Submitted by:

<p>Adel ElSafty, Principal Investigator University of North Florida School of Engineering 1 UNF Drive, Jacksonville, FL 32224-2645 Email Address: adel.el-safty@unf.edu Phone Number: (904) 620-1398</p>	<p>James Fletcher, Co-Investigator University of North Florida School of Engineering 1 UNF Drive, Jacksonville, FL 32224-2645 Email Address: jfletche@unf.edu Phone Number: (904) 620-1844</p>
<p>Thomas Fowler Undergraduate Engineering Student University of North Florida School of Engineering 1 UNF Drive, Jacksonville, FL 32224-2645 Email Address: n00880684@unf.edu</p>	<p>Dylan Jones Undergraduate Engineering Student University of North Florida School of Engineering 1 UNF Drive, Jacksonville, FL 32224-2645 Email Address: n01180016@unf.edu</p>

Submitted to: **Steven Nolan**, Project Manager
The Florida Department of Transportation
State Structures Design Office
605 Suwannee Street, MS 33
Tallahassee, FL 32399-0450
Email Address: Steven.Nolan@dot.state.fl.us
Phone: (850) 414-4272

Dr. Cheresa Y. Boston, Director of Sponsored Research
University of North Florida
Office of Research and Sponsored Programs
1 UNF Drive, Jacksonville, Florida 32224
Email: cheresa.boston@unf.edu
Phone: (904) 620-2455, Fax: (904) 620-2457

September 29, 2021

DISCLAIMER

The opinions, findings, and conclusions expressed in the publication are those of the authors and not necessary those of the State of Florida Department of Transportation.

0.1 Metric Conversion Table

Approximate Conversions to SI Units				
Symbol	Known	Conversion Factor	Find	Symbol
Length				
in	inches	25.4	millimeters	mm
ft	feet	0.305	meters	m
yd	yards	0.914	meters	m
Area				
in ²	square inches	645.2	square millimeters	mm ²
ft ²	square feet	0.093	square meters	m ²
yd ²	square yard	0.836	square meters	m ²
Volume				
ft ³	cubic feet	0.028	cubic meters	m ³
yd ³	cubic yards	0.765	cubic meters	m ³
gal	gallons	3.785	Liters	L
Mass				
oz	ounces	28.35	grams	g
lb	pounds	0.454	kilograms	kg
Temperature				
°F	Fahrenheit	5(F-32)/9 or (F-32)/1.8	Celsius	°C
Force and Pressure or Stress				
lbf	poundforce	4.45	Newtons	N
lb/in ²	poundforce/square inch	6.89	kilopascals	kPa
Illumination				
fc	foot-candles	10.76	Lux	lx
fl	foot-Lamberts	3.426	candela/m ²	cd/m ²
Approximate Conversions from SI Unites				
Symbol	Known	Conversion Factor	Find	Symbol
Length				
mm	millimeters	0.039	inches	in
m	meters	3.28	Feet	ft
m	meters	1.09	yards	yd
Area				
mm ²	square millimeters	0.0016	square inches	in ²
m ²	square meters	10.764	square feet	ft ²
m ²	square meters	1.195	square yard	yd ²
Volume				
m ³	cubic meters	35.314	cubic feet	ft ³
m ³	cubic meters	1.307	cubic yards	yd ³
L	liters	0.264	gallons	gal
Mass				
g	grams	0.035	ounces	oz
kg	kilograms	2.202	pounds	lb
Temperature				
°C	Celsius	1.8C+32	Fahrenheit	°F
Force and Pressure or Stress				
N	Newtons	2.225	poundforce	lbf
kPa	kilopascals	0.145	poundforce/square inch	lb/in ²
Illumination				
lx	lux	0.0929	foot-candles	fc
cd/m ²	candela/m ²	0.2919	foot-Lamberts	fl

0.2 Technical Report Documentation Page

1. Report No.	2. Government Accession No.	3. Recipient's Catalog No.	
4. Title and Subtitle BRIDGE DECK WITH LINK-SLAB For FPID: 435390-1-52-01: US 41 from Midway Blvd to Enterprise		5. Report Date	
		6. Performing Organization Code	
7. Author(s) Adel ElSafty and James Fletcher		8. Performing Organization Report No.	
9. Performing Organization Name and Address University of North Florida 1 UNF Drive Jacksonville, FL 32224		10. Work Unit No. (TRAVIS)	
		11. Contract or Grant No. BDV34 986-02	
12. Sponsoring Agency Name and Address		13. Type of Report and Period Covered Final Report	
		14. Sponsoring Agency Code	
15. Supplementary Notes			
16. Abstract The goal of the project is to investigate and monitor the performance of the link-slab that is reinforced with Basalt Fiber Reinforced Polymers bars, BFRP-RC. The research also provided recommendations for the instrumentation of the link-slabs, a suggested monitoring plan, and an instrumentation system to monitor the temperature, strain, and elongation of link-slabs. The research also installed the instrumentation to monitor the link-slab during concrete casting and after casting. The research team started measuring and monitoring the strains, deformations, and cracks in the link-slab. The team also investigated the performance of the link-slab, evaluated the data from installed instrumentation, analyzed the results, and provided conclusions. The strains experienced by the sensors indicated small strain levels compared to the BFRP ultimate strain levels. In addition to live load flexural effects, this type of thermal cycling could contribute to the concrete cracking over time in the link-slab if tension stresses build-up due to global shrinkage and creep restraint of the connected FSB spans. However, after about 90 days over the time of monitoring, the average strain in the mid-joint gauges did not change significantly indicating minimal creep and or shrinkage restraint was experienced to date by the link-slab since the initial casting date. The strains experienced by the sensors indicated small strain levels compared to the BFRP ultimate strain levels. The maximum daily strain change due to thermal effects is about 500 microstrain.			
17. Key Word		18. Distribution Statement	
19. Security Classif. (of this report) Unclassified	20. Security Classif. (of this page) Unclassified	21. No. of Pages	22. Price

0.3 Executive Summary

Bridge deck joints are costly to buy, install, and maintain; providing severe performance and maintenance problems. One of the solutions is to adopt jointless bridges and eliminate expansion joints in bridge decks. That has been an effective method of constructing bridges. It corresponds to reduced maintenance and improved bridge-deck life expectancy. Using a link-slab and making the bridge girders (partially continuous) continuous only for lateral and longitudinal load effects, provides lower cost, improved durability, longer spans, improved seismic performance, better resistance to wind loads and storm wave loads, improved structural integrity, and improved riding quality. There is a need for simple guidelines for design and detailing of the popular connection system for jointless bridge using a deck link-slab, that is continuous for lateral and longitudinal load effects, but not for vertical live load effects.

The aim of this research is to investigate the performance of the link-slab using BFRP-RC. In specific, the overall goal of the project is to investigate and monitor the performance of the link-slab that is reinforced with BFRP-RC on Bridge No. 019003 over Morning Star Waterway. The team investigated the feasibility of an innovative system for reducing or eliminating the number of bridge deck joints using link-slab. The research also provided recommendations for the instrumentation of the link-slab, a suggested monitoring plan, and an instrumentation system to monitor the temperature, strain, and elongation of link-slabs. The research also installed the instrumentation to monitor the link-slab during concrete casting and after casting. The research team started measuring and monitoring the strains, deformations, and cracks in the link-slab. The team also investigated the performance of the link-slab, evaluated the data from installed instrumentation, analyzed the results, and provided conclusions.

The research team investigated the concrete simple-span beams that are made continuous by pouring a continuity link-slab between the beam ends. The bridge has been instrumented with embedded and surface-mounted sensors and has been monitored to evaluate the performance of the new link-slab. Several types of sensors were used, and a data acquisition system recorded strains/deformations at a regular time interval. The preferred sensor types for this application are vibrating wire sensors with integrated thermistors (per FDOT request). The sensors were strategically located on both sides of the midline of the link slab to capture strains in the BFRP bars, strains in the concrete link-slab, and the gap between adjacent beams' ends.

All measurements have been corrected for temperature changes per recommendations of the gauge manufacturer. Data has been collected during service over two periods of approximately 3 months each. The data acquisition system has been able to keep record of strains developed in the BFRP reinforcement. The strains experienced by the sensors indicated small strain levels compared to the BFRP ultimate strain levels. In addition to live load flexural effects, this type of thermal cycling could contribute to the concrete cracking over time in the link-slab if tension stresses build-up due to global shrinkage and creep restraint of the connected FSB spans. However, after about 90 days over the time of monitoring, the average strain in the mid-joint gauges did not change significantly indicating minimal creep and or shrinkage restraint was experienced to date by the link-slab since the initial casting date. The strains

experienced by the sensors indicated small strain levels compared to the BFRP ultimate strain levels. The maximum daily strain change due to thermal effects is about 500 microstrain.

0.4 Contents

0.1	Metric Conversion Table	3
0.2	Technical Report Documentation Page.....	4
0.3	Executive Summary	5
0.4	Contents	7
0.5	List of Figures	8
0.6	List of Tables	9
1	Introduction	10
1.1	Background Statement	10
1.2	Research Approach	12
1.3	Literature Review.....	12
2	Instrumentation	13
2.1	Embedded sensors.....	13
2.1.1	Sensor Wiring and Cables:.....	20
2.1.2	Cable Routing	21
2.2	Data Acquisition	21
2.3	Sensor setup	24
3	Data Reduction	28
3.1	Data reduction for Strandmeters	28
3.2	Data reduction for Sisterbars.....	29
4	Results and Data Analysis	30
4.1	Amendments to the dataset	30
4.2	Graphs of reduced data	30
4.3	Samples of reduced data	35
4.4	Results and Analysis	36
5	Evaluation of FDOT Link-Slab Details	37
6	Summary	38
7	References	39
8	Appendix A Images and Illustrations of The Bridge and Sensor Layout	42
9	Appendix B Sensor Layout and Information	46
10	Appendix C Manufacturer’s instrument datasheets	51
11	Appendix D Literature Review	61
12	Appendix E Annotated Plans Details For Link-Slab MONITORING PROJECT BDV34 986-02	87

0.5 List of Figures

Figure 1.1: Link Slab Option	11
Figure 2.1: Location of embedded sensor array, top view	15
Figure 2.2: Schematic of Standmeter (Red) and Sisterbar (Green & Blue) placement	15
Figure 2.3: Link slab reinforcement and embedded sensors	16
Figure 2.4: Link-slab photos prior to setting reinforcement.....	17
Figure 2.5: Finished link slab and close up view	17
Figure 2.6: Data acquisition modules and wiring	18
Figure 2.7: Vandalized surface mounted crackmeters	18
Figure 2.8: Southwest outboard EDTs.....	19
Figure 2.9: External displacement transducers	19
Figure 2.10: Cable routing through EPS.....	21
Figure 2.11: Detail of embedded sensor routing, side view.....	21
Figure 2.12: Details of embedded sensors and wiring, top view	23
Figure 2.13: Sensor setup in LogView software.....	27
Figure 4.1: Graphed deformation from Strandmeters	31
Figure 4.2: Graphed strain from Strandmeters.....	32
Figure 4.3: Graphed load related strain from Sisterbars	33
Figure 4.4: Graphed actual strain from Sisterbars	34

0.6 List of Tables

Table 1: List of Geokon sensors serial numbers	23
Table 2: First 20 data points of Strandmeter deformation	35
Table 3: First 20 data points of Strandmeter microstrain.....	35
Table 4: First 20 data points of load related microstrain from Sisterbars	36
Table 5: First 20 data points of actual microstrain from Sisterbars	36

1 Introduction

1.1 Background Statement

Bridge deck expansion joints are costly to buy, install, and maintain. They have provided severe performance and maintenance problems as water and deck drainage contaminated with chemicals leak through the superstructure and onto the pier caps below, thus damaging or eventually compromising some vital parts of bridges such as prestressing cable anchorage systems, beams, bearings, substructure seat areas, and end diaphragms. Also, debris accumulation in the joints may restrain deck expansion (ElSafty 1994).

One of the proposed solutions is to adopt jointless bridges and eliminate expansion joints in bridge decks. This has been an effective method of constructing bridges in many states. It corresponds to reduced maintenance and improved bridge-deck life expectancy. It is possible to replace bearing devices with simple elastomeric pads, or totally integrate the superstructure with the supports. With the use of jointless bridge decks, there are no joints to purchase and reduced bearing maintenance, the riding surface is smoother, the initial and life-cycle cost are lower, and there may be some reduction in span bending moments and deflections, but this is not considered in the design. In conclusion, using a link-slab and making the bridge girders (partially continuous) continuous provides lower cost, improved durability, longer spans, improved seismic performance, better resistance to wind loads and storm wave loads, improved structural integrity, and improved riding quality. Current consensus seems to allow elimination of expansion joints on bridges as long as 650 feet. Much longer bridges have occasionally been constructed without reported distress. There is a need for simple guidelines for design and detailing of the popular connection system. An option for jointless bridge deck link-slab is shown in Fig. 1. A brief literature review of link-slab is provided in Appendix D.

The aim of this research is to investigate the performance of the link-slab using Basalt Fiber-Reinforced Polymer (BFRP) reinforcing bars in a Reinforced Concrete (RC) deck (structural overlay) on the Florida Slab Beams (FSB) for a two-span pedestrian bridge along US-41 over Morningstar Waterway. Details of the bridge link-slab are provided in Appendix E. The team evaluated the data from installed instrumentation, analyzed the results, and provided conclusions.

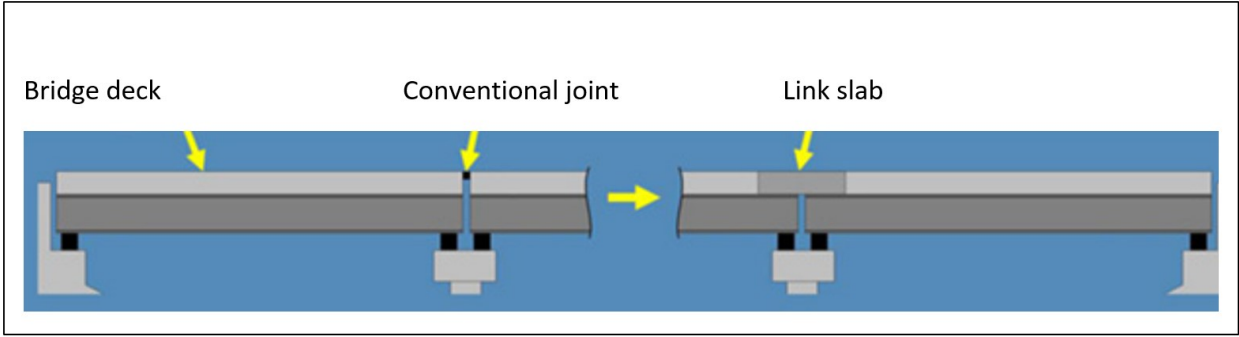


Figure 1.1: Link Slab Option

1.2 Research Approach

The methodology for addressing the problem was to break down the solution process into four tasks (deliverables) – (1) literature review, (2) recommendations on instrumentation and monitoring of the link slab, (3) installing instrumentation and monitoring the link slab after casting, (4) and evaluate the data from the instrumentation within the link slab.

The purpose of the literature review was to further investigate the feasibility of an innovative system for reducing or eliminating the number of bridge deck joints.

The purpose of the second task was to provide recommendations for the instrumentation of the link-slabs, a suggested monitoring plan, and an instrumentation system to monitor the temperature, strain, rotation, and elongation of different link-slabs.

The purpose of the third task was to install the instrumentation to monitor the FDOT designed link-slab during concrete casting and periodically for the following 90 days. For the investigated bridge link-slab, the research team started measuring and monitoring the strains, deformations, and cracks in the link-slab. Due to project delays a second period of monitoring for 75 days was possible.

The purpose of the fourth task was to investigate the performance of the link-slab. The data from the instrumentation was evaluated and provided enough information to draw preliminary conclusions.

The overall goal of the project is to investigate and monitor the performance of the link-slab that is reinforced with BFRP-RC on Bridge No. 019003 over Morning Star Waterway.

1.3 Literature Review

A literature review has been conducted on the link-slab and jointless bridge decks. The literature review is presented in Appendix D.

2 Instrumentation

The research team developed a monitoring plan and instrumentation system to monitor the temperature, strain, and elongation of link-slabs. The team investigated the concrete simple-span beams that are made continuous by pouring a continuity link-slab between the beam ends. The bridge has been instrumented with embedded and surface-mounted sensors and has been monitored to evaluate the performance of the new link-slab. Several types of sensors were used, and a data acquisition system recorded strains/deformations at a regular time interval. The preferred sensor types for this application are vibrating wire sensors with integrated thermistors (per FDOT request). The sensors were strategically located on both sides of the midline of the link slab to capture strains in the BFRP bars, strains in the concrete link-slab, and the gap between adjacent beams' ends.

The bridge link-slab monitoring system included sensors, data acquisition system, cabling and conduit. The system installation activities were coordinated between involved parties (FDOT technical team, Contractor and other subcontractors, the project manager, and the research team) to establish the installation schedule and implementation of both the embedded and surface-mounted sensors. The monitoring system including sensors were installed in coordination with the construction contractor and the FDOT representatives.

All measurements have been corrected for temperature changes per recommendations of the gauge manufacturer. Data has been collected periodically during service. Substantial delays occurred in data retrieval due to COVID-19 travel restrictions. As such, two periods (4.5 and 3.5 months) of monitoring data were available over a span of approximately one-year. The data acquisition system has been able to keep record of strains developed in the BFRP reinforcement.

2.1 Embedded sensors

The embedded sensors are for measuring strains within and across the link-slab. This was composed of a 3x3 array of Strandmeters and Sister bar paired to each other, for a total of 18 (9 pairs) embedded sensors. The Strandmeter measures deformation/strains in the BFRP link-slab reinforcement (Geokon model 4410 Strandmeter). The adjacent "Sister bar" (Geokon model 4911 Rebar Strainmeter) measures strain in the link-slab concrete at approximately the same location. It is recommended by BDI Inc. that the sister bar be tied off to its paired strandmeter via loose wire during installation.

Placement of the 3x3 array is a roughly symmetrical location of the 9 pairs of embedded sensors. From the southwest side of the bridge the first three pairs of sensors (labeled as row "A") were located on the fourth BFRP rebar from the southwest side of the link-slab. The second row of three sensor pairs (labeled as row "B") is located on the twelfth BFRP rebar from the

southwest side of the link-slab. The third row of three sensor pairs (labeled as row “C”) is located on the twenty-first BFRP rebar from the southwest side of the link slab. Each pair of sensors in a row is identified by its relative compass position. For example, the northernmost pair of embedded sensors is identified as the “NW-C” location (northwest side, row-C) and the other two pairs within that row are in the “Mid-C” and “SE-C” locations. This layout is shown in the following, Figure 2.1, Location of Embedded Sensor Array, Top View. Note the orientation of a Sister bar relative to its corresponding BFRP rebar is always toward the centerline of the bridge, while the accompanying strandmeter sits sets on the opposite side of the BFRP rebar.

The sensors were installed on 3/7/2020. The first set of data was recovered on 11/14/20 which contained data from 3/7/2020 to 8/2/2020. The second set of data was recovered on 2/28/20 which contained data from 11/14/2020 to 2/28/2021. Data was recorded once every hour.

Strandmeter (model 4410, Geokon): These deformation/strain sensors were clamped to the link-slab longitudinal reinforcement (BFRP rebars inside cast-in-place link-slab) at the specified locations. Special treatment per the product manual dictates surrounding sensor with grease prior to encasing inside concrete. BDI advised that the strandmeter sensor (model 4410) is preferable in this application because it is readily attached to a rounded surface (i.e. the reinforcement bars) and is more appropriate for embedment in concrete than the model 4151 alternative. ***Number of sensors: 9***

Sisterbar (model 4911, Geokon): These strain sensors are fabricated on a #4 epoxy-coated steel reinforcing bar. The standard stock length is 36 inches. For this link-slab, all the sisterbars had an overall length of 31 inches, with the transducer centered on the sensor. The sisterbar sensors were ordered from Geokon or BDI Inc. already custom cut to this length. One sisterbar is paired with each strandmeter (BFRP gauge) and placed adjacent to it in order to measure strain in the concrete surrounding reinforcement bars. The team followed the BDI suggestion to loosely tying each sisterbar adjacent to its accompanying strandmeter-mounted reinforcement bar with wire using the transverse link-slab reinforcing. ***Number of sensors: 9***

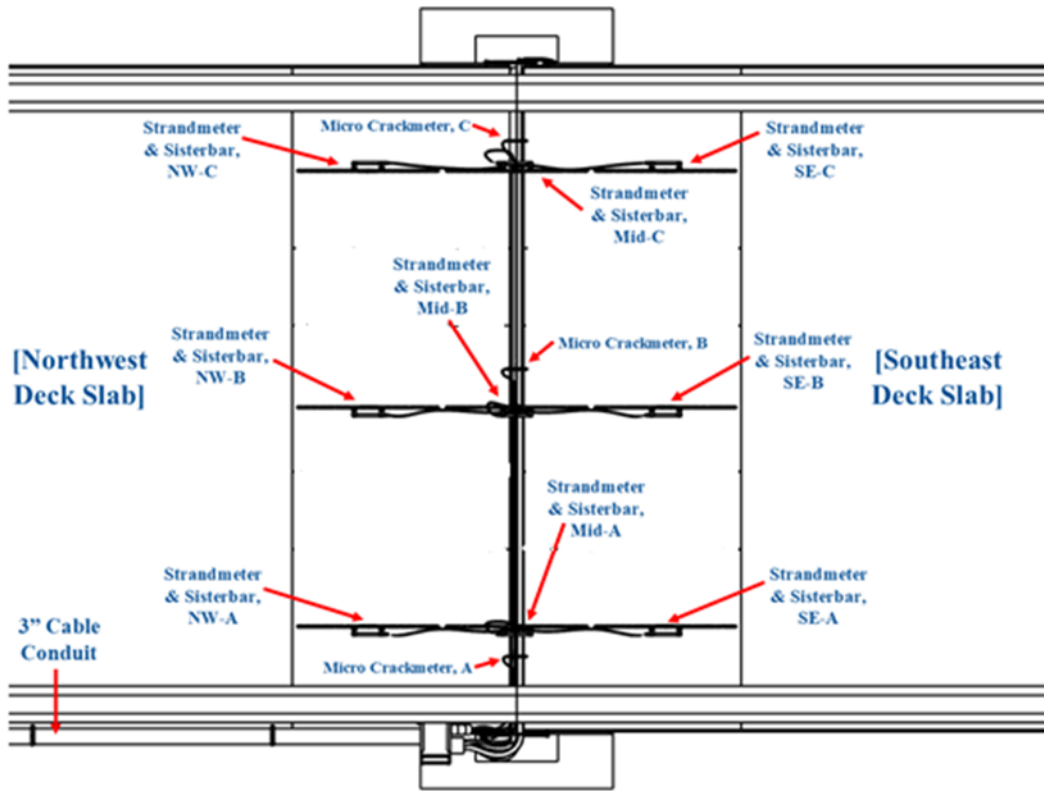


Figure 2.1: Location of embedded sensor array, top view

Figures 2.2 – 2.9 show the sensors installed in the link slab:

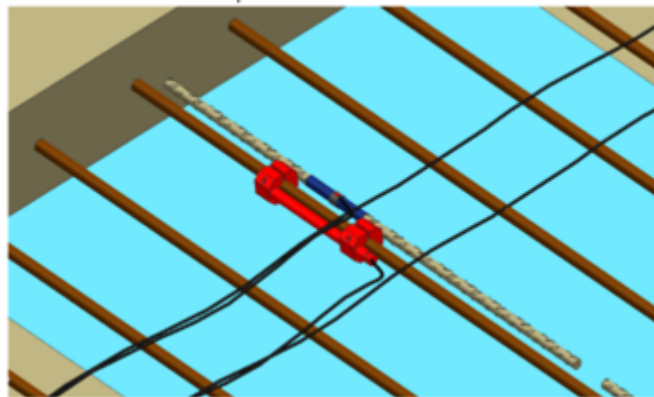


Figure 2.2: Schematic of Strandmeter (Red) and Sisterbar (Green & Blue) placement



Figure 2.3: Link slab reinforcement and embedded sensors



Figure 2.4: Link-slab photos prior to setting reinforcement



Figure 2.5: Finished link slab and close up view



Figure 2.6: Data acquisition modules and wiring



Figure 2.7: Vandalized surface mounted crackmeters

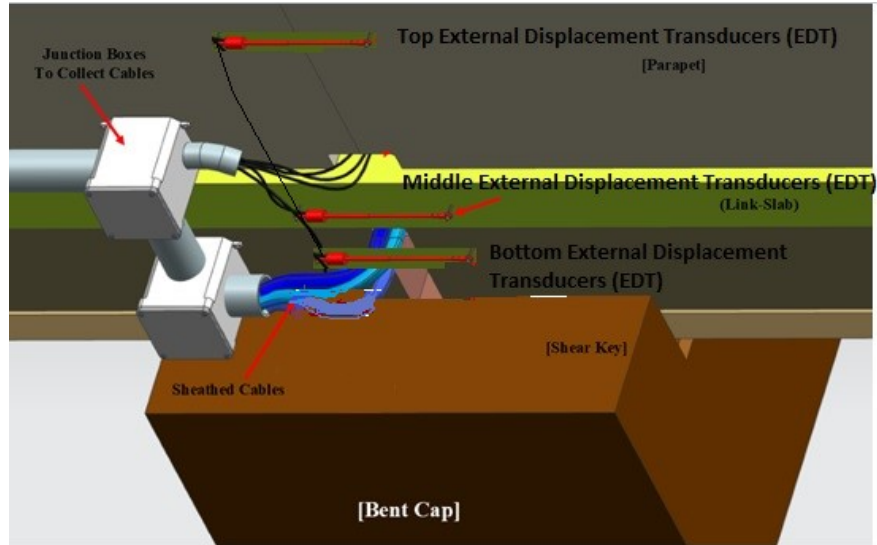


Figure 2.8: Southwest outboard EDTs



Figure 2.9: External displacement transducers

2.1.1 Sensor Wiring and Cables:

Connections between the sensors and data acquisition system is accomplished via a “Vibrating Wire” cable (abbreviated as VW cable). VW cable consists of five conducting elements: 2 twisted wire pairs (red/black & white/green), and a 24AWG stranded copper wire for grounding. A 0.0625-inch diameter blue PVC jacket protects the cable.

All cables were intended to be routed through a PVC conduit pipe from the dataloggers toward the northeast side of the link-slab, however, due to construction delays they are externally mounted on the southwest side of the link-slab. From this point, cables diverged in bundles to their respective sensor locations. Most of these cables partly or fully crossed beneath the transverse midline of the link-slab and do so within channels of the Expanded Poly-Styrene Gap Filler (EPS Gap Filler) between the northwest and southeast FSBs and Deck Slabs. Cables of the 3x3 Embedded Sensor Array were routed along their respective BFRP rebar toward the transverse midline of the link-slab, held close and securely to the rebar with zip-ties. At the midline, these cables exited through the link-slab bottom into channels at the top of the EPS Gap Filler.

Sensors were delivered with pre-attached heavy-duty VW cables. Special care was taken to protect the cables, especially at exit points for embedded sensors’ cables and around sharp edges. Protective containers were provided at exit points with enough room to store cable ends for protection against damage and accidental cutting during concrete casting and curing. High quality cable tags were used at multiple points along each cable in order to positively identify each cable and its associated sensor.

Cables running from the surface mounted Micro Crackmeters (Group #3) were held down with cable clips screwed down onto the link-slab. Unfortunately, these Micro Crackmeters were vandalized and damaged before any useful data could be retrieved.

2.1.2 Cable Routing

All cables were led from the dataloggers at the Southeast side of the link-slab. Three VW cables lead directly to the Outboard EDTs. 18 VW cables lead to the embedded Strandmeters and Sisterbars.

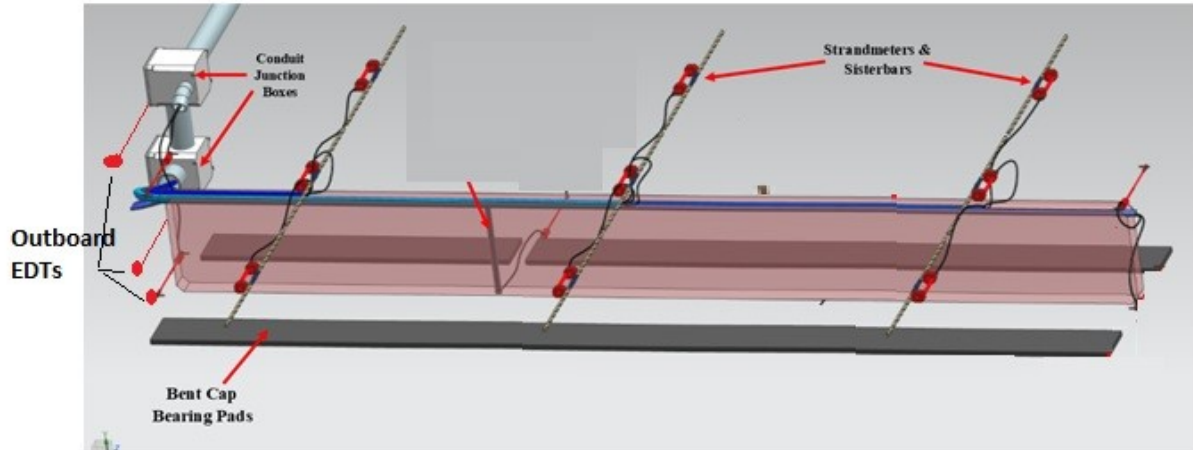


Figure 2.10: Cable routing through EPS

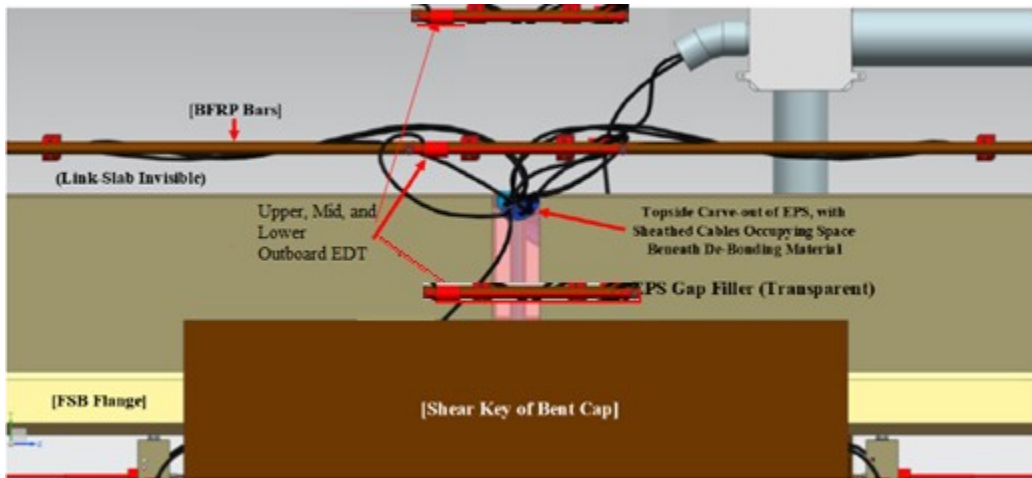


Figure 2.11: Detail of embedded sensor routing, side view

2.2 Data Acquisition

Data acquisition was accomplished by two Geokon brand, model 8002-16-1 dataloggers, also referred to as LC-2x16 datalogger units (also abbreviated as LC-2). Each of these units is capable of monitoring input from up to 16 VW cables for a total of 32 possible inputs, of which only 29 are planned for use. Storage capacity of the dataloggers is 320 KB of EEPROM type memory (data not lost upon de-energizing system), which provides storage for up to 3,555 readings from all 32 possible VW inputs. At an instrument reading rate of once per hour, this

provides a maximum window of 148 days or approximately 5 months to retrieve data before capacity is reached and data points are compromised. Datalogger internal power is supplied by either four alkaline D-cell batteries or a 12-volt external grid supply. Recorded sensor data was accessed by direct retrieval on a periodic basis. Interfacing with the LC-2 units has been accomplished either through an RS-232 Serial Interface or a USB 2.0 port, using LogView software.

The data acquisition system was located on the outboard side of the southwest facing parapet, near the midspan of the bridge. LC-2 Datalogger units were housed inside fiberglass NEMA 4X weatherproof enclosures. For future use and long-term security, three 12"x12" plastic junction boxes are provided for cable bundling and storage when Datalogger units are removed.

Strandmeter (model 4410, Geokon): These sensors measure deformation. *Number of sensors: 9*

Sister Bar (model 4911, Geokon): These sensors measure strain. *Number of sensors: 9*

Table 1: List of Geokon sensors serial numbers

Strandmeter Serial Numbers			
	A	B	C
SE	1947585	1947588	1947591
Mid	1947584	1947587	1947590
NW	1947583	1947586	1947589

Sister Bar Serial Numbers			
	A	B	C
SE	2009690	2009693	2009696
Mid	2009689	2009692	2009695
NW	2009688	2009691	2009694

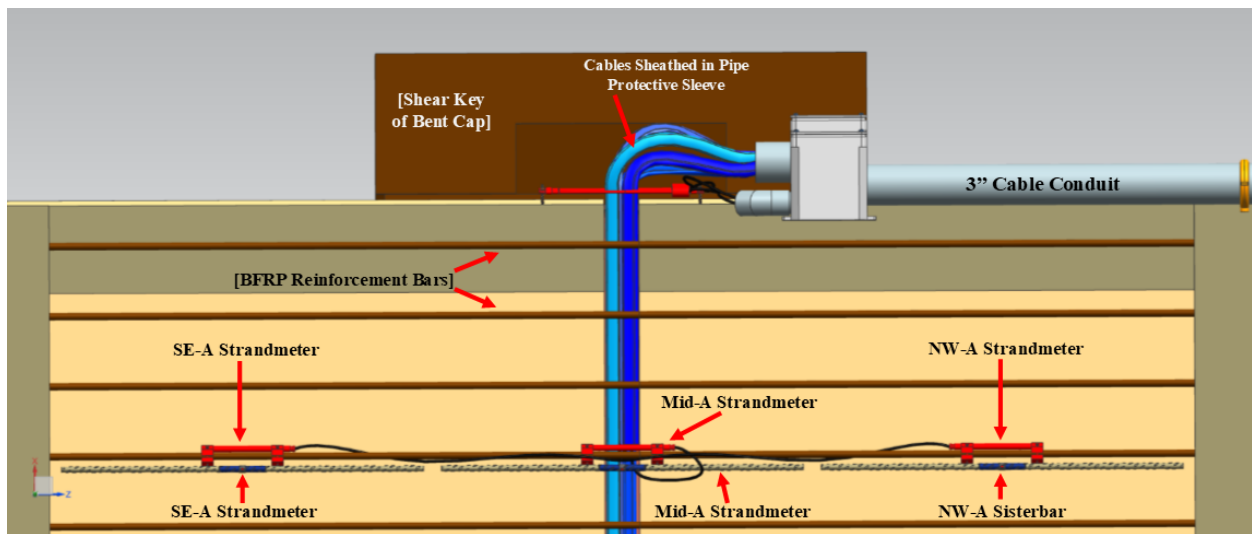


Figure 2.12: Details of embedded sensors and wiring, top view

2.3 Sensor setup

Figure 2.13 is a screen capture from the LogView data acquisition software that show the sensor setup information.

Datalogger No.1 Sensor Setup Info, Channels 1 Through 16:

General sensor information	Units conversion	Temperature correction
Sensor Id: G0307093733 Sensor Name: SE-A-Strand Description: 1947585 Model: 44xx Type: VIBRATING_WIRE Date created: Mar 7 2020	Measurement: default Input units: none Output units: none Conversion method: Linear Output calculation: $G(R1 - R0)$ Zero reading: 9000.794 Gage factor: 3.365E-5 Gage offset: 0.0	Allow temp correction: no Initial temp: 95.7 Temperature factor: 1.0 Convert temp to F: yes Thermistor Type: Standard
Sensor Id: G0307093734 Sensor Name: Mid-A-Strand Description: 1947584 Model: 44xx Type: VIBRATING_WIRE Date created: Mar 7 2020	Measurement: default Input units: none Output units: none Conversion method: Linear Output calculation: $G(R1 - R0)$ Zero reading: 8978.683 Gage factor: 8.484E-4 Gage offset: 0.0	Allow temp correction: no Initial temp: 97.7 Temperature factor: 1.0 Convert temp to F: yes Thermistor Type: Standard
Sensor Id: G0307093735 Sensor Name: NW-A-Strand Description: 1947583 Model: 44xx Type: VIBRATING_WIRE Date created: Mar 7 2020	Measurement: default Input units: none Output units: none Conversion method: Linear Output calculation: $G(R1 - R0)$ Zero reading: 8744.644 Gage factor: 8.465E-4 Gage offset: 0.0	Allow temp correction: no Initial temp: 97.2 Temperature factor: 1.0 Convert temp to F: yes Thermistor Type: Standard
Sensor Id: G0307093736 Sensor Name: SE-B-Strand Description: 1947588 Model: 44xx Type: VIBRATING_WIRE Date created: Mar 7 2020	Measurement: default Input units: none Output units: none Conversion method: Linear Output calculation: $G(R1 - R0)$ Zero reading: 8805.653 Gage factor: 8.238E-4 Gage offset: 0.0	Allow temp correction: no Initial temp: 92.1 Temperature factor: 1.0 Convert temp to F: yes Thermistor Type: Standard

<p>General sensor information</p> <p>Sensor Id: G0307093737 Sensor Name: Mid-B-Strand Description: 1947587 Model: 44xx Type: VIBRATING_WIRE Date created: Mar 7 2020</p>	<p>Units conversion</p> <p>Measurement: default Input units: none Output units: none Conversion method: Linear Output calculation: $G(R1 - R0)$ Zero reading: 8811.292 Gage factor: 8.508E-4 Gage offset: 0.0</p>	<p>Temperature correction</p> <p>Allow temp correction: no Initial temp: 90.1 Temperature factor: 1.0 Convert temp to F: yes Thermistor Type: Standard</p>
<p>General sensor information</p> <p>Sensor Id: G0307093738 Sensor Name: NW-B-Strand Description: 1947586 Model: 44xx Type: VIBRATING_WIRE Date created: Mar 7 2020</p>	<p>Units conversion</p> <p>Measurement: default Input units: none Output units: none Conversion method: Linear Output calculation: $G(R1 - R0)$ Zero reading: 8892.411 Gage factor: 8.495E-4 Gage offset: 0.0</p>	<p>Temperature correction</p> <p>Allow temp correction: no Initial temp: 91.8 Temperature factor: 1.0 Convert temp to F: yes Thermistor Type: Standard</p>
<p>General sensor information</p> <p>Sensor Id: G0307093739 Sensor Name: SE-C-Strand Description: 1947591 Model: 44xx Type: VIBRATING_WIRE Date created: Mar 7 2020</p>	<p>Units conversion</p> <p>Measurement: default Input units: none Output units: none Conversion method: Linear Output calculation: $G(R1 - R0)$ Zero reading: 8850.494 Gage factor: 8.508E-4 Gage offset: 0.0</p>	<p>Temperature correction</p> <p>Allow temp correction: no Initial temp: 93.7 Temperature factor: 1.0 Convert temp to F: yes Thermistor Type: Standard</p>
<p>General sensor information</p> <p>Sensor Id: G0307093740 Sensor Name: Mid-C-Strand Description: 1947589 Model: 44xx Type: VIBRATING_WIRE Date created: Mar 7 2020</p>	<p>Units conversion</p> <p>Measurement: default Input units: none Output units: none Conversion method: Linear Output calculation: $G(R1 - R0)$ Zero reading: 8780.526 Gage factor: 8.501E-4 Gage offset: 0.0</p>	<p>Temperature correction</p> <p>Allow temp correction: no Initial temp: 93.2 Temperature factor: 1.0 Convert temp to F: yes Thermistor Type: Standard</p>
<p>General sensor information</p> <p>Sensor Id: G0307093741 Sensor Name: SE-A-Sis Description: 2009690 Model: 49xx Type: VIBRATING_WIRE Date created: Mar 7 2020</p>	<p>Units conversion</p> <p>Measurement: default Input units: none Output units: none Conversion method: Linear Output calculation: $G(R1 - R0)$ Zero reading: 7997.503 Gage factor: 0.355 Gage offset: 0.0</p>	<p>Temperature correction</p> <p>Allow temp correction: no Initial temp: 98.1 Temperature factor: 1.0 Convert temp to F: yes Thermistor Type: Standard</p>

<p>General sensor information</p> <p>Sensor Id: G0307093742 Sensor Name: Mid-A-Sis Description: 2009689 Model: 49xx Type: VIBRATING_WIRE Date created: Mar 7 2020</p>	<p>Units conversion</p> <p>Measurement: default Input units: none Output units: none</p> <p>Conversion method: Linear</p> <p>Output calculation: $G(R1 - R0)$ Zero reading: 8124.18 Gage factor: 0.353 Gage offset: 0.0</p>	<p>Temperature correction</p> <p>Allow temp correction: no Initial temp: 99.1 Temperature factor: 1.0 Convert temp to F: yes Thermistor Type: Standard</p>
<p>General sensor information</p> <p>Sensor Id: G0307093743 Sensor Name: NW-A-Sis Description: 2009688 Model: 49xx Type: VIBRATING_WIRE Date created: Mar 7 2020</p>	<p>Units conversion</p> <p>Measurement: default Input units: none Output units: none</p> <p>Conversion method: Linear</p> <p>Output calculation: $G(R1 - R0)$ Zero reading: 7621.272 Gage factor: 0.353 Gage offset: 0.0</p>	<p>Temperature correction</p> <p>Allow temp correction: no Initial temp: 104.5 Temperature factor: 1.0 Convert temp to F: yes Thermistor Type: Standard</p>
<p>General sensor information</p> <p>Sensor Id: G0307093744 Sensor Name: SE-B-Sis Description: 2009693 Model: 49xx Type: VIBRATING_WIRE Date created: Mar 7 2020</p>	<p>Units conversion</p> <p>Measurement: default Input units: none Output units: none</p> <p>Conversion method: Linear</p> <p>Output calculation: $G(R1 - R0)$ Zero reading: 7833.814 Gage factor: 0.354 Gage offset: 0.0</p>	<p>Temperature correction</p> <p>Allow temp correction: no Initial temp: 93.9 Temperature factor: 1.0 Convert temp to F: yes Thermistor Type: Standard</p>
<p>General sensor information</p> <p>Sensor Id: G0307093745 Sensor Name: Mid-B-Sis Description: 2009692 Model: 49xx Type: VIBRATING_WIRE Date created: Mar 7 2020</p>	<p>Units conversion</p> <p>Measurement: default Input units: none Output units: none</p> <p>Conversion method: Linear</p> <p>Output calculation: $G(R1 - R0)$ Zero reading: 7879.003 Gage factor: 0.353 Gage offset: 0.0</p>	<p>Temperature correction</p> <p>Allow temp correction: no Initial temp: 100.8 Temperature factor: 1.0 Convert temp to F: yes Thermistor Type: Standard</p>
<p>General sensor information</p> <p>Sensor Id: G0307093746 Sensor Name: NW-B-Sis Description: 2009691 Model: 49xx Type: VIBRATING_WIRE Date created: Mar 7 2020</p>	<p>Units conversion</p> <p>Measurement: default Input units: none Output units: none</p> <p>Conversion method: Linear</p> <p>Output calculation: $G(R1 - R0)$ Zero reading: 7521.281 Gage factor: 0.354 Gage offset: 0.0</p>	<p>Temperature correction</p> <p>Allow temp correction: no Initial temp: 93.9 Temperature factor: 1.0 Convert temp to F: yes Thermistor Type: Standard</p>

<p>General sensor information</p> <p>Sensor Id: G0307093747 Sensor Name: SE-C-Sis Description: 2009696 Model: 49xx Type: VIBRATING_WIRE Date created: Mar 7 2020</p>	<p>Units conversion</p> <p>Measurement: default Input units: none Output units: none Conversion method: Linear Output calculation: G(R1 - R0) Zero reading: 7639.152 Gage factor: 0.356 Gage offset: 0.0</p>	<p>Temperature correction</p> <p>Allow temp correction: no Initial temp: 86.5 Temperature factor: 1.0 Convert temp to F: yes Thermistor Type: Standard</p>
<p>General sensor information</p> <p>Sensor Id: G0307093748 Sensor Name: Mid-C-Sis Description: 2009695 Model: 49xx Type: VIBRATING_WIRE Date created: Mar 7 2020</p>	<p>Units conversion</p> <p>Measurement: default Input units: none Output units: none Conversion method: Linear Output calculation: G(R1 - R0) Zero reading: 8050.535 Gage factor: 0.356 Gage offset: 0.0</p>	<p>Temperature correction</p> <p>Allow temp correction: no Initial temp: 85.5 Temperature factor: 1.0 Convert temp to F: yes Thermistor Type: Standard</p>

Datalogger No.2 Setup Info, Channels 1 & 2:

Note: The temperature was not converted to Fahrenheit

<p>General sensor information</p> <p>Sensor Id: G0307094734 Sensor Name: NW-C-Strand Description: 1947590 Model: 44xx Type: VIBRATING_WIRE Date created: Mar 7 2020</p>	<p>Units conversion</p> <p>Measurement: default Input units: none Output units: none Conversion method: Linear Output calculation: G(R1 - R0) Zero reading: 8570.04 Gage factor: 8.0E-4 Gage offset: 0.0</p>	<p>Temperature correction</p> <p>Allow temp correction: no Initial temp: 29.3 Temperature factor: 1.0 Convert temp to F: no Thermistor Type: Standard</p>
<p>General sensor information</p> <p>Sensor Id: G0307094735 Sensor Name: NW-C-Sis Description: 2009694 Model: 49xx Type: VIBRATING_WIRE Date created: Mar 7 2020</p>	<p>Units conversion</p> <p>Measurement: default Input units: none Output units: none Conversion method: Linear Output calculation: G(R1 - R0) Zero reading: 8177.211 Gage factor: 0.353 Gage offset: 0.0</p>	<p>Temperature correction</p> <p>Allow temp correction: no Initial temp: 29.8 Temperature factor: 1.0 Convert temp to F: no Thermistor Type: Standard</p>

Figure 2.13: Sensor setup in LogView software

3 Data Reduction

3.1 Data reduction for Strandmeters

The data outputted from the LC2 dataloggers for the strandmeters was in millimeters of deformation. This is obtained through the equation:

$$Deformation = (Current\ Reading - Initial\ Reading) * (Calibration\ Factor)$$

$$D = (R_1 - R_0) * G$$

The initial reading and calibration factor were inputted into the datalogger and used to calculate the output. To correct for the effects of temperature on the material, the following equation is used:

$$D_{Corrected} = [(R_1 - R_0) * G] + [(T_1 - T_0) * K]$$

Where K is the thermal coefficient of the transducer and can be found using:

$$K = [(R_1 * 0.00520) + 3.567] * G$$

Once the deformation was corrected for temperature effects, it was then used to calculate the strain based off the deformation using:

$$\mu = \left(\frac{D}{203.2} \right) * 10^6$$

This outputs the strain as microstrain.

3.2 Data reduction for Sisterbars

The data outputted from the LC2 dataloggers for the sister bars is in apparent (micro) strain. This is obtained through the equation:

$$\textit{Apparent Strain} = (\textit{Current Reading} - \textit{Intial Reading}) * (\textit{Calibration Factor})$$

$$\varepsilon_{\textit{apparent}} = (R_1 - R_0) * C$$

The initial reading and calibration factor were inputted into the datalogger and used to calculate the output. From the apparent strain, the temperature corrected load related strain and actual strain can be found.

$$\varepsilon_{\textit{load related}} = [(R_1 - R_0) * C] + [(T_1 - T_0) * K_{\textit{diff}}]$$

$$\varepsilon_{\textit{actual}} = [(R_1 - R_0) * C] + [(T_1 - T_0) * K_{\textit{steel}}]$$

Where K_{diff} is the difference between the coefficients of thermal expansion for steel and concrete.

4 Results and Data Analysis

4.1 Amendments to the dataset

The strandmeters and sister bars were installed before the link slab was cast. This left the sensors exposed directly to thermal effects. To see the deformation and strain in the concrete after it was poured, the data was zeroed and shifted to start at hour 92.

4.2 Graphs of reduced data

Figures 4.1 – 4.4 show graphs of the recorded data. Average daily strain at the Mid sensors appears constant from 90+ days, as shown in figures 4.1 – 4.4. As shown in Figure 4.4, there have been some outliers or daily strain changes and maximum differential recorded on the site from Sisterbars and BFRP bars. That could be due to any interference with the system electronics or other electronics systems in the close vicinity of the sensors or due to glitches caused sometimes by the data acquisition system that could cause spikes.

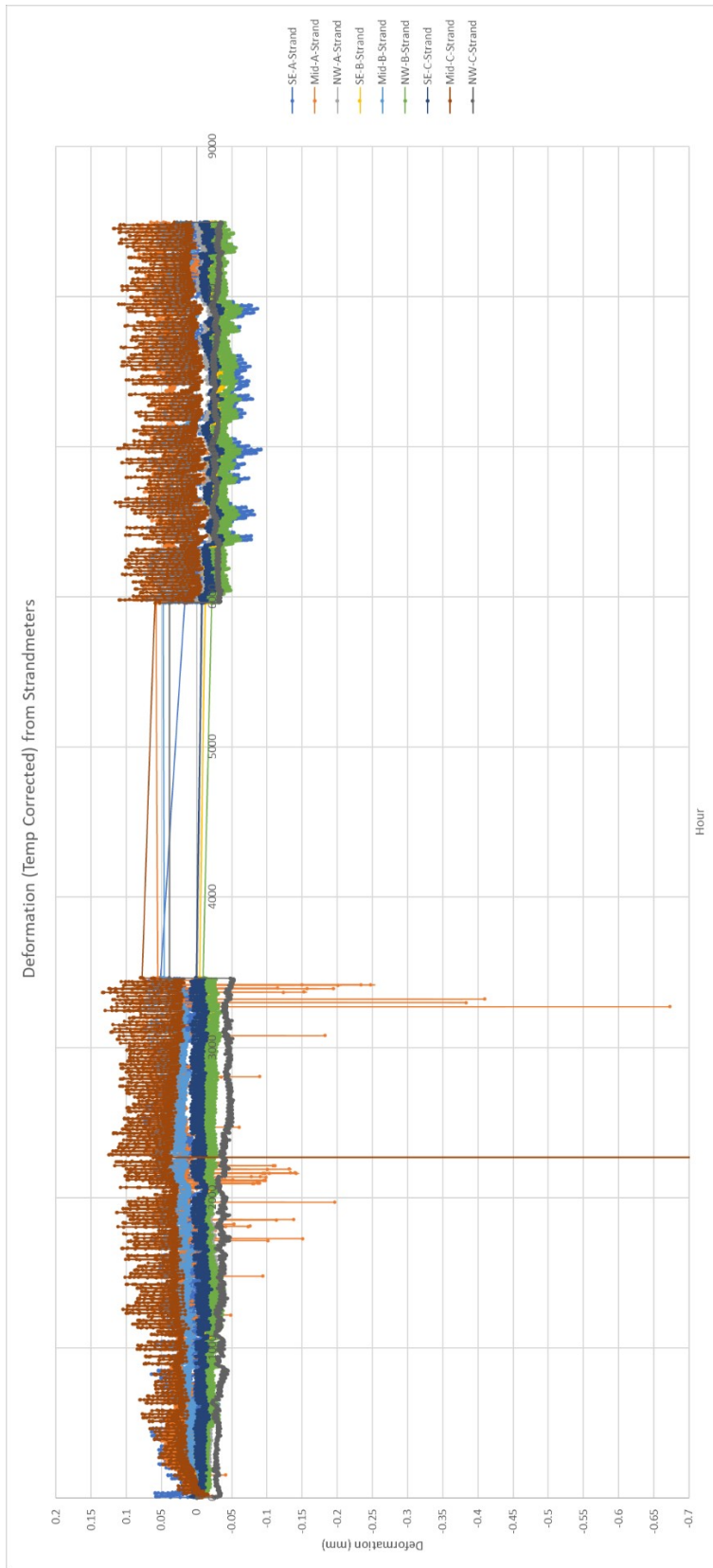


Figure 4.1: Graphed deformation from Strandmeters

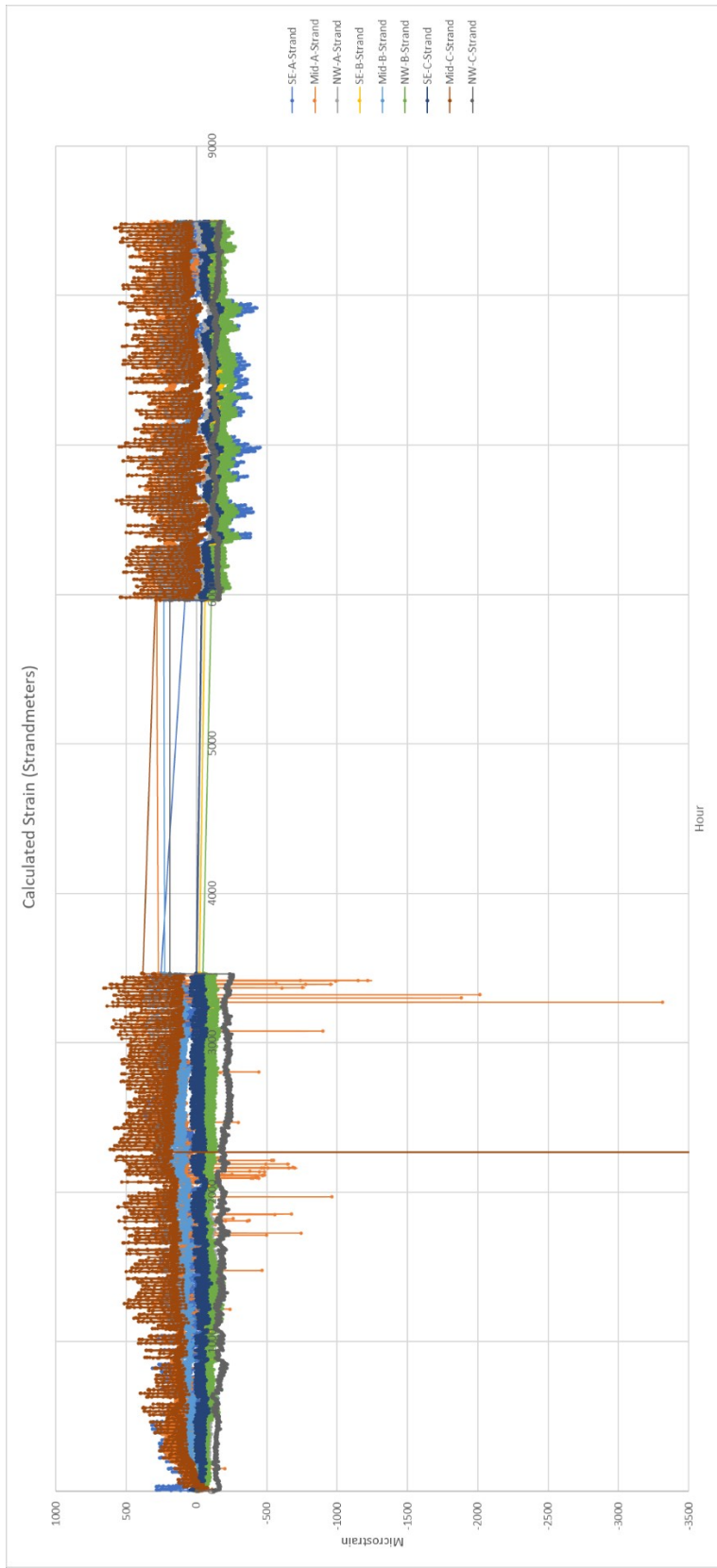


Figure 4.2: Graphed strain from Strandmeters

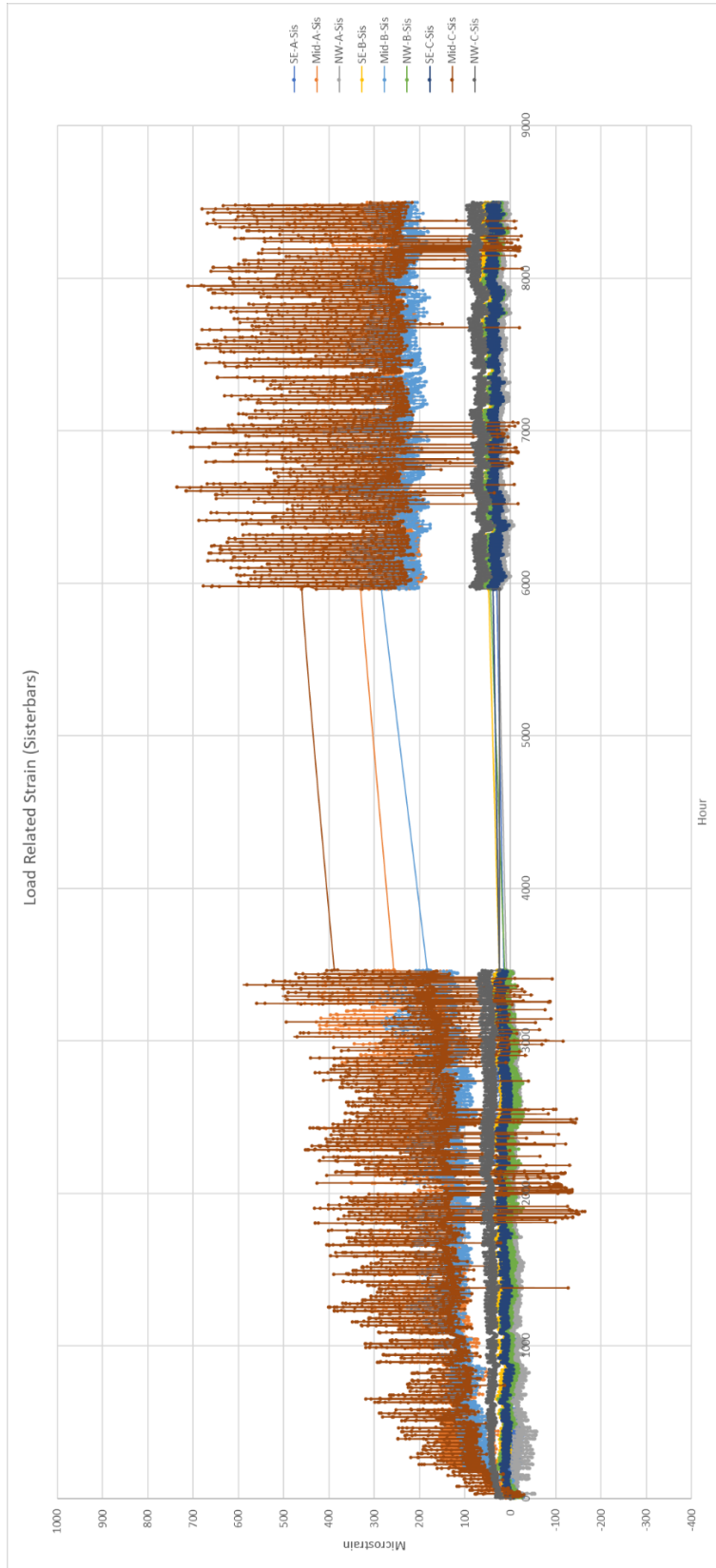


Figure 4.3: Graphed load related strain from Sisterbars

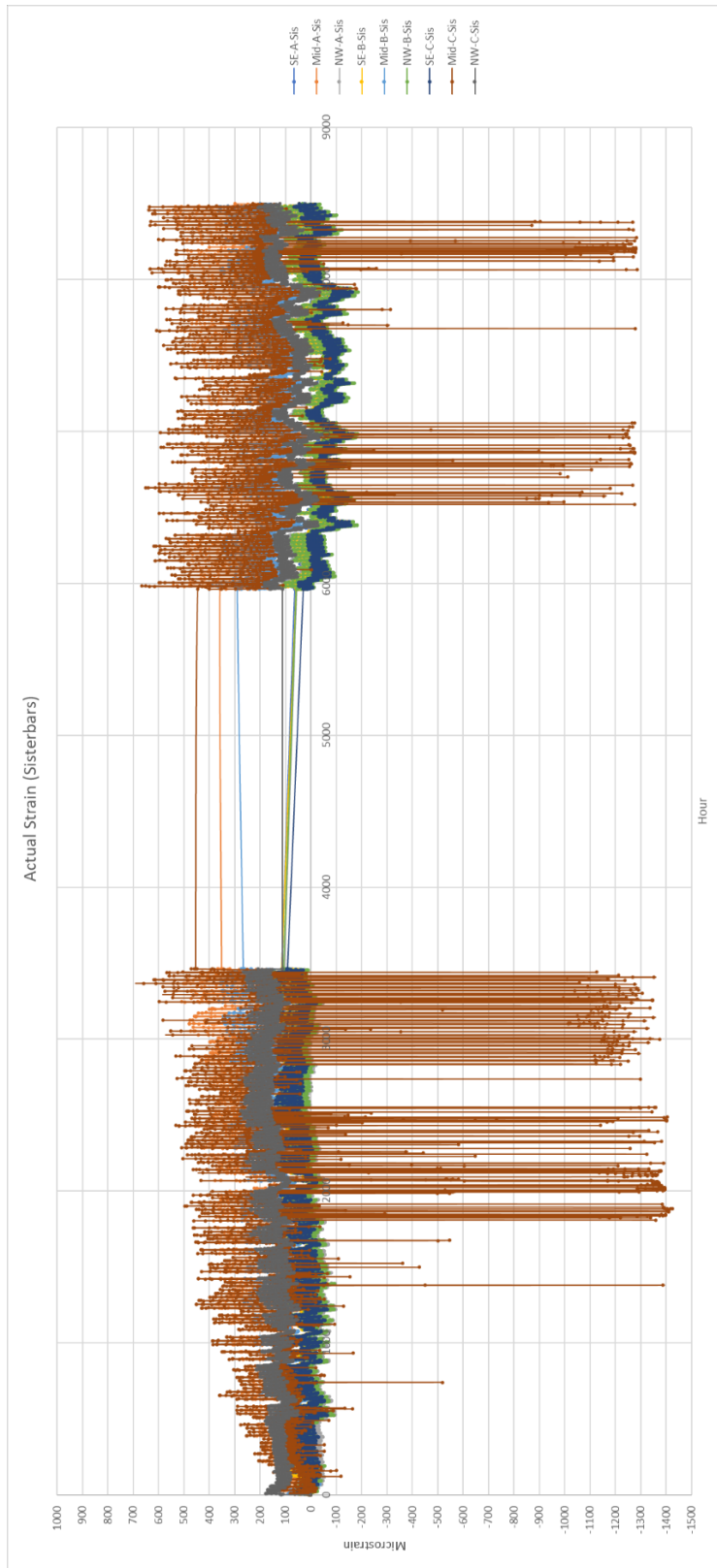


Figure 4.4: Graphed actual strain from Sisterbars

4.3 Samples of reduced data

Tables 2 – 5 show the first 20 reduced data points (hours).

Table 2: First 20 data points of Strandmeter deformation

1947585	1947584	1947583	1947588	1947587	1947586	1947591	1947590	1947589
Deformation (Temp corrected) - SE-A-Strand	Deformation (Temp corrected) - Mid-A-Strand	Deformation (Temp corrected) - NW-A-Strand	Deformation (Temp corrected) - SE-B-Strand	Deformation (Temp corrected) - Mid-B-Strand	Deformation (Temp corrected) - NW-B-Strand	Deformation (Temp corrected) - SE-C-Strand	Deformation (Temp corrected) - Mid-C-Strand	Deformation (Temp corrected) - NW-C-Strand
0	0	0	0	0	0	0.001	0.002	0.001
-0.02369748	-0.012723064	-0.005571296	-0.005157161	-0.003387939	-0.007150382	-0.011651521	-0.00277011	0.001
-0.045870424	-0.021867122	-0.005821181	-0.006081978	-0.007024604	-0.009361547	-0.014825541	-0.001136189	0.000303231
-0.078800397	-0.031089908	-0.009846981	-0.014642322	-0.015462199	-0.016420979	-0.02195966	-0.003906299	0.010322311
-0.097009548	-0.034668359	-0.01126572	-0.017330236	-0.019581462	-0.021389912	-0.025471965	-0.005382874	0.026954466
-0.106766578	-0.035233966	-0.013531903	-0.019733419	-0.021596313	-0.024692478	-0.028576377	-0.006657433	0.028973546
-0.112254906	-0.035681203	-0.014966941	-0.021022709	-0.02336244	-0.025752811	-0.029645985	-0.007840473	0.034179855
-0.118572678	-0.036944186	-0.016005872	-0.023368945	-0.02525293	-0.02902521	-0.032232995	-0.009569272	0.035721702
-0.123451193	-0.037575677	-0.016837017	-0.024364386	-0.027501655	-0.030267444	-0.034392162	-0.011824856	0.038386164
-0.127719893	-0.040628163	-0.018064268	-0.025478279	-0.02775038	-0.031509677	-0.035640887	-0.012152984	0.039747396
-0.13015915	-0.03983866	-0.018781787	-0.026122924	-0.029088664	-0.032236827	-0.035979172	-0.011935351	0.041018319
-0.132903315	-0.03895703	-0.01919736	-0.026592171	-0.028909546	-0.03366096	-0.035496574	-0.011481111	0.041592474
-0.135037665	-0.0390754	-0.019310985	-0.027236816	-0.029033908	-0.033782076	-0.036620937	-0.013263479	0.04407632
-0.135037665	-0.0390754	-0.019914879	-0.026942967	-0.029033908	-0.034176043	-0.036317456	-0.012954327	0.043863397
-0.134427851	-0.0390754	-0.019310985	-0.026767569	-0.028819987	-0.03357001	-0.035710495	-0.011717719	0.045650474
-0.135952386	-0.039285897	-0.018820718	-0.026824515	-0.028640869	-0.03538811	-0.036227897	-0.012263479	0.045650474
-0.133208222	-0.038864903	-0.018103199	-0.025298322	-0.026695624	-0.034054926	-0.033889613	-0.011171959	0.044953705
-0.1194874	-0.031733689	-0.011609765	-0.01743501	-0.019631117	-0.024631694	-0.025466867	-0.001439801	0.046347244
-0.099753713	-0.026102752	-0.003301484	-0.013405419	-0.015337836	-0.01496668	-0.02054667	0.003330309	0.046863397
-0.06468939	-0.020485214	-0.003012669	-0.010015914	-0.015273329	-0.013634398	-0.016964757	-0.002029052	0.045992626

Table 3: First 20 data points of Strandmeter microstrain

1947585	1947584	1947583	1947588	1947587	1947586	1947591	1947590	1947589
Strain (micro) - SE-A-Strand	Strain (micro) - Mid-A-Strand	Strain (micro) - NW-A-Strand	Strain (micro) - SE-B-Strand	Strain (micro) - Mid-B-Strand	Strain (micro) - NW-B-Strand	Strain (micro) - SE-C-Strand	Strain (micro) - Mid-C-Strand	Strain (micro) - NW-C-Strand
0	0	0	0	0	0	4.921259843	9.842519685	4.921259843
-116.6214565	-62.61350295	-27.41779724	-25.37972992	-16.67293031	-35.18888755	-57.34016156	-13.63243058	4.921259843
-225.7402762	-107.6137886	-28.64754306	-29.93099498	-34.56990118	-46.07060753	-72.96033977	-5.591481791	1.492277137
-387.7972313	-153.0015171	-48.45954995	-72.05867136	-76.09349823	-80.81190625	-108.0691922	-19.22391237	50.79877322
-477.4091953	-170.6120045	-55.44153593	-85.2865937	-96.36546024	-105.2653137	-125.354156	-26.49052039	132.6499297
-525.4260709	-173.3955035	-66.59400984	-97.11328031	-106.2810699	-121.5180997	-140.6317748	-32.7629584	142.5863471
-552.4355634	-175.5964732	-73.65620423	-103.4582128	-114.972639	-126.7362739	-145.8955941	-38.58500369	168.2079479
-583.5269602	-181.8119394	-78.76905364	-115.0046523	-124.2762283	-142.8406026	-158.626943	-47.09287526	175.7957783
-607.535398	-184.9196724	-82.85933317	-119.9034752	-135.3427886	-148.9539545	-169.2527643	-58.19318856	188.9082889
-628.5427811	-199.9417472	-88.89895768	-125.3852293	-136.5668291	-155.0673063	-175.3980677	-59.80799034	195.6072625
-640.547	-196.0563984	-92.43005487	-128.5576956	-143.1528722	-158.6457997	-177.0628534	-58.73696584	201.8618076
-654.0517463	-191.7176679	-94.47519464	-130.8669835	-142.2713868	-165.6543292	-174.6878633	-56.50153228	204.68737
-664.5554378	-192.3001972	-95.03437697	-134.0394497	-142.8834071	-166.2503752	-180.2211449	-65.27302746	216.9110237
-664.5554378	-192.3001972	-98.00629183	-132.5933402	-142.8834071	-168.1891877	-178.727639	-63.75161024	215.863175
-661.5543831	-192.3001972	-95.03437697	-131.7301618	-141.8306441	-165.2067404	-175.7406272	-57.66594134	224.657846
-669.0570199	-193.3361083	-92.62164444	-132.010409	-140.9491587	-174.1540824	-178.286897	-60.35176762	224.657846
-655.5522736	-191.2642862	-89.09054724	-124.4996141	-131.3761041	-167.5931417	-166.7795916	-54.98011506	221.2288633
-588.0285423	-156.1697291	-57.13466929	-85.80221417	-96.60982776	-121.218968	-125.3290706	-7.085634687	228.0868287
-490.9139415	-128.4584268	-16.24746038	-65.97154911	-75.48147795	-73.65491954	-101.1155017	16.38931558	230.6269545
-318.3532949	-100.8130632	-14.826125	-49.29091339	-75.16402047	-67.09841339	-83.4879784	-9.985494411	226.3416621

Table 4: First 20 data points of load related microstrain from Sisterbars

2009690	2009689	2009688	2009693	2009692	2009691	2009696	2009695	2009694
Load Related Strain (micro) - SE-A-Sis	Load Related Strain (micro) - Mid-A-Sis	Load Related Strain (micro) - NW-A-Sis	Load Related Strain (micro) - SE-B-Sis	Load Related Strain (micro) - Mid-B-Sis	Load Related Strain (micro) - NW-B-Sis	Load Related Strain (micro) - SE-C-Sis	Load Related Strain (micro) - Mid-C-Sis	Load Related Strain (micro) - NW-C-Sis
-0.119	0.168	0.099	0.01	0.494	-0.538	0.335	-0.098	0.28
-12.204	-13.313	-16.388	-11.471	-14.262	-14.519	-7.989	-12.149	1.076
-21.323	-22.407	-27.207	-18.658	-23.937	-23.639	-13.769	-14.558	0.65
-38.872	-40.961	-47.931	-34.357	-43.759	-37.144	-27.668	-26.971	-10.909
-47.267	-49.169	-55.961	-42.872	-51.814	-45.189	-35.685	-34.919	-16.298
-51.149	-53.505	-60.527	-46.555	-56.338	-49.749	-39.723	-38.71	-24.714
-54.004	-56.081	-63.185	-48.927	-58.797	-52.426	-42.276	-41.775	-31.836
-57.379	-59.102	-65.935	-52.577	-62.355	-55.776	-46.163	-44.865	-36.437
-59.2	-61.199	-68.234	-54.987	-64.707	-58.097	-48.033	-47.533	-38.889
-61.47	-63.427	-69.985	-56.735	-66.485	-59.711	-50.037	-49.071	-42.248
-62.685	-64.136	-71.056	-58.085	-67.657	-61.075	-51.536	-50.327	-44.737
-63.551	-65.425	-71.877	-59.097	-68.236	-61.844	-52.391	-51.287	-46.928
-64.448	-65.947	-73.06	-60.117	-69.458	-62.92	-53.135	-52.356	-48.011
-64.428	-66.093	-72.803	-59.635	-68.824	-62.598	-52.82	-52.053	-48.976
-63.781	-65.618	-72.553	-59.11	-68.43	-61.813	-52.445	-51.58	-49.824
-64.913	-66.578	-73.447	-60.152	-69.24	-62.866	-53.45	-52.558	-49.924
-62.805	-64.283	-71.361	-57.691	-66.757	-60.419	-50.903	-50.548	-49.494
-56.038	-56.911	-64.203	-47.684	-57.114	-49.166	-38.801	-38.227	-50.238
-46.007	-43.553	-47.919	-33.119	-40.233	-31.767	-25.167	-24.313	-48.126
-30.333	-29.074	-35.393	-24.246	-30.061	-22.301	-16.988	-16.404	-36.634

Table 5: First 20 data points of actual microstrain from Sisterbars

2009690	2009689	2009688	2009693	2009692	2009691	2009696	2009695	2009694
Actual Strain (micro) - SE-A-Sis	Actual Strain (micro) - Mid-A-Sis	Actual Strain (micro) - NW-A-Sis	Actual Strain (micro) - SE-B-Sis	Actual Strain (micro) - Mid-B-Sis	Actual Strain (micro) - NW-B-Sis	Actual Strain (micro) - SE-C-Sis	Actual Strain (micro) - Mid-C-Sis	Actual Strain (micro) - NW-C-Sis
-0.119	0.168	0.099	0.01	0.494	-0.538	0.335	-0.098	0.28
-57.854	-63.913	-81.838	-56.021	-72.562	-68.969	-37.689	-52.849	3.076
-111.523	-117.557	-145.457	-98.958	-127.887	-117.689	-70.419	-70.108	3.65
-198.372	-211.461	-249.231	-179.007	-226.909	-184.544	-136.018	-129.821	-44.909
-241.417	-254.319	-289.711	-222.172	-267.414	-223.939	-175.385	-166.919	-76.298
-261.249	-275.705	-312.427	-241.255	-290.088	-246.649	-195.373	-187.21	-116.714
-275.104	-288.181	-325.535	-253.527	-302.447	-259.226	-207.826	-201.275	-151.836
-291.129	-302.752	-339.285	-271.477	-319.755	-275.226	-226.563	-216.465	-173.437
-300.65	-313.649	-350.384	-282.687	-330.907	-286.347	-236.133	-229.033	-185.889
-312.27	-324.127	-359.285	-291.035	-339.835	-294.011	-246.387	-237.171	-201.248
-318.435	-328.686	-365.306	-298.435	-347.057	-301.425	-253.936	-243.377	-213.737
-323.151	-333.825	-368.877	-303.297	-349.286	-304.944	-258.641	-248.187	-222.928
-327.898	-338.197	-375.01	-308.717	-355.458	-310.42	-262.135	-253.656	-229.011
-327.878	-338.343	-374.203	-307.135	-353.174	-308.998	-260.72	-252.253	-233.976
-325.031	-336.218	-372.853	-304.41	-350.58	-306.013	-258.695	-250.68	-238.824
-330.563	-341.028	-377.597	-309.302	-355.24	-310.916	-263.55	-254.408	-238.924
-321.305	-331.033	-368.361	-298.041	-343.957	-299.669	-252.203	-245.798	-237.494
-290.888	-296.711	-334.803	-250.634	-298.564	-247.166	-195.551	-190.027	-241.238
-242.357	-233.853	-256.919	-177.769	-217.333	-164.317	-130.217	-122.213	-232.126
-162.883	-156.124	-189.943	-129.296	-159.861	-114.151	-87.388	-79.104	-177.634

4.4 Results and Analysis

The data show that the middle sensors experienced the highest amount of strain and deformation as expected. The max strain calculated from the Strandmeters is ~600 microstrain from the mid-a sensor. The max strain calculated from the Sisterbars is ~700 microstrain from the mid-c sensor.

5 Evaluation of FDOT Link-Slab Details

The research team conducted an evaluation of the link-slab design detail for FBS pedestrian bridge that is reinforced with Basalt Fiber Reinforced Polymer (BFRP) bars. The link-slab details are shown in Appendix E. The details of the link-slab for Bridge No. 019003 are presented in Figures E1 to E6 in Appendix E. The UHPC link-slab (Bridge 019004) was not reviewed as part of this project; yet some details of the UHPC link-slab are also shown in Appendix E.

The link-slab for Bridge No. 019003 is reinforced with longitudinal BFRP #5 bars spaced at 6 inch. The link-slab thickness of 6 inch (minimum) has a 2-inch concrete cover to the top surface of link-slab. The link-slab length is 8 ft – 2 inch, spanning over an open joint between the ends of the FSB beams. A construction joint is introduced at the location of the link-slab and the link-slab is debonded using roofing paper (or any other debonding material) from the supporting FSB beams for a debonding zone length of 5-1/2 ft. The deck thickness usually varies due to beam camber. The volume between the FSB beams (pockets and side face) and the debonding material shall be filled with Class II bridge deck concrete with SRA. The volume above the debonding material shall be filled with Class IV fiber-reinforced concrete.

The link-slab performed very well without showing any excessive cracking. The strains developed in the BFRP reinforcement and recorded by the sensors indicated small strain levels of about 600 microstrain compared to the BFRP ultimate strain values. After about 90 days over the time of monitoring, the average strain in the mid-joint gauges did not change significantly indicating minimal creep and/or shrinkage restraint was experienced to date by the link-slab since the initial casting date. The maximum daily strain change due to thermal effects is about 500 microstrain. In summary, the link-slab showed good performance. Further investigation should be conducted to monitor the long-term performance and live-load test effect using loading trucks. It is also recommended that the UHPC link slab to be investigated in future research projects.

6 Summary

The team investigated the concrete simple-span beams that are made continuous by pouring a continuity link-slab between the beam ends. The bridge has been instrumented with embedded and surface-mounted sensors and has been monitored to evaluate the performance of the new link-slab. No data is available from the initial installation of the surface mounted micro-crack meters A, B & C on the walking surface, as they were vandalized shortly after installation. If these sensors are to be re-installed in a later project, they should be put in a place that cannot be easily accessed by pedestrians.

Several types of sensors were used, and a data acquisition system recorded strains/deformations at a regular time interval. The preferred sensor types for this application are vibrating wire sensors with integrated thermistors (per FDOT request). The sensors were strategically located on both sides of the midline of the link slab to capture strains in the BFRP bars, strains in the concrete link-slab, and the gap between adjacent beams' ends.

All measurements have been corrected for temperature changes per recommendations of the gauge manufacturer. Data has been collected during service. The data acquisition system has been able to keep record of strains developed in the BFRP reinforcement. The strains experienced by the sensors indicated small strain levels compared to the BFRP ultimate strain levels.

In some cases, there have been some outliers or daily strain changes and maximum differential recorded on the site from Sisterbars and BFRP bars. That could be due to any interference with the system electronics or other electronics systems in the close vicinity of the sensors or due to glitches caused sometimes by the data acquisition system that could cause spikes.

In addition to live load flexural effects, this type of thermal cycling could contribute to the concrete cracking over time in the link-slab if tension stresses build-up due to global shrinkage and creep restraint of the connected FSB spans. However, after about 90 days over the time of monitoring, the average strain in the mid-joint gauges did not change significantly indicating minimal creep and or shrinkage restraint was experienced to date by the link-slab since the initial casting date. The maximum daily strain change due to thermal effects is about 500 microstrain.

Unfortunately, no live-load test was scheduled for this project due to time and budget restraints but should be considered on future projects.

7 References

- AASHTO. (2009). AASHTO LRFD bridge design guide specifications for GFRP reinforced concrete bridge decks and traffic railings, 1st Ed., Washington, DC.
- Alampalli, S. and Yannotti, A. P. (1998) “In-Service Performance of Integral Bridges and Jointless Decks” Transportation Research Record Journal of the Transportation Research Board 1624(1):1-7
- Au, A., Lam, C., Au, J., and Tharmabala, B (2013) “Eliminating Deck Joints Using Debonded Link Slabs: Research and Field Tests in Ontario” J. Bridge Eng., ASCE, 2013, 18(8): 768-778.
- Caner, A., and Zia, P. “Behavior and Design of Link Slabs for Jointless Decks” PCI Journal, Vol. 43, No. 3, pp. 68-80, May-June 1998.
- Caner, A., and Zia, P. (1998) “Behavior and Design of Link Slabs for Jointless Bridge Decks” PCI Journal, Page 68-80.
- Charuchaimontri, T., Senjuntichai, T., O’zbolt, J., and Limsuwan, E., (2008) “Effect of lap reinforcement in link slabs of highway bridges” Engineering Structures 30 (2008) 546–560.
- El-Safty, A. K.,” Analysis of Jointless Bridge Decks with Partially Debonded Simple Span Beams,” Ph.D. Dissertation, North Carolina State University, Raleigh, NC, 1994.
- ElSafty, A., and Okeil, A. M., (2008). “Extending the Service Life of Bridges Using Continuous Decks, PCI Journal - Precast/Prestressed Concrete Institute.” PCI, Vol. 53, No. 6, pp. 96-111. 30.
- Gastal, A.L. and Zia, P. (1989). “Analysis of Bridge Beams with Jointless Decks.” In: International Symposium on Durability of Structures, LISBON, Conference Report, Zurich, IABSE, ETH Honggrberg.
- Groli, G., Caldentey, A.P., Soto, A.G., Marchetto, F., and Parrotta, J.E. (2014) “Simplified serviceability design of jointless structures. Experimental verification and application to typical bridge and building structures” Engineering Structures 59 (2014) 469–483.
- Ho E. and Lukashenko, J., (2011) “LINK SLAB DECK JOINTS” 2011 Annual Conference of the Transportation Association of Canada, Edmonton, Alberta.
- Hong, Y. (2014) “Analysis and Design of Link Slabs in Jointless Bridges with Fibre Reinforced Concrete” PhD. Thesis, University of Waterloo, ON, Canada.
- Kendall, A., Keoleian, G, A., and Helfand, G.E., (2008) “Integrated Life-Cycle Assessment and Life-Cycle Cost Analysis Model for Concrete Bridge Deck Applications” J. Infrastruct. Syst., ASCE, 14(3): 214-222.
- Kim, Y. Y., Fischer, G., and Li, V. C. “Performance of Bridge Deck Link Slabs Designed with Ductile Engineered Cementitious Composite”, ACI Structural Journal, V. 101, No. 6, pp. 792-801, Nov-Dec 2004.

- Lepech., M. D. and Li. V.C. (2009) “Application of ECC for bridge deck link slabs” *Materials and Structures*, 42:1185–1195.
- Li, V. C., Fischer, V.C., Kim, G., Lepech, Y., Qian, M., Weimann, S., and Wang, S. (2003) “Durable Link Slabs for Jointless Bridge Decks Based on Strain-Hardening Cementitious Composites” Michigan Department of Transportation, Research Report RC-1438.
- Li, V.C., Lepech, M., and Li, M. (2005) “Field Demonstration of Durable Link Slabs for Jointless Bridge Decks Based on Strain-Hardening Cementitious Composites” Michigan Department of Transportation, Research Report RC- 1471.
- Mothe, R.N. (2006) “Partial continuity in prestressed concrete girder bridges with jointless decks” MSc. Thesis, Louisiana State University and Agricultural and Mechanical College.
- Okeil, A. M. and ElSafty, A. (2005). “Partial Continuity in Bridge Girders with Jointless Decks, Practice Periodical on Structural Design and Construction.” *ASCE Journal*, Vol. 10, No. 4, pp 229-238, doi:10.1061/(ASCE)1084-0680(2005)10:4(229).
- Okeil, A. M., Hossain, X., and Cai, C. S. (2013) “Field monitoring of positive moment continuity detail in a skewed prestressed concrete bulb-tee girder bridge” Spring 2013, *PCI Journal*, Page 80-90.
- Reyes, J. and Robertson, I.N., (2011). “PRECAST LINK SLABS FOR JOINTLESS BRIDGE DECKS.” Technical Report, Hawaii Department of Transportation
- Snedeker, K., White, D., and Kahn. L., (2011) “Evaluation of Performance and Maximum Length of Continuous Decks in Bridges – Part 1” *GDOT Research Project No. 09-07, Task Order No. 02-64. Report*, Page 130.
- Sun, C., N. Wang, and M. K. Tadros, M.K (2016). “Threaded Rod Continuity for Bridge Deck Weight.” *PCI Journal*, Precast/Prestressed Concrete Institute, Chicago, IL. V. 61, No. 3, pp. 47-67.
- Tadros, M.K. (2016), *Eliminating Expansion Joints in Bridges*, Concrete Bridge Technology, Aspire, pp. 32-35
- Thippeswamy, H.K., GangaRao, H.V.S., and Franco, J.M. (2002) “Performance Evaluation of Jointless Bridges” *J. Bridge Eng., ASCE*, 7(5): 276-289.
- Ulku, E., Attanayake, U., and Aktan, H., (2009) “Jointless Bridge Deck with Link Slabs Design for Durability” *Transportation Research Record: Journal of the Transportation Research Board*, No. 2131, Transportation Research Board of the National Academies, Washington, D.C., 2009, pp. 68–78.
- Virginia Department of Transportation (VDOT), Jeff Milton, (March 2013), 2013 Virginia Concrete Conference Joint Maintenance and Best Practices in Deck Joint Replacement
- Wendner, R. and Strauss, A. (2015) “Inclined Approach Slab Solution for Jointless Bridges: Performance Assessment of the Soil–Structure Interaction” *J. Perform. Constr. Facil., ASCE*, 29(2): 04014045.

- Wing, K. M. and Kowalsky, M. J. “Behaviour, Analysis, and Design of an Instrumented Link Slab Bridge” ASCE Journal of Bridge Engineering, Vol. 10, No. 3, pp. 331-344, May 2005.
- Xu, Z., Chen, B., Zhuang, Y., Tabatabai, H., and Huang, F. (2018) “Rehabilitation and Retrofitting of a Multispan Simply-Supported Adjacent Box Girder Bridge into a Jointless and Continuous Structure” J. Perform. Constr. Facil., ASCE, 32(1): 04017112.
- Zia, P., Caner, A., and ElSafty, A. (1995). “Jointless Bridge Decks.” Technical Report, FHWA/NC/95-006, North Carolina Department of Transportation (NCDOT).

8 Appendix A

Images and Illustrations Of The Bridge And Sensor Layout

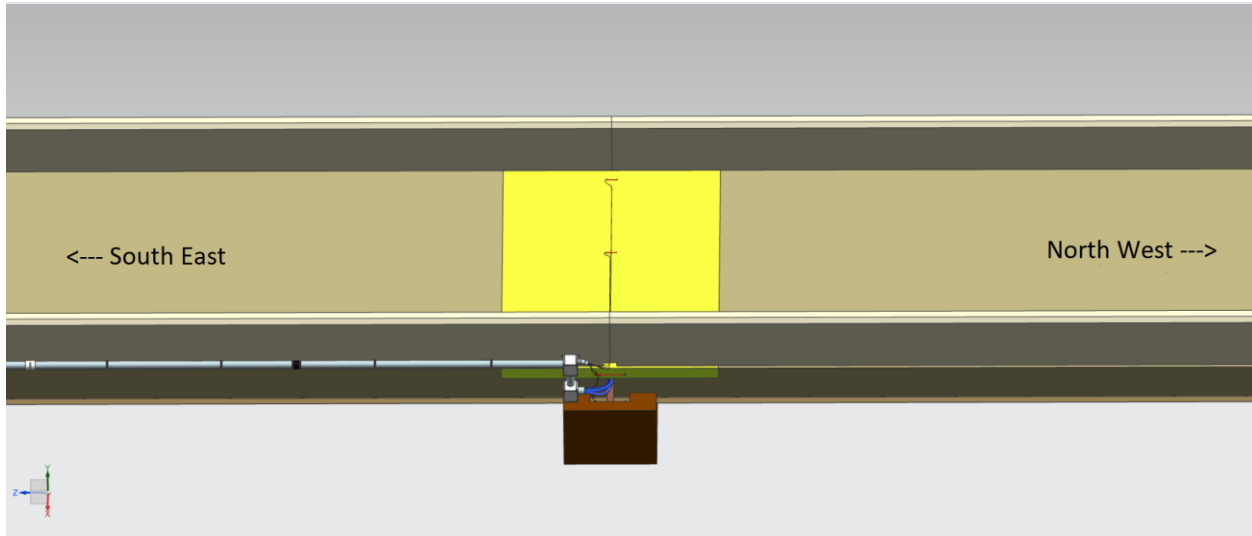


Figure A.1: Side View

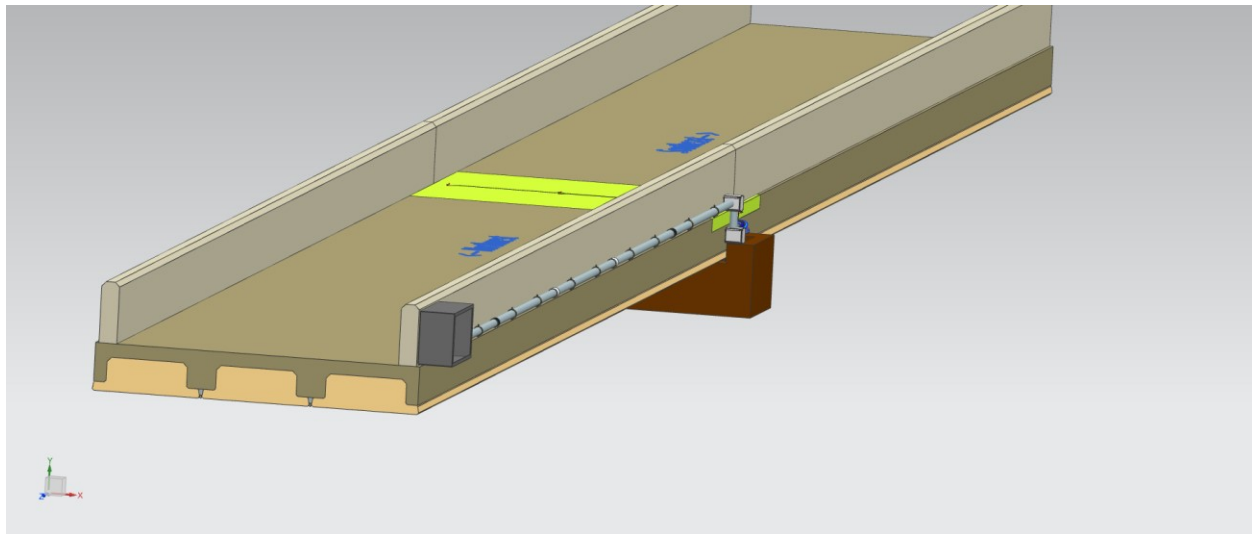


Figure A.2: Angled View

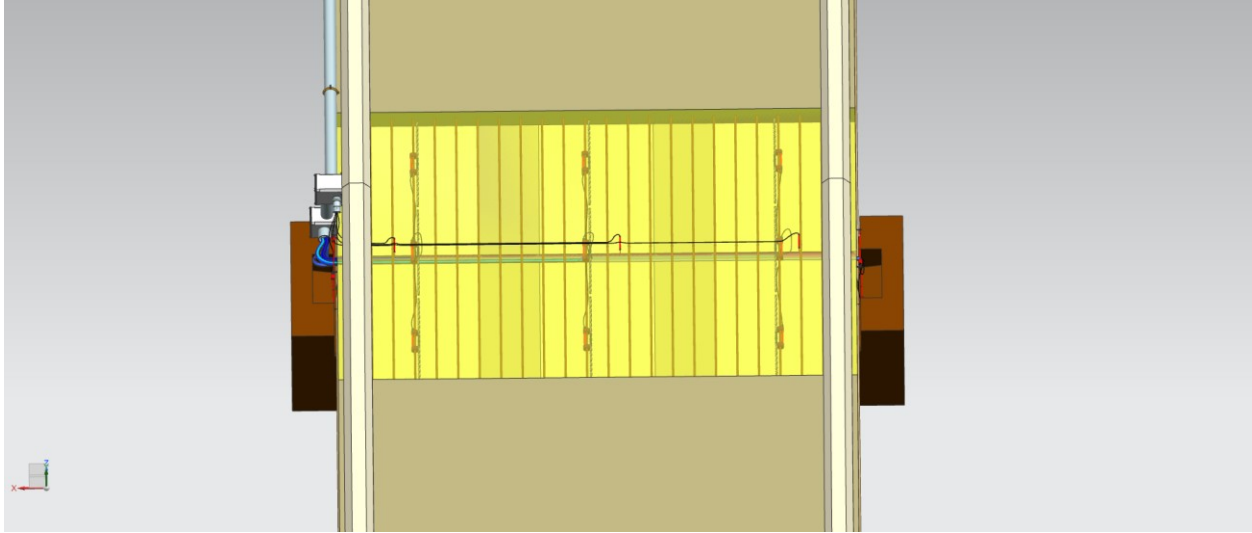


Figure A.3: Top View

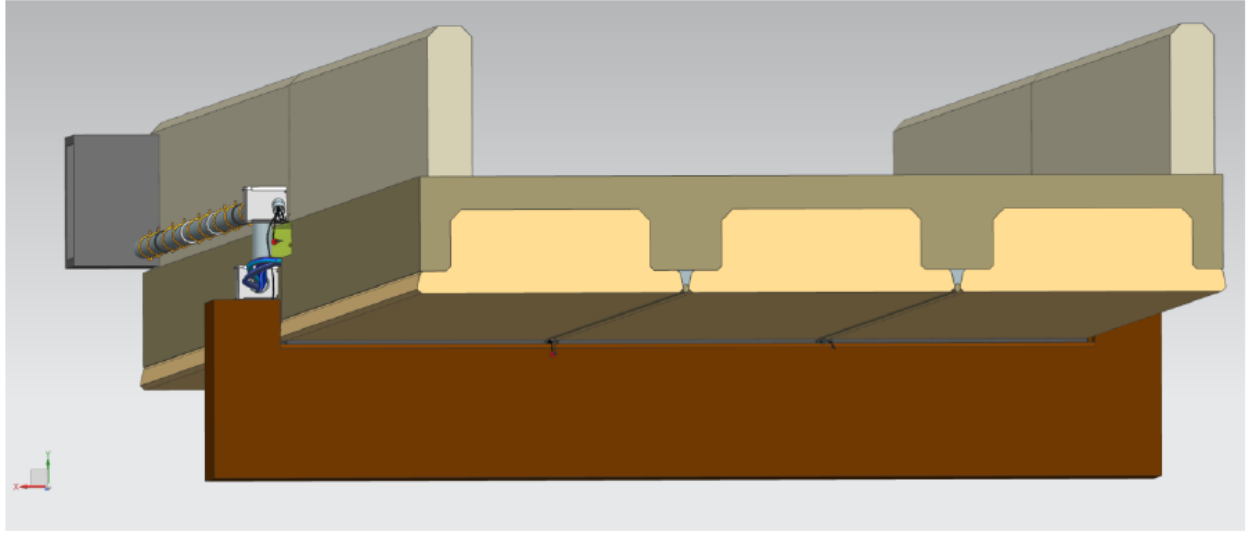


Figure A.4: End View

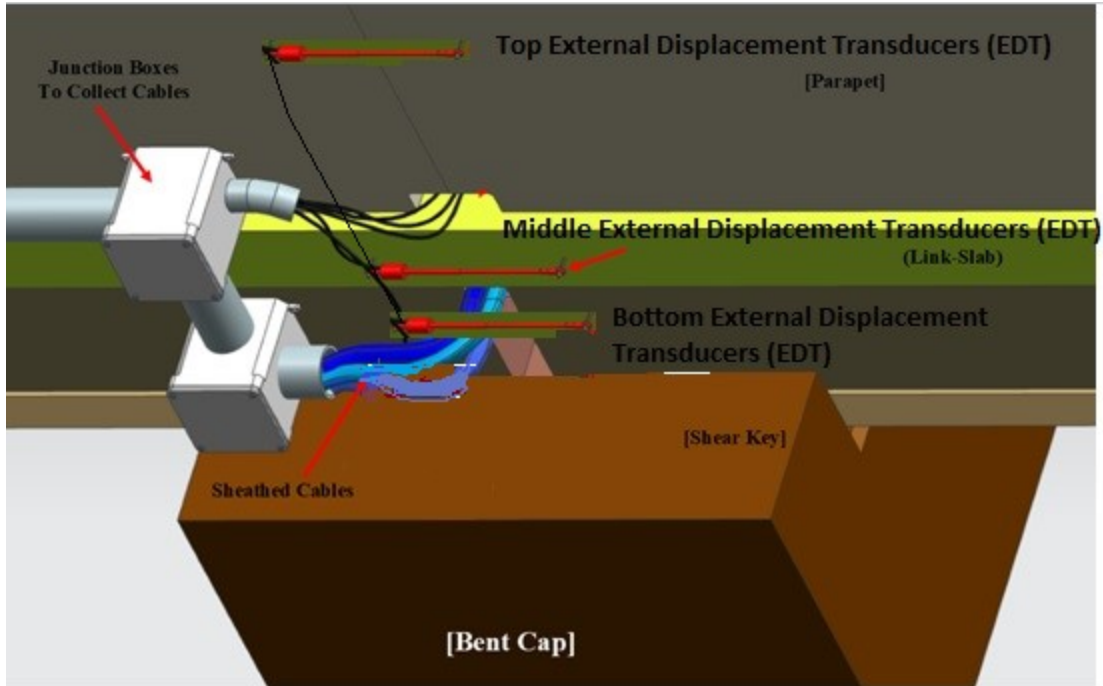


Figure A.5: Top View of Southwest Shear Key

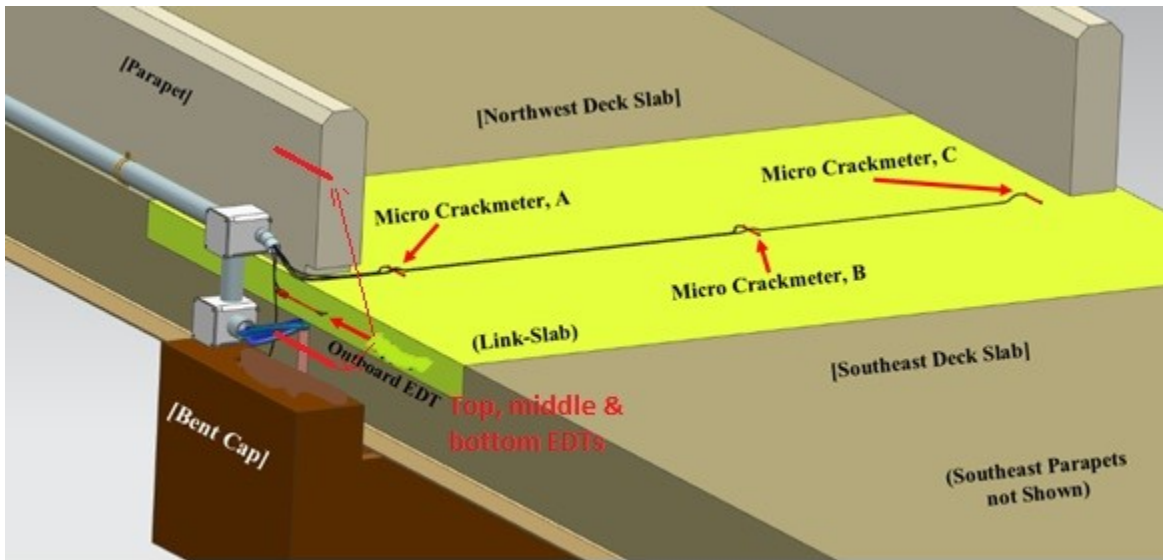


Figure A.6: Side View, Exposed

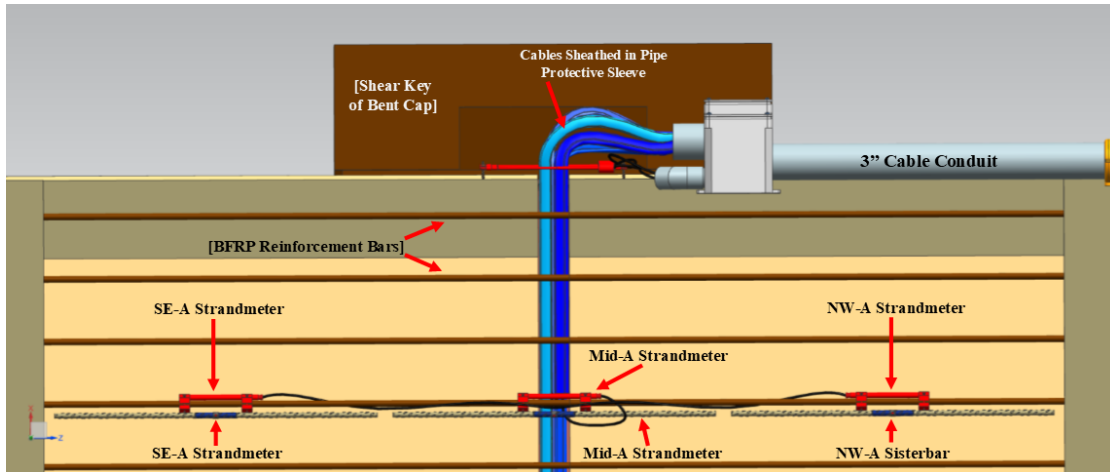


Figure A.7: Detail Link-Slab, Top View

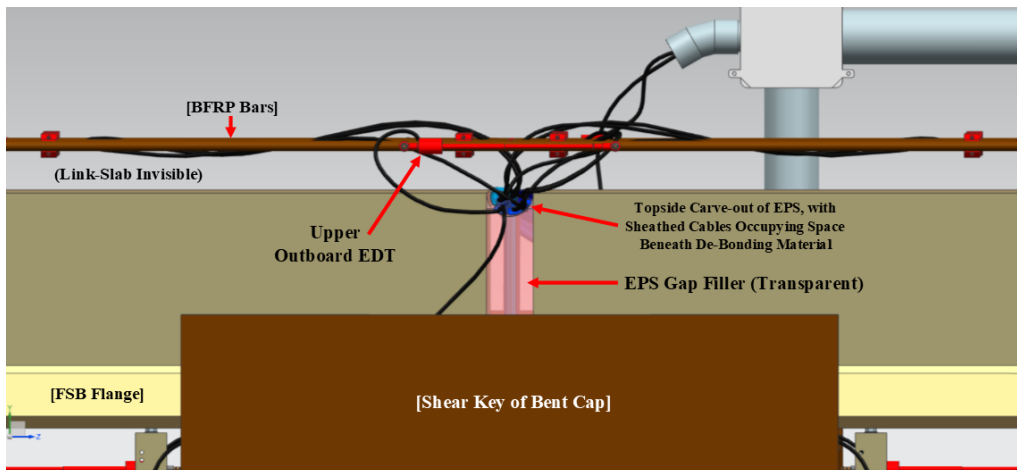


Figure A.8: Side View of Exposed Embedded Sensors and BFRP rebars

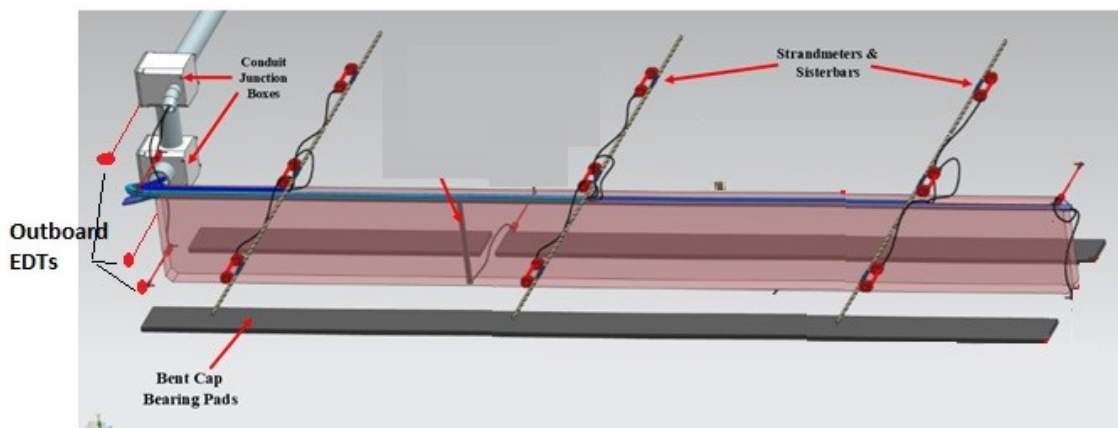


Figure A.9: Exposed View of Cable Routing (EPS is Translucent)

9 Appendix B

Sensor Layout and Information

Group #	Gauge Type/Model & Source	Resolution	Accuracy	Measuring Range	Dimensions	# of Units
1	<i>Strandmeter (4410, Geokon)</i>	<5 $\mu\epsilon$	(+/-) 0.003 mm	3 mm (15000 $\mu\epsilon$)	8" Long x 1.77" Wide Clamps	9
2	<i>Sisterbar (4911, Geokon)</i>	0.4 $\mu\epsilon$	(+/-) 7.5 $\mu\epsilon$	3000 $\mu\epsilon$	36" Length, #4 Size Rebar	9
3	<i>Micro Crackmeter (4422, Geokon)</i>	.001 mm	(+/-) 0.004 mm	4 mm	4.725" Long x 0.315" Diameter	3
4	<i>Crackmeter (4420-25, Geokon)</i>	.00625 mm	(+/-) 0.025 mm	25 mm	Gauge Length: 13.5", Dia:1"	4
5	<i>Crackmeter (4420-25, Geokon)</i>	.00625 mm	(+/-) 0.025 mm	25 mm	Gauge Length: 13.5", Dia:1"	2
6	<i>Datalogger (LC-2, Geokon)</i>	1 part in 20,000; Thermistor: 0.1 deg C	(+/-) 0.05% F.S. (450 to 4000 Hz); Thermistor: (+/-) 2.0% F.S.	450 to 4000 Hz; Thermistor: -30 deg C to 50 deg C	(LxWxH): 13.46" x 11.85" x 6.3"	2

Table B.1: Instrument Groups

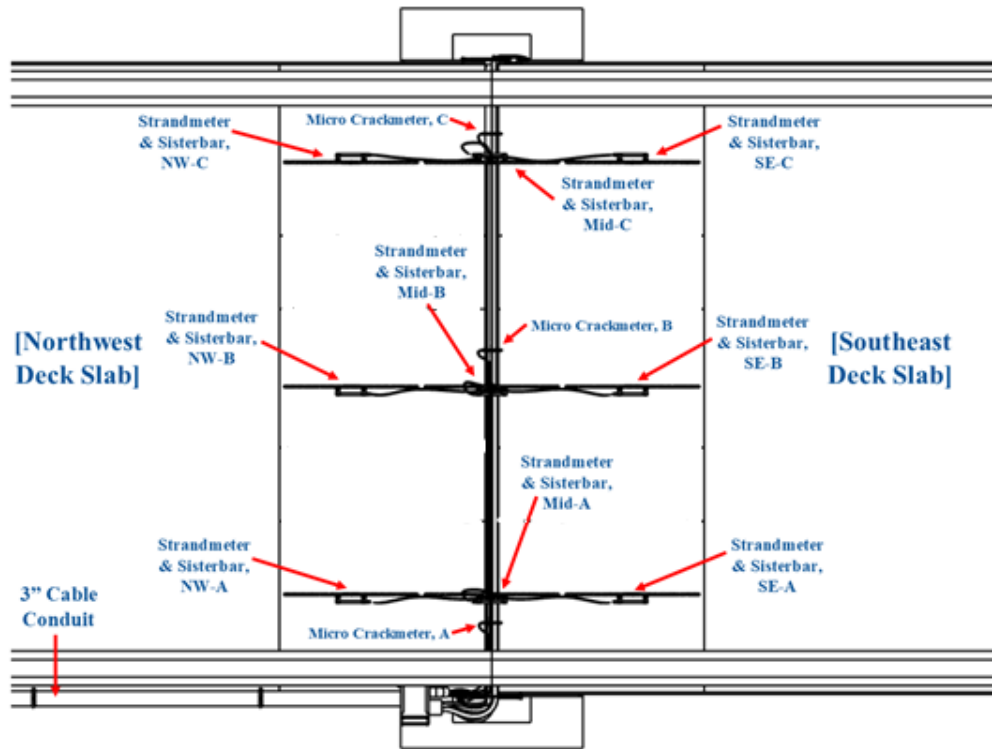


Figure B.2: Drawing, Labels of Embedded Array and Micro Crackmeters

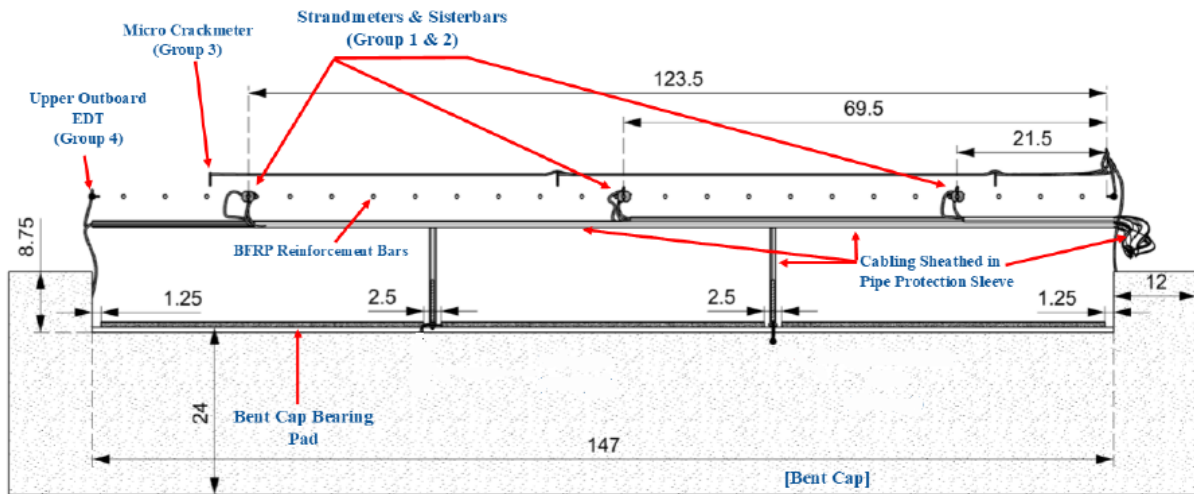


Figure B.3: Drawing, Bent Cap End View (Slabs, Beams, and Parapets not Shown)

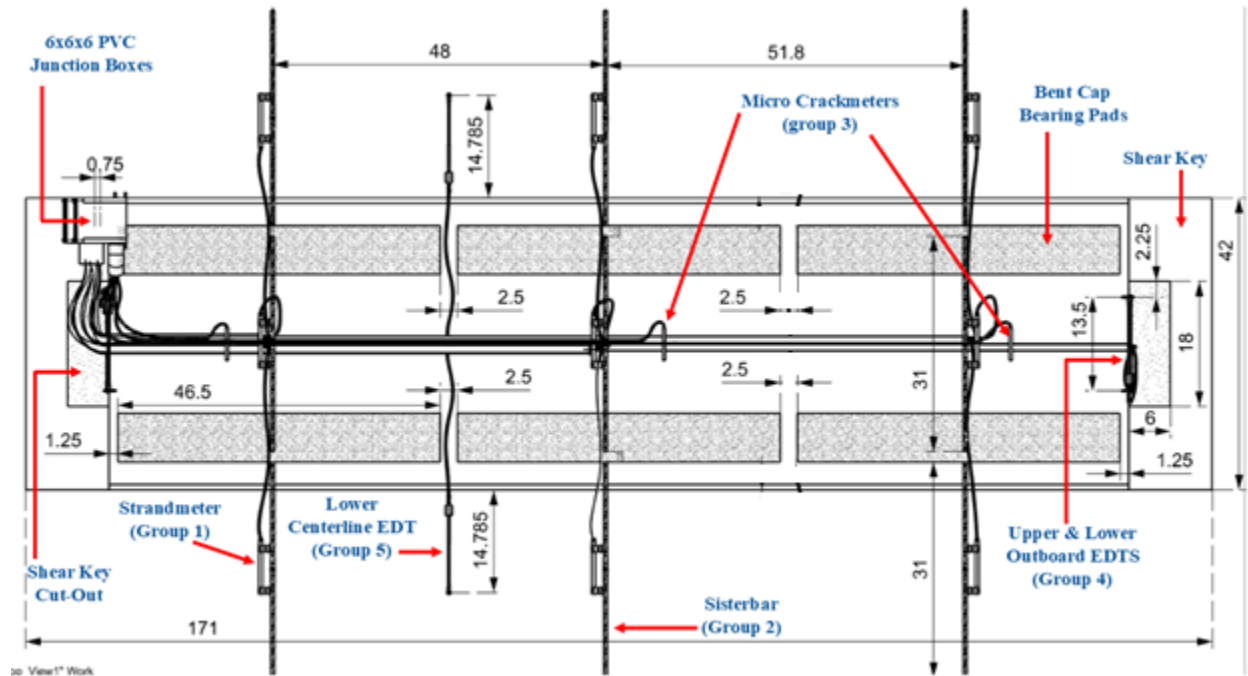


Figure B.4: Drawing, Bent Cap Top View (Slabs, Beams, and Parapets not Shown)

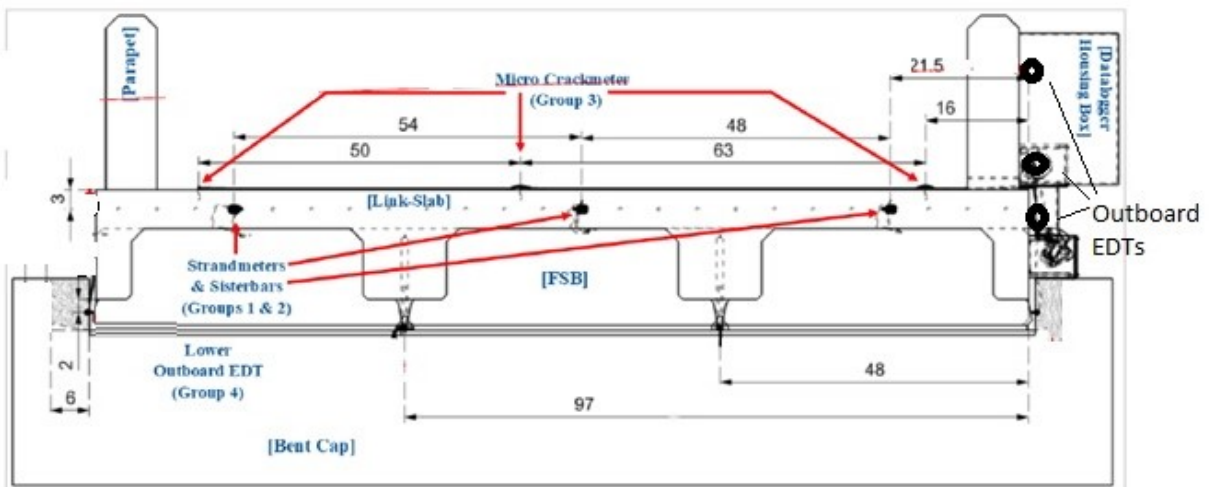


Figure B.5: Drawing, Bridge End View No.1

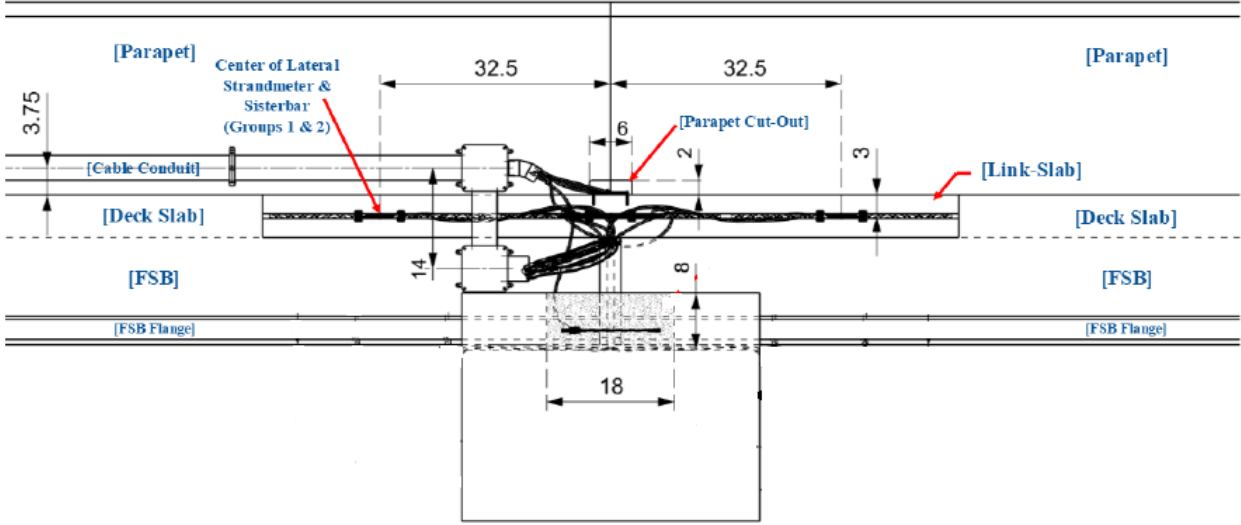


Figure B.6: Drawing, Bridge Side View No.2 (Detail of Link-Slab)

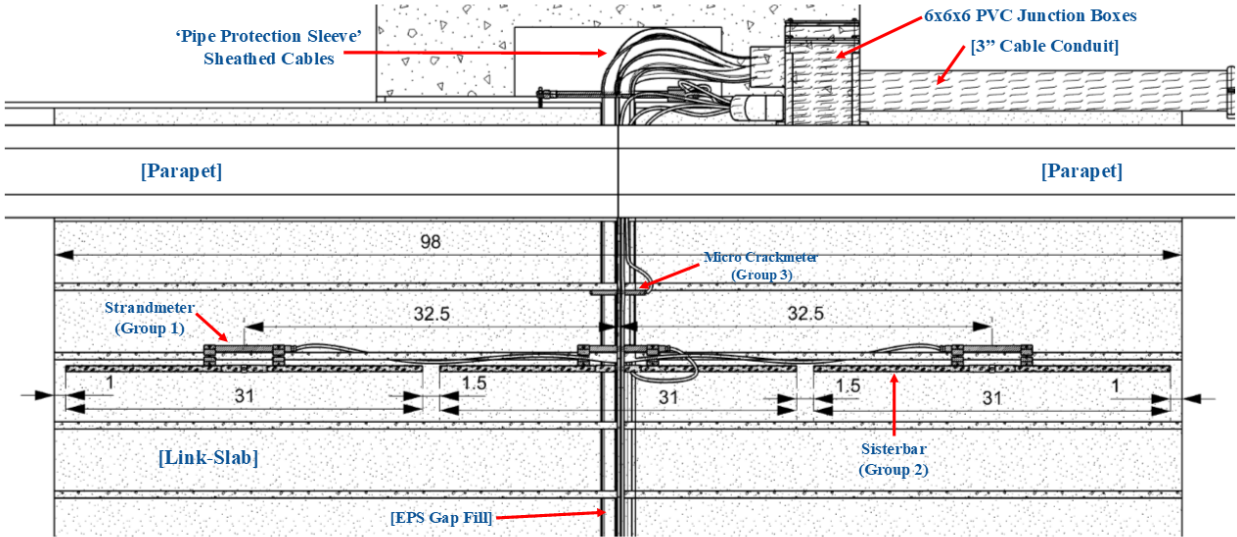


Figure B.7: Drawing, Top View Detail of Link-Slab (Southwest Side)

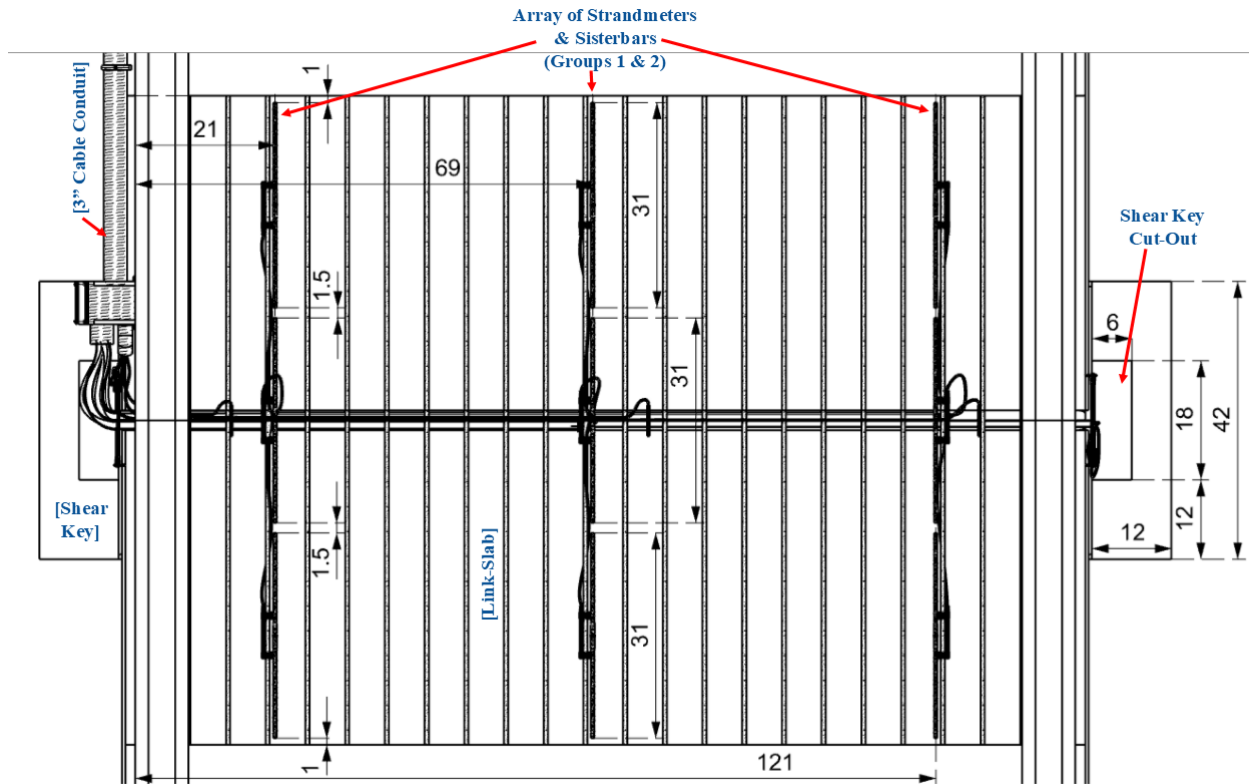


Figure B.8: Drawing, Top View of Whole Link-Slab

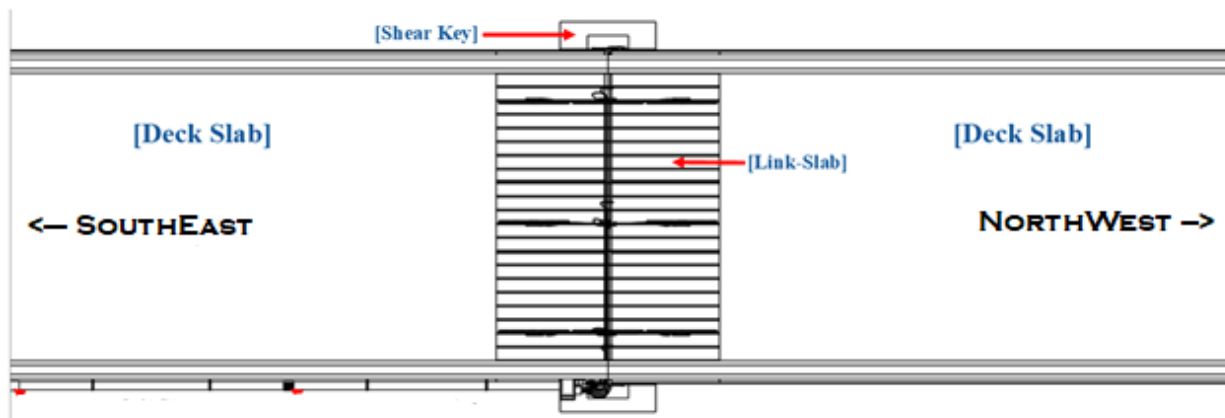


Figure B.9: Drawing, Top View of Bridge (Wide)

10 Appendix C
Manufacturer's instrument datasheets
(Credit: Geokon)

4400 Series

Vibrating Wire Displacement Transducers

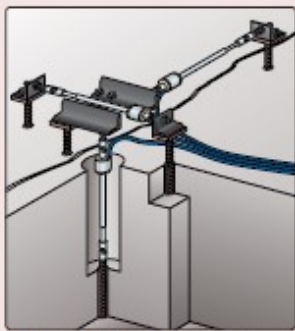
Applications

The 4400 Series are designed to measure or monitor the...

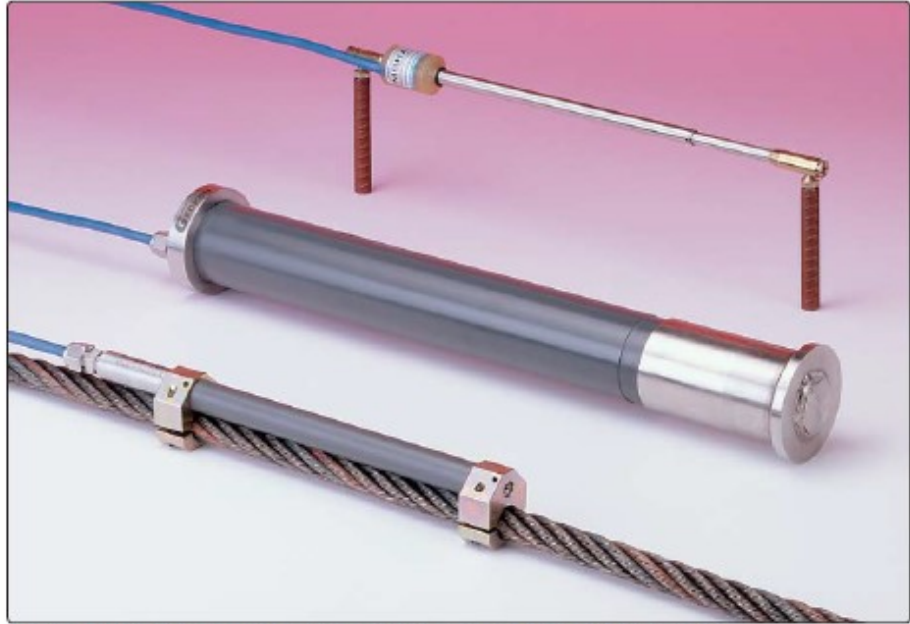
- Expansion or contraction of a joint
- Strains in tendons and steel cables
- Movement across surface cracks and joints
- Closures in underground excavations, tunnels, etc.
- Displacements associated with landslides
- Movement of boulders, snow, etc. on unstable slopes



• Model 4420 Crackmeter installation.



• Three Model 4420 Crackmeters configured as a single 3-D Crackmeter.



• Model 4410 Strandmeter (front), Model 4400 Embedment Jointmeter (center) and Model 4420 Crackmeter (rear).

Operating Principle

Geokon vibrating wire displacement transducers are designed to measure displacements across joints and cracks in concrete, rock, soil and structural members.

In essence, the transducer consists of a vibrating wire in series with a tension spring. Displacements are accommodated by a stretching of the tension spring, which produces a commensurate increase in wire tension.

The wire and spring are connected to a free-sliding rod which protrudes from, and is free to slide inside, a protective outer tube. An o-ring seal prevents water from entering.

The frequency signal is transmitted through the cable to the readout location, conditioned, and displayed on portable readouts or dataloggers.

Advantages and Limitations

The 4400 Series Displacement Transducers are fabricated entirely from stainless steel and are waterproof to 1.75 MPa, which, coupled with their excellent long-term stability, guarantees reliability and performance in even the harshest environments.

An advantage of vibrating wire displacement transducers over more conventional linear potentiometers (or LVDT's) lies mainly in the use of a frequency, rather than a voltage, as the output signal. Frequencies may be transmitted over long lengths of electrical cable without appreciable degradation caused by variations in cable resistance or leakage to ground. This allows for a readout location that may be over a thousand meters from the transducer.

Thermistors are provided with all transducers for temperature measurement.

Model 4400 Embedment Jointmeter

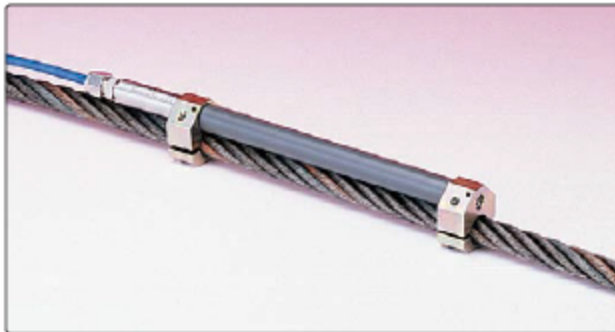


• Model 4400 Embedment Jointmeter shown with socket removed.

The Model 4400 is designed for use in construction joints; e.g. between lifts in concrete dams. In use, a socket is placed in the first lift of concrete and, when the forms are removed, a protective plug is pulled from the socket. The gage is then screwed into the socket, extended slightly and then concreted into the next lift. Any opening of the joint is then measured by the gage which is firmly anchored in each lift. The sensing gage itself, is smaller than the protective housing, and a degree of shearing motion is allowed for by the use of ball-joint connections on the gage.

A tripolar plasma surge arrestor is located inside the housing and provides protection from electrical transients such as those that may be induced by lightning.

Model 4410 Strandmeter



• Model 4410 Strandmeter

The Model 4410 Strandmeter is designed to measure strains in tendons and steel cables, including bridge tendons, cable stays, ground anchors, tiebacks, etc. Two clamps at each end of the strandmeter hold it firmly onto the cable. Various size clamps are available.

Model 4420 Crackmeter



• Model 4420 Crackmeter

The Model 4420 Crackmeters are designed to measure movement across joints such as construction joints in buildings, bridges, pipelines, dams, etc.; tension cracks and joints in rock and concrete.

The ends of the sensor are attached to anchors (with ball joints) that have been grouted, bolted, welded or bonded on opposite sides of the crack or fissure to be monitored. 3-D mounting brackets, which allow measurement of displacements in three orthogonal directions, and special clamps for attachment to a variety of earth reinforcements and geogrids, are also available.

Special versions are offered for underwater use, where water pressures exceed 1.7 MPa, and for use in cryogenic or elevated temperature regimes.

Model 4422 Micro Crackmeter



• Model 4422 Micro Crackmeter

The Model 4422 is a miniature crackmeter intended to measure displacements across surface cracks and joints. It has been specially designed for applications where access is limited and/or where monitoring instrumentation is to be as unobtrusive as possible (e.g. on historical structures or buildings).

Model 4425 Convergence Meter



• Model 4425 Convergence Meter

The Model 4425 Convergence Meter is designed to detect deformation in tunnels and underground caverns by measuring the contraction (or elongation) between 2 anchor points fixed in the walls of the tunnel or cavern.

The Model 4425 consists of a spring-tensioned vibrating wire transducer assembly, turnbuckle, 6 mm diameter connecting rods (stainless steel, fiberglass or graphite), rod clamp, and a pair of anchor points. Changes in distance between the 2 anchors are conveyed by the connecting rods and measured by the transducer.

The Model 4425 can operate in horizontal, inclined or vertical orientations. In areas where construction traffic is expected or where the instrument may be left in an exposed location, some form of protective housing should be considered.

Model 4430 Deformation Meter



• Model 4430 Deformation Meter

The Model 4430 Deformation Meter is designed to measure axial strains or deformations in boreholes in rock, concrete or soil. It can also be embedded in soils in embankments such as earth dams and highway fills. The Model 4430 can be installed in series to give a total deformation profile along a particular axis. Base lengths of the gage can vary from a minimum of 1 meter to over 25 meters.

When used in rock in horizontal or inclined downward boreholes, grouting is the most common method of installation. In vertical boreholes, a special grouting apparatus and hydraulic or snap-ring anchors are required. Direct placement or pre-wiring to a rebar cage allows use in concrete.

Model 4427 Long-Range Displacement Meter

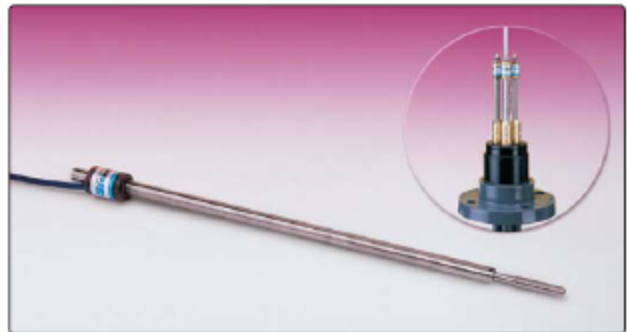


• Model 4427 Long-Range Displacement Meter

The Model 4427 Long-Range Displacement Meter is ideally suited for the measurement of large displacements associated with landslides. The Model 4427 can also be used for monitoring the movement of boulders, snow, etc., on unstable slopes.

The Model 4427 consists of a vibrating wire displacement transducer coupled to a spring motor drive by means of a lead screw. As the cable is pulled, the motor drum rotates and advances the lead screw. Thus the rotation is converted into a linear displacement which is measured by the vibrating wire displacement transducer.

Model 4450 Displacement Transducer



• Model 4450 Displacement Transducer and Extensometer Head Assembly (inset)

The Model 4450 Displacement Transducer provides remote readout capability for Borehole Extensometers (see the Geokon Model A-3, A-4, A-5, A-6 Rod-Type Borehole Extensometers data sheet for more information). They are particularly useful where other types of vibrating wire sensors are used and/or for installations where long cable runs are required.

The Model 4450 can also be installed between borehole anchors, in conjunction with the requisite length connecting rod, to provide a permanent, in-place incremental extensometer (contact Geokon for details).

Technical Specifications

Model	Standard Ranges ¹	Resolution	Accuracy	Nonlinearity	Temperature Range ¹	Dimensions
4400 Embedment Jointmeter	12.5, 25, 50, 100 mm	0.025% F.S.	±0.1% F.S.	<0.5% F.S.	-20°C to +80°C	Length: 406 mm Flange Diameter: 51 mm
4410 Strandmeter	20,000 µε	< 5 µε	±0.1% F.S.	<0.5% F.S.	-20°C to +80°C	Length: 203 mm Clamp Width: 45 mm
4420 Crackmeter	12.5, 25, 50, 100, 150 mm	0.025% F.S.	±0.1% F.S.	<0.5% F.S.	-20°C to +80°C	Lengths: 318, 362, 527 mm Coil Diameter: 25 mm
4422 Micro Crackmeter	3 mm (±1.5 mm)	0.001 mm	±0.1% F.S.	<0.5% F.S.	-20°C to +80°C	Length: 120 mm Diameter: 7.9 mm
4425 Convergence Meter	25, 50, 100, 150 mm	0.025% F.S.	±0.1% F.S.	<0.5% F.S.	-20°C to +80°C	Transducer Lengths: 356, 508, 838 mm Transducer Diameter: 25 mm
4427 Long-Range Displacement Meter	1, 2 m (without resetting)	0.025% F.S.	±1.0% F.S.	—	-30°C to +60°C	Enclosure (L × W × H): 610 × 152 × 152 mm
4430 Deformation Meter	25, 50, 100 mm	0.02% F.S.	±0.1% F.S.	<0.5% F.S.	-20°C to +80°C	Length: varies Flange Diameter: 50 mm
4450 Displacement Transducer	12.5, 50, 100, 150, 300 mm	0.02% F.S.	±0.1% F.S.	<0.5% F.S.	-20°C to +80°C	Lengths: 210, 212, 270, 410 mm Coil Diameter: 19 mm

¹Other ranges available on request.

Rebar Strainmeters and "Sister Bars"

Applications

Rebar Strainmeters are commonly used for measuring strains in...

- Concrete piles & caissons
- Slurry walls
- Cast-in-place concrete piles
- Concrete foundation slabs and footings
- Osterberg pile tests
- All concrete structures



• Close-up of Model 4911 shown as installed in concrete pile reinforcing cage.



• Model 4911A Rebar Strainmeter (front) and the Model 4911 "Sister Bar" (rear).

Operating Principle

Rebar Strainmeters and "Sister Bars" are designed to be embedded in concrete for the purpose of measuring concrete strains due to imposed loads. The Rebar Strainmeter is designed to be welded into, and become an integral part of, the existing rebar cage, while the "Sister Bar" is installed by tying it alongside an existing length of rebar in the rebar cage.

The rebar extensions on either side of the central strain-gauged area are long enough to ensure adequate contact with the surrounding concrete so that the measured strains inside the steel are equal to the strains in the surrounding concrete.

In use, Rebar Strainmeters and "Sister Bars" are usually installed in pairs on either side of the neutral axis of the structural member being investigated. This is done so that bending moments may be analyzed in addition to axial loads.

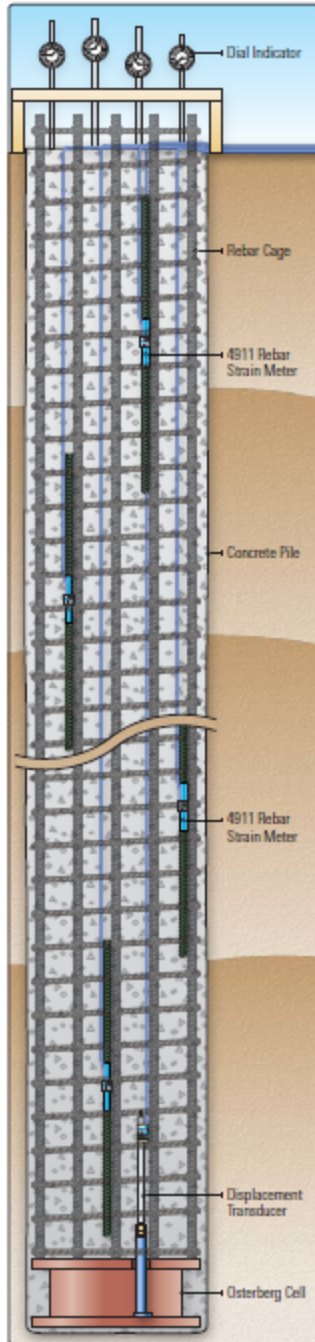
A built-in thermistor enables the measurement of temperatures and aids in the evaluation of thermally induced strains.

Advantages and Limitations

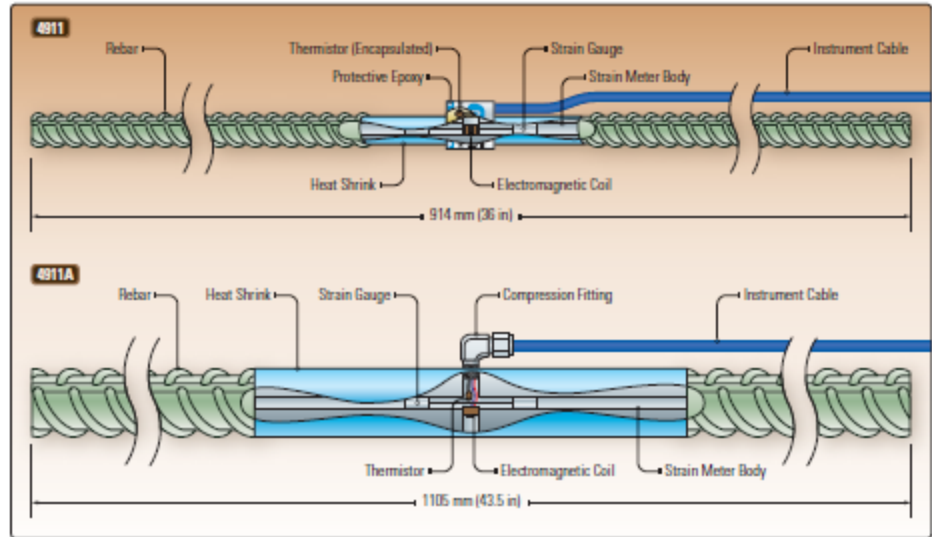
The main advantage of the Rebar Strainmeters and "Sister Bars" lies in their ruggedness. They are fully waterproof and virtually indestructible so that, if the cable is adequately protected, they are safe from damage during the concrete placement.

Each Rebar Strainmeter and "Sister Bar" is individually calibrated and tested for weld strength. The Rebar Strainmeter requires the services of an experienced welder who can guarantee full-strength welds, whereas the "Sister Bar" is very easy to install.

The single vibrating wire strain sensor, located along the axis of the strainmeter, is not affected by the bending of the strainmeter itself. It also has the advantage of all vibrating wire sensors, namely: long-term stability, it can be used with long cables and it's relatively unaffected by moisture intrusion into the cables.



● Installation of the Model 4911 in an Osterberg Cell pile test. (For more information regarding Osterberg Cell pile testing, please contact Loadtest, Inc. — www.loadtest.com.)



● Illustration of the Model 4911 "Sister Bar" and Model 4911A Rebar Strainmeters and their various components.

System Components

A vibrating wire strain gauge sensor is fixed axially inside a short, central length of round steel bar. This central section is de-bonded from the surrounding concrete by means of a plastic coating, and is extended by welding a length of rebar to each end. The Model 4911A Rebar Strainmeter is available in various sizes to match the size of the rebar cage into which it is to be welded, whereas the Model 4911 "Sister Bar" comes in one size only (#4 rebar, at approximately 12.7 mm in diameter).

A thermistor to measure temperature changes can be included in the 4911 and 4911A sensors.

Readouts and Cables

The 4911 Series Rebar Strainmeters are read using the Model GK-404 or GK-405 Readouts. Alternatively, the LC-2 Series or 8600 Series Dataloggers can be used.

The 4911 Series Rebar Strainmeters use the Model 02-250V6 4 pair, 22 AWG cable.

Technical Specifications

	4911	4911A
Standard Range	3000 $\mu\epsilon$	3000 $\mu\epsilon$
Resolution	0.4 $\mu\epsilon$	0.4 $\mu\epsilon$
Accuracy ¹	$\pm 0.25\%$ F.S.	$\pm 0.25\%$ F.S.
Nonlinearity	< 0.5% F.S.	< 0.5% F.S.
Temperature Range ²	-20°C to +80°C	-20°C to +80°C
Rebar Sizes	#4 (Sister Bar)	#6, 7, 8, 9, 10, 11, 14
Length	914 mm	1105 mm

¹Accuracy established under laboratory conditions.

²Other ranges available on request.

LC-2 Series Dataloggers

Applications

The LC-2 Series Dataloggers are used to read all GEOKON® vibrating wire instruments. Sensors that can be read and monitored include...

- Piezometers
- Precision water level sensors
- Crackmeters
- Settlement systems
- Temperature sensors



• Model 8002-WP-2 (LC-2WP) Waterproof Single-Channel Datalogger.



• Model 8002-16-1 (LC-2x16) 16-Channel, Model 8002-4-1 (LC-2x4) 4-Channel and Model 8002-1-1 (LC-2) Single-Channel Dataloggers.

Operating Principle

The Model 8002 LC-2 Series Dataloggers are designed to read both the vibrating wire element and the integral thermistor of any GEOKON vibrating wire sensor.

The LC-2 (internal hard wired transducer connection), LC-2A (10-pin transducer connector option) and LC-2WP (waterproof option) are designed to be standalone, single-channel dataloggers, which makes them especially useful for the remote and continuous monitoring of isolated sensors.

The LC-2x4 is a self-contained, 4-channel version (vibrating wire with thermistor) of the LC-2, and the LC-2x16 is a 16-channel (vibrating wire with thermistor) version.

The LC-2, LC-2x4 and LC-2x16 are housed inside Fiberglass NEMA 4X enclosures, which makes them very robust, weather-proof and particularly well-suited to operation in harsh environments. The LC-2WP is a waterproof version housed inside a rugged PVC enclosure. Low power consumption provides long battery life and the condition of the main batteries is reported as an element in the data array.

Data memory consists of 320K bytes of EEPROM. This translates into a memory storage capacity of 16,000 arrays for the LC-2 and LC-2A, 10,666 arrays for the

LC-2x4 and 3,555 arrays for the LC-2x16. Each array consists of the datalogger ID, day (Julian or month/day format), time (HHMM), seconds, main battery voltage, datalogger temperature, vibrating wire sensor reading (in engineering units), the sensor temperature and array number. The array transmission is in comma delineated ASCII text, for easy importation into popular spreadsheet programs.

Up to 6 intervals may be specified from a logarithmic table, with a maximum of 255 iterations. The programmed intervals can be started or stopped once at preset times of the day.

Power

The Model 8002 LC-2 Series Dataloggers are powered by easily accessible alkaline or lithium (optional) D cells. Additional power options, including internal and external 12 V batteries and solar panels, are available (please contact GEOKON for more information).

Communications

The Model 8002 LC-2 Series Dataloggers are available with an RS-232 Serial Interface or with a direct USB 2.0 connection; patch cords are supplied for this purpose.

Technical Specifications

	Single-Channel	4-Channel	16-Channel
	LC-2, LC-2A, LC-2WP*	LC-2x4, LC-2x4A	LC-2x16
Measurement Accuracy	±0.05% F.S. (450-4000 Hz)	±0.05% F.S. (450-4000 Hz)	±0.05% F.S. (450-4000 Hz)
Measurement Resolution	1 part in 20,000	1 part in 20,000	1 part in 20,000
Program Memory	24K FLASH	24K FLASH	24K FLASH
Data Memory	320K EEPROM	320K EEPROM	320K EEPROM
Data Connection	RS-232, USB or RS-485	RS-232, USB or RS-485	RS-232, USB or RS-485
Storage Capacity (Arrays)	16,000 ¹	10,666	3,555
Temperature Range	-30°C to +50°C	-30°C to +50°C	-30°C to +50°C
Temperature Measurement	(accuracy) 2.0% F.S. (resolution) 0.1 °C	(accuracy) 2.0% F.S. (resolution) 0.1 °C	(accuracy) 2.0% F.S. (resolution) 0.1 °C
Communication Speed	9600 bps	9600 bps	9600 bps
Communication Parameters	8 data bits, no parity, 1 stop bit	8 data bits, no parity, 1 stop bit	8 data bits, no parity, 1 stop bit
Power Supply	3 VDC (2 Alkaline 'D' cells)	3 VDC (2 Alkaline 'D' cells)	3 VDC (4 Alkaline 'D' cells)
Communication Current	< 100 mA	< 100 mA	< 100 mA
Measurement Current	< 250 mA	< 250 mA	< 250 mA
Quiescent Current	< 500 µA	< 500 µA	< 500 µA
Scan Interval	3 - 86,400 seconds (24 hours)	10 - 86,400 seconds (24 hours)	30 - 86,400 seconds (24 hours)
Operating Time (20°C)	3 days - 3 years, depending on scan interval	8 days - 2 years, depending on scan interval	8 days - 2 years, depending on scan interval
Sensor Connection	(LC-2, LC-2WP*) Hard wired (LC-2A) 10-pin Connector	(LC-2x4) Hard wired (LC-2x4A) 10-pin Connector	(LC-2x16) Hard wired (LC-2x16A) 10-pin Connector
L x W x H H x B	(LC-2, LC-2A) 122 x 120 x 91 mm (LC-2WP*) 211 x 168 mm	260 x 160 x 91 mm	342 x 301 x 160 mm ²

¹8,000 arrays when used with LogView software. ²Does not include mounting feet.

Ordering Information

	Single-Channel	4-Channel	16-Channel
Data Connection	LC-2, LC-2A, LC-2WP*	LC-2x4	LC-2x16
RS-232	8002-1-1, 8002-1A-1	8002-4-1, 8002-4A-1	8002-16-1, 8002-16A-1
USB	8002-1-2, 8002-1A-2, 8002-WP-2*	8002-4-2, 8002-4A-2	8002-16-2, 8002-16A-2
RS-485	8002-1-3, 8002-1A-3	8002-4-3	8002-16-3

Software

LogView Software simplifies the task of configuration, communication, monitoring, data collection and data reduction using the Model 8002 (LC-2) Series Dataloggers.

LogView is compatible with **Windows®** 2000, XP, XP Pro, Vista and 7.

Please see the Model 8001-3 LogView Software data sheet for more information.

*PLEASE NOTE: THE MODEL 8002-WP-2 (LC-2WP) WATERPROOF SINGLE-CHANNEL DATALOGGER IS NOT CE APPROVED.

Instrumentation Cables

Applications

GEOKON® cables are of the highest quality materials and construction. They are designed to be matched with the appropriate instrument for a variety of geotechnical and hydrological applications. Standard and specialized cables are available for...

- Typical applications
- High temperature environments
- Extra abrasion resistance
- Heavy duty use



• The Model 4500HT High Temperature Piezometer depicts a **Teflon®** cable threaded inside stainless steel tubing.



• Standard GEOKON cables.

Cable Design

GEOKON cables are made from individual stranded copper conductors encased in an insulation material. Individual, insulated conductors are twisted into pairs, bundled inside a conductive Mylar-type shielding material and then covered by an outer jacket made from the most suitable material. In addition, cables may be water blocked, armored, or may contain steel or **Kevlar®** cables for additional strength, or plastic tubes for circulation fluids, or for venting to atmosphere.

Cable Conductors

In general, the number of conductors in a cable is determined by the number of sensors to be connected to the cable, and the number of conductors required by each sensor.

The type of conductor normally used is stranded, 22 AWG tinned copper. Stranded conductors are more flexible than solid conductors, which makes the cable easier to handle during installation.

Cable Shielding and Insulation

Shielding provides protection from electromagnetic radiation coming from nearby electrical equipment, lightning strikes and fields surrounding power lines, transformers, etc. GEOKON multi-conductor cables are individually shielded and twisted in pairs, which helps minimize common mode interference. Drain wires connected electrically to Mylar-type shields provide a simple means of connecting all the shields to a common ground. For applications with very high levels of EMI, such as in pumping wells, a special cable with a braided shield can be provided.

Plastic insulation is typically used on the individual copper conductors. Polyethylene or polypropylene insulation is used at normal temperatures and **Teflon** is most often used for high temperature.

Outer Jackets

GEOKON cable jackets are thicker than regular commercial types, and pressure extruded, which produces cables that are rounder, firmer and easier to grip and seal at the point of entry on the sensor. A wide variety of outer jacket materials is available depending on the end use:

Neoprene: A synthetic rubber compound commonly used for outdoor applications, with good resistance to gasoline, oils etc. Ordinary rubber should never be used.

PVC: A common choice for its good electrical properties and for being water-proof. It should not be used at low temperatures where it becomes brittle.

Polyurethane: This material is very resistant to cuts and abrasions making it useful for cables that are subject to repeated rough handling. It is not as water resistant as PVC but has better low temperature capabilities.

High Density Polyethylene: An excellent material that is highly resistant to environmental attack and exhibits excellent low temperature characteristics. Unfortunately, like **Teflon**, the material is so slippery that splicing and potting compounds will not stick to it.

Teflon: This material is essential wherever sensors and cables are subject to high temperature. It has outstanding resistance to environmental attack and has excellent low temperature properties. However, splicing and potting compounds will not adhere to it.

Other compounds such as **Kevlar** or **Kapton®** etc. may be required where there is a need for low smoke emissions, flame retardant, or resistance to nuclear radiation.

Armor

Armored cables are most often needed for sensors installed in earth embankments or landfills where large forces are exerted on the cable by compaction equipment and earth moving vehicles, and by settlement, "weaving," and side-ways spreading of the embankment as it is built. Armored cables should not be connected directly to strain gauges or crackmeters because the stiffness of the cable would pull on the gauge and alter the readings. Armored cable is not necessary in concrete. The armor usually takes the form of a helically laid layer of steel wire. In very severe situations, regular cable may be put inside stainless steel tubing.

Vented Cables

Special cables are available which contain plastic tubes inside of them as well as the usual conductors. These tubes can be used to transport air or other fluids. This kind of cable is required for vented piezometers, where a single vent tube allows the inside of the pressure sensor to be connected to the ambient atmosphere to provide automatic barometric compensation.

Cable Splices

Cable splicing is best done using commercially available splicing kits containing butt splice connectors and epoxy potting compounds. These help provide a waterproof and mechanically strong splice. Armored cables are difficult to splice if the mechanical strength is to be maintained; special mechanical connections need to be fabricated which will grip the armor firmly.

Technical Specifications

Model	Conductors	Conductor Insulation	Drain Wire	Cable Jacket*	Nominal O.D.	Temp. Range
02-187P6	4-conductor, 2 twisted pairs, 22 AWG 7/30	8 mil HDPP	24 AWG	Blue PU	4.75 mm (±0.25 mm)	-20 °C to +80 °C
02-187V3	4-conductor, 2 twisted pairs, 22 AWG 7/30	8 mil HDPP	24 AWG	Red PVC	4.75 mm (±0.25 mm)	-20 °C to +80 °C
02-250P4	4-conductor, 2 twisted pairs, 22 AWG 7/30	8 mil HDPP	24 AWG	Green PU	6.35 mm (±0.25 mm)	-20 °C to +80 °C
02-250T	4-conductor, 2 twisted pairs, 22 AWG 19/34	10 mil FEP	24 AWG	White Teflon with aluminum polyester foil shielding	5.20 mm (±0.25 mm)	-80 °C to +200 °C
02-250V6	4-conductor, 2 twisted pairs, 22 AWG 7/30	10 mil HDPP	24 AWG	Blue PVC	6.35 mm (±0.25 mm)	-20 °C to +80 °C
02-313P1	4-conductor, 2 twisted pairs, 22 AWG 7/30	10 mil HDPP	24 AWG	Black PU with Integral stranded steel wire	7.95 mm (±0.38 mm)	-20 °C to +80 °C
02-335V78	4-conductor, 2 twisted pairs, 24 AWG 7/32	10 mil HDPP	24 AWG	Yellow PU with Integral 0.125" Ø PE vent tube	8.50 mm (±0.38 mm)	-20 °C to +80 °C
02-500PE1A	4-conductor, 2 twisted pairs, 22 AWG 7/30	10 mil HDPP	24 AWG	Black PVC Inner; Black MDPE outer, with served armor	12.70 mm (±0.38 mm)	-20 °C to +80 °C
03-250V0	6-conductor, 2 twisted pairs, 24 AWG 7/32	10 mil HDPP	24 AWG	Black PVC	6.35 mm (±0.38 mm)	-20 °C to +80 °C
04-375V9	8-conductor, 4 twisted pairs, 22 AWG 7/30	10 mil HDPP	22 AWG	Violet PVC	9.50 mm (±0.38 mm)	-20 °C to +80 °C
04-500VT10	8-conductor, 4 twisted pairs, 22 AWG 7/30	10 mil HDPP	22 AWG	Gray PVC with Integral 0.125" Ø PE vent tube	12.70 mm (±0.38 mm)	-20 °C to +80 °C
05-375V12	10-conductor, 5 twisted pairs, 22 AWG 7/30	10 mil HDPP	22 AWG	Tan PVC	9.50 mm (±0.38 mm)	-20 °C to +80 °C
06-312V0	12-conductor, 6 twisted pairs, 24 AWG 7/32	10 mil HDPP	24 AWG	Black PVC	7.95 mm (±0.38 mm)	-20 °C to +80 °C
06-500V7	12-conductor, 6 twisted pairs, 22 AWG 7/30	10 mil HDPP	22 AWG	Orange PVC	12.70 mm (±0.38 mm)	-20 °C to +80 °C
12-625V5	24-conductor, 12 twisted pairs, 22 AWG 7/30	10 mil HDPP	22 AWG	Brown PVC	15.90 mm (±0.38 mm)	-20 °C to +80 °C

*All outer cable jackets are pressure extruded. In addition, other cable jackets are available for special applications.

FEP - Fluorinated Ethylene Propylene (Teflon) | HDPP - High Density Polypropylene | MDPE - Medium Density Polyethylene | PE - Polyethylene | PP - Polypropylene | PU - Polyurethane | PVC - Polyvinylchloride

GEOKON | **TRUSTED MEASUREMENTS**

GEOKON
48 Spencer Street
Lebanon, NH 03766 · USA

www.geokon.com
e: info@geokon.com
p: +1-603-448-1562

GEOKON is an
ISO 9001:2015
registered company

The **GEOKON** logo and word mark are registered trademarks with the United States Patent and Trademark Office. | **GEOKON** maintains an ongoing policy of design review and reserves the right to amend products and specifications without notice. | **Teflon**® **Kevlar**® and **Kapton**® are registered trademarks of E.I. du Pont de Nemours and Company or its affiliates. | All other trademarks are the property of their respective owners.

©GEOKON. All Rights Reserved. | Rev-G-04/11/2019

11 Appendix D

Literature Review

The national bridge inventory indicates that a big percentage of the highway bridges in United States are designed as single or multiple simple-span girders supported at the piers and abutments and separated by joints (FHWA 2004). These joints are provided at the girder ends of each simple span to allow the movement of the deck and superstructure due to temperature changes, shrinkage, creep, and other effects. These deck joints generally lead to water, sometimes contaminated with chlorides, leaking through the joints causing deterioration and corrosion of the bridge deck, girders, bearing, and supporting systems. Joints can also get filled with debris and fail to allow expansion and contraction of the superstructure. Therefore, the joint systems affect the durability of bridge structures and do not provide a reliable and leak-proof performance. In addition, joints and bearings can be expensive to install and maintain.

A growing trend in bridge design has been toward the elimination of joints and bearings in the bridge superstructure. Yet, the behavior of jointless bridge deck is not precisely known and the designs could have some uncertainties. Despite the numerous benefits of jointless bridge decks, there is no standardized design procedures for these bridges and there is only a list of specifications and design recommendations available. Therefore, there is a need to further investigate the feasibility of an innovative system for reducing or eliminating the number of bridge deck joints. The alternatives include using a concrete or ultra-high-performance concrete (UHPC) link-slab reinforced with steel or fiber-reinforced polymer (FRP) rebar to join adjacent bridge decks without imposing girder continuity.

Over many years, the use of jointless bridges has proven to be an excellent alternative to preserve bridges from the adverse effects of debris, leaking water, and salt induced corrosion damage. The jointless bridge option had also proven to be an economical option that provided several inherent design advantages. In the AASHTO LRFD Bridge Design Specifications, there are no requirements for maximum bridge length allowed without expansion joints. Most state highway agencies allow eliminating joints for bridges whose lengths are less than 350 feet for bridges with steel beams and 650 feet with concrete beams; however, there are some bridges over 1000 ft long that have performed well without expansion joint (Tadros 2016).

Several researchers indicted the effect of deck continuity over the piers on the moment developed in the spans, the reduction in deflection and vibration than simple span bridge girders, the improved durability and riding quality after eliminating the joints. Gastal and Zia (1989) performed an analysis of bridge beams with jointless decks. ElSafty (1994) conducted an analysis and investigation of jointless bridge decks with partially debonded simple span beams. Zia et al. (1998) investigated casting fully-continuous deck over simply supported girders with partial debonding of the deck from the girders ends at supports, using both numerical and experimental analysis, as shown in Fig. 2. Okeil and Elsafty (2005) investigated the partial continuity in bridge girders with jointless decks and the effect of the system's support configuration on the axial force developed in the link-slab. Caner and Zia (1998) presented the results of a test program to investigate the behavior of link-slabs connecting two adjacent simple-span girders and proposed a simple method for designing the link-slab. ElSafty and Okeil (2008) also investigated extending the service life of bridges using continuous decks, as shown in Fig. 3 and Fig. 4.

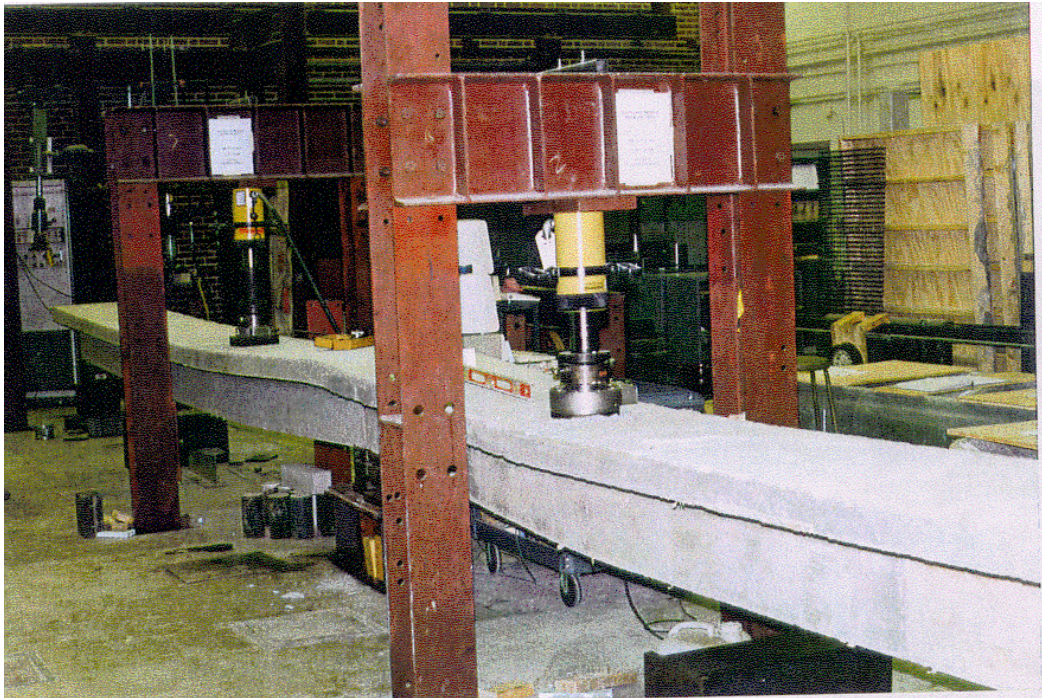


Fig. 2: Testing of a 2-span bridge model - Zia et al. (1998)

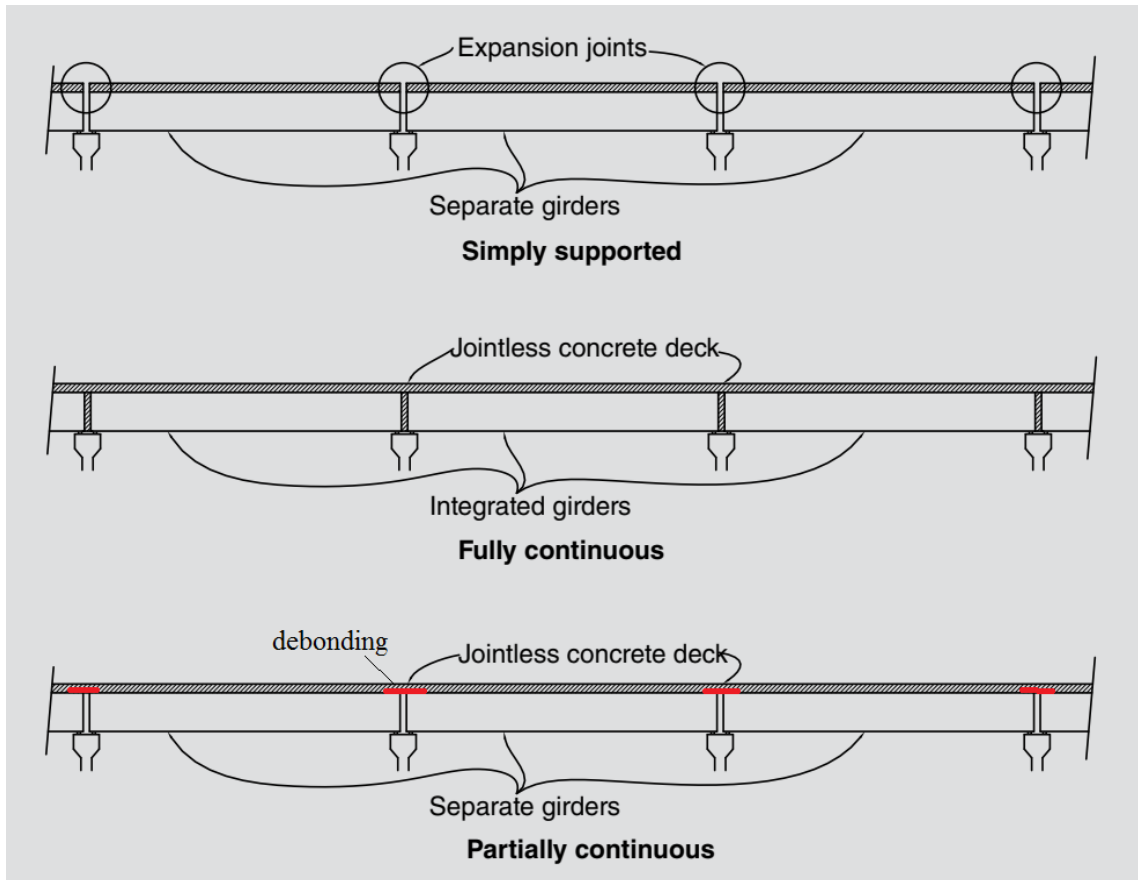


Fig. 3: Some types of jointless bridge decks

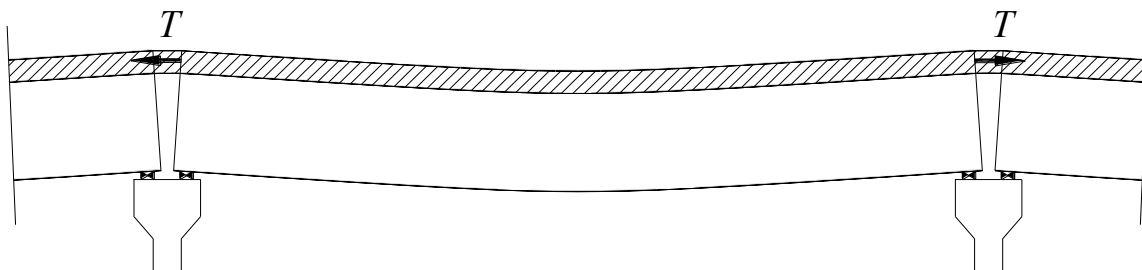


Fig. 4: Continuity caused by linking concrete decks in adjacent spans

Thippeswamy et al. (2002) conducted an investigation on jointless bridges to study the behavior of jointless bridges supported on piles and spread footings and subjected to varying load conditions. In addition, time-dependent material properties have also been investigated. In their study, Thippeswamy et al. (2002) presented synthesized analytical data to understand the performance under varying load combinations, field testing and monitoring results of a jointless

bridge West Virginia, and effects of primary versus secondary loads, boundary conditions, and system flexibility on induced stresses at various bridge locations.

Reyes and Robertson (2011) investigated the use of high-performance fiber-reinforced cementitious composite (HPFRCC) reinforced with glass fiber reinforced polymer (GFRP) bars as link-slabs to replace the bridge expansion joints. Several small-scale specimens were tested. Then, a full scale test specimen with a full scale bridge expansion joint was investigated to characterize the performance of HPFRCC with GFRP reinforcing bars. The full-scale bridge expansion joint specimen emulated an expansion joint condition of a composite steel girder to concrete deck slab section. The link-slab was subjected to cyclic axial strains in both tension and compression and later in direct tension until failure. It was found that the cast-in-place link-slab had the advantage of providing good continuity with the bridge deck. The failure was due to rupture of the anchorage at the ends of the link-slab.

Virginia DOT also suggested the shown link-slab detail, Fig. 5.

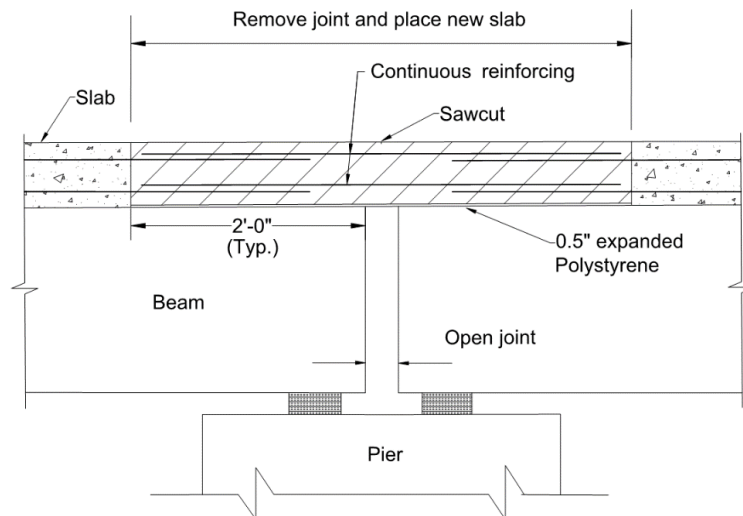


Fig. 5: Use of link-slab by VDOT for rehabilitation work to eliminate expansion joint

Virginia DOT also listed the following types of joint systems used in Virginia, as shown in Figs. 6-13:

- **Armored Joints – Open or Sealed**

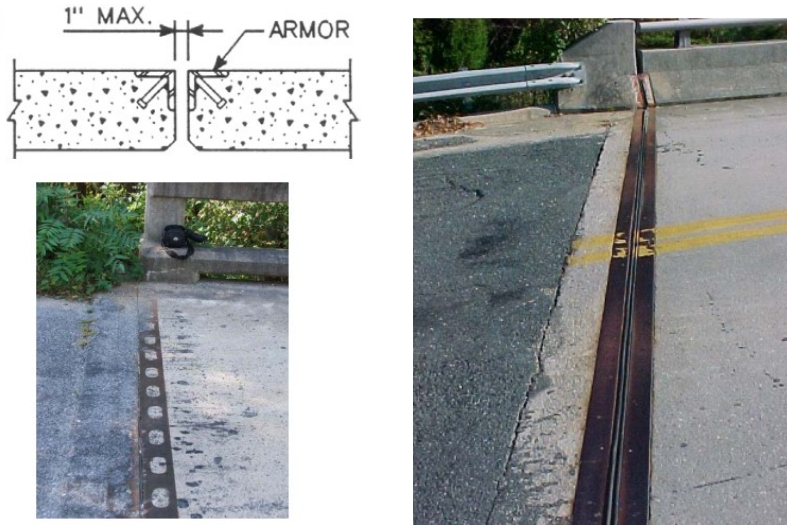


Fig. 6: Armored Joints

- **Hot Poured Sealer /Expansion Material**

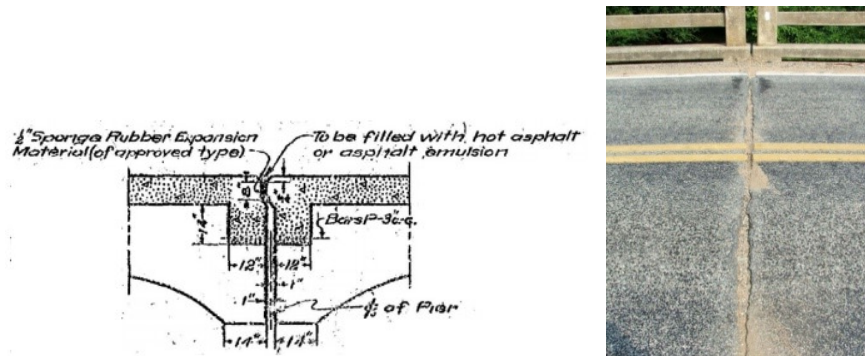


Fig. 7: Hot Poured Sealer

- **Preformed Elastomeric Compression Seals**

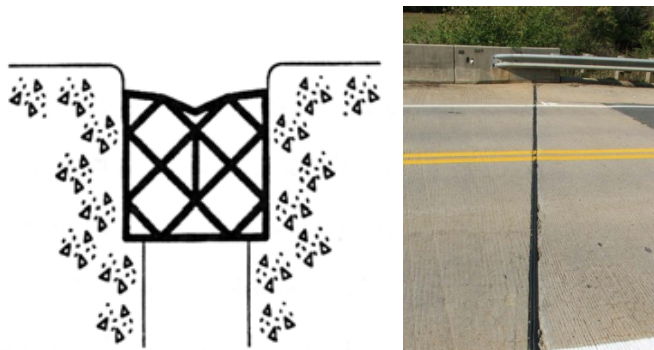


Fig. 8: Preformed Elastomeric Compression Seals

- **Poured (Silicone) Seals**

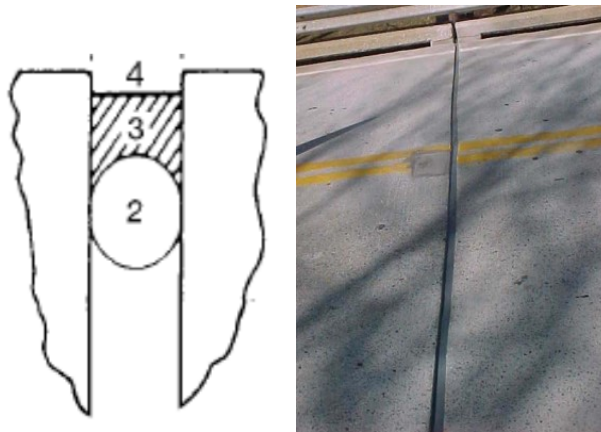


Fig. 9: Poured (Silicone) Seals

- **Asphalt Plug Joints**

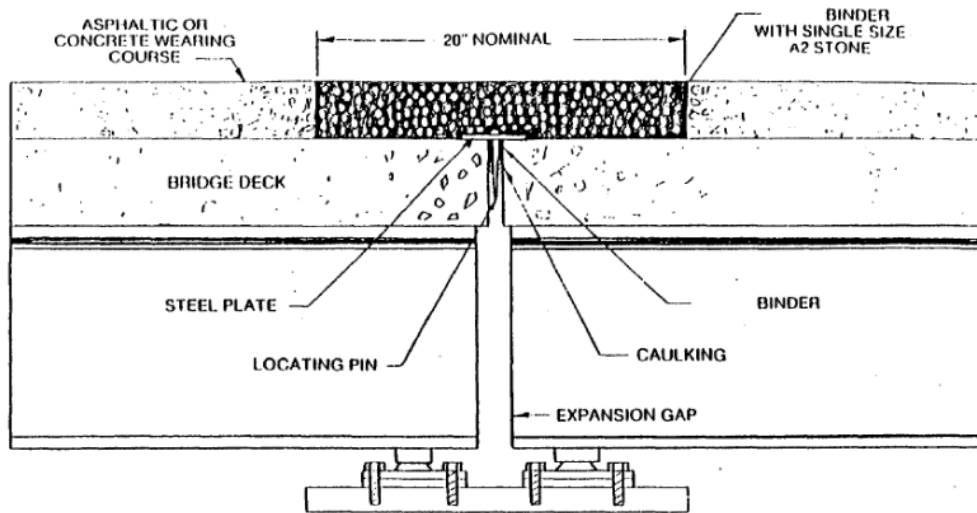


Fig. 10: Asphalt Plug Joints

- Strip Seals

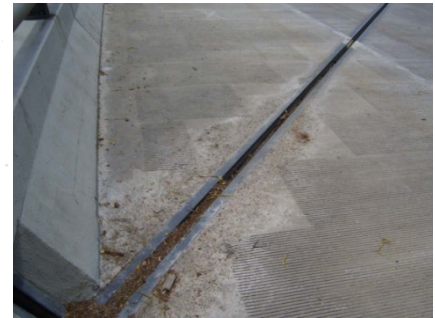
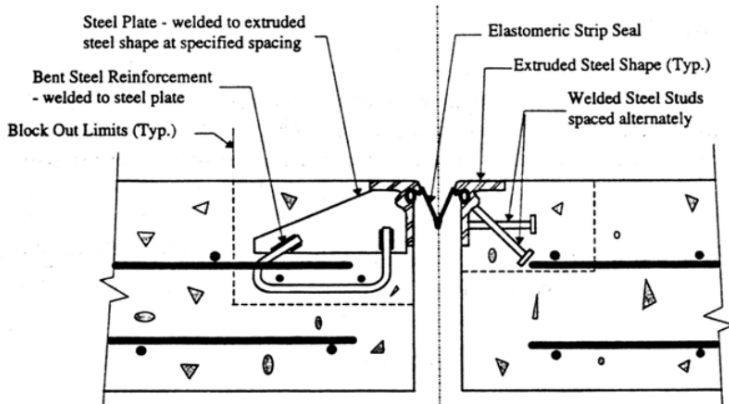
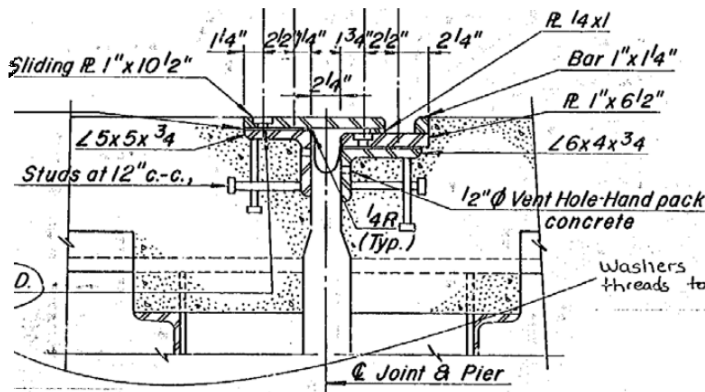


Fig. 11: Strip Seals

- Sliding Plate Joints



- Finger Joints

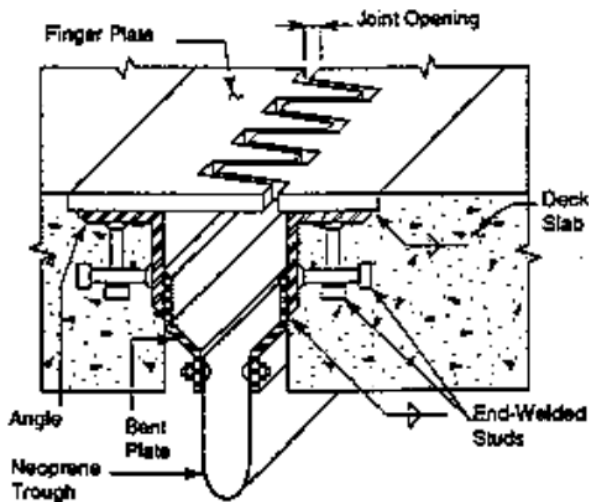


Fig. 12: Finger Joints

- **Cushion Seal (Elastomeric Expansion Dam)**

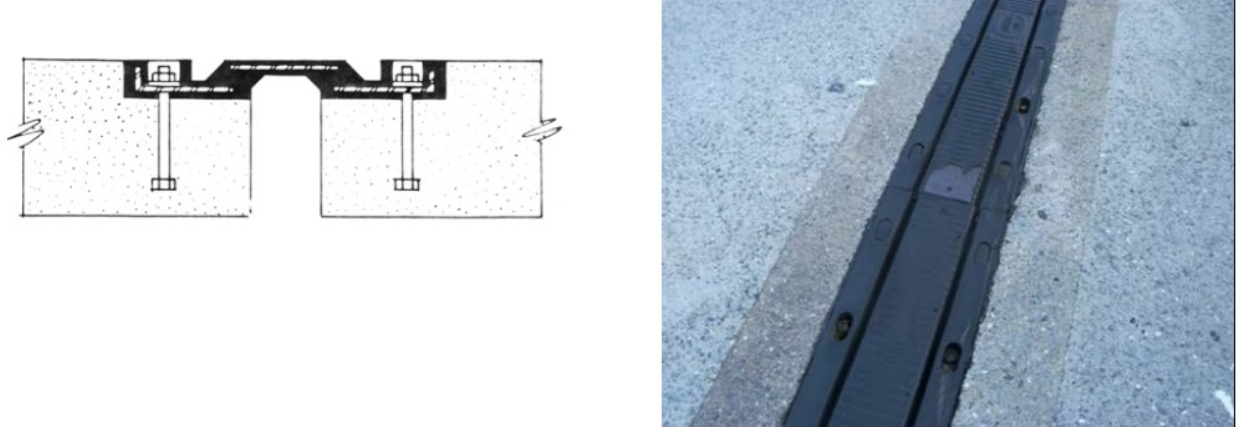


Fig. 13: Cushion Seal (Elastomeric Expansion Dam)

Xu et al. 2018 discussed an approach taken to rehabilitate the Shili Bridge by eliminating expansion joints and retrofitting the structure from simply-supported concrete box girders into a continuous bridge. Condition assessments were performed before retrofitting. In addition, several design options and construction procedures were considered and analyzed. Static and dynamic load tests were carried out after the completion of rehabilitation. The lessons learned in this project are presented and discussed. This practical and novel methodology was a step forward toward improving safety, sustainability, reliability, and quality of such existing bridges in China and elsewhere. It was concluded that Continuity of side-by-side box girders not only eliminated joints between the spans, but also reduced the positive moment at midspan by introducing negative dead load bending moment over the supports. Removal of joints over the abutments enhances bridge durability and eliminates the typical bump at the ends of a bridge. These factors would contribute to improved bridge durability, better ride quality, and reduced maintenance costs. The rehabilitation and strengthening of Shili Bridge provide a basis for the retrofitting of similar existing bridges to address durability and deterioration problems. Providing continuity can also reduce the amount of strengthening materials (CFRP and metal plates) that may be needed along the bottom of the girders. This is because the length of the positive bending moment region would be shortened after continuity of girders is achieved, thus reducing construction quantities and achieving overall cost savings. Steps must be taken to limit any restraints to the free sliding of the approach slab. A separation is needed between the sliding approach slab and the curbs to ensure that the approach slab can slide as freely as possible.

Groli et al. (2014) conducted an experimental campaign aimed at validating a previously published simplified serviceability design method of the columns of long jointless structures. The proposed method was also extended to include tension stiffening effects which proved to be significant in structures with a small amount of reinforcement subjected to small axial loading. This refinement allowed significant improvement of predictions for this type of element. The campaign involved columns with different reinforcement and axial load ratios, given that these parameters had been identified as crucial when designing columns subjected to imposed displacements. Experimental results were presented and discussed, with particular regard to cracking behaviour and structural stiffness. Considerations on tension stiffening effects were also made. Finally, the application of the method to typical bridge and building cases was presented, showing the feasibility of jointless construction, and the limits which should be respected.

Mothe (2006) investigated the behavior of the link-slab and its effect on the behavior of the bridge system as a whole. The scope of the study was to develop FE models to analyze the variation of forces, stresses and moments in the link-slab as well as the level of continuity generated in the girder system. The analysis was carried out for different bridge parameters which are likely to affect the behavior of link-slab; namely, bearing stiffness, skew angle, span lengths and debonding length ratio of link-slab. The study helped in understanding the effects of the aforementioned factors on the behavior of the link-slab and the system. The study also proposed development of a modified three moment equation for different parameters. The parameters which influence the three-moment expression are the bearing stiffnesses, material properties and geometric information. A thorough parametric study is required to validate the expression. The results can be used for development of a design procedure for the link-slab and the expression can be used for analysis of the link-slab. The results obtained showed that the link-slab behaves more like a tensile member rather than a bending member with the increase in bearing stiffness and debonding length ratios. This observation was consistent in all the bridge types and skew angles considered for the study.

Ho and Lukashenko (2011) described the available design methodologies and provide an example of its application for a bridge retrofit. Link-slabs are currently being installed in new bridge construction, and also used to replace expansion joints in the rehabilitation of existing structures. The applicable use of link-slabs in the field is limited by variables such as girder end rotation from applied loads, bridge skew, and girder depth. Link-slabs are designed to flex, however excessive deflection causes potential for the development of wide cracks, exposing the interior steel reinforcement to susceptibility of corrosion. The concrete deck is typically composite with the supporting steel or concrete girders but is debonded in the link-slab region to increase the link-slab curvature length, resulting in a reduced slab flexure and minimizing cracking. Although flexural cracking cannot be completely eliminated, water ingress into the cracks can be controlled by the following design considerations: limiting deck crack opening width by limiting end girder rotation; application of waterproofing membrane on top of concrete deck; and use of fiber reinforced concrete in the link-slab. It was indicated that examples of successful link-slab applications have been implemented in Ontario, Canada and Michigan, USA. The benefits of the use of link-slabs include reduced costs for maintenance of expansion joints, and less reinforcing steel in the deck resulting in less construction time and cost. Also with the elimination of expansion joints, there is less likelihood of chlorides permeating through the joint and causing corrosion and damage to the reinforced deck and substructure components. The use of link-slabs are slowly gaining acceptance as Canadian Ministries of Transportation learn more about their benefits of reduced maintenance costs over the lifespan of new or rehabilitated structures. It is recommended that these link-slabs be monitored over their service lives to better determine their long-term effectiveness.

Kendall et al. (2008) developed and applied an integrated life-cycle assessment and life-cycle cost analysis model to enhance the sustainability of concrete bridge infrastructure. The objective of that model was to compare alternative bridge deck designs from a sustainability perspective that accounts for total life-cycle costs including agency, user, and environmental costs. A conventional concrete bridge deck and an alternative engineered cementitious composite link-slab design were examined. Despite higher initial costs and greater material related environmental impacts on a per mass basis, the link-slab design results in lower life-cycle costs and reduced environmental impacts when evaluated over the entire life cycle. Traffic delay caused by construction comprises 91% of total costs for both designs. Costs to the funding agency comprise less than 3% of total costs, and

environmental costs are less than 0.5%. These results showed life-cycle modeling is an important decision-making tool since initial costs and agency costs are not illustrative of total life-cycle costs. Additionally, accounting for construction-related traffic delay was vital to assessing the total economic cost and environmental impact of infrastructure design decisions.

New York DOT

New York DOT has been building integral bridges as well as jointless decks since the late 1970s. They performed well from the beginning, but a recent study evaluated their performance to identify details possibly needing improvement in future construction. Ratings obtained during a field survey of numerous integral bridges and jointless bridge abutments were analyzed, as well as condition ratings assigned by bridge inspectors during their biennial inspections (Alampalli and Yannotti 1998). Results indicate that these bridges have been functioning as designed and showed superior performance when compared with conventional bridges. These types thus should be used whenever possible to eliminate joints in bridge construction. Details needing improvement were identified. On the basis of these observations, design changes have been recommended for future construction. Integral bridges will be limited to structures having skews less than 30 degrees pending further study. A research project was initiated for further examination of construction practices and assumptions made during the design process.

North Carolina DOT

Gastal and Zia (1989) performed an analysis of bridge beams with jointless decks. ElSafty (1994) conducted an analysis and investigation of jointless bridge decks with partially debonded simple span beams. Zia et al. (1998) investigated casting fully-continuous deck over simply supported girders with partial debonding of the deck from the girders ends at supports, using both numerical and experimental analysis, as shown in Fig. 2. Okeil and Elsafty (2005) investigated the partial continuity in bridge girders with jointless decks and the effect of the system's support configuration on the axial force developed in the link-slab. Caner and Zia (1998) presented the results of a test program to investigate the behavior of link-slabs connecting two adjacent simple-span girders and proposed a simple method for designing the link-slab. ElSafty and Okeil (2008) also investigated extending the service life of bridges using continuous decks. Wing and Kowalsky (Wing 2005) evaluated the link-slab concept proposed earlier by Caner and Zia (1998),

constructed, and instrumented a full-scale jointless bridge and its link-slabs for performance evaluation. This study has concluded that although the design rotation of the link-slab, obtained by assuming simply-supported deck, was 0.002 radian, actual rotation was far below this value. However, to control crack width, link-slabs were still heavily reinforced, thus stiffening the slab and decreasing its ability to act as a hinge between the adjacent decks. In addition, the study suggested that the performance of reinforced concrete link-slabs was highly affected by the construction quality, which most often results in large crack width.

Michigan DOT

ECC: To overcome the problem of heavily reinforced link-slabs, Engineered Cementitious Composites (ECC) were proposed to replace conventional concrete slabs. ECC are high performance fiber reinforced cementitious composites that have high durability and strain capacity over 400 times that of a normal concrete. The tensile strain of ECC material was associated with a large number of microcracks that have a limited crack width between 50 μm and 70 μm at 1% tensile strain. These cracks do not increase in width with increasing the tensile strain even up to failure (4% strain) (Lepech and Li - 2009). Kim et al. (2004) have evaluated the performance of bridge deck link-slabs designed with ductile ECC experimentally using full-scale slabs. The results of these experiments have shown significant enhancements in deflection capacity and crack width control of link-slabs when constructed using ECC material.

Li et al. (2003 and 2005) conducted a research project with Michigan DOT describing the development of durable link-slabs for jointless bridge decks based on strain hardening cementitious composite - engineered cementitious composite (ECC). Specifically, the superior ductility of ECC was utilized to accommodate bridge deck deformations imposed by girder deflection, concrete shrinkage, and temperature variations, providing a cost-effective solution to a number of deterioration problems associated with bridge deck joints. Current design concept of link-slabs was first examined to form the basis of design for ECC link-slabs. Microstructurally optimized ECC material, with good workability and satisfactory mechanical properties was then developed. After the material design, the shrinkage, shrinkage crack resistance and the freeze-thaw behavior of the pre-selected mix proportion was investigated and revealed excellent for the durability concern. Improved design of ECC link-slab/concrete deck slab interface was confirmed

in numerical analysis and further strengthened by excellent reinforcement pullout and shear stud pushout behavior in ECC. Based on the above findings, monotonic and subsequent cyclic tests of full-scale ECC link-slab specimens were performed and compared with those of a conventional concrete link-slab. It was revealed that the inherent tight crack width control of ECC decouples the dependency of crack width on the amount of reinforcement. This decoupling allows the simultaneous achievement of structural need (lower flexural stiffness of the link-slab approaching the behavior of a hinge) and durability need (crack width control) of the link-slab. Overall investigation supported the contention that durable jointless concrete bridge decks may be designed and constructed with ECC link-slabs. Finally, a simple design guideline was presented. Also, the results of full-scale mixing trials and demonstrations were summarized, and recommendations were made along with batching sequences and mix designs for large scale mixing. A summary of construction practices and procedures was also included, followed by the results of full-scale load testing on the completed ECC link slab demonstration bridge. The load tests concluded that the ECC link-slab functions as designed under bending loads.

The Michigan DOT incorporated link-slabs during deck replacements and deep resurfacing. Field performance assessment documented full-depth cracking of most of the link-slabs. These cracks allow surface water infiltration, which leads to accelerated deterioration. Ulku et al. (2009) conducted a study to address link-slab design and performance issues. The literature is inconsistent with the influence of design parameters on link-slab performance. The objective was to document the link-slab behavior of its design parameters, to propose a method to calculate the link-slab moment and axial force, and to propose recommendations for updating current design details and construction procedures. Single-girder, two-span, finite element assemblage models under various types and levels of loads in conjunction with the link-slab design parameters were used to evaluate the moments and axial forces developed in the link-slab. Analysis showed that support conditions underneath the link-slab greatly influence the link-slab moment and axial force. Use of moment interaction diagram is recommended for the design. A detailed analysis and design example is presented incorporating live load, temperature gradient load, and the support configurations.

Lepech and Li (2009) investigated the application of ECC in a bridge deck link-slab. The unique ultra-high tensile ductility and tight crack width of self-consolidating ECC was exploited in this

application to improve bridge deck constructability, durability, and sustainability. Design guidelines and material specifications were developed for implementation of this ECC link-slab technology. A construction project implementing these guidelines and specifications was conducted in 2005 on an ECC-concrete bridge deck in southeast Michigan, USA. A full-scale load test was conducted to explore the structural response of the constructed ECC link-slab. These load tests validated that the incorporation of an ECC link-slab in placement of a conventional expansion joint did not alter the simply supported nature of the bridge spans, and that ample strain capacity of the ECC is reserved for temperature induced straining as designed. Two years after this ECC link-slab was placed, the performance of this link-slab remains unchanged. With further long term performance monitoring and additional demonstration experience, ECC link-slab can be an effective replacement of conventional expansion joints resulting in significantly reduced bridge deck maintenance needs.

Georgia DOT

Snedeker et al. (2011) evaluated the performance history of continuous bridge decks in the State of Georgia, to determine why the current design detail works, to recommend a new design detail, and to recommend the maximum and/or optimum lengths of continuous bridge decks. The continuous bridge decks have continuous reinforcement over the junction of two edge beams with a construction joint for crack control. It was indicated that the current technical literature and current practices and design procedures were synthesized and summarized. GDOT maintenance reports were reviewed, and preliminary field evaluations were conducted to determine the performance of the continuous deck detail. The effects of bridge movement due to thermal strains, shrinkage, and live loads were considered in simplified analytical studies to better understand the demands placed on the GDOT continuous deck detail. A summary of the preliminary design and length recommendations were provided upon completion of Part 1 of the research.

Europe

In recent years, the so called jointless or integral bridge design has seen a significant rise in popularity in Europe. Whereas in the last decades, designers preferred clearly defined statical systems and only adopted jointless design principles for small structures, the new generation of engineers pushes for integral design wherever possible. This development is to some degree

motivated by a paradigm shift towards life-cycle cost-orientated design. Integral bridge structures lack joints and bearings, which typically are the least durable elements and thus remove the need for costly inspections and replacements. However, the obvious advantage of reduced direct and indirect maintenance costs entails novel and complex design solutions, especially for the transition area between structure and soil body. Furthermore, their statically indeterminate nature leads to increased importance of the soil–structure interaction. Both aspects are associated with significant uncertainty.

Wendner and Strauss (2015) focused on the probabilistic performance assessment of an inclined approach slab solution for integral bridge structures of up to 150 m of total length. Findings are presented by the example of a recently constructed and ever since monitored 67-m-long prototype structure. Monitoring data recorded by a multisensor monitoring system during the first 30 months after construction serves as inputs for a probabilistic, extreme value-based assessment of critical design assumptions. In particular, (1) the modeling of boundary conditions, (2) the activated degree of earth pressure against the abutment wall, and (3) the strain distribution in the fiber-reinforced soil above the inclined approach slab were investigated. It was concluded that the combination of short and long extensometers represents a robust and cost-effective monitoring approach for relative and absolute abutment movements that has already been adopted by Austrian bridge owners. The obtained information can be used to investigate the soil–structure interaction in terms of actual boundary conditions and developing earth pressure, in case no other sensor system is available. Based on the observed linear relationship between temperature within the deck slab and recorded abutment movements, it was found that the recorded displacements account for only 42% of the expected displacements, assuming free thermal expansion. Hence, the assumption of free thermal expansion during the design of the dilatation area is highly conservative by itself. In the current engineering practice, the assumption of free thermal expansion compensates for the lack of experience regarding the actual performance of the approach slab that represents a hidden safety margin. The observed strain field is in agreement with the theoretical assumptions, showing a high strain concentration near the tip of the slab and indicating an inclined area of localized deformation going up to the surface.

Charuchaimontri et al. (2008) investigated the influence of lap reinforcement in link-slabs of highway bridges under four independent boundary conditions by using a three-dimensional nonlinear finite element code based on the microplane model. Numerical solutions for load–deflection relationships, internal force distribution and failure cracking planes are presented for link-slabs with different details of lap reinforcement. A full-scale test was performed on three reinforced concrete long span link-slabs with various lap reinforcement details subjected to mid-span loading. The comparison indicated a good agreement between the results from finite element analysis and the experiment. The model can be used to predict the effective moment of inertia of the link-slab under mid-span loading, end rotation and end translation for the development of design criteria for a link-slab.

MTO

To address this problem of joints in bridges, the Ministry of Transportation of Ontario (MTO) has recently rehabilitated a number of bridge decks using a debonded link-slab system to replace the deck joints at the pier locations. MTO recently carried out an experimental research study of the long-term performance of the system on scale test models that were subjected to extensive cyclic loading in the laboratory. It also conducted a load test of a recently rehabilitated structure to study its structural behavior both before and after the link-slab was constructed. The test structure was instrumented with sensors that measured deflections and strains in the link-slab and girders.

Au et al. (2013) described the experimental research study on link-slab and the behavioral load tests that were carried out, and discusses the results obtained. The experimental study showed that the long-term performance of the link-slab was not affected by the extensive cyclic loading to which the model was subjected, and the load testing of the test structure showed that it satisfied the serviceability limit state requirements of the Canadian Highway Bridge Design Code, thus validating the design methodology of the system.

PCI

Details of jointless bridge superstructures are available in the PCI publication, “The State-of-the-Art of precast/Prestressed Integral Bridges,” authored by the Subcommittee on Integral Bridges of the Committee on Bridges.

THE USE OF FRC and FRP REBAR IN LINK-SLABS

Several researchers have investigated the use of Fiber-Reinforced Polymers (FRP) for bridge deck reinforcement (NCHRP – 2003) as alternatives to conventional steel reinforcement to provide corrosion resistant reinforcement that increases bridge service life and achieve economic and environmental benefits

FRC

Materials with high tensile strain capacity, such as fiber-reinforced concrete (FRC), can be used for application in the link-slab to improve the strength, durability, and cracking characteristics of the link-slab. Hong (2014) established a computational model of an existing bridge (Camlachie Road Underpass). It is found that the model and modelling approach in SAP2000 closely predicted the field test results obtained by the Ministry of Transportation of Ontario (MTO). Additionally, it is established that the horizontal stiffness of the elastomeric bearings is very low and therefore the supports are representative of roller supports. Therefore, axial forces are not generated when there are no horizontal restraints in the supports.

Hong (2014) examined the properties of FRC from experimental tests. Four-point bending tests are used to estimate the ultimate and service stresses of FRC using procedures from the fib Model Code (2010). It is found that the results from the fib Model Code are in agreement with the experimental beam tests by Cameron. Therefore, it is concluded that the fib Model Code procedures are valid for calculating the ultimate and service stresses in FRC and are used in the computational and analytical models. Hong 2014 conducted a parametric study to provide a better understanding of link-slab bridge behavior to assess the impact of design decisions on the bridge response. It is found that the use of hooked steel fibres minimized the crack width of the link-slab, and a debonded length a 5% to 7.5% is found to be optimal based on cost and serviceability. Moreover, it is found that fibres are more effective when less steel reinforcements are used in the link-slab. Lastly, a parametric study is conducted on the computational model using non-linear analysis by including FRC in the computational model in the form of plastic hinges. It is concluded that the computational model has shown signs of cracking at the pier supports, which is consistent with the site observations during the MTO field test for the Camlachie Road Underpass. Hong 2014 developed an analytical model (i.e., design guideline) on the analysis and design of link-slab

bridges with FRC. It is found that the proposed analytical model is able to closely represent the link-slab bridge behavior with very small difference (2-3%), whereas the current method of analysis using Caner and Zia's approach shows a larger prediction error (16%). For the link-slab design with FRC, it is found that fibres in reinforced concrete helped increase the bending moment capacity of the link-slab by more than 10% compared to normal reinforced concrete (without fibres). The use of polypropylene fibres and hooked steel fibers in the link-slab reduces the required steel reinforcement by 3.5% and 21%, respectively, and the crack width of the link-slab reduces by more than 3 times with the addition of fibres. Okeil et al. (2013) conducted a field study in Louisiana investigating the performance of a skewed prestressed concrete bulb-tee girder bridge made continuous. The study presented details of the monitoring system developed for this project, which has been in service for more than two years. Temperature, strain, rotation, and elongation readings are presented. It was concluded that positive moments develop in bridges employing the new continuity detail. They are caused by creep and thermal effects that cause upward camber at midspans, which leads to positive moments at continuous girder ends. Seasonal and daily temperature variations can induce large restraint moments in the bridge, especially temperature gradients. The level of restraint moment due to the combined seasonal and daily temperature effects is probably the most important factor in the design of this detail because the designer has no influence on the temperatures at the bridge site. The other positive-moment-inducing factor (girder creep caused by prestressing forces) can be greatly reduced by not establishing continuity until after a large portion of the creep takes place.

Hawaii DOT

Reyes and N. Robertson (2011) in the report of the State of Hawaii Department of Transportation indicated that a cast-in-place link-slab has the advantage of providing good continuity at the ends of the FRCC section to the concrete or bridge deck, meaning it can be built to be flush with the bridge deck. However, because of the limitation of permanent strain in the link-slab, the effectiveness of the slab in compression is reduced. Therefore, a precracked link-slab would be more appropriate in most applications. The study also indicated that because HPRCC concrete requires a long setting and curing time to reach its optimal strength, it may not be practical to cast-in-place especially when time is a construction consideration. The study also suggested that pre-cast slabs has the advantage of pre-cracking but are limited by the bond of the link-slab to the

existing concrete. It suggested bonding through vertical dowels installed at an angle so that the slab is essentially pulled downward during tension loads, or a combination of vertical dowels and horizontal GFRP bars that would be more effective than either acting alone

TYPES OF BEAM CONTINUITY AT PIERS

There are several alternatives to create a link-slab and or jointless superstructure over the piers. AASHTO LRFD specifications (2009), Article 5.14.1.4 allows designers to use any one of the shown methods of design. Some examples of these jointless superstructure are listed as follows:

(a) Continuous deck slab or link-slabs supported by simple span beams

Most of the concrete beam bridges in Florida are currently built using continuous deck over the joint between beams/girders at a pier. A typical detail is shown in Fig. 14. The details do not include beam end diaphragms or debonding between the deck and beam. The absence of end diaphragms in these details significantly simplifies construction but may not be feasible in states subjected to significant seismic activities. Some of the details include a saw-cut or tooled crack control joint in the deck over the pier that may be filled with sealant.

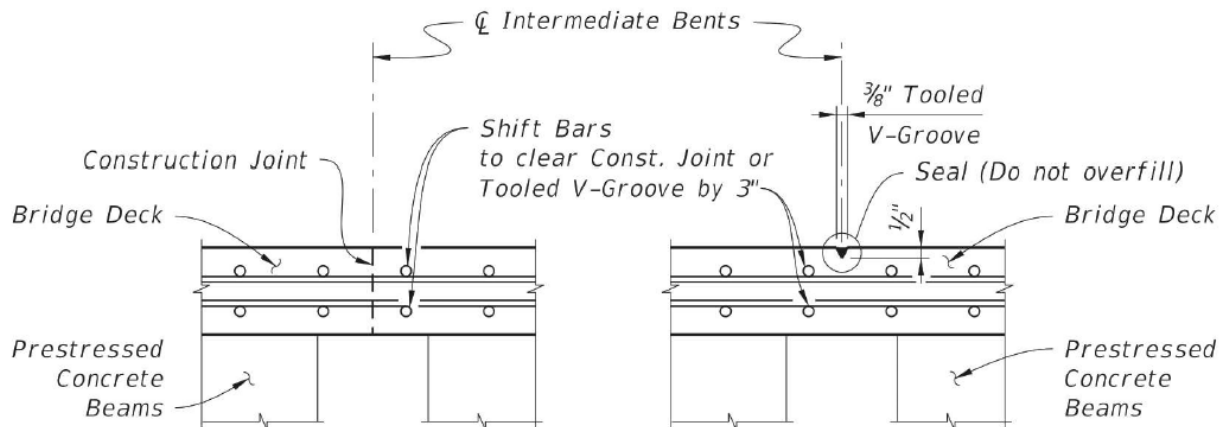


Fig. 14: Florida Department of Transportation details for continuous slab over joint between simple spans. Figure: Florida Department of Transportation Structures Detailing Manual

A similar method is also adopted using a link-slab to connect the simply-supported girders/beams with a continuous deck, while part of the slab is debonding from the girder ends at both sides of the joint. This detail of the link-slab with debonding results in a reduction in developed strains

and cracking in the continuous deck slab since it distributes the deformations over a greater length. This method has a simpler construction than a fully continuous superstructure and is considered as a cost-effective way of developing a jointless deck. To control cracking, a groove is formed, preinstalled or cut transversely in the deck at the pier centerline and may be filled with a sealant. Several researchers [ElSafty (1994); Zia et al. (1995)] provided early recommendations for design and construction of link-slabs. They recommend debonding the end 5% of the deck slab from the ends of the beams to reduce strains and control cracking in the link-slab region. Recommended analysis is to impose the end rotations of the beams on the slab. The resulting stress in the deck reinforcement should be limited to 40 ksi and cracking should be checked with current AASHTO LRFD specifications crack control provisions.

Virginia DOT

An example of a link-slab system used to remove expansion joints when rehabilitating bridges in Virginia is shown in Fig. 15. In this detail, which is used for relatively short spans, the debonded length is a constant 2 ft (VDOT 2013).

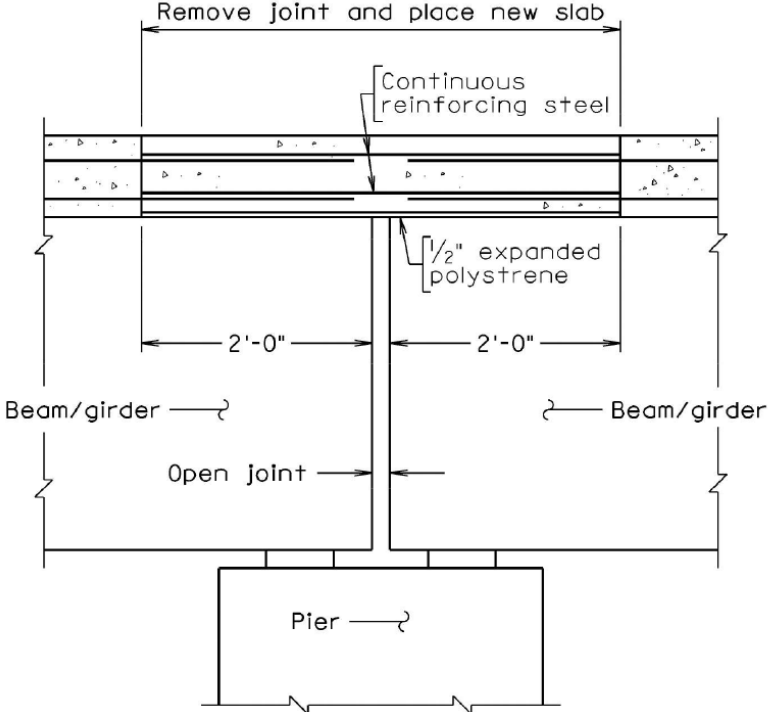


Fig. 15: Link-slab detail used by Virginia Department of Transportation to eliminate expansion joint in rehabilitation projects

(b) Continuous-for-Live-Load Beams

The prestressed concrete beams are set on bearings as simple spans and the diaphragm concrete may be placed partial height (Fig. 16). The deck concrete is then placed on the simple-span beams. Longitudinal deck reinforcement that extends over the pier region is designed to resist all subsequent loads, such as live load, as a continuous span composite superstructure. This system has been performing well for more than 40 years.

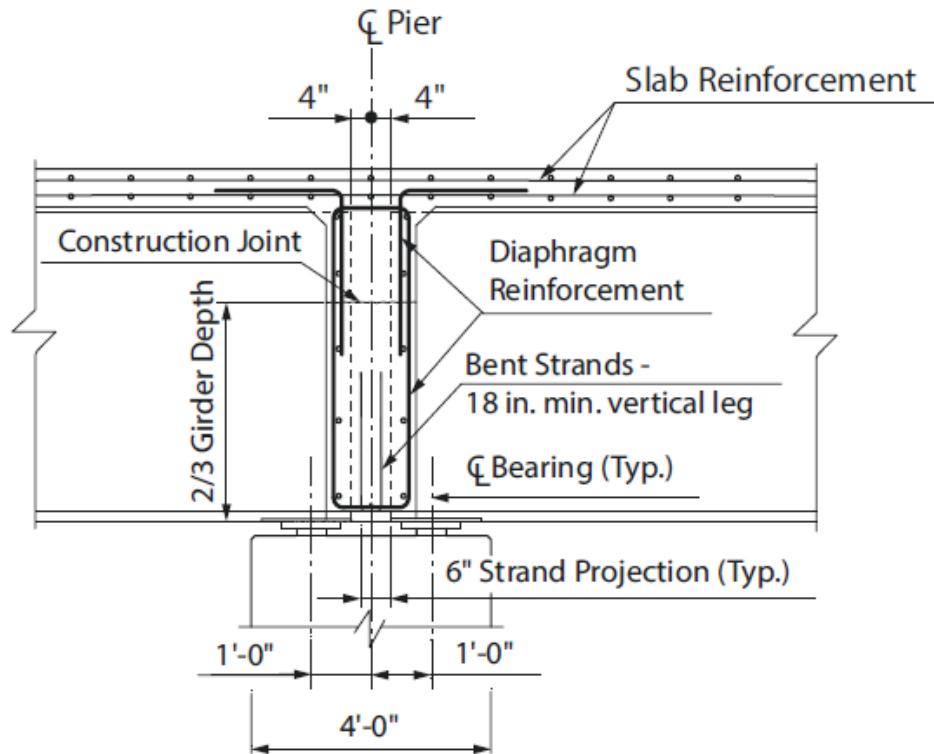


Fig. 16: Example of pier diaphragm details with either fixed or expansion bearings (Tadros 2016)

(c) Threaded Rod Continuity System

A method called threaded rod continuity was reported by Sun et al. (2016), where beams were made continuous using high-strength threaded rods placed on top of the beams in the negative moment zone over the piers. The rods were embedded in a concrete placement on the top flange of the beam that is constructed at the same time as the continuity diaphragm, as shown in Fig. 17. The result is a continuous beam for deck weight as well as all subsequent loads. This system, while slightly more complicated than the continuous-for-live-load system, allows for further

optimization of the capacity of the beams. Also, as an additional benefit, the negative moment due to deck weight generally offsets the long-term positive restraint moment at the pier, eliminating the need for bars or strands extending from girders to provide a positive moment connection.

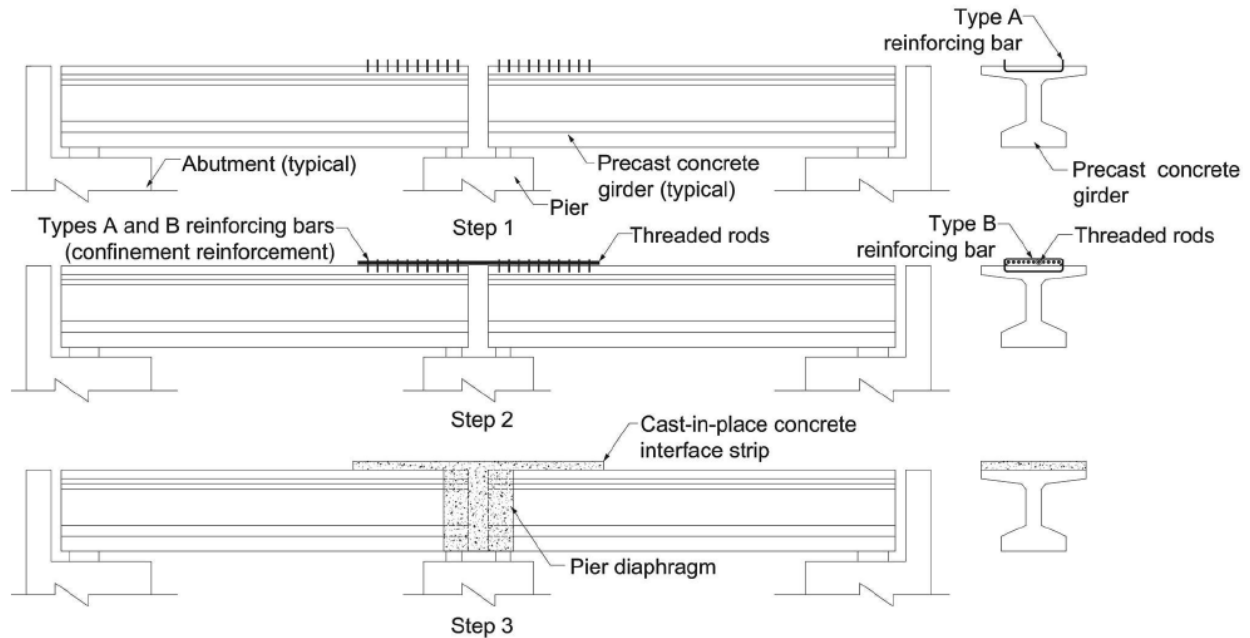


Fig. 17: Construction steps of implementing threaded rod continuity system prior to deck placement (Sun et al. 2016)

(d) New Link-slab System Details

Louisiana Transportation Research Center proposed a link-slab to be designed with enough FRP reinforcement to withstand the loads placed on the slab. Also, when possible, the link-slab was designed to be uncracked while under typical service loads. Design has been in accordance with the newest ACI 440 criterion. When creating the FRP link-slab, special measures should be considered to anchor the FRP reinforcement to the existing bridge deck during the installation of a link-slab in an existing deck. Using FRP grating or FRP bars for the creation of a link-slab in a new bridge or a complete bridge deck replacement was considered.

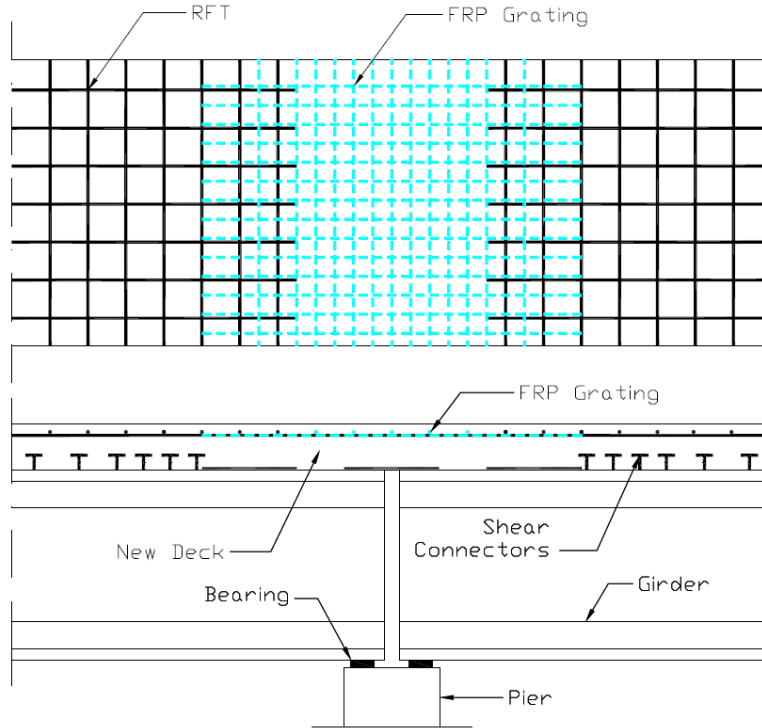


Fig. 18: FRP grating as reinforcement for new link-slab.

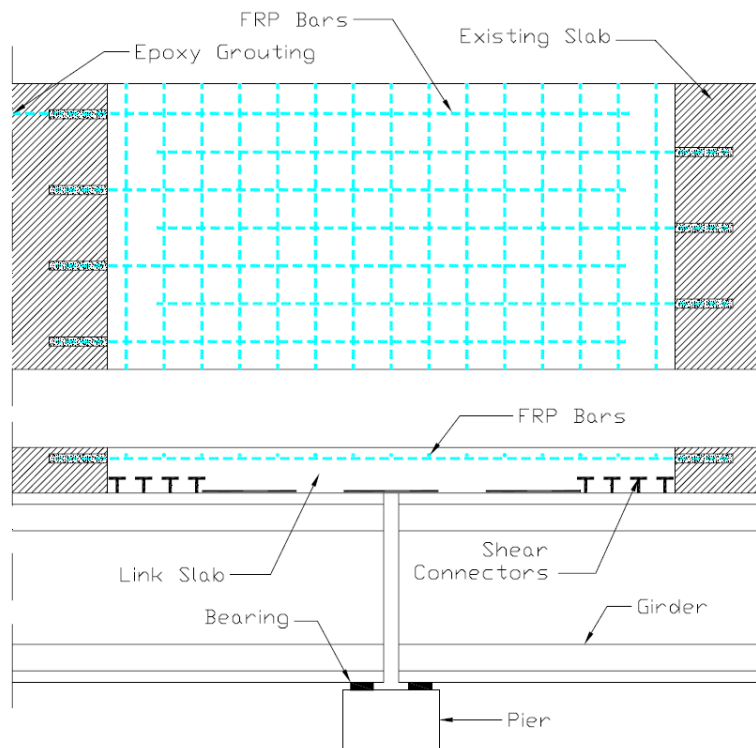


Fig.19: FRP rebar for use in link-slab installed in existing deck

INSTRUMENTATION OF THE LINK-SLAB

Researches have indicated that the link-slabs were instrumented using real-time strain inducers, thermocouples, and pH meters. Data was collected during field tests and service. The data logger has record when certain strains were reached in the FRP reinforcement.

Okeil, et al. (2013) investigated a precast prestressed-concrete simple-span girders that were made continuous by pouring a continuity diaphragm between the girders ends. Special reinforcement was extended from the girders' bottom flanges into the diaphragm to ensure continuity under positive moments that result from time-dependent effects such as creep, shrinkage, and temperature gradient. The bridge has been instrumented with embedded and surface-mounted sensors and was monitored for over 2 years to evaluate the performance of the new continuity detail. A live-load test was carried out to evaluate the response of the new detail under truck loads. A bridge segment was monitored that was a three-span continuous superstructure, 242 ft (73.8 m) long with a 45-degree skewed layout. American Association of State Highway and Transportation Officials (AASHTO) bulb-tee girders (BT-72) were used for the construction of this segment. Because of the bridge's symmetry, only one of the identical intermediate bents was monitored. A 96-channel monitoring system was designed to record essential performance measures for evaluating the continuity detail. Several sensor types were chosen to measure temperatures, strains, rotations, crack widths, and gaps. All sensors used the vibrating wire technology, which is known to be more suitable for long-term monitoring projects because they do not suffer from drifting. Embedded as well as surface-mounted sensors were employed.

Six types of sensors were used, and the monitoring system included 66 active sensors. The sensors were strategically located at midspan and on both sides of the continuity diaphragm to capture the important measures that are most influenced by continuity, such as strains in hairpin bars and the gap between adjacent girder ends. The relative movement between the bottom flanges at the ends of the adjacent girders on both sides of the continuity diaphragm was investigated using the gapmeters installed at girders. Rotations on both sides of the continuity diaphragm were recorded. All measurements were corrected for temperature changes per recommendations of the gauge manufacturer. Figure 20 shows a schematic of the sensor locations. Okeil et al. (2013) provide more details about the instrumentation. Figure 21 shows instrumentation options and details.

Live load test on the monitored segment was conducted to assess the continuity detail's performance under truck loads. Dump trucks weighing 54.1 and 57.0 kip (24.5 and 25.9 tonnes) were used to load the bridge in nine static loading cases.

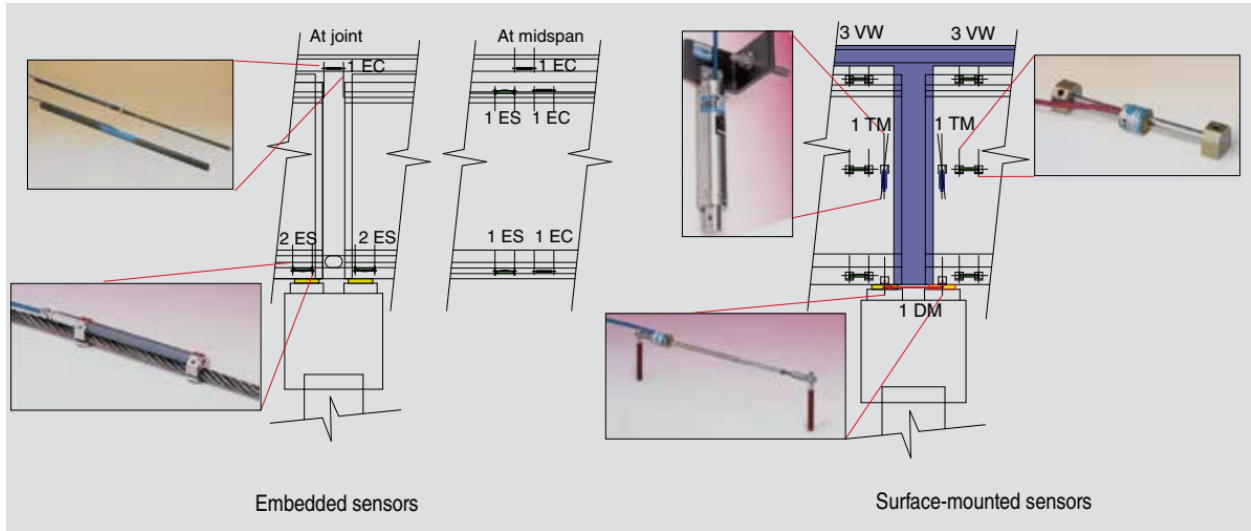
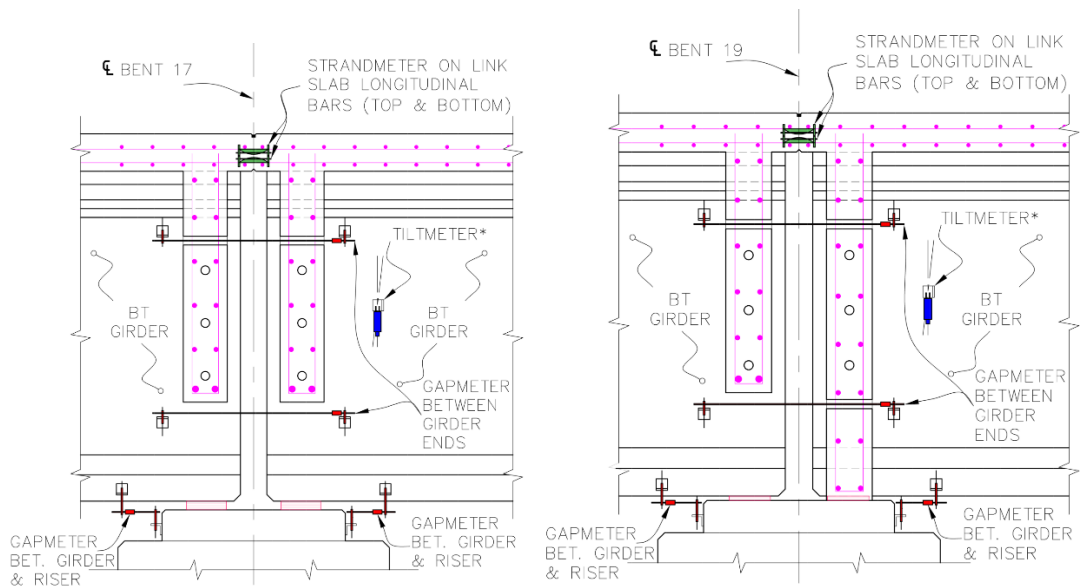


Fig. 20: Distribution of sensors at each monitored location. Note: DM = gapmeter gauge; EC = sisterbar gauge; ES = strandmeter gauge; TM = tiltmeter gauge; VW = vibrating wire strain gauge.



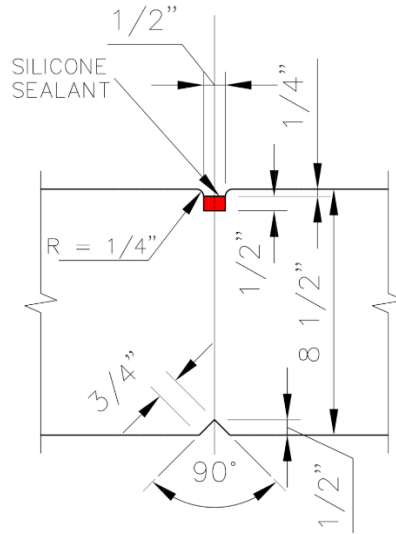


Fig. 21: Details of typical instrumentations

The monitoring of the tested bridge indicated that the continuity detail has the ability to transfer forces from one girder to the adjacent girder across the continuity diaphragm, as evidenced by the recorded data under long-term effects as well as live loads.

The authors concluded that seasonal and daily temperature variations can induce large restraint moments in the bridge, especially temperature gradients. The level of restraint moment due to the combined seasonal and daily temperature effects is probably the most important factor in the design of this detail because the designer has no influence on the temperatures at the bridge site. The other positive-moment-inducing factor, such as girder creep caused by prestressing forces, can be reduced by not establishing continuity until after a large portion of the creep takes place. The results from the instrumentation and monitoring also indicated that the live load test revealed that the continuity detail transferred negative and positive moments across the diaphragm. The strains from the live load test were lower than long-term effects. Even if the actual design load was to be applied (approximately twice the test live load), the strains would still be small. Therefore, the live load case should be considered in the design; however, it is not the most demanding action on the detail.

12 Appendix E

ANNOTATED PLANS DETAILS FOR LINK-SLAB MONITORING PROJECT BDV34 986-02

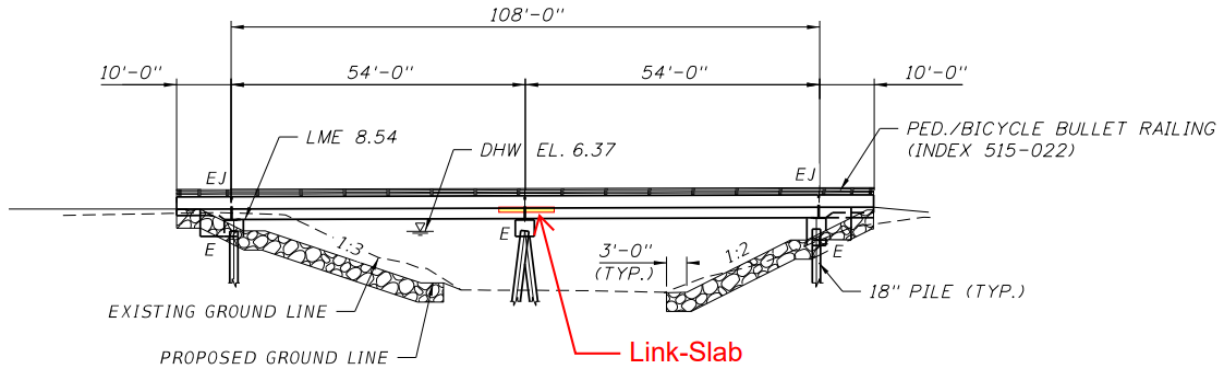
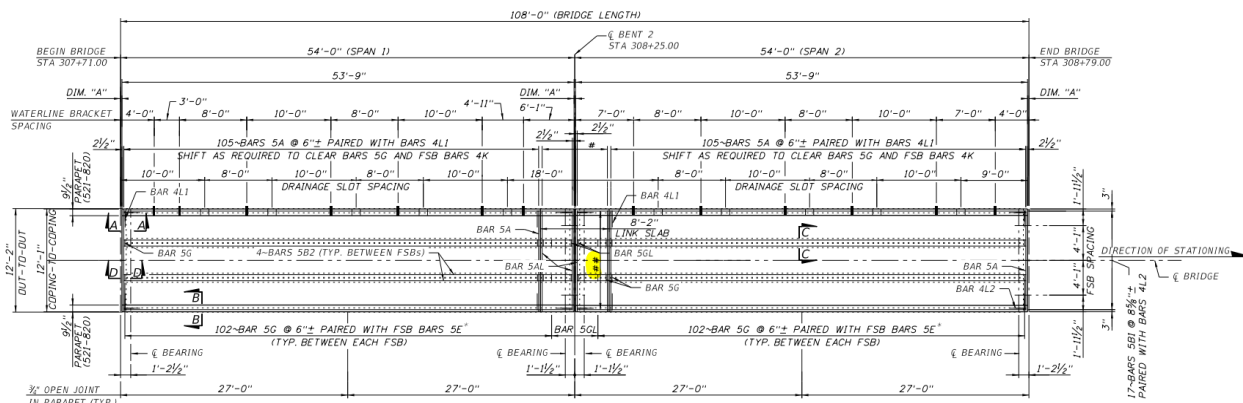


Figure E.1: Elevation of the Bridge with the link-slab (Bridge No. 019003)



These longitudinal bars are replaced with Basalt FRP under BDV34 986-02 monitoring project

LINK SLAB REINFORCING:
 # 17-BAR 5A @ 6"±
 # 24-BAR 5L1 @ 6"± PAIRED WITH FSB 5E"
 # 24-BAR 5L2 @ 6"±

Figure E.2: Plan view of the Bridge with the link-slab (Bridge No. 019003)

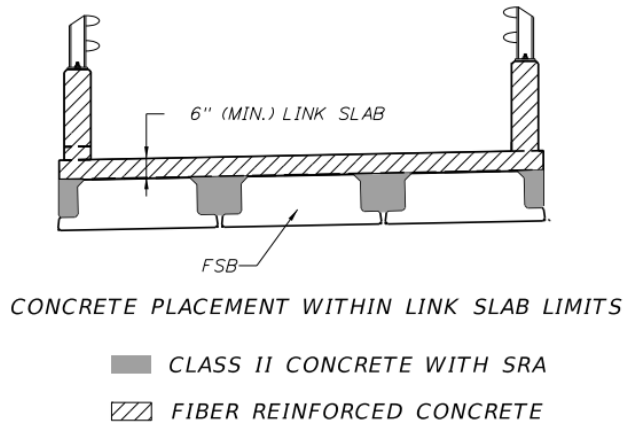
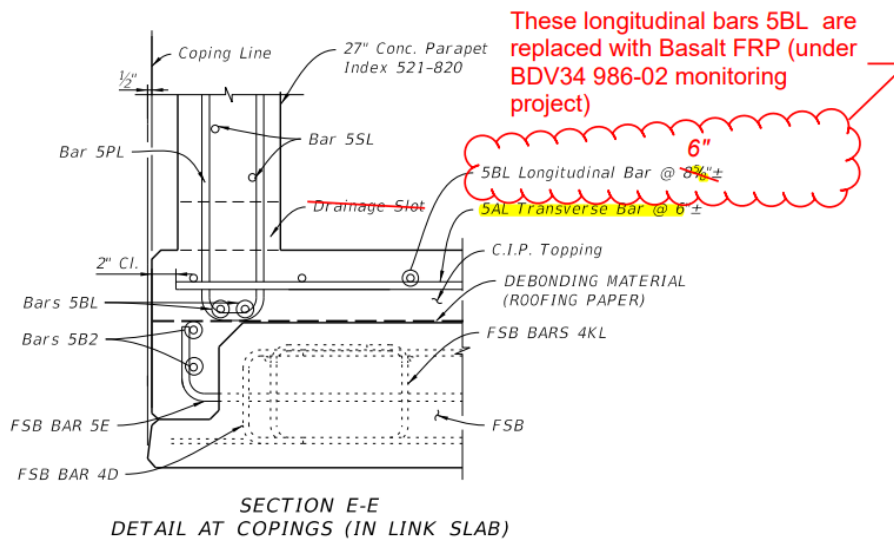


Figure E.5: Concrete within the link-slab (Bridge No. 019003)



Pedestal reinforcing bars within the limit of the link slab shall be GFRP Bars and shall be incidental to the cost of the parapet.

Figure E.6: Concrete within the link-slab (Bridge No. 019003)

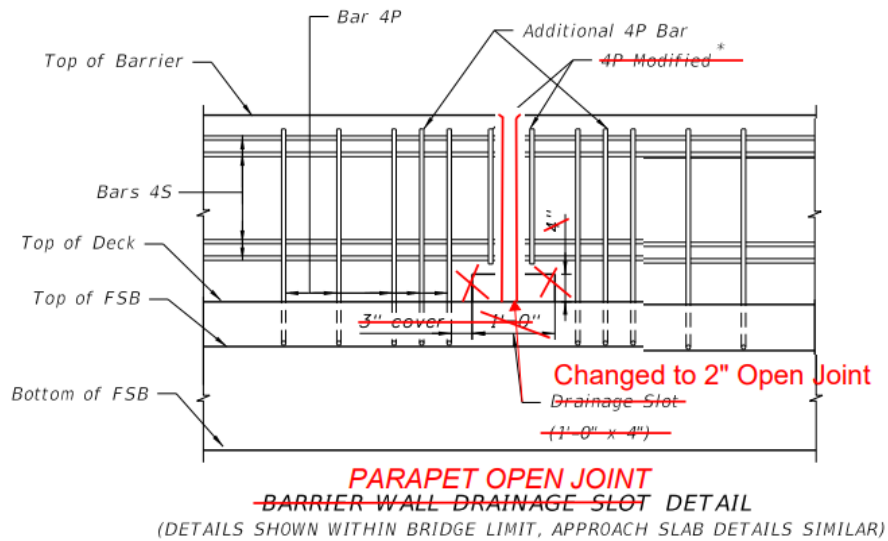


Figure E.7: Detail of the link-slab (Bridge No. 019003)

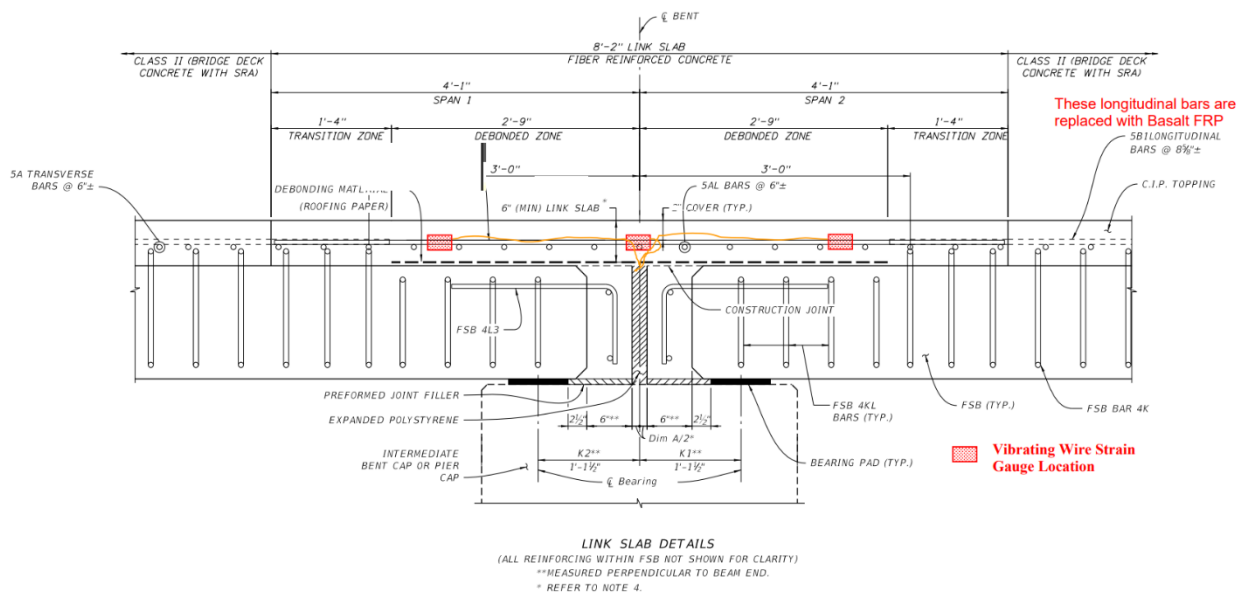
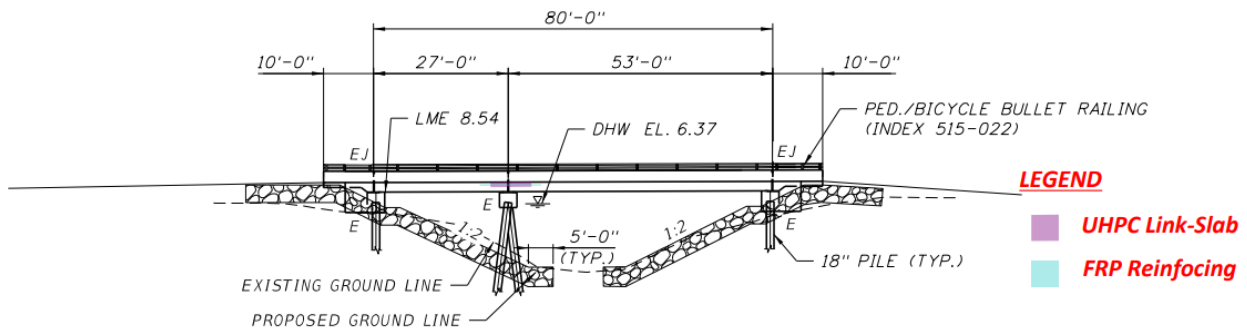


Figure E.8: Longitudinal Section Detail of the link-slab (Bridge No. 019003)



ELEVATION

Figure E.9: Elevation of Bridge No. 019004

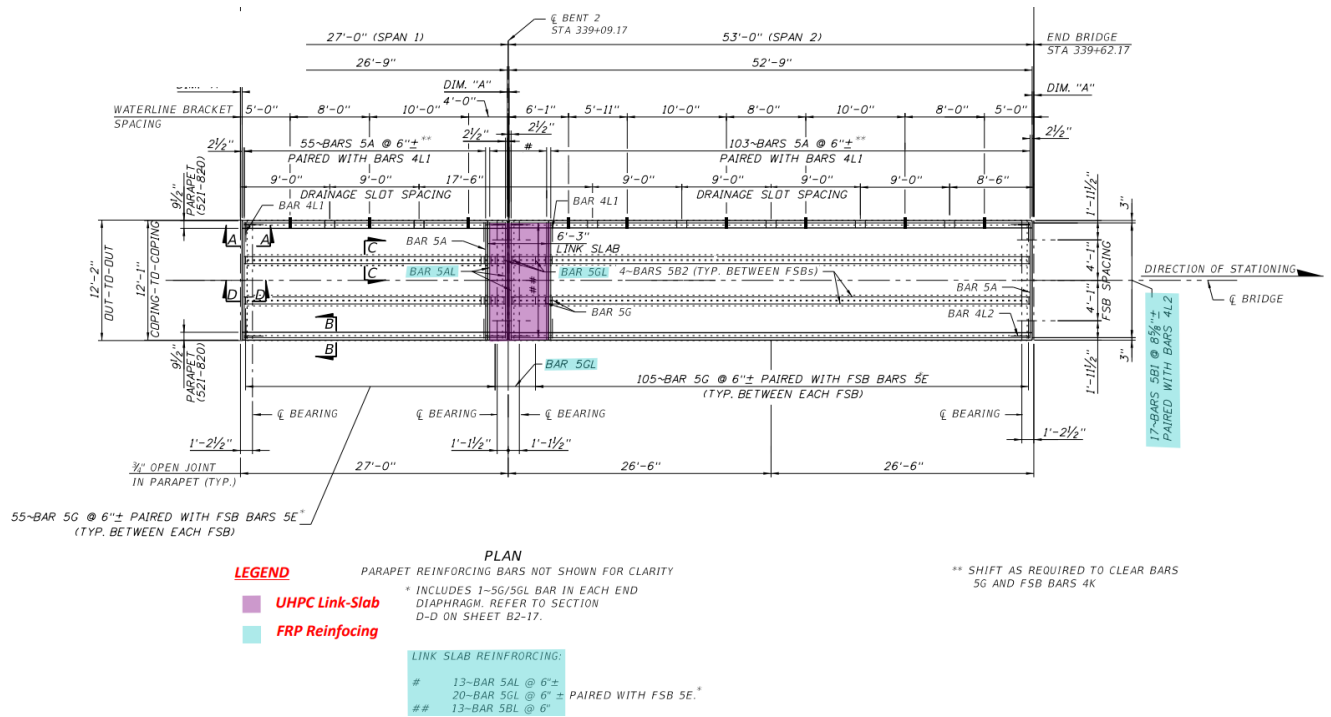


Figure E.10: Plan View of Bridge No. 019004

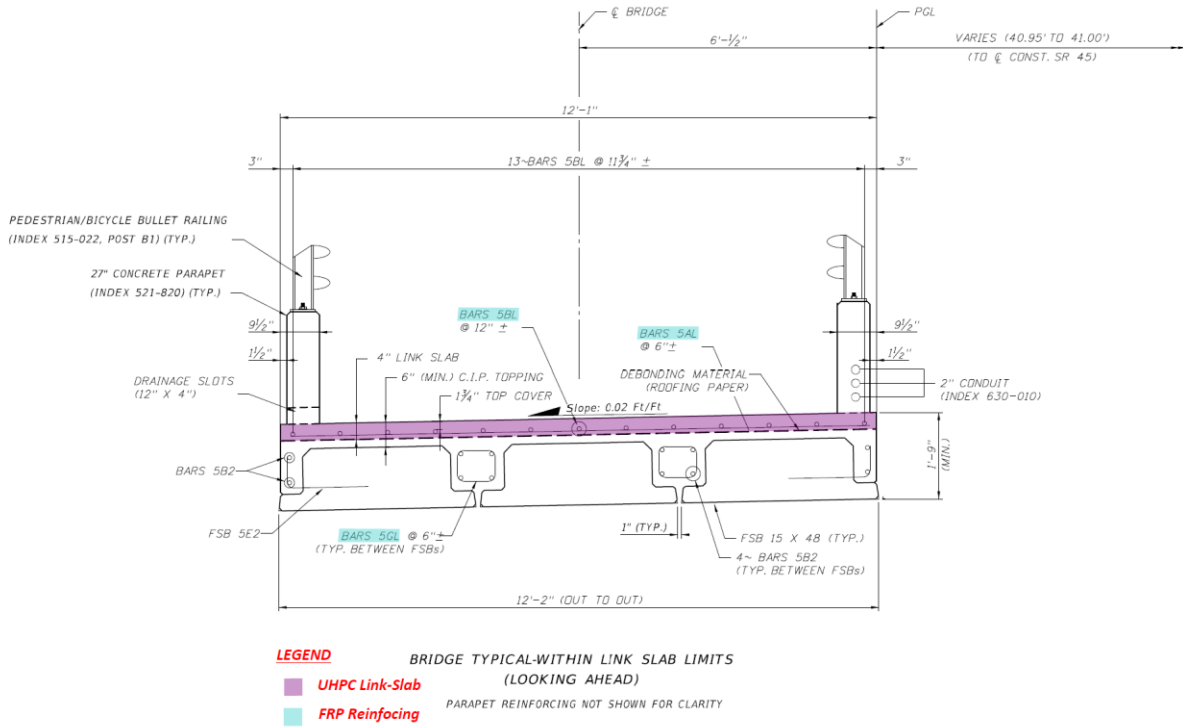


Figure E.11: Sectional cut of link-slab (Bridge No. 019004)

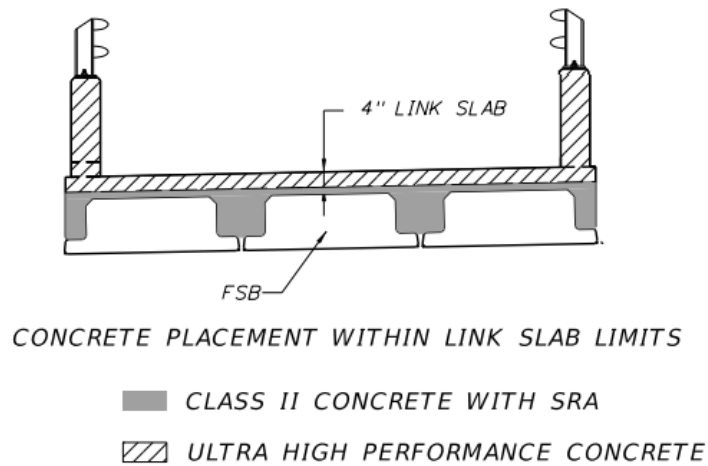


Figure E.12: Concrete within the link-slab (Bridge No. 019004)

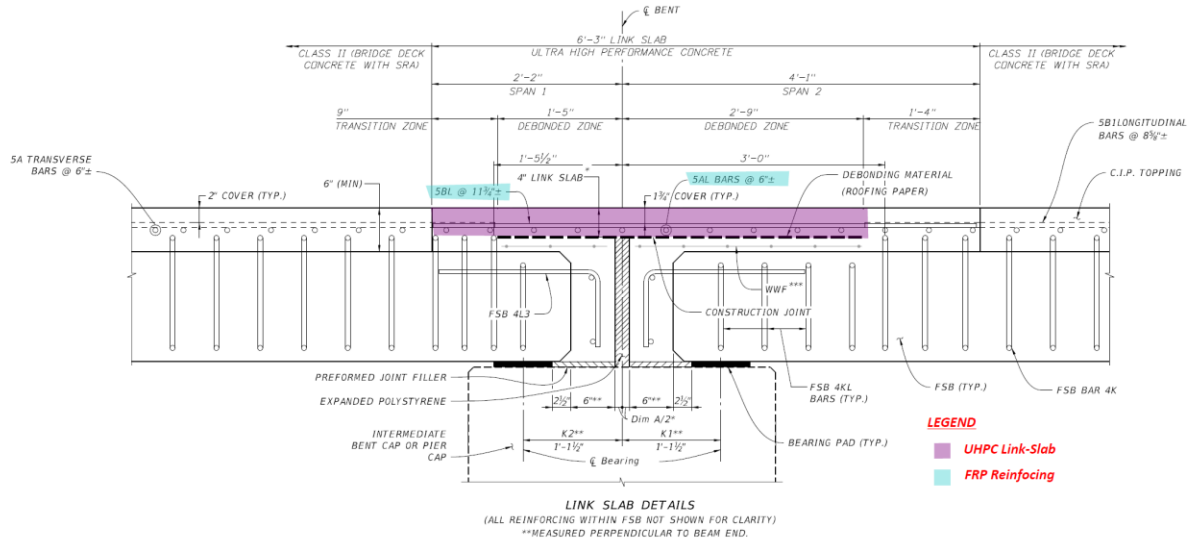


Figure E.13: Link-slab side view (Bridge No. 019004)

Appendix C

**Test Report Number: R-5.10 12-08-20 FDOT - “Evaluation of Non-Metallic
Fiber Reinforced Polymer (FRP) Bars For Concrete Reinforcement” (BFRP
Closed Stirrups)**

(10 pages)

CERTIFIED TEST REPORT

EVALUATION OF NON-METALLIC FIBER REINFORCED POLYMER (FRP) BARS FOR CONCRETE REINFORCEMENT - Per FDOT Section 932-3, Table 3-4 -

Report Number: R-5.10_12-08-20_FDOT
Date: June 4, 2021

REPORT PREPARED FOR:



FDOT State Structures Design Office
Attn: Steven Nolan, P.E.
(Advanced Materials for Structural Durability & Resiliency)
605 Suwannee St, Tallahassee, FL. 32399
Ph: 850-414-4272, steven.nolan@dot.state.fl.us
Website: <https://www.fdot.gov/design/Innovation/>

PROJECT REF:

BFRP Stirrups Tensile Testing - St Joe Inlet bulkhead

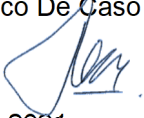

Quality System: The Structures and Materials Laboratory (SML) maintains a quality system in compliance with ISO 17025-2017, accredited under International Accreditation Service (IAS), testing laboratory TL-478 and is a qualified laboratory by the Florida Department of Transportation (FDOT) number ISM028. All the test results presented herein are linked through unbroken chain data. Analyzed data is obtained directly from the recorded raw data during testing, from which the test results are presented. This report contains analyzed tabulated data results.

Procedures: All tests and services are conducted in accordance with the SML Quality Manual (Version 6.0) revised November 30, 2019; relevant standard operating procedures (SOPs); and with the applicable requirements of the reference standard test methods, unless otherwise stated.

Disclosure: This document may contain confidential information; please contact an authorized entity prior to distributing. Conclusions reached and opinions offered in this document are based upon the data and information available to at the time of its issue, and may be subject to revision as additional information or data becomes available.

Certified Test Report

Controls:	
Superseded Report	New report
Reason for Revision	n/a
Effective Date	June 4, 2021

Test Report Approval Signature:	
Quality review Approval	<p>I indicate that I have reviewed this Test Report and agree with the contents it presents, and find it meets all applicable laboratory requirements and policies. I approve for its release to the customer.</p> <p>Name: Francisco De Caso Signature:  Date: June 4, 2021</p>
Technical review Approval	<p>I indicate that I have reviewed this Test Report and agree with the contents it presents, and find it meets all applicable laboratory requirements and policies. I approve for its release to the customer.</p> <p>Name: Antonio Nanni Signature:  Date: June 4, 2021</p>

1. EXECUTIVE SUMMARY

This report provides results on supplemental testing of basalt fiber reinforced polymer (BFRP) stirrups to support documentation for the STIC – BFRP Standardization project with FHWA. The scope of testing is limited to one production lot and minimum of three test repetitions samples as reported herein. Based on the results provided here, the bar/s from stirrups as described in this report meet the requirements as set forth within Florida Department of Transportation (FDOT) Nonmetallic Accessory Materials for Concrete Pavement and Concrete Structures, Section 932-3, Table 3-4. Refer to Section 2 the material sample information; Section 3 for the summary test results and Section 4 for the individual tabulated results.

2. BAR SAMPLE INFORMATION

Sample No.*	Manufacturing Lot/ID/Ref.	Nominal Bar Denomination	Material type
1	<i>Not available</i>	#4B V-ROD Bent bar. Stirrup	BFRP



SAMPLE RECEIVED: 12 open stirrup pieces, #4 nominal size, 19 3/4" x 17 3/4"
Scale in Inches (in.). Sampling: Provided by client

3. SUMMARY TEST RESULTS

SAMPLE No. 2: #4B V-ROD						
Test ID	Standard Test Method	Test Description	Units	Acceptance Criteria	Test Value	Test Result
DSC	ASTM E2160	Average Degree of Cure	%	≥ 95	100	Pass
	ASTM D3418	Average Glass Transition Temp.	°F	≥ 212	272	Pass
FC	ASTM D2584	Average Fiber Content (by weight)	%	≥ 70	77	Pass
MA	ASTM D570	Average Moisture Absorption	%	≤ 0.25	0.13	Pass
MXA	ASTM D792	Average Measured Cross-Sectional Area	in ²	0.185 to 0.263	0.257	Pass
TNS	ASTM D7205	Guaranteed Tensile Load	kips	≥ 21.6	≥ 21.6	Pass
		Average Tensile Modulus of Elasticity	Msi	≥ 6.5	8.2	Pass
HSS	ASTM D4475	Average Horizontal Shear Strength	ksi	>5.5	7.1	Pass

4. SPECIFIC TEST DATA

Test data is uniquely identified in the report using the following nomenclature: “XXXY-Z” where ‘XXX’ refers to the test ID as referenced in the first column of Section 3; ‘Y’ refers to the sample number as referenced in the first column of Section 2; and Z is the test sample repetition number. Note dates referenced within this report use the *mm/dd/yyyy* format.

4.1. ENTHALPHY OF POLYMERIZATION (DSC)

Test Standard Method: [ASTM E2160-04 \(2018\)](#), Standard test method for heat of reaction of thermally reactive materials by differential scanning calorimetry, and [ASTM D3418-15](#), Transition temperatures and enthalpies of fusion and crystallization of polymers by differential scanning calorimetry.

Test Description: Determine the degree of cure (DC) and glass transition temperature (T_{mg}) via differential scanning calorimetry (DSC).

Technician/Analyst: Karla Pabellon and Juan Manuel Palacios

Test Date: 04/16/2021

Specimen Size: Slice of the bar cross-section yielding a minimum of 5 mg of material.

Test Result: PASS: DC \geq 95% and $T_{mg} \geq 212^{\circ}\text{F}$

Test Data:

Sample ID	Specimen ID	Initial Mass M_i mg	Mass Change M_{Δ} %	Degree of Cure, DC*	Glass Transition Temperature, T_{mg}	
				%	$^{\circ}\text{C}$	$^{\circ}\text{F}$
	DSC1-01	26.49	0.012	99.9	135	275
	DSC1-02	27.85	0.012	99.7	134	274
#4B V-ROD	DSC1-03	30.15	0.003	99.8	131	267
	Average			99.8	133	272
	Stand. Dev.			0.1	2.4	4.2
	COV (%)			0.1	1.8	1.6

* Note that the total heat of reaction (H_t), which is derived from the unreacted resin system (neat resin), is conservatively assumed value of 100 J/g to compute the degree of cure.

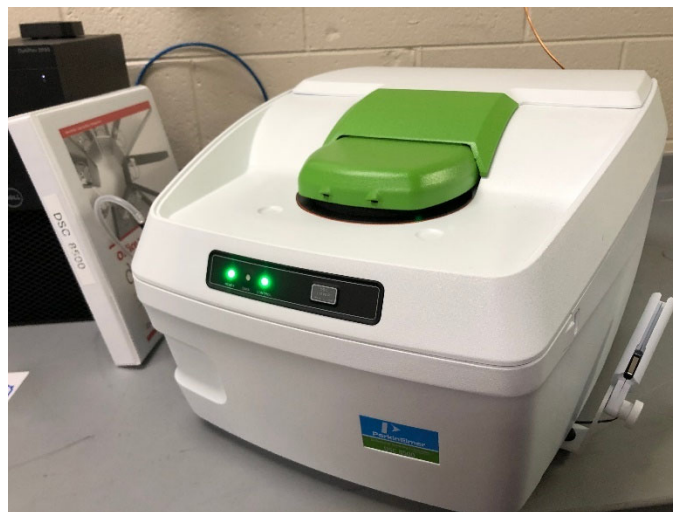


Figure 4.1 - Test set up showing DSC in operation

4.2. FIBER CONTENT (FC)

Test Standard Method: [ASTM D2584-18](#), Standard Test Method for Ignition Loss of Cured Reinforced Resins.

Test Description: Determine the fiber content (FC) by weight (mass).

Technician/Analyst: Sebastian Garcia-Herreros and Juan Manuel Palacios

Test Date: 04/19/2021

Specimen Size: Bent bar: 25.0 mm (1.0 in.) extracted at geometric center radius of bent.

Test Result: PASS: FC \geq 70% by weight

Test Data:

Lot and Nominal Bar Size	Specimen ID	Weight of Specimen	Weight of residue	Fiber Content
		W ₁ g	W ₂ g	FC %
#4B V-ROD	FC1-01	17.769	13.763	77.5
	FC1-02	18.275	14.070	77.0
	FC1-03	15.329	11.852	77.3
	Average			77.3
	Sn-1			0.2
	CV (%)			0.3

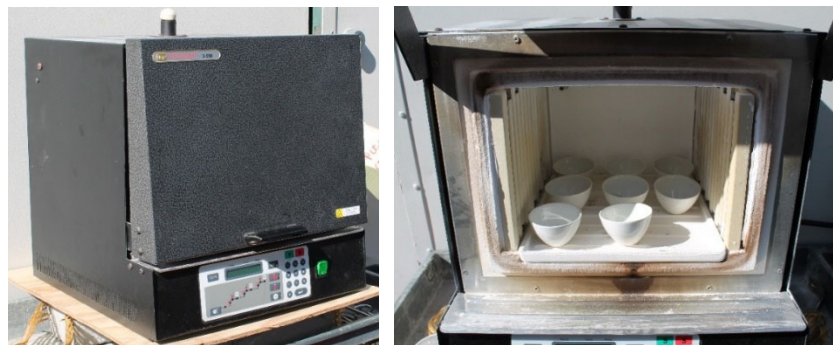


Figure 4.2 – Fiber content furnace test set up



(a)



(b)

Figure 4.3 – Fiber content representative test samples (a) pre-testing, and (b) post-test (ignition)

MOISTURE ABSORPTION (MA)

Test Standard Method: [ASTM D570 - 98 \(2018\)](#), Standard Test Method for Water Absorption of Plastics, Procedure 7.1 and,.

[ASTM D5229/D5229M-14](#), Standard Test Method for Moisture Absorption Properties and Equilibrium Conditioning of Polymer Matrix Composite Materials (Procedure B).

Test Description: Determine the short-term level of moisture absorption when immersed in distilled water at 122°F ±3°F for 24 hours.

Technician/Analyst: Juan Manuel Palacios

Test Date: 04/01/2021

Specimen Size: Bent bar: 25.0 mm (1.0 in.) extracted at geometric center radius of bent.

Test Result: PASS: $W_{24} \leq 0.25 \%$

Test Data:

Lot and Nominal Bar Size	Specimen ID	Initial Mass M_i g	Final Mass M_{24} g	Short-term Absorption (24 hrs.) W_{24} %
#4B V-ROD	MA1-01	8.9846	9.0004	0.18
	MA1-02	9.1162	9.1267	0.12
	MA1-03	8.8169	8.8255	0.10
	Average			0.13
	S_{n-1}			0.04
	CV (%)			31.7



Figure 4.4 – Test set up for measurement of moisture absorption,

4.3. CROSS-SECTIONAL AREA (MXA)

Test Standard Method: [ASTM D7205/D7205M - 06 \(2016\)](#) Standard test method for Tensile Properties of Fiber Reinforced *Polymer* Matrix Composite Bars and, [ASTM D792-13](#) Standard Test Methods for Density and Specific Gravity (Relative Density) of Plastics by Displacement

Test Description: Determine the measured of cross-sectional area by volume of water displacement method.

Technician/Analyst: Sebastian Garcia-Herreros and Juan Manuel Palacios

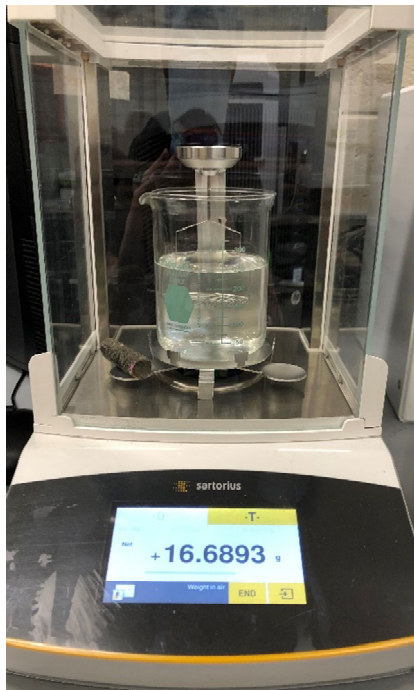
Test Date: 03/31/2021

Specimen Size: Specimen nominal length dimensions were 38.1 mm (1.5 in.). For the bent bars the specimen was extracted from the leg of the bend (i.e. the straight portion).

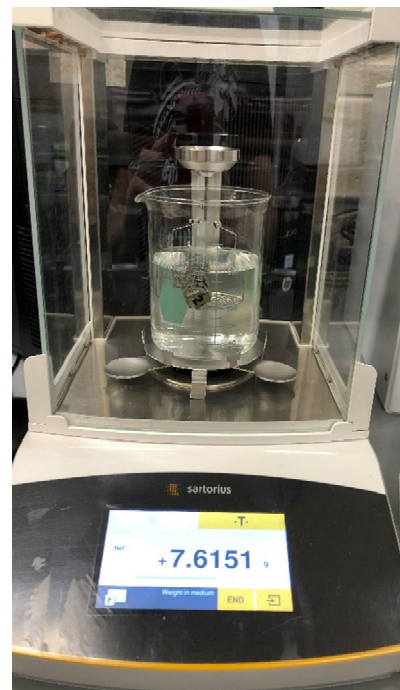
Test Result: PASS:
 #4B, A shall be between 0.185 in² to 0.263 in²;

Test Data:

Lot and Nominal Bar Size	Specimen ID	Ave. Length L		Volume V		Measured Area A		Weight/unit length	
		mm	in.	mm ³	in ³	mm ²	in ²	kg/m	lbs/ft
#4B V-ROD	MXA1-01	51.39	2.023	8515	0.52	165.68	0.257	0.325	0.218
	MXA1-02	51.28	2.019	8513	0.52	165.99	0.257	0.324	0.218
	MXA1-03	53.68	2.113	8871	0.54	165.26	0.256	0.324	0.218
	Average	52.12	2.052	8633	0.53	165.65	0.257	0.324	0.218
	Sn-1	1.35	0.053	206	0.01	0.37	0.001	0.001	0.000
	CV (%)	2.6	2.6	2.4	2.4	0.2	0.2	0.2	0.2



(a)



(b)

Figure 4.5 – Test set up for measurement of cross-sectional area, (a) Specimen weight, and (b) Immersed specimen

4.4. TENSILE PROPERTIES (TNS)

Test Standard Method: [ASTM D7205/D7205M - 06 \(2016\)](#) Standard test method for Tensile Properties of Fiber Reinforced *Polymer* Matrix Composite Bars.

Test Description: Determine the guaranteed tensile load, ultimate tensile load carrying capacity, tensile modulus of elasticity and computed ultimate strain based on an assumed linear elastic behavior.

Technician/Analyst: Alexander Corletto and Juan Manuel Palacios

Test Date: Sample 1: 05/07/2021; Samples 2 and 3: 6/3/2021

Specimen Size: The specimens deviated from ASTM D7205 due to the limited sampled length. Total sample length was 15 in. FRP anchors were used to grip the sample with a total length of 5in. resulting in a clear gauge length of 5 in. A 4 in. extensometer was used in compliance with ASTM D7205.

Test Result: PASS: $E \geq 6.5$ Msi. P_{max} shall be ≥ 21.6 kips;

Test Data:

Sample ID	Specimen ID	Peak Load		Nominal Area		Ultimate Tensile Strength, UTS		Modulus of Elasticity		Strain ϵ
		P_{max} kN	kips	A mm ²	in ²	f_{tu} MPa	ksi	E GPa	Msi	
#4B V-ROD	TNS1-01	142.86	32.1	129	0.20	1107.2	160.6	58.0	8.42	1.91
	TNS1-02	135.08	30.4			1046.9	151.8	55.8	8.09	1.88
	TNS1-03	158.36	35.6			1227.3	178.0	56.2	8.15	2.18
	Average	145.43	32.7			1127.1	163.5	56.7	8.22	1.99
	S_{n-1}	11.85	2.7			91.8	13.3	1.2	0.18	0.17
	CV (%)	8.1	8.1	8.1	8.1	2.1	2.1	8.5		

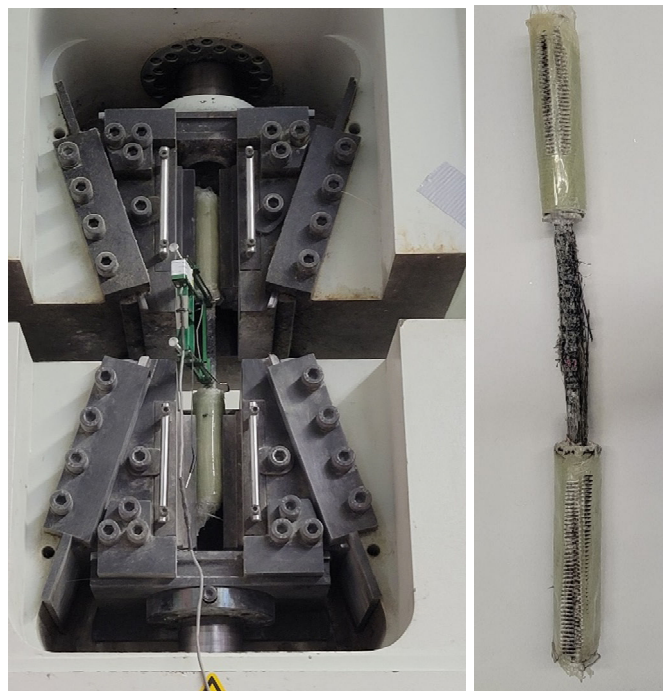


Figure 4.6 –Tensile test set-up (left) and representative failure mode (right)

4.5. HORIZONTAL SHEAR STRENGTH (HSS)

Test Standard Method: ASTM D4475 - 02(2016) Standard Test Method for Apparent Horizontal Shear Strength of Pultruded Reinforced Plastic Rods By the Short-Beam Method.

Test Description: To determine the ultimate and guaranteed horizontal shear strength.

Technician/Analyst: Sebastian Garcia-Herreros and Juan Manuel Palacios

Test Date: 04/28/2021

Specimen Size: Specimen nominal length dimensions were 76.2 mm (3 in). The specimen was extracted from the leg of the bend (i.e. the straight portion).

Test Result: PASS: S > 37.92 MPa (5.5 ksi)

Test Data:

Lot and Nominal Bar Size	Specimen ID	Peak Load		Nominal Diameter		Apparent Horizontal Shear Strength S	
		P _{max}		Ø _{nom}		S	
		kN	kips	mm	in	MPa	ksi
#4B V-ROD	HSS1-01	9.50	2134	12.70	0.500	49.97	7.25
	HSS1-02	9.42	2117			49.57	7.19
	HSS1-03	9.14	2053			48.07	6.97
	Average	9.35	2101	49.20	7.14		
	S _{n-1}	0.19	43	1.00	0.15		
	CV (%)	2.0	2.0	2.0	2.0		



Figure 4.7 – Horizontal shear strength test set-up.

◆ END OF TEST REPORT ◆

*** END OF REPORT ***

